

DYNAMIC ANALYSIS OF MULTI CRACKED ROTOR THROUGH EXTENDED LAGRANGIAN MECHANICS

THESIS

**Submitted in Delhi Technological University
for the Award of the Degree of**

DOCTOR OF PHILOSOPHY

in

ENGINEERING

By

**ANUJ KUMAR JAIN
(2K13/PH.D/ME/01)**



**DEPARTMENT OF MECHANICAL, PRODUCTION,
INDUSTRIAL, AND AUTOMOBILE ENGINEERING
DELHI TECHNOLOGICAL UNIVERSITY
DELHI -110042 (INDIA)**

JUNE 2018

Copyright ©Delhi Technological University-2018
All rights reserved

Dedicated to
My Beloved Parents



DELHI TECHNOLOGICAL UNIVERSITY

DELHI-110042 (INDIA)

DECLARATION

I hereby declare that the thesis entitled “**Dynamic Analysis of Multi Cracked Rotor Through Extended Lagrangian Mechanics**” submitted by me, for the award of the degree of *Doctor of Philosophy* to **Delhi Technological University (Formerly Delhi College of Engineering)** is a record of *bona fide* work carried out by me under the guidance of **Prof. Vikas Rastogi & Prof. Atul Kumar Agrawal**.

I further declare that the work reported in this thesis has not been submitted and will not be submitted, either in part or in full, for the award of any other degree or diploma in this University or any other Institute or University.

Anuj Kumar Jain

Enrollment No.: 2K13/Ph.D/ME/01

Department of Mechanical, Production,
Industrial, and Automobile Engineering
Delhi Technological University
Bawana, Delhi-110042

Place: New Delhi

Date:



DELHI TECHNOLOGICAL UNIVERSITY

DELHI-110042 (INDIA)

CERTIFICATE

This is to certify that the thesis entitled “**Dynamic Analysis of Multi Cracked Rotor Through Extended Lagrangian Mechanics**” submitted by **Mr. Anuj Kumar Jain** to Delhi Technological University, Delhi, for the award of the Degree of “*Doctor of Philosophy*” in Mechanical Engineering is a bonafide record of research work carried out by him. Anuj Kumar Jain has worked under our supervision and has fulfilled the requirements for the submission of this thesis, which to our knowledge has reached requisite standards.

The results contents in this thesis are original and have not been submitted to any other Institution or University for the award of any degree or diploma.

Dr. Vikas Rastogi
Professor
Department of Mechanical, Production,
Industrial, and Automobile Engineering
Delhi Technological University
Shahbad Daulatpur, Bawana Road
Delhi-110042, India

Dr. Atul Kumar Agrawal
Professor
Department of Mechanical, Production,
Industrial, and Automobile Engineering
Delhi Technological University
Shahbad Daulatpur, Bawana Road
Delhi-110042. India

ACKNOWLEDGEMENTS

First and foremost I am thankful to almighty GOD for keeping me fit, healthy and energetic during entire course of my Ph.D work.

I would like to express my gratitude to Prof. Yogesh Singh, Vice chancellor, Delhi Technological University, Delhi for providing this opportunity to carry out this work in this prestigious institute.

I would like to thanks Prof. R.S Mishra, DRC Chairman and Prof. Vipin Kumar, Head of the department, Department of Mechanical, Production, Industrial, and Automobile Engineering, for their support to finish this work.

With pleasure, I would like to express my greatest gratitude to my supervisors Prof. Vikas Rastogi, Professor and Prof. Atul Kumar Agrawal, Professor, Department of Mechanical, Production, Industrial, and Automobile Engineering, Delhi Technological University for their proficient guidance, intelligent approach, constructive critique, whole hearted and ever available help, which has been the primary impetus behind the research. Without the wise advice and able guidance, it would have been impossible to complete the thesis in this manner.

I wish to record my thanks and gratitude to our all Internal and External SRC experts, Prof. P. M. Pathak (IIT, Roorkee, U.K.), Prof. Rakesh Sehgal (NIT, Jammu), Prof. Ravinderjit Singh Walia (Delhi Technological University, Delhi), Prof. Rajesh Agrawal (Delhi Technological University, Delhi) for their valuable guidance, critical and constructive discussion during this work.

I also convey my sincere thanks to my seniors Dr. Chandan Kumar, Dr. Loveleen Bhagi for their patience and active support.

I would like to thank my fellow lab mates especially Ashish Gupta, Anuj Sharma, Ravindra Kannoja, Amardeep, Kunal, for helping and encouraging me throughout my research.

Thanks are due to the wonderful friends in my life who were always on the stand by to bring me to positivity, hope and smiles when things didn't seem favouring and it seemed a far-fetched journey. Special mention is deserved for all my other peers especially Dr. Narayan Agrawal, Dr. Pkeshi Bansal, Dr. Satnam Singh, Dr. Kishore Guru, Mr. Dinesh Kumar Nishad who have always been my guiding light when I didn't believe in myself.

I am greatly indebted to my parents, my elder brother Mr. Mr. Sanjay Kumar Jain, Mr. Rajiv Kumar Jain for their love and blessings to see me scaling greater heights of life. One who matters most in my Ph.D work is my wife Dr. Rashmi Jain without whose motivation and encouragement, pursuit of this Ph.D work would have never been possible. I thank her for her care and relieving me entirely from the domestic work. Last but not the least I am thankful to my son Charitra Jain, whose single smile could remove all the tiredness of my work.

Above all, I would thank Almighty for blessing such an affectionate & efficient people playing great asset for me.

(Anuj Kumar Jain)

ABSTRACT

The initiation of fatigue cracks or other defects in structures or machines or their elements cause a reduction in stiffness and also change the dynamic characteristics of the machine. Dynamic analysis of cracked rotor is an emerging area of research due to its practical importance and several issues are associated with this analysis due to its complexity and increasing demand of reliable crack detection techniques. It has been found in archival literature that various crack detection methodologies have been used to analyze the dynamic behaviour of a cracked rotor. The vibration problems of cracked rotor generally pose nonlinearity due to its breathing phenomena. Moreover, the theoretical and computational analysis of the non-linear problems seems to be complex and very expensive even with today's powerful computers. In this work, extended Lagrangian formalism is used for the dynamic analysis of multi-cracked rotor.

Another significant issue for the analysis of vibration of cracked rotor, is the analysis of symmetry breaking of cracked rotor, which is also analyzed in this work. However, this symmetry of rotor is disturbed if there is a small difference in material or geometric properties, caused due to initiation of a crack. The study investigates the dynamic behaviour of a finite asymmetric rotor through extended Lagrangian mechanics. Two case studies are analyzed and presented to develop analytical framework for these systems. Computational models are also developed through bondgraph modeling technique and simulations are carried out and compared with analytical results.

Further, an extended Lagrangian–Hamiltonian formalism is employed to a continuous multi-cracked rotor system. Analytical formulation for amplitude and natural frequency is being derived through this extended Lagrangian–Hamiltonian methodology. Computational model through bondgraphs are being created. Simulations are carried out for various crack depth to analyze the dynamic behaviour of multi-crack rotor system.

Finally, an experimental framework is being developed for the validation of simulation and analytical results. Variation of stiffness due to crack depth and effects of second crack are also determined. Amplitude of vibration at various speeds and different crack depths of multi-crack rotor are examined. NVGate® software is being used for capturing the various signals in running mode of machines. Experimental results validate the analytical and computational results to a great extent. Therefore, it is concluded that the extended Lagrangian methodology is one of the effective and accurate methods to determine dynamic characteristics of a multi-cracked shaft. It may be used for real-time monitoring of the rotor system in various industries.

TABLE OF CONTENTS

	<i>Page No.</i>
<i>Declaration</i>	<i>i</i>
<i>Certificate</i>	<i>ii</i>
<i>Acknowledgement</i>	<i>iii</i>
<i>Abstract</i>	<i>v</i>
<i>Table of Contents</i>	<i>vii</i>
<i>List of Figures</i>	<i>xi</i>
<i>List of Tables</i>	<i>xvi</i>
<i>List of Abbreviations and Nomenclature</i>	<i>xvii</i>
Chapter 1: Introduction	1-28
1.1 Motivation	1
1.2 Literature review	4
1.2.1 Evolution of rotor dynamics era	6
1.2.2 Studies based on breathing phenomenon	6
1.2.3 Studies related with finite element modeling	7
1.2.4 Wavelet transform and wavelet finite element	10
1.2.5 Hilbert-Huang transform	11
1.2.6 Other techniques used in the analysis of cracked rotor	12
1.2.7 Latest developments in analysis of cracked rotor	15
1.2.8 Proposal through extended Lagrangian-Hamiltonian formulation	19
1.3 Significance of bondgraph modeling	21
1.4 Contribution of the present work	25
1.5 Organization of the thesis	27
Chapter 2: Methodology	29-44
2.1 Introduction	29
2.2 Concept of umbra-time and umbra-Lagrangian	30

	<i>Page No.</i>
2.2.1 Variational approach/theory of umbra-Lagrange's equation	34
2.3 Correlation between symmetry and conservation laws	35
2.3.1 Extended Noether's theorem for finite and continuous systems	36
2.3.2 Symmetry breaking approach	37
2.3.3 Symmetry breaking phenomenon for the cracked-rotor system	38
2.4 Concept of umbra-Hamiltonian	40
2.4.1 Importance of umbra-Hamiltonian	41
2.5 Umbra-Lagrangian & the system generated through system bondgraphs	42
2.6 Summary of the chapter	42
Chapter 3: Analytical and Computational Framework for Discrete Rotor with Asymmetries	45-80
3.1 Introduction	45
3.2 Noether's theorem and its extension for finite rotor	48
3.3 Case study–I: Analysis of finite multi-rotor system with asymmetries due to stiffness using extended Lagrangian formalism	50
3.3.1 Umbra-Lagrangian for multi-rotor system with asymmetric stiffness	53
3.3.2 Extended Noether's equation for multi-rotor system with asymmetric stiffness	54
3.3.3 Umbra-Hamiltonian for multi-rotor system with asymmetric stiffness	57
3.3.4 Simulation study and validation	61
3.4 Case study–II: Analysis of finite multi-rotor system with asymmetries due to mass using extended Lagrangian formalism	65
3.4.1 Umbra-Lagrangian for multi-rotor system with asymmetric in mass	67
3.4.2 Extended Noether's equation for multi-rotor system with asymmetric due to mass variation	68
3.4.3 Umbra-Hamiltonian for multi rotor system with asymmetric mass	70
3.4.4 Simulations study and validation	74
3.5 Summary of the chapter	78

	<i>Page No.</i>
Chapter 4: Analytical and Computational Framework for Continuous Rotor with Multi-crack	81-126
4.1 Introduction	81
4.2 Umbra-field formulation for continuous system through Variational approach	81
4.2.1 Generalized variational approach and umbra-Lagrangian density function	81
4.2.2 Variational formulation for continuous one-dimensional (1-D) rotor shaft	85
4.2.3 Extended form of Noether's theorem for continuous system	89
4.3 Analytical framework for continuous rotor with multi-cracks through extended Lagrangian approach	93
4.3.1 Extended Noether's theorem for multi-cracked rotating shaft	96
4.4 Development of computational framework and analysis of multi-cracked rotor system	98
4.4.1 Generation of motion equation	99
4.4.2 Cracked model	101
4.4.3 Bondgraph modeling of multi-crack rotating shaft	107
4.4.3.1 Bondgraph modeling of velocity transformation	107
4.4.3.2 Bondgraph modeling of uncracked rotating shaft	108
4.4.3.3 Bondgraph modeling of cracked rotating shaft	115
4.4.3.4 Lumping of mass and polar moment of (rotary) inertia	117
4.4.3.5 Integrated model of a multi-cracked rotor shaft	119
4.4.4 Simulation study of multi-cracked rotor system	120
4.4.4.1 Simulation results for un-cracked rotor	121
4.5 Summary of the chapter	124
Chapter 5: Development of Experimental Framework and Validation for Multi-crack Rotor	127-156
5.1 Introduction	127
5.2 Experimental test rig	128

	<i>Page No.</i>
5.2.1 Rotor system and its metallic structure	128
5.2.2 DC motor and speed controller	130
5.2.3 Flexible coupling	131
5.2.4 Self aligned bearing	132
5.2.5 Acceleration sensor & tachometer	133
5.3 Signal acquisition and display system	134
5.4 Experimental setup for stiffness measurement	137
5.5 Experimental methodology	139
5.5.1 Formation of crack in the test specimen	139
5.5.2 Stiffness evaluation	139
5.5.3 Dynamic analysis of multi-cracked rotor	140
5.6 Results and discussions	142
5.6.1 Variation in shaft stiffness	142
5.6.2 Comparison between analytical and experimental amplitude	148
5.6.3 Validation of natural frequency through impact hammer test	149
5.8 Summary of the chapter	154
Chapter 6: Conclusion and Future Directions	157-160
6.1 Conclusions	157
6.2 Directions for future research	160
Appendices	161-198
Appendix-A: Bondgraph Elements	161
Appendix-B: Flexibility Co-efficient of an Open Crack	167
Appendix-C: Terminology of Manifolds and Vector Fields	169
Appendix-D: Classical Lagrange's Equation	175
Appendix-E: Umbra-Hamiltonian Theorem	181
Appendix-F: Karnopp's Algorithm	185
Appendix-G: General Condition for Symmetry	195
References	199-210
Publication from the Present Work	

LIST OF FIGURES

<i>Figure No.</i>	<i>Titles</i>	<i>Page No.</i>
Figure 2.1:	Schematic representation of umbra theory	31
Figure 3.1:	Rotor 1 and rotor 2 driven through a DC motor	51
Figure 3.2:	Bondgraph model of multi rotors with artificial flow sources to obtain umbra-Lagrangian in stiffness asymmetries case	52
Figure 3.3:	% Change in amplitude of rotor 1 Vs % change in stiffness	63
Figure 3.4:	Frequency of rotor Vs asymmetries in stiffness	63
Figure 3.5:	Amplitude of the rotor Vs excitation frequency with different stiffness variation	64
Figure 3.6:	Threshold frequency Vs time with different stiffness variation	64
Figure 3.7:	Bondgraph model of multi rotors with artificial flow sources to obtain umbra-Lagrangian in mass asymmetries case	66
Figure 3.8:	Amplitude of the rotor 1 Vs excitation frequency with different mass variation	75
Figure 3.9:	3-Dimensional representation of variation in amplitude of the rotor1, excitation frequency & mass variation	76
Figure 3.10:	Frequency (ω) of rotor 1 Vs mass asymmetries (mass reduced)	77
Figure 3.11:	Frequency (ω) of rotor 1 Vs mass asymmetries (mass added)	77
Figure 4.1:	Representation of a continuous rotor with homogenous rigidity and mass	87
Figure 4.2:	Representation of a DC motor driven rotor shaft coupled by a dissipative coupling	93
Figure 4.3:	Continuous rotor shaft with in-span concentrated discrete stiffness	93
Figure 4.4:	Schematic diagram of multi crack test specimen	95

<i>Figure No.</i>	<i>Titles</i>	<i>Page No.</i>
Figure 4.5:	Co-ordinate system representation of a cracked rotor	100
Figure 4.6:	The closing-opening behavior of a hinge model for small cracks	102
Figure.4.7:	Different angular positions of the crack during single rotation of the cracked shaft continuous balance controller	102
Figure 4.8:	Closing-opening hinge crack model and static displacement in rotational co-ordinate	103
Figure 4.9:	Word bondgraph and capsule representation of fixed-rotating frame velocity transformation in block diagram	108
Figure 4.10:	Generalized forces, displacements and moments of a Rayleigh beam in (a) X-Z plane direction and (b) Y-Z plane direction	109
Figure 4.11:	C- field representing the beam element stiffness matrix in X-Z direction	110
Figure 4.12:	C- field representing the beam element stiffness matrix in Y-Z direction	110
Figure 4.13:	C- field representing the beam element modeling for the stiffness of the shaft in any direction	112
Figure 4.14:	Generalized C- field representing the beam element modeling for stiffness of the shaft	112
Figure 4.15:	Bondgraph model of single rigid element of shaft	113
Figure 4.16:	Bondgraph model of un-cracked rotating shaft	114
Figure 4.17:	Word bondgraph capsule representation of a rotating shaft	115
Figure 4.18:	Beam element model	116
Figure 4.19:	Representation of cracked rotor element	116
Figure 4.20:	C- field representing the stiffness matrix for cracked beam element	117
Figure 4.21:	Lumping of three consecutive shaft elements (capsules) showing mass and rotary inertia on the middle element	118

<i>Figure No.</i>	<i>Titles</i>	<i>Page No.</i>
Figure 4.22:	Integrated system of multi-crack rotor shaft connected by dissipative coupling using capsules represented through bondgraph	120
Figure 4.23:	Limit orbits of Rotor Shaft for uncracked shaft	122
Figure 4.24:	Limit orbits of Rotor Shaft for 1 mm cracked shaft	122
Figure 4.25:	Limiting orbits of the trajectories of the different test specimen (Intact, single and double crack shaft) at different crack depth	123
Figure 5.1:	Experimental test rig for dynamic analysis	128
Figure 5.2:	Actual Rotor system for dynamic analysis	129
Figure 5.2:	Front view and top view of rotor system	129
Figure 5.4:	Schematic diagram of test specimens	130
Figure 5.5:	(a) DC Motor (b) Speed controller	131
Figure 5.6:	Flexible coupling	132
Figure 5.7:	Self aligned bearing	132
Figure 5.8:	Acceleration sensor	133
Figure 5.9:	Tachometer sensor	134
Figure 5.10:	Front panel of OR36	135
Figure 5.11:	Back panel of OR36	136
Figure 5.12:	Display of signal	136
Figure 5.13:	Schematic diagram of experimental set-up of stiffness measurement	138
Figure 5.14:	Cross sectional view of rotating angle between crack and loading direction	140
Figure 5.15:	Variation in stiffness with the single crack depth	142
Figure 5.16:	Variation in stiffness with the multi crack depth (when crack 1 depth is fixed at 5 mm).	143
Figure 5.17:	Some of the angular positions of the crack during one rotation of the shaft	143
Figure 5.18:	Stiffness of cracked rotor at different angular orientation	145

Figure No.	Titles	Page No.
Figure 5.19:	Frequency Vs acceleration for un-cracked shaft and single cracked shaft	146
Figure 5.20:	Frequency Vs acceleration for multi-cracked shaft	147
Figure 5.21:	Frequency Vs acceleration for intact shaft, single cracked shaft & multi-cracked shaft various mode.	147
Figure 5.22:	Analytical Vs experimental value of amplitude at different crack depth	148
Figure 5.23:	Experimental set-up for impact hammer test	150
Figure 5.24:	Frequency Vs acceleration and frequency Vs forces for intact shaft (FFT analysis)	151
Figure 5.25:	Frequency Vs phase change and frequency Vs (acceleration/force) for intact shaft	151
Figure 5.26:	Frequency Vs acceleration and frequency Vs forces for 5 mm single crack shaft (FFT analysis)	152
Figure 5.27:	Frequency Vs phase change and frequency Vs (acceleration/force) for 5 mm single crack shaft	152
Figure 5.28:	Frequency Vs acceleration and frequency Vs forces for a multi-crack shaft of 5 mm and 3 mm crack (FFT analysis)	153
Figure 5.29:	Frequency Vs phase change and frequency Vs (acceleration/force) for a multi-crack shaft of 5 mm and 3 mm crack	153
Appendix Figures		
Figure D.1:	Two possible trajectories $q(\tau; m)$ and $q(\tau; t)$ from $q(\tau_0)$ to $q(\tau_1)$ in configuration space M at two times	177
Figure F.1 (a):	Schematic diagram of a system with a DC motor and a rotating disk in viscous medium	187
Figure F.1 (b):	Bondgraph model of system represented by Figure F.1 (a)	187
Figure F.2 (a):	Causalled bondgraph model of system represented by Figure F.1 (a) with artificial flow sources	188
Figure F.2 (b):	Umbra-Lagrangian generator bondgraph of system represented by Figure F.1 (a)	188

<i>Figure No.</i>	<i>Titles</i>	<i>Page No.</i>
Figure F.3 (a):	Schematic diagram of a mass-spring-damper system	190
Figure F.3 (b):	Umbra-Lagrangian generator bondgraphs of system as shown in Figure F.3 (a)	190
Figure F.4:	Umbra-Lagrangian generator bondgraphs with compacted artificial flow sources	191
Figure F.5:	Umbra-Lagrangian generator bondgraphs showing non-Hamiltonian components	193

LIST OF TABLES

<i>Table No.</i>	<i>Titles</i>	<i>Page No.</i>
Table 3.1:	Simulation parameters	62
Table 3.2:	Simulation parameters	75
Table 4.1:	Simulation parameters	121
Table 5.1:	Detail of test specimen	130
Table 5.2:	Specification of DC motor	131
Table 5.3:	Accelerometer specification	133
Table 5.4:	Tachometer specification	134
Table 5.5:	Change in stiffness in various crack depth	144
Table 5.6:	Stiffness of shaft as a function of rotation angle	144
Table 5.7:	Comparison of natural frequencies	154
Appendix Tables		
Table A.1:	Definition of bondgraph elements with integral causality	163

LIST OF ABBREVIATIONS

1-D	One Dimensional
2-D	Two Dimensional
3-D	Three Dimensional
FEM	Finite Element Method
CWT	Continuous Wavelet Transforms
BSWI	B-spline Wavelet on the Interval
WFE	Wavelet Finite Element
HHT	Hilbert–Huang Transform
ADC	Amplitude Deviation Curve
SDC	Slope Deviation Curve
CCL	Crack Closure Line
GA	Genetic Algorithm
CZM	Cohesive Zone Model
SEDF	Strain Energy Density Factor
MTS	Maximum Tangential Stress
STFT	Short Time Fourier Transform
LEFM	Linear Elastic Fracture Mechanics
TMM	Transfer Matrix Method
CZM	Cohesive Zone Model
AMB	Active Magnetic Bearing
DOF	Degrees of Freedom
BG	Bondgraph
ASTM	American Society for Testing Material Engineering
ISO	International Standard Organisation
Bold face letter	Vector quantity

NOMENCLATURE

$(\dot{\quad})$	Super dot indicates time derivative
$(\acute{\quad})$	Super dash indicates space derivative
A_1, A_2	Amplitude of rotor 1 & rotor 2
EI	Rigidity of the continuous rotor
$F(\tau)$	External force with time fluctuation
$F_1(\tau)$	Force 1 with time fluctuation
$F_2(\tau)$	Force 2 with time fluctuation
G	Gauge Function
H	Real time Hamiltonian
H^*	Umbra-Hamiltonian
\mathcal{H}	Umbra-Hamiltonian density
$\mathcal{H}_i, \mathcal{H}_e$	Interior and exterior umbra-Hamiltonian density
I	Cross-section moment of inertia
I_d	Rotary inertia of the rotor
I_p	Inertia of the beam through principal axis
I_{hub}	Moment of inertia of the spinning hub
$I_{p_{hub}}$	Polar moment of inertia of the hub
I_{stat}	Inertance of stator coil of induction motor
I_{stat}^*	Two phase equivalent inertance of stator coil of three phase induction motor
J	Total polar moment of inertia of the rotor shaft
J_l, J_r	Rotary inertia at the left and right end of the shaft
$K_1(\eta), K_2(\eta)$	Time varying stiffness of rotor 1 & rotor 2
$\Delta K(\eta)$	Time varying asymmetry in stiffness for rotor 1 in x-direction
l'	Element length
L	Lagrangian of the system, Length of the rotating shaft
L^*	Umbra-Lagrangian of the system

\mathcal{L}	Umbra-Lagrangian density
M	Total mass (shaft mass+ hub mass)
M_L, M_R	Limped mass at the left and right end of the shaft
M_{x_l}, M_{x_r}	Bending moments at left and right side of the model
R	Damping coefficient of the damper
R_1, R_2, R_3	Damping resistances, Thermal resistances
R_i, R_a	Damping coefficient of the rotor 1 (internal and external respectively)
R_i', R_a'	Damping coefficient of the rotor 2 (internal and external respectively)
R_b	Resistance of bearings
R_c	Damping coefficient of dissipative coupling
R_i	Internal damping of rotor
R_{ex}	External damping (tensorial nature) of spinning shaft
R_{stat}	Resistance in stator coil of the induction motor
\mathbf{V}	Infinitesimal generator of rotational SO (2) group
$\mathbf{V}^j, \mathbf{V}^k$	j^{th} or k^{th} infinitesimal generator of symmetric group
$\mathbf{V}_t^j, \mathbf{V}_t^k$	Real time component of j^{th} or k^{th} infinitesimal generator
$\mathbf{V}_\eta^j, \mathbf{V}_\eta^k$	Umbra time component of j^{th} or k^{th} infinitesimal generator
V^p	p^{th} infinitesimal generator of symmetric group
V_τ^p	Real time component of p^{th} infinitesimal generator
V_η^p	Umbra time component of p^{th} infinitesimal generator
V_R	Real-time potentials for resistive elements
V^*	Total-umbra potential
V_c^*	Umbra-potential for compliance elements
V_p^*	Umbra-potential for external forces
V_R^*	Umbra-potential for resistive elements

$V_{S_1}, V_{S_2}, V_{S_3}$	Three phase voltages applied to induction motor
V_{x_l}, V_{x_r}	Generalized forces at left and right side of the model
T_1, T_2	Temperatures at the two faces of the thermal conductor
T^*	Umbra-kinetic energy
T_c^*	Umbra-co-kinetic energy
a	Cross sectional area of the rotor
e	Generalized force
f	Generalized velocity
m, m_1, m_2	Mass ,modulatory variable
t	Trajectorial variable
n	Mode number
p_{x_1}, p_{y_1}	Linear momentum of rotor 1 in x and y direction
p_{x_2}, p_{y_2}	Linear momentum of rotor 2 in x and y direction
p_θ	Angular momentum
$p(\tau)$	Real-time momentum
$p(\eta)$	Umbra-time momentum
$q(\tau)$	Generalized displacement in real time
$q(\eta)$	Generalized displacement in umbra-time
$\dot{q}(\tau)$	Generalized velocity in real time
$\dot{q}(\eta)$	Generalized velocity in umbra-time
$u_i(\tau)$	Real displacement coordinates of continuous shaft
$u_i(\eta)$	Umbra- displacement coordinates of continuous shaft
$x(\cdot), x_i(\cdot)$	Linear displacements
$x_i(\cdot), y_i(\cdot)$	Displacements in umbra time / real time, where $i = 1 \dots n$
$\dot{x}_i(\cdot), \dot{y}_i(\cdot)$	Velocities in umbra time / real time, where $i = 1 \dots n$
$\ddot{x}_i(\cdot), \ddot{y}_i(\cdot)$	Acceleration in real time, where $i = 1 \dots n$
τ	Real-time

Subscript	
c	Dissipative couplings
i	Internal damping, interior, coordinate number
n	Mode number
$eqrot$	Equivalent rotor
$stat$	Stator
τ	Real-time component
η	Umbra-time component
t	Translational
e	Exterior
$prev$	Previous
$next$	Next
rot	Rotational

Greek Symbols	
Ω	Excitation frequency
Ω^*	Non-dimensional excitation frequency
Ω_n	Natural frequency of the rotor shaft
Ω_{th}	Threshold excitation frequency
α	Non-dimensional bearing resistance parameter, angular rotation of the shaft
ϕ_n	Model function for pin-pin end conditions
η	Umbra-time
λ	Position of the discrete damper
μ_{ex}	External damping of the continuous shaft
μ_i	Internal damping of the beam
$\theta()$	Angular displacement in umbra-time or real time
$\dot{\theta}()$	Angular velocity of the shaft in umbra-time or real time, Shaft spinning speed
ρ_i	Rotary inertia density of the shaft
ω	Natural frequency of the shaft in electromechanical system, Angular velocity

ω^*	Non-dimensional spinning speed of the shaft
ω_{th}	Threshold speed of rotor

Bond Graph Elements

0	Common effort junction
1	Common flow junction
I	I-element or Inertial element
C	C-element or compliant element
R	R-element or dissipative element
SE	Source of effort
SF	Source of flow
TF	Transformer
GY	Gyrator
P	Momentum
Q	Displacement
e_i	Generalized effort in i^{th} bond
f_i	Generalized flow in i^{th} bond

Chapter 1

Introduction

1.1 Motivation

The rotating components of machines like turbines, pumps, generators and high speed compressor, which are subjected to the extreme loading conditions, has widespread applications in various fields ranging from aircrafts, automobiles, and power generation equipments. Rotor shaft can be regarded as one of the components prominent amongst various parts of rotating machineries. The defects in shaft may be due to manufacturing conditions or due to loading conditions (cyclic loading) and the fatigue cracks are quite prevalent in rotating shaft. The different kinds of defects such as notches, slits, cracks, and asymmetries in components of machines may lead to a catastrophic failure of rotating machine shafts. Cracks on the shafts may be due to different causes namely, fluctuating bending stresses, fatigue stresses, torsional stresses, creep and corrosion (*Patel and Darpe, 2008*). For this reason, cracked rotors have attracted the attention of researchers since last 50 years.

In the power plant, equipments such as steam turbines and steam generators, the stresses caused by thermal loadings are generally accountable for high stress intensity factors that are further responsible for crack initiation and propagation. This failure may cause hazardous working conditions, and may turn up in human injuries, as well as great economic and equipment losses. One of the most common losses of rotor in mechanical structures is the development and propagation of cracks. A crack may propagate even for a small imperfection on the surface or inner volume of rotor material and it is most likely to originate from zones of high stress concentration.

Generally, the initiation of fatigue cracks or other defects in structures or machines or their elements cause a reduction in stiffness and also change the dynamic characteristics of the machine. Dynamic analysis of cracked rotor is an emerging area of research due to its practical importance. Owing to its complex behavior and ever increasing need as a realistic tool of crack detection, multiple issues associated with this analysis must require to give due consideration. Vibrations of cracked rotors frequently exhibit nonlinear behavior due to breathing phenomenon. This type of behaviour limits the application of conventional approach, such as model analysis, and harmonic response methods for their analysis. In addition to this, the analysis of the non-linear behavior using theoretical and computational approaches, is generally of complex nature and includes high computational costs. All these observations and limitations leads to the development of accurate, efficient, and reliable theoretical and computational framework for modeling the vibrational response of cracked rotor.

Extensive literature survey (*Dimarogonas, 1996; Gasch, 1993; Kumar and Rastogi, 2009; Sabnavis et al., 2004; Wauer, 1990*) reveal that researchers have used various analytical and simulation techniques in the field of rotordynamics; however limited literatures (*Kumar, 2013; Mukherjee, 1994, 2001; Mukherjee and Karmakar, 2000; Mukherjee et al., 2006, 2007, 2009, 2011; Rastogi, 2005; Rastogi and Kumar, 2009*) are available on dynamic analysis through extended Lagrangian mechanics. It is a well known fact that the crack containing rotating machine components causes the forces generated through non potential fields and dissipative source. The application of classical Lagrange's equation is not preferred for studying the dynamic behavior of such system involving non holonomic constraints, non-potential forces, dissipative forces, gyroscopic forces and general class of systems with time fluctuating parameters. Therefore some

additional information of system interior and exterior need to be given to generate extended Lagrangian equations, which may be applicable to the crack rotor system.

Another challenge in the analysis of nonlinear vibration of cracked rotor is posed by the breaking of symmetry of the rotor. The cracks induced in the rotor disturb the symmetry of rotor. This problem can be simplified and dealt with by introducing the concept of cyclic symmetry in the vibrational analysis of cracked rotor, which relies on assuming every sector of the rotors to be an identical and symmetric. However, minor variations in the material or geometric characteristics of the rotor caused due to initiation of a crack, may result in the loss of symmetry of rotor.

Furthermore, in the search of realistic modeling approaches for analysis of multi-crack rotor, the application of finite element method, and other solid modeling approaches are more likely to appear in the list. On the other hand, bondgraph modeling technique proved to be very promising in the system modeling as it effectively represents the essential dynamics by facilitating the system modeling from the physical paradigm itself. Therefore, the bondgraph technique is profitably used to obtain the numerical results. This technique greatly improves the computational efficiency of the analysis. In modeling the behavior of continuous cracked rotor; the computational time and accuracy of results obtained are significantly dependent on the complexity of the crack model formulation. To be more specific, the damping property and flexibility matrix of rotor shaft is thought to be the key parameters that have a significant impact in controlling the accuracy, reliability and computational time for the analysis. Therefore it is important for the creation of computational model of a continuous cracked rotor to incorporate all these factors in order to effectively determine its dynamic behaviour.

To validate the accuracy of the result obtained from the theoretical and computational analysis, experimental analysis is essentially required to be carried out. This also facilitates the actual implementation of the proposed methodology. The development of experimental test rig is required for conforming the results obtained by analytical and simulation model. In line with the above discussion, the objectives of the present research are to acquire in depth understanding of analogy of vibrations developed in multi-cracked rotor system using extended form of Lagrangian-Hamiltonian approach and further to develop a novel explicit equation for capturing the system behavior. The multi-cracked rotor is being investigated as finite system as well as continuous system for the parametric analysis. The major objectives for the present work are outlined as

- To develop an analytical & computational frameworks for discrete asymmetric multi-rotor system through extended form of Lagrangian formulation.
- To extend the analytical frameworks for continuous multi-cracked rotor system through extended Lagrangian formalism.
- Computational investigation of dynamic behaviour of multi-cracked rotor system using bondgraph technique.
- To validate the results obtained from theoretical analysis by developing experimental framework for the analysis of multi-crack rotor system and to develop experimental test rig for the same.

1.2 Literature review

The occurrence of crack in a rotor shaft is one of the most critical issues to address the performance of heavy rotating machinery. This analysis is very essential to ascertain the

smooth, effective and efficient operation and performance of the machine and hence, has been given due consideration by various researchers throughout the globe. In the last 50 years, significant progress has been made in the field of cracks detection and analysis. Beginning from 1970, a huge contribution in terms of research papers on crack detection and its effects had been made by various researchers in the archival literature. Various review paper have been also published on a regular time interval by various researcher like *Wauer* (1990), *Gasch* (1993), *Dimarogonas* (1996), *Sabnavis et al.* (2004). Some recent papers were presented by *Papadopoulos* (2008), *Kumar and Rastogi* (2009) and *Sekhar* (2011).

For crack detection and study of dynamic behavior in cracked rotor, various techniques and approaches have been used like finite element method, Hilbert-Huang transform, wavelet transform, nonlinear dynamics, breathing mechanism, transfer matrix method, harmonic balance technique, Floquet theory, and direct optical observation. Noticeable progresses have reported in crack detection research during these years. Due to a large demand of more powerful rotor for power plants and gas turbine etc., it requires a more reliable and accurate technique to show the inception and propagation of cracks in a rotating machine elements. An alternate method based on the symmetry analysis is being presented to analyze the dynamics of a multi-crack rotor. The cyclic symmetry of the rotor has been used to investigate the dynamic of multi-crack rotor through symmetry breaking approach. Different modeling methods applied to investigate the dynamic behaviour of crack rotor presented in this section by various researchers time to time. The next subsections will present the review and classification of existing literature.

1.2.1 Evolution of rotor dynamics era

Rankine has initially studied the dynamic behaviour of a rotor system, which was followed by Jeffcott. Since 1970, a lot of attention on dynamic behaviour of cracked rotor has been given by many researchers for different points of analysis. *Wauer* (1990) has made a significant review on studies and investigations of cracked rotor in the last few decades. *Gasch* (1993) has presented a nice survey on a simple rotor. *Dimarogonas* (1996) and *Sabnavis et al.* (2004) have also presented a review paper. *Kumar and Rastogi* (2009) have reported a brief review based on different methodologies used by various researchers for dynamic analysis of a cracked rotor. *Mayes and Davis* (1984) have analyzed the effects of a transverse crack on multi-rotor bearing system. Firstly, *Dimargonas and Papadopoulos* (1983) have investigated the dynamics of cracked rotor by taking the transverse crack occurring as a result of fatigue of shaft material resulting from the excessive bending moment. *Dimargonas and Papadopoulos* (1987) have also studied the coupling of bending and torsional vibration of a cracked Timoshenko shaft using 6X6 matrix for flexibility due to change in stiffness and also analyzed the dynamic behaviour of a cracked rotor.

1.2.2 Studies based on breathing phenomenon

When cracked shaft rotates under the external load, the crack opens and closes regularly per revolution, it is called breathing. Due to the action of bending moment the stress distribution around the crack produces the breathing mechanism. *Georgantzinis and Anifantis* (2008) explained association of local flexibilities with a breathing crack in a rotating shaft and provided a simulation of rotating load on a fixed beam and then, simulation results were used for the cracked analysis. *Patel and Darpe* (2008) have used two well known models for crack breathing simulation in rotors. First was the

switching crack model, representing the switching of rotor stiffness values from one coinciding fully opened crack condition to another coinciding closed crack condition and vice versa. Second is response-dependant breathing crack model should be used to follow the true breathing behavior of the cracked rotors, presented by *Jun et al.* (1992). *Chasalevris and Papadopoulos* (2009) have investigated cross-coupled bending vibrations of a rotor-bearing system with a transverse breathing crack.

Al-Shudeifat et al. (2010) have given an efficient technique for analysis of the behaviour of the cracked rotor system. Behaviour of the whirl orbits, vibration amplitudes and frequencies of a damaged rotor-disk-bearing system may help in detecting the crack at the beginning of its growth. This may be found while generating waterfall plots. Orbit shapes changes at critical and subcritical rotor speeds at very low crack depths. Hence, tracking the change in orbit shapes in the neighbourhoods of subcritical rotor speeds at low crack depths can be used as an earlier indication of a propagating breathing crack. *Guo et al.* (2013) have investigated stability analysis for transverse breathing cracks in rotor systems by a new breathing function for the cross-coupling stiffness were developed to represent the breathing mechanism more accurately. The effects of crack depth and rotating speed on the dynamic properties of the rotor system were studied by using Floquet theory. They also compare the stability diagrams for the systems with and without damping.

1.2.3 Studies related with finite element modelling

The main feature of FEM is three dimensional (3-D) visualization, which makes it a suitable tool for the study of crack formation and propagation mechanism. The suitability of finite element method (FEM) may be attributed to its ease of applicability

and hence, many researchers have adopted the finite element technique for dynamics analysis of crack in rotating shaft. Finite element method saves time and money by allowing reductions in equations while solving the equation systems. *Ichimonji and Watanabe* (1988) have investigated a slant fatigue crack usually occurred from the torsional moment on a shaft. They have analyzed the dynamics of a simple rotor for qualitative analysis using a 3D finite element method. *Sekhar and Prabhu* (1994) have studied the vibration and stress fluctuation in cracked shafts and investigated a simply supported shaft with a transverse crack for the vibrational characteristics. Finite element analysis (FEA) has been carried out for free and force vibrations. *Sekhar and Prasad* (1999) have performed the dynamic analysis of a rotor system for a slant crack in the shaft. Using FEM analysis of the rotor bearing system for flexural vibration, they observed the reduction in the eigen frequencies of all the modes with an increase in depth of crack. For the same crack location, it is noticed that small decrease in eigen frequencies in slant crack as compared to transverse crack.

Sekhar (1990) has analyzed the vibration characteristics of a cracked rotor with two transverse open cracks using finite element analysis (FEA) for flexural vibrations. He observed that for two cracks of different depths, the larger crack has more pronounced effect on the eigen frequency as compared to the smaller one. *Sekhar and Dey* (2000) have investigated effects of cracks on rotor system instability and applied FEM and consider various parameters and shaft internal damping (viscous and hysteretic damping) and geometric parameters. It has been noticed that the instability speed has been reduced considerably with increase in crack depth and influenced more with hysteretic damping compared to viscous damping. *Nandi* (2004) has presented a

simple method for reduction of finite element model of nonaxisymmetric rotors on nonisotropic spring.

Bachschnid et al. (2008) have investigated the rotor shaft affected by a helicoidal crack by 3D finite element non linear models. This model has been used for calculating deflections of a cracked specimen and breathing behavior, which has loaded with bending and torsion loads. After that they compared helicoidal crack to transverse crack model results. Positive Torsion loads increase deflections, when torsion opens the crack and stiffness will reduce. *Patel and Darpe* (2009) have investigated coupled lateral-torsional vibrations response for crack and rub faults using FE model.

Han et al. (2012) have analyzed slant cracked geared rotor by using finite element model. Using the concept of fracture mechanics, they have examined three methods for whirling analysis, parametric instability analysis and steady-state response analysis. The effects of slant crack upon the whirling characteristics, parametric instability and steady-state response for the system under unbalance force and tooth error excitations are investigated. It has been observed that in presence of the slant crack on the transmission shaft, the whirling frequencies of the system are drastically reduced. For the same crack depth, the frequency reduction value of slant crack is lower than that of transverse crack. *Al-Shudeifat* (2013) has worked on the finite element modeling of the asymmetric cracked rotor and introduced finite element model of the time-varying stiffness matrix is for a cracked rotor with an open transverse crack. He has shown that the open crack model excites the backward subcritical whirl. It is verified here that the whirl orbits with inner loops are a unique signature for the breathing crack rather than the open crack.

Darpe (2007) has investigated the dynamics of a Jeffcott rotor with slant crack describing the flexibility matrix for the slant crack. *Georgantzinou and Anifantis* (2008) have studied the effect of crack breathing phenomenon on the time varying flexibility in a spinning shaft. They considered the quasi-static approximation in the extended form of nonlinear contact-FEM formulation. They have predicted the partial contact of crack surfaces, and reported the suitability of this method to evaluate the instantaneous crack flexibilities.

1.2.4 Wavelet transform and wavelet finite element

Since the last 10 years, a great interest has been shown by the researcher in the wavelet theory. Fault diagnosis of rotary machines has promoted continued advancement of measurement as well as signal-processing technologies. Wavelet transform can be used as a mathematical tool that transfers a signal in time domain into a different form. The wavelet transform can be categorized as CWT, DWT, and WPT. This method can be suitably applied for detection of depth of damage at a particular location using model frequencies, and model shape etc. *Adeswusi and Al-Bedoor* (2001) have investigated an overhang rotor with a propagating transverse crack using discrete wavelet transform. He concluded that crack reduces the critical speed of the rotor. He has also presented such results in 2D graphs (scalograms) and 3D graphs (space-scale energy distribution graphs).

Sekhar (2003) has investigated crack detection through wavelet transform for a run-up rotor. He has found subharmonic resonant peaks (using CWT) when the cracked rotor is passing through its critical speed. These peaks are not apparent in frequency spectrum as well as in time response. Based on wavelet transform techniques, *Darpe* (2007) has developed a method to detect transverse surface crack in a rotating shaft.

Wavelet coefficient is highly sensitive to the depth of crack and even a very shallow crack (5% of rotor diameter) can be detected. The value of this coefficient for bending vibration in horizontal direction is highly sensitive to depth of crack and hence can be used for early detection of crack in rotors.

Deng and Wang (1998) have used the discrete wavelet transform to investigate a crack along the length of a beam. *Prabhakar et al.* (2001) has been shown the effectiveness of wavelet transforms for detection and monitoring of cracks. *Sekhar* (2003) has used continuous wavelet transforms (CWT) to detect transverse cracks considering the time domain signals of the decelerating rotor.

Xiang et al. (2006) have also proposed a finite element method of a B-spline wavelet on the interval (FEM BSWI) Euler beam model for detecting crack location as well as crack size in a beam. The simulation and experimental results showed the high performance of the BSWI Euler beam element. B-spline wavelets have the best approximation properties among all known wavelets method. *Dong et.al* (2009) have used wavelet finite element (WFE) model to determine the depth and location of a transverse surface crack in a rotor system. The rotor system is modeled using FEM BSWI, while the crack is assumed as a weightless rotational spring. Another novel method based on empirical mode decomposition and Laplace wavelet was proposed to obtain modal parameters with high precision. The results of the proposed approach were confirmed by experimental analysis and various crack parameters were identified.

1.2.5 Hilbert-Huang transform

Hilbert–Huang Transform developed by Norden E. Huang has a good potential for dynamic and nonlinear data analysis, especially for time-frequency-energy domain

representations. HHT gave results much sharper than the wavelet. It has been found that HHT appears to be a better tool compared to fast Fourier transform and continuous wavelet transform for natural fatigue crack characterization in a rotating rotor in all experiment cases. *Li et al.* (2012) have investigated the influence of acceleration and crack depth on the rotor through experiments. The results of experiment showed that HHT is a better tool for crack detection. *Lin et al.* (2012) have used HHT to search AE signal time–frequency–energy features of nature fatigue cracks on rotating shaft. *Babu et al.* (2008) have used Hilbert-Huang transform for detection and monitoring of a crack in a transient rotor. It is very usefull for identification for very small crack depth; where continuous wavelet transforms fail. *Guo and Peng* (2007) have used HHT for possibilities and observance of crack in transient behavior of a cracked rotor. HHT is a promising tool for analyzing rubbing vibration signal that exhibited nonlinear and non-stationary properties, particularly for identifying cracks of small depths.

1.2.6 Other techniques used in the analysis of cracked rotor

Besides the techniques and methodology discussed in previous sections, some other techniques and methods have been developed by several researchers for the analysis of a cracked rotor. An extensive approach including theoretical, numerical and experimental analysis for a crack detection in rotating parts of machines is given by *Stoisser and Audebert* (2008). Theoretically, they have derived a lumped cracked beam model from 3-D formulation of the problem of elasticity with unilateral contact conditions on the crack lips. That is valid for any shape and number of cracks in the beam section and extended to cracks not located in a cross-section. Cracked beam rigidity can also calculate as a function of the rotation angle, in case of pure bending load or bending plus shear load, which has been validated through experimental results.

Saridakis et al. (2008) have used neural networks, genetic algorithms (GA) and fuzzy logic for the identification of cracks in shafts by using coupled response measurements. It is an efficient tool for real-time crack identification.

Chasalevris and Papadopoulos (2008) have investigated coupled horizontal and vertical bending vibrations of a stationary shaft with two cracks. They found that coupling becomes stronger when cracks are in phase, if cracks are opposite then the coupling turns weaker. They have also validated that deeper crack makes the coupling phenomenon more intense. *Xiang et al.* (2008) have detected crack location and its depth in a shaft. Rayleigh-Euler and Rayleigh-Timoshenko beam elements of B-spline wavelet on the interval (BSWI) were constructed to discretize slender shaft and stiffness disc, respectively. Wavelet-based modeled cracked shaft was used to obtain precise frequencies; which were used in crack detection process and the normalized crack location and depth was detected using genetic algorithm (GA). *Sinou* (2008) has investigated that the super-harmonic components of 2X and 3X revolution could be used to detect a crack in the sub-critical speed region in rotor systems. Crack–unbalance interaction does affect the vibration amplitudes of super as well as sub harmonic frequency. Super harmonic frequency components can be used to detect the presence of a crack in the rotor even crack–unbalance orientation and the unbalance magnitude are not known.

Babu and Sekhar (2008) have developed a new technique amplitude deviation curve (ADC) or slope deviation curve (SDC) for the detection of two cracks in a rotor-bearing system. It is a good investigating tool for online detection of crack parameters even small cracks around 0.1 times the shaft diameter. *Jun and Gadala* (2008) have

presented the analysis of dynamic behavior of crack containing rotor. In this research, they have considered an additional slope for crack breathing. They have used fracture mechanics concept formulate the response of cracked rotor on the basis of transfer matrix method. *Gasch* (2008) has worked on dynamic behaviour of the Laval rotor with a transverse crack in the elastic shaft. He has used Floquet's method and results presented in an overview diagram. *Szolg et al.* (2009) have used stochastic approach based on the Monte Carlo simulations for crack detection and identification in the rotating shafts. They have used hinge-model and fundamentals of the fracture mechanics for a local shaft weakening as well as mutual coupling of shaft flexural, torsional and axial motions due to a cross-sectional anisotropy caused by the crack. All results obtained from Monte Carlo simulation have been verified through experimental results.

Darpe et al. (2004, 2006) have evaluated the coupling between longitudinal, lateral and torsional vibrations of a rotating shaft using response-dependent non-linear breathing crack model. Assuming the closed part of the crack surface is bounded by "crack closure line" (CCL), they concluded that it can be represented by a segment, orthogonal to the crack tip that can be drawn from that point on the crack tip. *Chasalevris and Papadopoulos* (2009) have used the parameters such as position, depth and relative angle to characterized the cracks. They firstly introduced the concept of compliance calculation in analysis of cracked shafts with rotated cracks. The bending compliance matrix of the crack was developed using the method of integration of the strain energy density function over an opened crack surface.

In another study, *Karthikeyan et al.* (2007) have analyzed the crack localization and sizing as represented in a beam model. They applied the free and forced response

measurement method in their analysis. *Jain and Kundra* (2004) have applied a model based on inline investigation of unbalance induced due to transverse fatigue crack developed in a rotor system. *Gosiewski* (2009) has introduced control oriented approach in rotor dynamics application. *Lin and Chu* (2009) have investigated flexural vibrations of a rotor system with transverse or slant crack. They have investigated a 45° slant crack on Jeffcott type rotor system. They developed four types of directional motion equations namely, two transverse, one torsional and one longitudinal direction. The study has revealed that a bending–torsion coupling was resulted due to eccentricity of the rotor. *Tsai and Wang* (1997) have used transfer matrix method (TMM) for free-vibrational analysis of multi-crack rotor. Cracks were assumed to be in the opening mode (first mode of fracture). The effects of relative distances along axis and orientations of cracks, both were considered in free vibration analysis. *Durali and Borhan* (2003) have investigated discrete dynamic modeling of rotating Timoshenko shaft with transverse cracks using bondgraph. The next sub-section will highlight some recent development in multi-crack rotor analysis.

1.2.7 Latest developments in analysis of cracked rotor

Since 2010, several recent methodologies have been introduced for identification of multiple cracks and its analysis. *Singh and Tiwari* (2010) have proposed an identification methodology to identify number of cracks and their location on a cracked shaft. The methodology used transverse forced response of a cracked shaft at several frequencies to reduce the effect of noise in the signal; these responses have been predicted by FE modeling. The identification algorithm has defined crack probability functions, which provided the number of cracks present in the shaft and their approximate locations over it. They have also introduced a multi-objective optimization

function; which was solved by using the non-dominated sorting genetic algorithm-II. Informations obtained from the identification algorithm (at the first stage) were used to define the design space for the GA at the second stage. They have used this method on simply supported shaft having two cracks and got satisfactory results.

Han and Chu (2011) have compared straight front crack model with elliptical front crack. They have found elliptical front crack model which has found to be more accurate and realistic for modelling the transverse surface crack in the rotor shaft. The local flexibilities of an elliptical cracked shaft solved by means of numerical integration technique. Once, the elliptical front and shape variation are considered, obtained flexibility values are reduced, specially for the deeper surface cracks. *Al-Shudeifat and Butcher* (2011) have introduced two new breathing functions, which represented the actual breathing effect on the cracked element stiffness matrix. The new breathing functions were used in formulating the time-varying finite element stiffness matrix for the cracked rotor system. The analytical results of this approach have been verified with previously published results, obtained using approximate formulas for the breathing mechanism. The comparison has showed that the previously used breathing function is a weak model for evaluating the breathing mechanism in the cracked rotor even for the small crack depths. The new breathing functions have given more accurate results for the dynamic behaviour of the cracked rotor system for a wide range of the crack depths even for the critical and subcritical speeds of rotor shaft.

Rubio et al. (2011) have investigated static behaviour of a shaft with an elliptical crack. Flexibility functions for cracked shafts having elliptical cracks, based on the polynomial fitting of the stress intensity factors were obtained. The static

displacements in bending of the shaft for different support have been calculated under the consideration of different size and shape of elliptical crack. The obtained results have been compared with FEM analysis and experimental results. *Cheng et al.* (2011) have investigated the influence of crack breathing and imbalance orientation angle on the characteristics of the critical speed of a cracked rotor. They have used angle between the crack direction and the shaft deformation direction for determining the opening and closing of the crack and also, investigated the effect of nonlinear breathing of the crack and imbalance orientation angle on the stability, peak response and critical speed of the rotor. They have found basic characteristics of a cracked rotor near its critical speed, which are similar to those of an uncracked rotor. *Ricci and Pennacchi* (2012) have used a real hyperstatic rotor model with several degrees of freedom. They have analyzed stability in the presence of the transverse crack by the multi dimensional Floquet theory. They have also developed an algorithm to execute multi-dimensional Floquet analysis.

Bovsunovsky (2012) has formulated the relationship between the crack size and the energy dissipation in a crack. He has introduced the principle mechanisms of energy dissipation in a surface fatigue crack at torsional vibration through direct experimental investigation. He has explained that that energy dissipation in the non-propagating transverse crack at torsional vibration was caused mainly by the plastic zone along the crack front rather than by the friction of crack faces. *Liong and Proppe* (2013) have proposed a cohesive zone model for the evaluation of the stiffness losses in the cross-section that contained a crack. Since LEFM has major limitations and the cohesive zone model (CZM) described material failure on a phenomenological basis (i.e. without considering the material microstructure). Cohesive zone model generally depends only

on the material, not on the geometry. *Li et al.* (2013) have introduced a simple method for calculating stress intensity factors of transverse cracked shaft subjected to tension, bending and shear. They have formulated stress intensity factor in terms of the crack depth. They have found that initial crack growth angle of bending-shear mixed mode calculated by the SEDF (Strain Energy Density Factor)-criterion was a slightly bigger than that one calculated with MTS (Maximum Tangential Stress)-criterion. *Silani et al.* (2013) have worked on a new breathing crack model. They have also introduced a computer code. Two investigations have been performed on the rotor, one with constant speed and another start-up and only open part of the crack considered in each angular position. The results explained that detection of the crack during start-up was easier. They found that short time Fourier transform (STFT) can clearly identify small cracks as compare to transient response.

Guo et al. (2017) have validated theoretical results of the dynamics behaviour through experimental investigation. The breathing crack in the rotor is simulated by a real fatigue crack. They have decomposed dynamic responses into several subcomponents by the EMD method. The experimental results were well corroborated with the theoretical analysis, which indicated that EMD based crack detection method is practicable. In another research, *Singh and Tiwari* (2018) have investigated crack effects in flexible rotor systems supported with active magnetic bearing (AMB). They have introduced an algorithm, which identified the crack force in form of additive crack stiffness and simultaneously estimates the disc unbalances, end support bearing stiffness and active magnetic bearing dynamic parameters as well. The algorithm has been tested in a simple rotor system for the measurement of noise and bias errors in the system

parameters, and found to be robust. The next section will highlight the various extension of Lagrangian-Hamiltonian formulation.

1.2.8 Proposal through extended Lagrangian-Hamiltonian formulation

Various literatures (*Dimarogonas, 1996; Gasch, 1993; Kumar and Rastogi, 2009; Sabnavis et al., 2004; Wauer, 1990*) reveal that researchers have used various analytical and simulation techniques in the field of rotordynamics; however limited literatures (*Kumar, 2013; Mukherjee, 1994, 2001; Mukherjee and Karmakar, 2000; Mukherjee et al., 2006, 2007, 2009, 2011; Rastogi, 2005; Rastogi and Kumar, 2009*) are available on extended Lagrangian mechanics. It is a well-known fact classical Lagrange's equation cannot analyze the dynamics of systems, where asymmetric rotating component produces non potential and dissipative forces. It fails to solve systems having nonpotential forces, gyroscopic forces, dissipative forces, nonholonomic constraints, and time fluctuating parameters. Analysis of such problems requires the additional informations of system's interior and exterior to be given at first hand for generating extended Lagrangian equations based on bondgraphs theory (*Karnopp et al., 1990; Breedveld and Dauphin-Tanguy, 1992; Gawthrop and Smith, 1996*). These extended Lagrangian equations coupled with bondgraphs simulation may be used to solve the problem of asymmetric rotating component. In the problems involving symmetries, it is easy to derive useful information such as constant of motion and these symmetries reduce the complexity of the dynamical systems such as cracked rotor. For problems involving asymmetries, a lot of effort is required to solve the complex system.

It has been reported that Noether's theorem (*Noether, 1918, 1971*) plays a significant role in determination of invariants of motion. Further, theorem allows

exploitation of symmetries of the system to arrive at invariant of motion. Extended form of Noether's theorem with umbra's Hamiltonian provides the insight of dynamics of the asymmetric rotor system. To extend the scope of Lagrangian-Hamiltonian mechanics, a new proposal of additional time like variable "umbra (virtual)-time" was proposed by *Mukherjee* (1994) and this new concept of umbra (virtual)-time leads to a peculiar form of equation, which is termed as umbra-Lagrange's equation. Virtual/umbra-time also introduced a novel concept named as umbra-Hamiltonian, which provides an understanding of dynamics of system with symmetries when used along with the extended form of Noether's theorem.

One of the significant advantages of using the umbra-Lagrangian formalism is its underlying variational principle (*Rastogi*, 2005), which uses recursive minimization of functional for their development. By using this formulation a general class of system can be derive by applying a least action principle. Further *Rastogi* (2005) has expressed all these notions in an extended manifold comprising of virtual/umbra, and real time and real time displacements and velocities. The umbra-Lagrangian theory has given the fruitful outcomes, when it is used to study invariants of motion for non-conservative mechanical and thermo-mechanical systems. Using umbra Lagrangian theory, *Mukherjee et al.* (2007) have studied the dynamics of an electro-mechanical system consisting of an induction motor running an elastic rotor. *Mukherjee et al.* (2009) have also investigated the dynamics of a one-dimensional rotor having internal damping conditions and applying dissipative coupling. In addition, *Rastogi and Kumar* (2009) have investigated the dynamics of asymmetric rotor by extended form of Lagrangian-Hamiltonian mechanics. This work had augmented the scope of umbra-Lagrangian in the field of rotor dynamic research. In a study, *Kumar* (2013) has investigated the

dynamic behavior of a single cracked rotor system through Extended Lagrangian formalism. No such work is available in archival literature on dynamic analysis of multi-crack rotor system through extended Lagrangian mechanics.

This work investigates the dynamic behaviour of multi-cracked rotor through extended Lagrangian formalism. This is in order to enlarge the range of extended Lagrangian formalism employed for any discontinuous rotor system in terms of cracks. The bondgraphs are profitably used to obtain umbra-Lagrangian of the system. Further, the experimental results are corroborated with analytical results to consolidate the extended Lagrangian theory applicable for rotordynamics problem.

1.3 Significance of bondgraph modelling

Modeling of engineering systems through bondgraphs is based on exchange of power amongst the basic elements of the system and several energy domains can be represented in a unified manner. In 1960's, *Paynter* (1961) gave the revolutionary idea of portraying systems in terms of power bonds, connecting the elements of the physical system to the so-called junction structures which were manifestations of the constraints. This power exchange portrayal of a system is called bondgraph which can be both power and information oriented.

The bondgraph causality concept, introduced by *Karnopp et al.* (1990), describes the orientation of the flow of calculus schemes within the system model. This constitutes the physical level of the description contained in the bondgraph representation. In his work, *Karnopp* (1977) introduced the concept of artificial flow sources and proposed the algorithmic generation of Lagrange's equation for complex systems with the help of their bondgraph models. This is supposed to emphasize the

role of generalized velocity in the analysis. A modified procedure of this method is given by *Dijk* (1994). Few other contributions in this line, devoted to mathematical formulations of dynamical systems are as presented by *Brown* (1981, 2006) and *Karnopp* (1983). *Breedveld and Hogan* (1994) were also credited with the multi-bondgraph representation of Lagrangian mechanics. *Thoma* (1990) have given a graphical method for simulation by bondgraph. *Gawthrop and Smith* (1996) have done Meta Modeling for dynamic system through bondgraph. *Breedveld and Dauphin-Tanguy* (1996) have presented bondgraphs for modeling the engineering systems. This modeling technique may be conveniently applied to analyze the real problem by engineers. *Granda* (1985) have proposed a method of generation of physical system differential equation using bondgraphs. *Borutzky* (2015) has presented bondgraph model-based fault diagnosis of hybrid systems.

Advancing the idea given by *Karnopp's* (1977) further to broader class of systems, *Mukherjee and Samantaray* (1997) introduced a detailed procedure to generate umbra-Lagrangian through system bondgraphs. In this approach two similar bondgraphs of the system are created. One of them is based on real time and another one on umbra (virtual)-time. The junction structures are modified and introduced the bonds connecting the two diagrams known as trans-temporal bonds. Rest of the procedure follows the *Karnopp's* approach to arrive at the umbra-Lagrangian of the system.

Banerjee and Karmakar (2007) have developed a bondgraph model of a free rail wheelset rolling on curved track using sub models called capsules. A railway truck running on flexible tangent track has been modeled by *Saha et al.* (2008) through bondgraph formulism considering an eighteen degree of freedom vehicle with six

degree of freedom for each wheelset and truck unit. Kalkar's linear creep formulation has been used for rail-wheel contact forces. Truck-critical speeds and stability behaviour were studied through simulations. Bondgraph model of a truck running on a flexible curve track has been created with eighteen degrees of freedom by *Banerjee et al.* (2009). The truck stability and curving behaviour have been studied through simulations. A bondgraph model of a free railway wheelset rolling on flexible curved track has been developed using module-based approach by *Banerjee and Karmakar* (2014). Wheelset model was made without linearity approximation using subsystem models. Different subsystem models were integrated together to develop a complete bondgraph model of a wheelset for simulation on a rigid railway track. Bondgraph technique has been applied for modeling and simulating the behaviour of railway vehicle drive system by reproducing actual railway operating conditions along a standard section of track (*Lozano et al.*, 2010). *Pacejka* (1987) have presented the application of bondgraph technique in modeling dynamic vehicle systems. The method was explained through applications in the development of symmetrical (vertical, pitch, longitudinal), anti-symmetrical (lateral, yaw) and combined 3-dimensional motion models of a motor vehicle. *Margolis and Shim* (2001) presented a four-wheel, nonlinear vehicle dynamic model with electrically controlled brakes and steering, as well as control at each suspension corner. Controllers were not modeled in actual but are demonstrated through simulation. *Khurshid and Malik* (2007) have applied the bondgraph formalism for the analysis of an automobile crash. An optimum design has been obtained through parametric studies to find a safe design of an automobile to enhance the possibility of survival of vehicle occupant in case of accident. *Bera et al.* (2011) have developed an integrated vehicle braking system dynamics and control

modeling procedure for a four-wheel vehicle. The bondgraph model has been developed in a modular and hierarchical modeling environment and was simulated to evaluate the performance of the anti-lock braking system under different operating conditions.

A vector bond approach which effectively leads to a compact form of Hamiltonian bondgraph structure and naturally to Hamilton's equation of motion is proposed by *Cho* (1998) for the modeling of general multi-body dynamic system. *Vaz et al.* (2003) have presented an example of two links spatial manipulator to discuss certain issues involved in the modeling of robotics manipulators using bondgraph technique and presented expression of its Jacobian along with simulation results. The dynamic analysis of a two-stage pressure rate controllable relief valve has been studied by *Dasgupta and Watton* (2008). The system is modeled through bondgraph approach considering non-linear characteristics of the valve. *Balino* (2009) has used bondgraph methodology to model compressible fluid flows with viscous and thermal effects. A procedure for causality assignment has been derived for satisfying the second law of thermodynamics. A comprehensive model of a closed-loop servo-valve controlled hydro-motor drive system has been developed using bondgraph technique by *Dasgupta and Murrenhoff* (2011). The dynamic performance of the complete system has been studied with respect to the variation of the parameters of the PI controller that drive the servo-valve. An extended Lagrangian formulation has been proposed by *Mukherjee et al.* (2009) for a one-dimensional continuous system with gyroscopic coupling. The formulation has been used to study the dynamics of an internally and externally damped rotor driven through a dissipative coupling. *Lee and Chang* (2012) have presented a bondgraph model of a hydraulic excavator. *Fakri and Vilkaži* (2014) have modeled and controlled the

wheelchair electric drive using bondgraph technique. A control scheme for interaction torque control at the interface of the end-effector and the environment using bondgraph was proposed by *Pathak et al. (2009)*. *Nacusse and Junco (2015)* have presented two dual controlled switched bondgraph structure called generalized switched junction structures. These structures can represent all interconnections enforced by commutations involving bondgraph elements around standard 0- and 1-junctions. The generalized switched junction structures incorporate some algebraic constraints into their equation sets which in the bondgraph domain can be represented with residual sinks, in order to make them able to fix the causality assignment even under ideal switching.

The present research work utilizes the ability of the bondgraphs to obtain umbra-Lagrangian of the multi-cracked rotor system based on the physical paradigm of the system. Bondgraph technique offers flexibility in modelling and formulation of system equations. A very large system may also be modelled as a combination of sub-system models which are joined together at their interaction port to create an integrated system model. Bondgraph equations normally use generalized displacement and generalized momenta as state variables. The modelling, simulation and animation based on bondgraph is performed using Symbol Shakti[®] (*Mukherjee and Samantaray, 2006*), a bondgraph modelling software.

1.4 Contribution of the present work

The focus of the thesis is mainly directed towards application of extended form of Lagrangian-Hamiltonian mechanics to analyze the dynamic behaviour of multi-cracked rotor system. This thesis contributes to analyze, investigate and solve the problems involved in dynamic behaviour of multi-crack rotor system.

- **Concept of umbra Lagrangian equation and symmetry breaking approach**

This thesis deals with an extension of Lagrangian-Hamiltonian mechanics that incorporates dissipative and non-potential fields, and non integrable constraints in a compact form, such that one may obtain invariants of motion or possible invariant trajectories through an extended Noether's theorem. A new concept of umbra (virtual) time has been applied for this extension. This leads to a new form of equations, which is termed as umbra-Lagrange's equation. The idea of umbra-time is then carried forward to prepare a novel concept of Umbra-Hamiltonian. The role of symmetry and symmetry breaking concept has also been accomplished for the multi-crack rotor system to analyze the dynamic behaviour.

- **Analysis of finite asymmetric rotor system through extended Lagrangian formalism**

The introduction of the concept of umbra time extends the classical manifold over which the systems evolve and an extension of Lagrangian-Hamiltonian mechanics over vector fields in the extended space has been presented for finite systems. An extended Noether's theorem along with an Umbra-Hamiltonian is employed to get invariant of motion or provide invariant trajectories. As a case study, an asymmetric multi-rotor system with a DC motor having asymmetries in stiffness is analyzed using this approach. The behavior of the asymmetric rotor is analyzed and validated through simulations. Likewise, an asymmetric multi-rotor system having asymmetry in mass is also analyzed through this approach.

- **Investigation of continuous multi-cracked rotor system through Extended Lagrangian formalism**

The umbra Lagrangian formulation for a continuous set of generalized coordinates has been developed in order to describe continuous systems. The invariants of umbra

lagrangian density are obtained through extension of Noether's theorem over manifolds. The dynamic behavior of internally and externally damped rotor with multi-crack with dissipative coupling has been analyzed through this approach. The bondgraph modeling of this system has also been presented and the effect of variation in stiffness has been investigated and some significant results have been obtained.

- **Experimental frame work for cracked rotor system**

The thesis also presents experimental framework for the investigations of dynamic behaviour of a multi-crack rotor system. The experimental setup is developed and a rotor shaft having single and multi transverse cracks are being analyzed. Experiments are also being conducted to obtain the variation in stiffness at various crack depth for single as well as multi cracks. The experimental analysis is carried out to validate the theoretical and simulation results.

1.5 Organization of the thesis

The chapters of the thesis are arranged as follows. *First Chapter* is introductory in nature. It gives a review of earlier work in this field and summary of the thesis. *Second Chapter* is explaining umbra-Lagrange and umbra-Hamiltonian concept for asymmetric multi-rotor system. *Third Chapter* deals with development of analytical and computational framework to analyze the dynamics of discrete asymmetric rotor systems using extended Lagrangian-Hamiltonian mechanics. This chapter also includes two case studies of asymmetric rotor system. The bondgraph models of discrete multi-rotor are also presented in this chapter. The *Fourth Chapter* presents the investigation of dynamic behaviour of continuous rotor system with a single and multi transverse crack through extended Lagrangian formalism. The *Fifth Chapter* presents the experimental

analysis of a multi-crack rotor system for the validation of theoretical results. *Chapter Six* concludes the thesis and presents the scope for further research. The *Appendix A* is devoted to an introduction of bondgraph elements. *Appendix B* presents the flexibility co-efficients of an open crack. *Appendix C* gives an overview of basic terminology of manifolds and vector fields. In *Appendix D*, classical Lagrange's equation is summarized. In *Appendix E*, concepts of umbra-Hamiltonian are explained. In *Appendix F*, Karnopp's algorithm is summarized, general condition for symmetry is briefly explained in *Appendix G*.

2.1 Introduction

In this chapter, the fundamental ideas of extended Lagrangian-Hamiltonian mechanics is explained. The brief review presented here highlights the principle ideas of extended Lagrangian philosophy and introduces the notation and philosophy of umbra-Lagrangian that will be used throughout this research work. The chapter starts with an introduction of umbra-Lagrangian and umbra (virtual)-time which is an extension of a classical Lagrange's equation. In *Appendix D*, formulation between the classical Lagrange's equation and the variational principle is briefly presented. The variational principle for umbra-Lagrange's equation is also presented in this chapter.

The foremost advantage of Lagrange's equations is that it is easier to apply dynamical systems. Besides this, it correlates the close association between symmetry properties and conservation laws of the dynamical system. Relationship among symmetries and conservation laws through classical Noether's theorem are also discussed in *Appendix G*. The need to extended Noether's theorem for umbra-Lagrange's equation for finite and continuous systems is also emphasized in this chapter. The idea of umbra-Hamiltonian is also presented, however its related theorem are also detailed in *Appendix E*, which are coupled to the extended Noether's theorem in order to obtain an cognizance of the dynamics of systems that attain symmetries. The chapter also details the principle of symmetry breaking along with its application to a multi-cracked rotor system.

Further, the creation of umbra-Lagrangian through extended Karnoop algorithm is also presented using bondgraphs. Bondgraph is advantageously utilized for accounting of the umbra and the real component of the systems.

2.2 Concept of umbra-time and umbra-Lagrangian

In Literature, Mukherjee and their colleagues (*Mukherjee et al.*, 2006, 2007, 2009, 2011; *Mukherjee*, 1994, 2001; *Rastogi and Mukherjee*, 2011) have coined a novel extension of Lagrange's equation. An application of this unique and innovative methodology, in order to attain the motion invariants of the dynamical systems was demonstrated. This novel approach included decomposition of energy (or work) into virtual and real energy components by introducing the concept of 'umbra (virtual) time'. Since 'umbra/virtual' was applied to every form of energies in the system, therefore Lagrangian was termed as 'umbra-Lagrangian'. This innovative approach of 'umbra-Lagrangian' and umbra-Lagrange's equation accompanied by relevant energies has been illustrated by *Mukherjee et al.* (2011). The basic formulation presented by *Mukherjee* (1994, 2001), *Mukherjee and Samantaray* (1997) that leads to umbra-Lagrangian and umbra-Lagrange's equation can be depicted in Figure 2.1 with the detailed nomenclature of energies and forces.

- D'Alembert's concept of permitting displacements, with frozen real time is effectively presented through umbra (virtual)-time terminology.
- Umbra (virtual)-time may be considered as the interior time of a system.
- Kinetic, co-kinetic and potential energies stocked in storage elements like inertial fields and symmetric compliant can be explained as functions in umbra (virtual)-time (umbra-velocities and umbra-displacements).

- The effort of any external force, gyroscopic element, resistive element or field (treated as anti-symmetric resistive field), lever or transformer element (as they are combination of gyrators), sensing element and anti-symmetric compliant field generally rely on velocities and displacements in real time. The potentials associated with all such elements are derived by estimation of work-done through umbra-displacements.

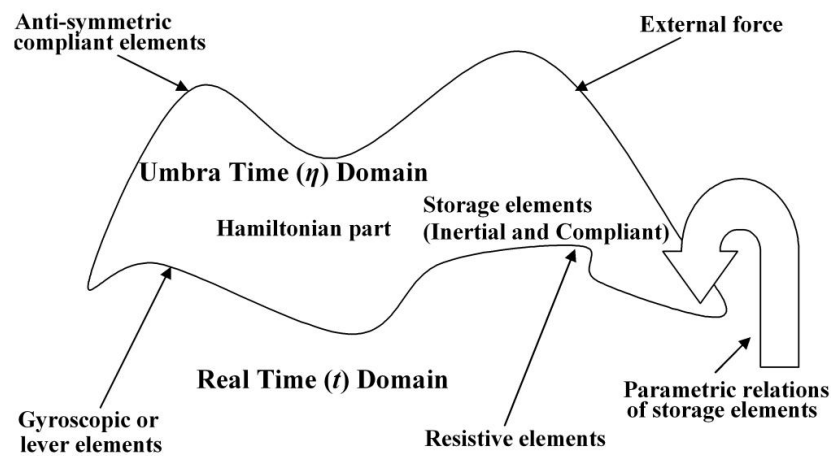


Figure 2.1: Schematic representation of umbra theory

Generally, there are two types of elements that are required to formulate the umbra-Lagrangian for a dynamic system. First type of elements are those, which contain energies that are expressed through umbra-displacements and umbra-velocities and termed as storage elements. Rest of the elements are of second type, for which the efforts returned are expressed totally through real time and their umbra-potential are acquired by umbra-displacement of the corresponding element. These two types of elements can be recognized through discretizing the system into dynamical units or systems basic entities. Bondgraphs are one of the best available tools that show the complete dynamics of a system and generate the classical or umbra-Lagrangian expressions.

The concept of umbra-Lagrangian along with relevant energy terms may be presented stepwise as

1. All temporal fluctuations of parameters are in real time.
2. The potential and co-kinetic energies are expressed using generalized displacements and velocities as functions of umbra time.

The umbra-potential (for potential forces only) is expressed as

$$V_c^*(\tau, \mathbf{q}(\eta)) = \int_0^{\mathbf{q}(\eta)} \mathbf{e}(\tau, \mathbf{q}(\eta)) d\mathbf{q}(\eta), \quad (2.1)$$

where a bold face letter denotes a vector quantity. A time varying stiffness spring, whose umbra-potential energy can be represented as

$$V_c^*(\tau, x(\eta)) = \int_0^{x(\eta)} K(\tau)x(\xi) dx(\xi) = \frac{1}{2}K(\tau)x^2(\eta)$$

Similarly, the umbra-kinetic energy is evaluated as

$$T^*(\tau, \mathbf{q}(\eta), \mathbf{p}(\eta)) = \int_0^{\mathbf{p}(\eta)} \mathbf{f}(\tau, \mathbf{q}(\eta), \mathbf{p}(\eta)) d\mathbf{p}(\eta) \quad (2.2)$$

and the umbra co-kinetic energy is obtained as

$$T_c^*(\tau, \dot{\mathbf{q}}(\eta)) = \dot{\mathbf{q}}(\eta)\mathbf{p}(\eta) - T^*(\tau, \mathbf{q}(\eta), \mathbf{p}(\eta)) \quad (2.3)$$

The umbra co-kinetic energy for a varying mass is defined as

$$T_c^*(\tau, \dot{x}(\eta)) = \int_0^{\dot{x}(\eta)} m(\tau)\dot{x}(\xi) d\dot{x}(\xi) = \frac{1}{2}m(\tau)\dot{x}^2(\eta)$$

3. Based on the philosophy that resistive fields contemplate the motion states in real time as an external observer since it opens the system, the umbra-potential is expressed by associating it with generalized resistive fields. The force created by them does work on the system through umbra generalized displacements presented as

$$V_R^* = \int_0^{q(\eta)} \mathbf{e}(\tau, \mathbf{q}(\tau), \dot{\mathbf{q}}(\tau)) d\mathbf{q}(\eta), \quad (2.4)$$

As an example, umbra-potential for a damper whose damping coefficient is time varying may be expressed as

$$V_R^* = \int_0^{x(\eta)} R(\tau) \dot{x}(\tau) dx(\xi) = R(\tau) \dot{x}(\tau) x(\eta)$$

It is important to notice that in classical approach, one may include energy dissipative forces through Rayleigh potentials, which can be expressed

$$V_R = \frac{1}{2} \dot{\mathbf{q}}(\tau) [R] \dot{\mathbf{q}}(\tau) \quad (2.5)$$

Even if any anti-symmetric part of $[R]$ is present in Eq. (2.5), it does not contribute to V_R . Although, the present methodology as considered in Eq. (2.4), can incorporate both the gyroscopic effects (anti-symmetric part) as well as the dissipative (symmetric part) through the resistive field for which the corresponding umbra-potential can be written as

$$V_R^* = \dot{\mathbf{q}}(\tau) [R] \mathbf{q}(\eta) \quad (2.6)$$

4. The umbra-potential integrated with external generalized forces may be evaluated as

$$V_p^*(\tau, \mathbf{q}(\eta)) = - \int_0^{q(\eta)} \mathbf{F}(\tau, \mathbf{q}(\tau), \dot{\mathbf{q}}(\tau)) d\mathbf{q}(\eta), \quad (2.7)$$

To elaborate, one may evaluate the umbra-potential for some random external force $\mathbf{F}(\tau)$ as

$$V_p^*(\tau, x(\eta)) = - \int_0^{x(\eta)} \mathbf{F}(\tau) dx(\xi) = -\mathbf{F}(\tau) x(\eta)$$

The entire umbra-potential is expressed by adding all the potentials denoted by Eqs. (2.1), (2.4) and (2.7) and written as

$$V^*(\tau, \mathbf{q}(\tau), \dot{\mathbf{q}}(\tau), \mathbf{q}(\eta)) = V_c^*(\tau, \mathbf{q}(\eta)) + V_R^*(\tau, \mathbf{q}(\tau), \dot{\mathbf{q}}(\tau)) + V_p^*(\tau, \mathbf{q}(\eta)), \quad (2.8)$$

and the umbra-Lagrangian would, therefore, be presented as

$$L^*(\tau, \mathbf{q}(\tau), \dot{\mathbf{q}}(\tau), \mathbf{q}(\eta), \dot{\mathbf{q}}(\eta)) = T_c^*(\tau, \dot{\mathbf{q}}(\eta)) - V^*(\tau, \mathbf{q}(\tau), \dot{\mathbf{q}}(\tau), \mathbf{q}(\eta)), \quad (2.9)$$

Mukherjee (1994, 2001), presented a set of equations for a general class of systems, which can be written as

$$\frac{d}{d\tau} \left\{ \lim_{\eta \rightarrow \tau} \frac{\partial L^*}{\partial \dot{\mathbf{q}}_i(\eta)} \right\} - \lim_{\eta \rightarrow \tau} \frac{\partial L^*}{\partial \mathbf{q}_i(\eta)} = 0, \quad \text{where } i = 1 \dots \dots n, \quad (2.10)$$

The variational formulation in this form of Lagrange's equation was presented by *Rastogi* (2005).

2.2.1 Variational approach/theory of umbra-Lagrange's equation

A generalized variational principle or the principle of least action is presented in brief that results in a peculiar form of the umbra-Lagrange equation. The extended least action principle may be written as, "For general systems, there are dynamic paths in such a way that they recursively minimize the integral of their umbra-Lagrangians considering the real-time velocities and displacements as modulatory variables and umbra-time velocities and displacement as trajectorial variables with fixed end point conditions". It may also be expressed mathematically as

$$L^*(\mathbf{q}(\tau), \dot{\mathbf{q}}(\tau), \mathbf{q}(\eta), \dot{\mathbf{q}}(\eta), \tau) = L(\mathbf{q}(\tau, m), \dot{\mathbf{q}}(\tau, m), \mathbf{q}(\tau, t), \dot{\mathbf{q}}(\tau, t), \tau)$$

where $\mathbf{q}(\tau, t)$ and $\mathbf{q}(\tau, m)$ are elements of a homotopic family and named as trajectorial and modulatory variables. The action integral to be recursively minimized, which may be presented as

$$I = \int_{\tau_1}^{\tau_2} L(\mathbf{q}(\tau, m), \dot{\mathbf{q}}(\tau, m), \mathbf{q}(\tau, t), \dot{\mathbf{q}}(\tau, t), \tau) d\tau \quad (2.11)$$

For trajectorial occurrences having stated end constraints, minimization of the integral in Eq. (2.11) is carried out leading to a trajectory function. Again, by considering those as modulatory and these trajectory function can be minimized for trajectorial occurrences. This procedure may be repeated under similar conditions and termed as recursive minimization of functionals. This procedure converges rendering the modulatory and trajectorial members identically. The relationship between symmetry and conservation laws may be presented in the next sub-section.

2.3 Correlation between symmetry and conservation laws

Symmetry has always played a key role in analytical mechanics, from fundamental formulations to basic principle like conservation law to concrete applications. The main focus of this work is to highlight the role of symmetry in certain classes of dynamical systems. In last decade, many researchers have been using symmetry techniques for studying integrable and chaotic systems, stability and bifurcation in engineering applications. Moreover, this technique is greatly used to obtain a new insight into the dynamics of rigid, fluid, elastic and plasma systems. Mechanics and symmetry principle establishes an essential framework for all these areas, which is beneficial to physicist as well as engineers.

The definition of symmetry as presented by *Weyl* (1992) can be briefly defined, “A thing is symmetrical if one can subject to a certain operation and it appears exactly the same after the operation.” To broaden the more extensive idea of symmetry, the German mathematician *Noether* (1971) discovered the most fundamental justification for

conservation laws and symmetries. Noether's theorem can be explained for each symmetry operation, there is a corresponding conservation law. The conservation of momentum results due to the homogeneity of space. Invariance under translation in time results in the law of conservation of energy, whereas conservation of angular momentum results from the isotropy of space. Noether's theorem develops conservation laws from symmetries under assumption that the principle of least action is the basic law that governs the motion of a particle in classical mechanics. This theorem further presents the concept that a physical quantity corresponding to the symmetries is a constant of motion, which does not alter along entire path of the particle. In general terminology, a system is considered symmetric if there is no change in the system dynamics by imposing any change in the system. This relation is formulated through Noether's theorem. Which states that "If a Lagrangian is invariant under a family of transformations, its dynamical system has a constant of motion, and that constant can be found from knowledge of the Lagrangian and the transformation." The correlation of symmetry and Lagrangian may also be possible with the concept of Noether's theorem. The next sub-section will present the extended Noether's theorem for finite and continuous system.

2.3.1 Extended Noether's theorem for finite and continuous systems

Noether (1971) stated that every differentiable symmetry of the action of a physical system brings about a conservation law. The classical Noether's theorem mainly depends on the particular structure of dynamical frameworks, where the influence of dissipation, constraints, gyroscopic coupling and time fluctuating parameters are not taken into consideration. An extended version of Noether's theorem has been achieved, which includes non-potential and dissipative fields, and non-integrable constraints in a concise form, such that conservation laws (invariants of motion) or

possible invariant limit trajectories on which some dynamical quantity remains invariant may be obtained.

In this thesis, the Noether's theorem is extended to finite as well as continuous systems and found to be more suitable for use in engineering applications such as rotordynamics applications. It is found that such effects of dissipative or non-potential fields are usually ignored by physicists, since these effects are insignificant in the larger scale of phenomena to which this theorem is applied. However an extension of Noether's theorem for a general class of systems in engineering applications with a new concept of umbra-time provides a novel approach to depict the dynamics of the systems, which generates significant information about the dynamical behaviour of the systems. The details of the extension of Noether's theorem for discrete and continuous transformation are presented separately in *Chapter 3* and *Chapter 4*.

2.3.2 Symmetry breaking approach

It is a common phenomenon that symmetry breaking generates asymmetric contribution in a symmetric environment. It is one of the novel approaches to explain the self organized pattern formation. Using of this theorem, cosmologists have found that the universe is scattered in clusters with the greater part of the universe vacant, the formation of jet streams, ocean currents and the continental drifts is investigated by the earth scientists, material scientists study the theory of phase transition and biologists attempt to explain how living organism acquired forms through cell division and morphogenesis as given by *Weyl (1992); Prigogine, (1967)*.

In physics, symmetry breaking is a phenomena, in which the system's output is decided by the analysis of response of a system crossing a critical point to

infinitesimally small fluctuations, by determining the branch of a bifurcation is determined and analyzed. To an external observer, who is unaware of the fluctuations (or "noise"), the choice appears arbitrary. This process is termed as symmetry breaking because such transitions usually bring the system from an orderly state (symmetric) into a disorderly state (asymmetric). Symmetry breaking is thought to play a major role in pattern formation. The concept of symmetry breaking can be broadly classified into two basic categories.

- (a) *Explicit symmetry breaking* - In this symmetry breaking approach, the basic laws governing the system are not invariant under symmetry in question.
- (b) *Spontaneous symmetry breaking*- In this symmetry breaking approach, the basic laws governing the system is invariant but system is not because of the parameters of the systems. Such a symmetry breaking is parameterized by order parameters. A special case of this type of symmetry breaking is dynamical symmetry breaking due to some change in parameter. The present work is mainly focused on application of spontaneous symmetric breaking approach into rotor dynamic applications.

2.3.3 Symmetry breaking phenomenon for the cracked-rotor system

For investigation of dynamic behaviour and the vibration, a cracked rotor can be enormously improved by presenting the concept of cyclic symmetry, each variable parameters (including material properties and geometry) is inferred to be similar. However, the cyclic symmetry of cracked rotor system is wrecked due to the small differences in geometric or material properties. Generally, this small difference appear in the form of change in shaft material such as stiffness variation, mass or damping

properties and change in geometry due to initiation and propagation of crack in the rotor structure. Although the difference is less in terms of material properties, it may have drastic effects on the system response. In particular, this symmetry breaking in terms of shaft material property can cause localization of vibration and the stress concentration due to the initiation and propagation of crack. Due to this, the stress levels and amplitude are sharply increased. Therefore, many research activities have been conducted for analyzing the vibration in rotor machinery.

However, there are relatively few literature available to date concerning the symmetry breaking of rotor shaft due to cracking. The studies by *Akira* (2009) considered the cyclic symmetry in the case of turbine blade for the forced vibration response of blade disks with cracked blades. *Hou* (2006) investigated crack induced mistuning analytically, using a lumped mass beam model, where the local stiffness loss because of crack was implemented with a flexible matrix method. However above studies used simplified model for crack and were limited to the mistuning of turbine blades. Most importantly, all the models have not considered the symmetry breaking due to the material property change due to a crack (stiffness or mass of the rotor). Also, nonlinearity effect of the crack was not modeled for the continuous cracked rotor.

Kumar (2013) has investigated the dynamic response of a single cracked-rotor system through extended Lagrangian mechanics. Extended form of Lagrangian-Hamiltonian equations were employed and variation in stiffness due to crack depth variation for a single-crack rotor analysis was evaluated.

Motivated by the concept of symmetry and symmetry breaking approach, this thesis highlights the application of this approach for the analysis of the dynamics of a

multi-crack rotor. The Noether's theorem along with the concept of umbra-Hamiltonian brings out some significant insight into the system behaviour.

2.4 Concept of umbra-Hamiltonian

Mathematically, the umbra-Hamiltonian (*Mukherjee*, 1994, 2001) may be represented as

$$H^*[\mathbf{q}(\eta), \mathbf{p}(\eta), \mathbf{q}(\tau), \dot{\mathbf{q}}(\tau), \tau] = \dot{\mathbf{q}}(\eta)\mathbf{p}(\eta) - L^*[\mathbf{q}(\eta), \dot{\mathbf{q}}(\eta), \mathbf{q}(\tau), \dot{\mathbf{q}}(\tau), \tau], \quad (2.12)$$

where the umbra-momentum is

$$\mathbf{p}(\eta) = \frac{\partial L^*}{\partial \dot{\mathbf{q}}(\eta)}$$

The real momentum may be obtained as

$$\mathbf{p}(\tau) = \lim_{\eta \rightarrow \tau} \frac{\partial L^*}{\partial \dot{\mathbf{q}}(\eta)}$$

Taking total differential of Eq. (2.12), one obtains

$$\begin{aligned} dH^* &= \frac{\partial H^*}{\partial \mathbf{p}(\eta)} d\mathbf{p}(\eta) + \frac{\partial H^*}{\partial \mathbf{q}(\eta)} d\mathbf{q}(\eta) + \frac{\partial H^*}{\partial \mathbf{q}(\tau)} d\mathbf{q}(\tau) + \frac{\partial H^*}{\partial \dot{\mathbf{q}}(\tau)} d\dot{\mathbf{q}}(\tau) + \frac{\partial H^*}{\partial \tau} d\tau \\ &= \dot{\mathbf{q}}(\eta) d\mathbf{p}(\eta) - \frac{\partial L^*}{\partial \mathbf{q}(\eta)} d\mathbf{q}(\eta) - \frac{\partial L^*}{\partial \mathbf{q}(\tau)} d\mathbf{q}(\tau) - \frac{\partial L^*}{\partial \dot{\mathbf{q}}(\tau)} d\dot{\mathbf{q}}(\tau) \\ &\quad - \frac{\partial L^*}{\partial \tau} d\tau + \left(\mathbf{p}(\eta) - \frac{\partial L^*}{\partial \dot{\mathbf{q}}(\eta)} \right) d\dot{\mathbf{q}}(\eta) \end{aligned}$$

The relations which may be derived, are

$$\dot{\mathbf{q}}(\eta) = \frac{\partial H^*}{\partial \mathbf{p}(\eta)} \quad (2.13)$$

$$\frac{\partial H^*}{\partial \mathbf{q}(\eta)} = - \frac{\partial L^*}{\partial \mathbf{q}(\eta)} \Rightarrow \lim_{\eta \rightarrow \tau} \frac{\partial H^*}{\partial \mathbf{q}(\eta)} = - \dot{\mathbf{p}}(\tau) \quad (2.14)$$

and the other relations acquired are

$$\frac{\partial H^*}{\partial \mathbf{q}(\tau)} = -\frac{\partial L^*}{\partial \mathbf{q}(\tau)}$$

$$\frac{\partial H^*}{\partial \tau} = -\frac{\partial L^*}{\partial \tau}$$

The umbra-Hamiltonian H^* is having two mathematical elements as H_i^* and H_e^* . H_i^* is the interior form of Hamiltonian, which is independent of any function of real time, real velocity and real displacement, and H_e^* is the rest of the umbra-Hamiltonian, termed as the exterior Hamiltonian. Thus, one may write

$$H^* = H_i^*\{\mathbf{q}(\eta), \mathbf{p}(\eta)\} + H_e^*\{\mathbf{q}(\eta), \mathbf{p}(\eta), \mathbf{q}(\tau), \dot{\mathbf{q}}(\tau), \tau\} \quad (2.15)$$

The theorems of the umbra-Hamiltonian (*Mukherjee*, 1994, 2001) are now detailed in *Appendix E*.

2.4.1 Importance of umbra-Hamiltonian

The augmentation of Noether's hypothesis assumes an essential part in deciding the invariants or so constants of motion and invariant trajectories, on which few physical entity becomes constant. Although, the dynamical quantity, which are conserved, can be found out just by considering the umbra-Hamiltonian of the framework. Therefore, the notion of umbra-Hamiltonian is extremely important to acquire the conserved dynamical quantity by means of related theorems and the corollary presented in *Appendix E*. In this way, combined aspects of extended Noether's theorem and umbra-Hamiltonian provide the interior nature of the dynamics of systems with symmetries.

2.5 Umbra-Lagrangian and the system generated through bondgraphs

In the case of mathematical models of dynamical systems, the equations for any dynamical system can be easily and systematically generated from the bondgraph. The bondgraph representation of a system may be created in total notion from the mathematical model of the system. Generally, there are two types of elements that are required to formulate the umbra-Lagrangian for a dynamic system. First type of elements are those, which contain energies that are expressed through umbra-displacements and umbra-velocities and termed as storage elements. Rest of the elements are of second type, for which the efforts returned are expressed totally through real time and their umbra-potential acquired by the umbra-displacement of the respective elements. These two types of elements can be recognized by discretizing the system into dynamical units or systems basic entities. After these elements and their ports are identified from the bondgraph model of the system, an extended bondgraph is created, which has three components: (i) an umbra-time component (ii) a real time component (iii) a trans-temporal component. The procedure for getting umbra-Lagrangian and the steps followed are separately provided in *Appendix F*, which is an extended version of Karnopp's algorithm. It is very important to note that a bondgraph model helps in the identification of two important varieties of elements, along with the real and umbra time variables, thus leading to the umbra-Lagrangian functional. Once the umbra-Lagrangian is achieved, many dynamical aspects of umbra-Lagrange's equation can be employed effectively to obtain dynamical behaviour of the system.

2.6 Summary of the chapter

In this chapter, some fundamental concepts of extended Lagrangian-Hamiltonian mechanics have been presented. The concepts of umbra-Lagrange and umbra-

Lagrangian equation have been given by its point by point foundation. The underlying variational philosophy, which results in this modified form of equation, has also been discussed.

The role of symmetry in dynamical system hypothesis has been examined, which highlights the conservation laws of dynamical framework. The classical Noether's theorem is mathematically explained, which showed a relationship between symmetry property and corresponding conservation law. It has been realized that extension of classical Noether's theorem for finite or continuous system must incorporate dissipation and non-potential forces in a compact form to obtain invariants of motion or invariants trajectories, on which some physical entities turn out to be conserved. This augmentation of Noether's theorem for finite and continuous system along with its application will be dealt separately in the later chapters.

The concept of umbra-Hamiltonian with two theorems has been exhibited, which are accompanied by extended Noether's theorems to impart detailed interior of the dynamics of systems. Finally, generation of umbra-Lagrangian through bondgraph modeling has been discussed. Bondgraphs turn out to be a helpful modeling technique to group the umbra and the real components of the systems. The extended Lagrangian-Hamiltonian mechanics for finite systems will be discussed along with various multi rotor cases. These entire concepts will be implemented to analyze the dynamics of finite rotor or continuous rotor in *Chapter 3* and *Chapter 4*.

Analytical and Computational Framework for Discrete Rotor with Asymmetries

3.1 Introduction

In recent decade, several researchers (*Babu et al.*, 2008; *Chasalevris and Papadopoulos*, 2009; *Darpe*, 2007; *Georgantzinou and Anifantis*, 2008; *Patel and Darpe*, 2008; *Rubio*, 2011; *Singh and Tiwari*, 2011) have studied non-linear response of asymmetric rotor and its variation with system parameters by employing various analytical techniques and methods. Several papers on Lagrangian mechanics are studied in archival literature. It is the fact that any asymmetries in revolving element consists of a non-potential and dissipative forces; and in such situation, original Lagrange's equation cannot provide the dynamic interior of the system and loose generality in the presence of non-holonomic constraints, dissipative forces, non-potential forces, gyroscopic forces and other general class of systems with time fluctuating parameters.

Lagrangian formulation is preferred because of its inherent properties of depicting conservation laws and important symmetry properties of dynamical systems. In literature, few attempts have been made by several authors to extend the scope of Lagrange's equation so that forces with holonomic constraints, effects of dissipation, constraints of nonconservative dynamical system can be included in this equation. Another important characteristics shown by Lagrange's equation is its connection with symmetry properties and possible constant of motions of dynamical systems.

Various researchers (*Djukic, 1973; Djukic et al., 1989; Vujanovic, 1978; Vujanovic et al., 1989*) have published several research papers to show connection between symmetries conservation laws. (*Vujanovic, 1978; Vujanovic et al., 1989*) have formulated a novel methodology to obtain constants of motion of general dynamic system with non potential forces and non holonomic constraints. This new formulation by *Vujanovic (1978)* was entirely based on the quantities of non-conservative holonomic system, which is based on the differential variational principle of D'Alembert.

The knowledge of invariants of motion of dynamical system is very significant in the analysis of dynamical systems such as multi-rotors. There exists a close connectivity of symmetries with invariant of motions (*Karnopp, 1977; Mukherjee and Samantaray, 1997*) of such systems. Generally, symmetric properties of dynamical system present a close insight to evaluate the invariants of motion of the dynamical system as they disintegrate the complex dynamics of the dynamical systems such as multi-rotor with cracks. In this direction, Noether's theorem (*Noether, 1971*) has played a prominent contribution to derive invariance properties. Thus, Noether's theorem provides exploration of symmetric properties of the dynamical system to obtain constant of motion. Extension of Noether's theorem along with umbra's Hamiltonian provides a great deal of insight to obtain dynamic behaviour of an asymmetric rotor system.

Rastogi (2005) has worked on extension of the Lagrangian-Hamiltonian mechanics for finite system. He has included dissipative and non-potential fields and non-integrable constraints. However, his study was limited to symmetric system only.

Kumar (2013) has also used same phenomenon for asymmetric system. He has considered a single crack rotor for such analysis.

There are various causes for unbalancing in dynamics system. So it is not easy to predict the dynamics signature of any such asymmetric system. It is a great challenge for engineers / scientist. Initiation and propagation of crack in a rotor is a very critical for the health structure of rotor system. Development of crack in a rotor due to fatigue generally changes the stiffness of shaft and ultimately the whole rotor system becomes asymmetric. Extended Lagrangian formalism has been applied to analyze a symmetrical electromechanical system, and continuous system (*Kumar, 2013; Mukherjee et al., 2006, 2007 and 2009; Rastogi, 2005*). However, this work deals with the application of extended Lagrangian – Hamiltonian mechanics on the asymmetric rotor system. As a case study, an analytical model is developed considering symmetry breaking of a discrete rotor due to asymmetries in stiffness. The amplitude and natural frequencies has been determined analytically. A computational model for asymmetric rotor system was also created by using bondgraph modeling technique, which was simulated on the Symbol-Shakti[®] software (*Mukherjee and Samantaray, 2006*) to analyze the dynamic behaviour.

In another case study, a similar analytical framework with asymmetries in mass has been developed. A computational model for the analytical framework was also developed by using unified bondgraph simulation methodology. Symbol-Shakti[®] software (*Mukherjee and Samantaray, 2006*) was used for simulation work. The effects of excitation frequency, change in mass asymmetry has been noticed. Different graphs have also plotted to explain the insight dynamics of framework. These graphs have also showing good agreement between analytical and simulated results.

3.2 Noether's theorem and its extension for finite rotor

Noether's theorem plays a significant contribution to achieve an insight dynamics of dynamical system. The theorem (Noether, 1971) states that, if the Lagrangian of a system is invariant under a family of single parameter groups, then each such group renders a constant of motion. The extended Noether's theorem, presented in papers (Mukherjee et al., 2011; Rastogi and Mukherjee, 2011) may provide invariants of motion, or invariant trajectories, on which some dynamical parameters lies constant. The Umbra-Lagrangian can be evolved on an enlarged manifold, which incorporates umbra as well as real displacements and velocities and real time (Mukherjee et al., 2011), i.e

$$L^* = L^*(\tau, \mathbf{q}(\tau), \dot{\mathbf{q}}(\tau), \mathbf{q}(\eta), \dot{\mathbf{q}}(\eta)) \quad (3.1)$$

where, $\dot{\mathbf{q}}(\tau)$ is a real time velocity and $\dot{\mathbf{q}}(\eta)$ is an umbra time velocity. Deviated from classical expression, the nomenclature needs single but enlarged manifold incorporating of real and umbra displacements and velocities and real time. The umbra-Lagrangian of any dynamical system allows several one-parameter transformation groups, and further the infinitesimal generator (Kumar and Rastogi, 2012; Mukherjee et al., 2007) corresponding to p^{th} parameter (or group) may be decomposed as follows:

$$\mathbf{V}^p = \mathbf{V}_\eta^p + \mathbf{V}_\tau^p, \text{ where } p = 1 \dots m \quad (3.2)$$

The general forms for \mathbf{V}_η^p and \mathbf{V}_τ^p would be:

$$\mathbf{V}_\eta^p = \sum_{i=1}^n \alpha^{p,i} \frac{\partial}{\partial \mathbf{q}_i(\eta)} + \beta^{p,i} \frac{\partial}{\partial \dot{\mathbf{q}}_i(\eta)}, \quad (3.3)$$

and

$$\mathbf{V}_\tau^p = \sum_{i=1}^n \gamma^{p,i} \frac{\partial}{\partial \mathbf{q}_i(\tau)} + \xi^{p,i} \frac{\partial}{\partial \dot{\mathbf{q}}_i(\tau)}, \quad (3.4)$$

where $\alpha^{p,i}, \beta^{p,i} = \frac{d\alpha^{p,i}}{d\eta}$ and $\gamma^{p,i}, \xi^{p,i} = \frac{d\gamma^{p,i}}{d\tau}$ are functions of real and umbra displacement and real time. The functions of Eq. (3.4) remains unchanged under the p^{th} transformation, which may be presented as

$$\mathbf{V}^p(L^*) = \mathbf{0} \quad (3.5)$$

By the using of the Eq. (3.2) and Eq. (3.5) and taking limit $\eta \rightarrow \tau$, one obtains

$$\text{Lim}_{\eta \rightarrow \tau} \{ \mathbf{V}_\eta^p(L^*) \} + \text{Lim}_{\eta \rightarrow \tau} \{ \mathbf{V}_\tau^p(L^*) \} = 0 \quad (3.6)$$

By using Eq. (3.3) in above Eq. (3.6), one obtains

$$\text{Lim}_{\eta \rightarrow \tau} \sum_{i=1}^n \left[\alpha^{p,i} \frac{\partial L^*}{\partial \mathbf{q}_i(\eta)} + (\alpha^{\dot{p},i}) \frac{\partial L^*}{\partial \dot{\mathbf{q}}_i(\eta)} \right] + \text{Lim}_{\eta \rightarrow \tau} \{ \mathbf{V}_\tau^p(L^*) \} = 0 \quad (3.7)$$

Where superscript $(\dot{\quad})$ represents the derivative with respect to umbra time. Umbra-Lagrange's Eq.(3.1) may be represent in following form

$$\text{Lim}_{\eta \rightarrow \tau} \frac{\partial L^*}{\partial \mathbf{q}_i(\eta)} = \frac{d}{d\tau} \left\{ \text{Lim}_{\eta \rightarrow \tau} \frac{\partial L^*}{\partial \dot{\mathbf{q}}_i(\eta)} \right\} \quad (3.8)$$

Using Eq. (3.8) in Eq. (3.7)

$$\sum_{i=1}^n \left[\alpha^{p,i} \left\{ \frac{d}{d\tau} \left(\text{Lim}_{\eta \rightarrow \tau} \frac{\partial L^*}{\partial \dot{\mathbf{q}}_i(\eta)} \right) \right\} + \text{Lim}_{\eta \rightarrow \tau} (\alpha^{\dot{p},i}) \frac{\partial L^*}{\partial \dot{\mathbf{q}}_i(\eta)} \right] + \text{Lim}_{\eta \rightarrow \tau} \{ \mathbf{V}_\tau^p(L^*) \} = 0$$

$$\frac{d}{d\tau} \left\{ \sum_{i=1}^n \alpha^{p,i} \left(\lim_{\eta \rightarrow \tau} \frac{\partial L^*}{\partial \dot{\mathbf{q}}_i(\eta)} \right) \right\} + \lim_{\eta \rightarrow t} \{ \mathbf{V}_\tau^p(L^*) \} = 0$$

The extended Noether's theorem may now be expressed as

$$\frac{d}{d\tau} \left\{ \lim_{\eta \rightarrow \tau} \sum_{i=1}^n \frac{\partial L^*}{\partial \dot{\mathbf{q}}_i(\eta)} \mathbf{V}_\eta^p(\mathbf{q}_i(\eta)) \right\} = - \lim_{\eta \rightarrow \tau} \{ \mathbf{V}_\tau^p(L^*) \}, \text{ with } p = 1 \dots \dots m \quad (3.9)$$

The left-hand side term in Eq. (3.9) provides classical Noether's rate equation, whereas the right hand side term is an additional, which is termed as the modulatory convection term.

The modulatory term is useful to obtain the dynamical insight of the rotor-motor system.

3.3 Case study–I: Analysis of finite multi-rotor system with asymmetries due to stiffness using extended Lagrangian formalism

Recently various researchers have been concerned towards the study of dynamical behaviour of cracked rotor. In order to investigate the dynamical behaviour of finite rotor system with asymmetries due to stiffness, extended Lagrangian formulation has been proposed in this case study. It has been observed that stiffness plays a significant role in rotordynamics, in which past studies are majorly based on single crack rotor system (*Mukherjee et al., 2007*). This study conducts an experimental, analytical and computational analysis of multi-crack rotor system, whereas computational and analytical results will also be validated with experimentation. Primarily section represents the analytical model of multi-crack system, which will be followed by computational and experimental study.

A multi-rotor-system with asymmetries are being analyzed through extended Lagrangian formulation (*Jain et al., 2018*). In this analytical model, a shaft is carrying

two rotors, which are mounted on equal distances. The rotors are composed of internal as well as external damping and transverse stiffness is included due to flexural behaviour of the shaft (*Kumar and Rastogi, 2012*). The shaft is driven by DC motor as shown in Figure 3.1. Thus, one may evaluate stiffness and damping properties in two orthogonal directions. In this evaluation, dampers may incorporate external as well as internal damping. One of the rotors consist small asymmetries in stiffness parameter. It is assumed that mass of the discs of rotors are much more than that of the shaft, henceforth, mass of the shaft is ignored in this dynamics.

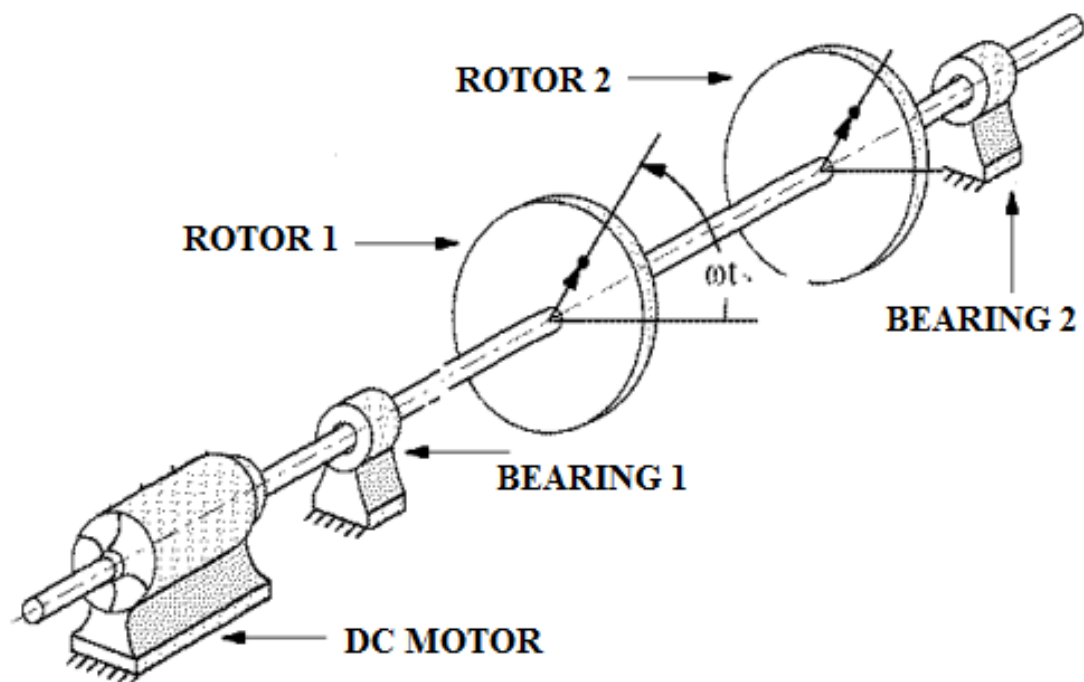


Figure 3.1: Rotor 1 and rotor 2 driven through a DC motor

The bondgraph model of the physical system is shown in Figure 3.2, which contains causalled bond for generation of system equations and simulation results (*Mukherjee et al., 2007*). The modulated gyrator element has been used to portray the additional circulatory effects due to internal damping. Bonds 4, 27, 28, 29, 30 represent the

artificial flow sources to obtain umbra-Lagrangian of the system. The rate of rotation of shaft has been recorded by bond 20, which is flow activated C-bond.

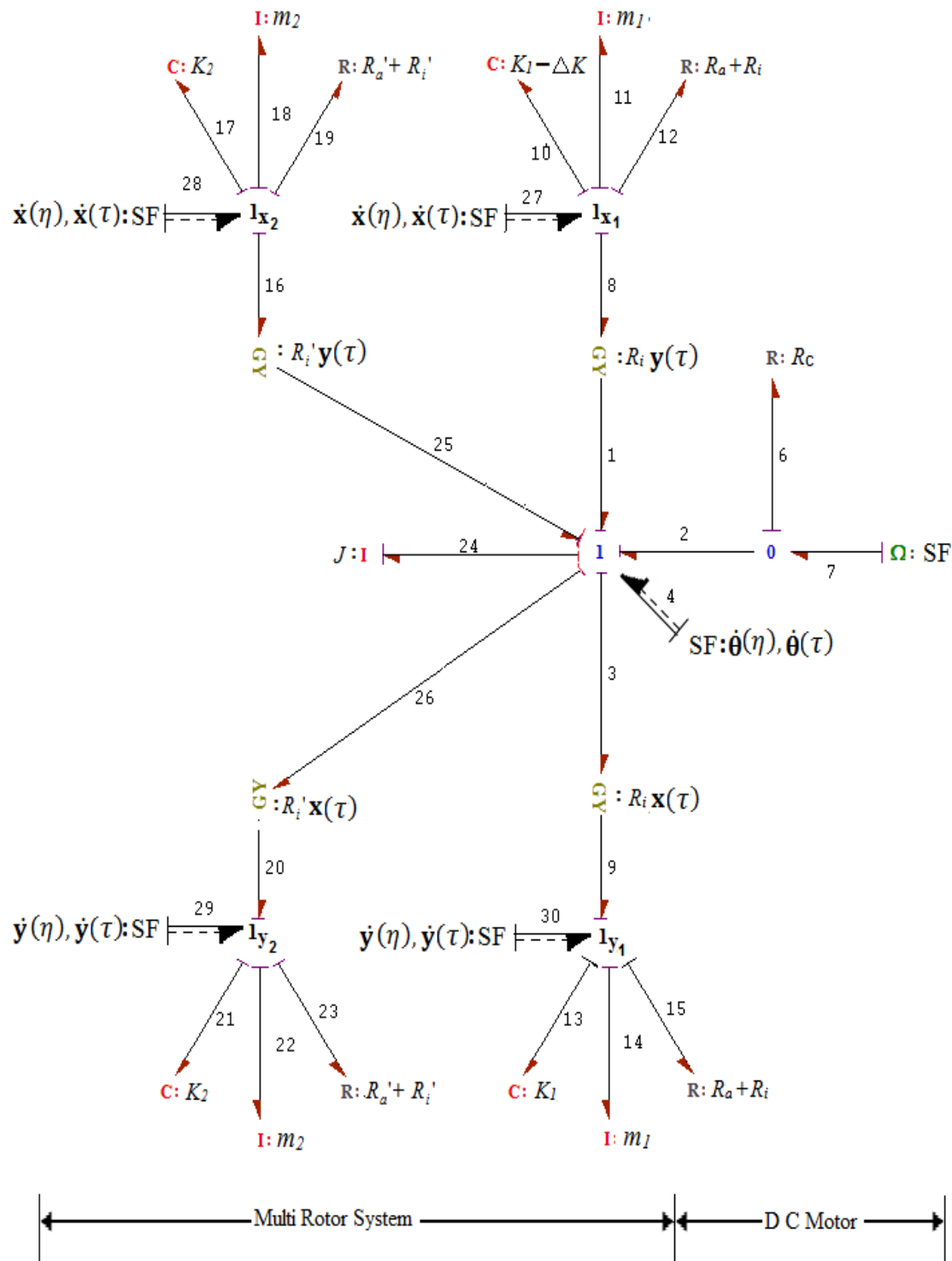


Figure 3.2: Bondgraph model of multi rotors with artificial flow sources to obtain umbra-Lagrangian in stiffness asymmetries case

Model represents the interaction of energy in the system. In the pictorial representation, ΔK shows the change in stiffness in X direction in rotor1, which makes the system asymmetric. This change in stiffness (ΔK) may be due to initiation and propagation of crack in the discrete rotor1.

3.3.1 Umbra-Lagrangian for multi-rotor system with asymmetric stiffness

The umbra-Lagrangian may be formulated following the steps of extended Karnopp's algorithm discussed in *Appendix 6*. The umbra-Lagrangian corresponding to the bondgraph model shown in Figure 3.2 may be expressed as

$$\begin{aligned}
L^* = & \frac{1}{2} [m_1 \{\dot{\mathbf{x}}_1^2(\eta) + \dot{\mathbf{y}}_1^2(\eta)\} \\
& - \{(K_1(\eta) - \Delta K(\eta))\mathbf{x}_1^2(\eta) + K_1\mathbf{y}_1^2(\eta) + J\dot{\boldsymbol{\theta}}^2(\eta)\} \\
& + m_2 \{\dot{\mathbf{x}}_2^2(\eta) + \dot{\mathbf{y}}_2^2(\eta)\} - K_2(\eta) \{\mathbf{x}_2^2(\eta) + \mathbf{y}_2^2(\eta)\}] \\
& - [\mathbf{x}_1(\eta)\mathbf{y}_1(\eta)] \begin{bmatrix} 0 & R_i \dot{\boldsymbol{\theta}}(\tau) \\ -R_i \dot{\boldsymbol{\theta}}(\tau) & 0 \end{bmatrix} \begin{Bmatrix} \mathbf{x}_1(\tau) \\ \mathbf{y}_1(\tau) \end{Bmatrix} \\
& - [\mathbf{x}_2(\eta)\mathbf{y}_2(\eta)] \begin{bmatrix} 0 & R_i \dot{\boldsymbol{\theta}}(\tau) \\ -R_i \dot{\boldsymbol{\theta}}(\tau) & 0 \end{bmatrix} \begin{Bmatrix} \mathbf{x}_2(\tau) \\ \mathbf{y}_2(\tau) \end{Bmatrix} \\
& - (R_a + R_i) \{\mathbf{x}_1(\eta)\dot{\mathbf{x}}_1(\tau) + \mathbf{y}_1(\eta)\dot{\mathbf{y}}_1(\tau)\} \\
& - (R_a' + R_i') \{\mathbf{x}_2(\eta)\dot{\mathbf{x}}_2(\tau) + \mathbf{y}_2(\eta)\dot{\mathbf{y}}_2(\tau)\} \\
& - [R_i \{\mathbf{x}_1(\tau)\dot{\mathbf{y}}_1(\tau) - \mathbf{y}_1(\tau)\dot{\mathbf{x}}_1(\tau)\} \\
& + R_i' \{\mathbf{x}_2(\tau)\dot{\mathbf{y}}_2(\tau) - \mathbf{y}_2(\tau)\dot{\mathbf{x}}_2(\tau)\} - R_c \{\dot{\boldsymbol{\theta}}(\tau) - \Omega\}] \boldsymbol{\theta}(\eta)
\end{aligned} \tag{3.10}$$

In Eq. (3.10), m_1 & m_2 is the mass of the rotor, K_1 & K_2 is the stiffness of the two span of the shaft, ΔK is the change in stiffness of right span of the shaft. J is the moment of inertia of the rotor mass, R_i and R_a are the internal and external damping of the rotor1,

R_i' and R_a' are the internal and external damping of the rotor 2, $x(\eta)$ and $y(\eta)$ are the displacements in real or Umbra time, θ is the angular displacements in η or τ times, and R_c is the resistance of dissipative coupling.

The BG model of the system shown in Figure 3.2 reveals that discrete multi-rotor system is SO(2) symmetric (symmetry for the rotor amplitude in mechanical coordinates). The rotational symmetries of umbra-Lagrangian of the finite rotor system may be achieved through the vector field. The umbra-Lagrangian of rotor system admits one parameter transformation groups, so infinitesimal generator (Hassani, 1999; Olver, 1986) of the rotational SO(2) group is termed as V' . The infinitesimal generators V' may be written as

$$\begin{aligned}
 V' = & y(\eta) \frac{\partial}{\partial x(\eta)} - x(\eta) \frac{\partial}{\partial y(\eta)} + y(\tau) \frac{\partial}{\partial x(\tau)} - x(\tau) \frac{\partial}{\partial y(\tau)} + \dot{y}(\eta) \frac{\partial}{\partial \dot{x}(\eta)} \\
 & - \dot{x}(\eta) \frac{\partial}{\partial \dot{y}(\eta)} + \dot{y}(\tau) \frac{\partial}{\partial \dot{x}(\tau)} - \dot{x}(\tau) \frac{\partial}{\partial \dot{y}(\tau)}
 \end{aligned} \tag{3.11}$$

The derivation of above infinitesimal generators is detailed in *Appendix 3*. One may obtain the invariance (symmetries) of umbra-Lagrangian of finite asymmetric rotor system of Eq. (3.10) through Eq. (3.11), which may be expressed in case $\Delta K \rightarrow 0$

$$\{V'(L^*)\} = 0$$

3.3.2 Extended Noether's equation for multi-rotor system with asymmetric stiffness

From Eq. (3.9), applying the extended Noether's theorem, one may obtain the Noether's rate equation for rotor 1 as

$$\begin{aligned}
\lim_{\eta \rightarrow \tau} (dL^*(V')) &= \frac{d}{d\tau} [m_1(\dot{\mathbf{x}}_1(\tau)\mathbf{y}_1(\tau) - \dot{\mathbf{y}}_1(\tau)\mathbf{x}_1(\tau)) - \Delta K\mathbf{y}_1(\tau)\mathbf{x}_1(\tau)] \\
&= -\dot{\theta}(\tau)R_i(\mathbf{x}_1^2(\tau) + \mathbf{y}_1^2(\tau)) + (R_a + R_i)(\mathbf{x}_1(\tau)\mathbf{y}_1(\tau) \\
&\quad - \dot{\mathbf{x}}_1(\tau)\mathbf{y}_1(\tau))
\end{aligned}$$

or

$$\begin{aligned}
\frac{d}{dt} [m_1(\dot{\mathbf{x}}_1(\tau)\mathbf{y}_1(\tau) - \dot{\mathbf{y}}_1(\tau)\mathbf{x}_1(\tau)) - \Delta K\mathbf{y}_1(\tau)\mathbf{x}_1(\tau)] \\
= -\dot{\theta}(\tau)R_i(\mathbf{x}_1^2(\tau) + \mathbf{y}_1^2(\tau)) + (R_a + R_i)(\mathbf{x}_1(\tau)\dot{\mathbf{y}}_1(\tau) \\
- \dot{\mathbf{x}}_1(\tau)\mathbf{y}_1(\tau))
\end{aligned} \tag{3.12}$$

In Eq. (3.12), the left hand side is the classical Noether's rate equation and this momentum may be equated by making the modulatory convection term on right side to be zero on some invariant trajectories with following assumptions

$$\mathbf{x}_1(\tau) = A_1 \cos \omega_1 \tau, \tag{3.13}$$

$$\mathbf{y}_1(\tau) = A_1 \sin \omega_1 \tau \tag{3.14}$$

where ω_1 is the natural frequency of limiting orbit of the rotor 1. The modulatory convection term of Eq. (3.12) provides

$$-\dot{\theta}(\tau)R_i A_1^2 = -A_1^2 \omega_1 (R_i + R_a) \tag{3.15}$$

$$\dot{\theta}(\tau) = \frac{\omega_1 (R_a + R_i)}{R_i}$$

$$\dot{\theta}(\tau) = \omega_1 \left(1 + \frac{R_a}{R_i} \right) \tag{3.16}$$

One may achieve Noether's rate equation for the rotor two, which can be expressed as

$$\begin{aligned}
\frac{d}{d\tau} [m_2 \{ \dot{x}_2(\tau) y_2(\tau) - \dot{y}_2(\tau) x_2(\tau) \}] \\
= -\dot{\theta}(\tau) R_i' \{ x_2^2(\tau) + y_2^2(\tau) \} \\
+ (R_a' + R_i') \{ x_2(\tau) \dot{y}_2(\tau) - \dot{x}_2(\tau) y_2(\tau) \}
\end{aligned} \tag{3.17}$$

Again, assuming the modulatory convection term of Eq. (3.17) to be zero on some invariant trajectories with following assumptions

$$x_2(\tau) = A_2 \cos \omega_2 \tau, \tag{3.18}$$

$$y_2(\tau) = A_2 \sin \omega_2 \tau \tag{3.19}$$

where ω_2 is the natural frequency of limiting orbit of the rotor 2. The modulatory convection term of Eq. (3.17) derives

$$\dot{\theta}'(\tau) = \frac{\omega_2 (R_a' + R_i')}{R_i'}$$

which finally yields

$$\dot{\theta}'(\tau) = \omega_2 \left(1 + \frac{R_a'}{R_i'} \right) \tag{3.20}$$

In Eqs. (3.16) and (3.20), $\dot{\theta}(\tau)$ and $\dot{\theta}'(\tau)$ are the shaft spinning speeds of rotor one and rotor two. The Noether's rate equation of rotor 1 due to asymmetries comes out to be

$$\frac{d}{d\tau} [m_1 \{ \dot{x}_1(\tau) y_1(\tau) - \dot{y}_1(\tau) x_1(\tau) \} - \Delta K(\eta) y_1(\tau) x_1(\tau)] = 0 \tag{3.21}$$

\longleftrightarrow symmetric \longrightarrow \longleftarrow asymmetric \longrightarrow

The Eq. (3.21) consists two significant terms, if asymmetric term equated to zero, i.e. there is no asymmetry in stiffness, one may obtain invariants of motions as

$$\frac{d}{d\tau} [m_1 \{\dot{\mathbf{x}}_1(\tau) \mathbf{y}_1(\tau) - \dot{\mathbf{y}}_1(\tau) \mathbf{x}_1(\tau)\}] = 0 \quad (3.22)$$

3.3.3 Umbra-Hamiltonian for multi-rotor system with asymmetric stiffness

The umbra-Hamiltonian of the system may be written as

$$H^* = H_i^* \{\mathbf{q}(\eta), \mathbf{p}(\eta)\} + H_e^* \{\mathbf{q}(\eta), \mathbf{p}(\eta), \mathbf{q}(\tau), \dot{\mathbf{q}}(\tau), \tau\} \quad (3.23)$$

This may be expressed as

$$H^* = H_i^* + H_e^* \quad (3.24)$$

Where

$$\begin{aligned} \{H_i^*\} = \frac{1}{2} & \left[\left\{ \frac{\mathbf{p}_{x_1}^2(\eta)}{m_1} + \frac{\mathbf{p}_{y_1}^2(\eta)}{m_1} \right\} + \{K_1(\eta) - \Delta K(\eta)\} \mathbf{x}_1^2(\eta) + K_1(\eta) \mathbf{y}_1^2(\eta) \right. \\ & \left. + \left\{ \frac{\mathbf{p}_{x_2}^2(\eta)}{m_2} + \frac{\mathbf{p}_{y_2}^2(\eta)}{m_2} \right\} + K_2(\eta) \{\mathbf{x}_2^2(\eta) + \mathbf{y}_2^2(\eta)\} + \frac{1}{J} \mathbf{p}_\theta^2(\eta) \right] \end{aligned} \quad (3.25)$$

$$\begin{aligned} \{H_e^*\} = [\mathbf{x}_1(\eta) \mathbf{y}_1(\eta)] & \begin{bmatrix} 0 & R_i \dot{\boldsymbol{\theta}}_1(\tau) \\ -R_i \dot{\boldsymbol{\theta}}_1(\tau) & 0 \end{bmatrix} \begin{bmatrix} \mathbf{x}_1(\eta) \\ \mathbf{y}_1(\eta) \end{bmatrix} \\ & + [\mathbf{x}_2(\eta) \mathbf{y}_2(\eta)] \begin{bmatrix} 0 & R_i \dot{\boldsymbol{\theta}}_2(\tau) \\ -R_i \dot{\boldsymbol{\theta}}_2(\tau) & 0 \end{bmatrix} \begin{bmatrix} \mathbf{x}_2(\eta) \\ \mathbf{y}_2(\eta) \end{bmatrix} \\ & + (R_a + R_i) \{\dot{\mathbf{x}}_1(\tau) \mathbf{x}_1(\eta) + \dot{\mathbf{y}}_1(\tau) \mathbf{y}_1(\eta)\} \\ & + (R'_a + R'_i) \{\dot{\mathbf{x}}_2(\tau) \mathbf{x}_2(\eta) + \dot{\mathbf{y}}_2(\tau) \mathbf{y}_2(\eta)\} \\ & + [R_i \{\mathbf{x}_1(\tau) \dot{\mathbf{y}}_1(\tau) - \mathbf{y}_1(\tau) \dot{\mathbf{x}}_1(\tau)\} \\ & + R'_i \{\mathbf{x}_2(\tau) \dot{\mathbf{y}}_2(\tau) - \mathbf{y}_2(\tau) \dot{\mathbf{x}}_2(\tau)\} + R_c \{\dot{\boldsymbol{\theta}}(\tau) - \Omega\}] \boldsymbol{\theta}(\eta) \end{aligned} \quad (3.26)$$

In Eq. (3.24), the interior Hamiltonian H_i^* does not related to any functional of real displacement, real velocities and real time whereas H_e^* depends on rest of

umbra-Hamiltonian comprising all real & virtual displacement, velocities and real time.

Applying the theorem 2 of Umbra-Hamiltonian, one may obtain:

$$\begin{aligned}
\lim_{\eta \rightarrow \tau} \left[\frac{dH_e^*}{d\eta} \right] &= R_i \dot{\theta}_1(\tau) \{ \dot{x}_1(\tau) y_1(\tau) - \dot{y}_1(\tau) x_1(\tau) \} \\
&+ (R_a + R_i) \{ \dot{x}_1^2(\tau) + \dot{y}_1^2(\tau) \} \\
&+ R'_i \dot{\theta}_2(\tau) \{ \dot{x}_2(\tau) y_2(\tau) - \dot{y}_2(\tau) x_2(\tau) \} \\
&+ (R'_a + R'_i) \{ \dot{x}_2^2(\tau) + \dot{y}_2^2(\tau) \} \\
&+ [R_i \{ x_1(\tau) \dot{y}_1(\tau) - y_1(\tau) \dot{x}_1(\tau) \} \\
&+ R'_i \{ x_2(\tau) \dot{y}_2(\tau) - y_2(\tau) \dot{x}_2(\tau) \} + R_c \{ \dot{\theta}(\tau) - \Omega \}] \dot{\theta}(\tau)
\end{aligned} \tag{3.27}$$

Assuming once again an orbit

$$x_1(\tau) = A_1 \cos \omega_1 \tau, y_1(\tau) = A_1 \sin \omega_1 \tau, \text{ and } x_2(\tau) = A_2 \cos \omega_2 \tau, y_2(\tau) = A_2 \sin \omega_2 \tau$$

one may obtain

$$\begin{aligned}
\lim_{\eta \rightarrow \tau} \left[\frac{dH_e^*}{d\eta} \right] &= -R_i \dot{\theta}_1(\tau) A_1^2 \omega_1 + (R_a + R_i) A_1^2 \omega_1^2 - R'_i \dot{\theta}_1(\tau) A_1^2 \omega_2 \\
&+ (R'_a + R'_i) A_1^2 \omega_2^2
\end{aligned} \tag{3.28}$$

$$\begin{aligned}
\lim_{\eta \rightarrow \tau} \left[\frac{dH_e^*}{d\eta} \right] &= + [R_i A_1^2 \omega_1 + R_c \{ \dot{\theta}_1(\tau) - \Omega \}] \dot{\theta}_1(\tau) \\
&+ [R'_i A_2^2 \omega_2 + R'_c \{ \dot{\theta}_2(\tau) - \Omega \}] \dot{\theta}_2(\tau)
\end{aligned} \tag{3.29}$$

Setting Eq. (3.28) equal to zero and compare the same coefficient yields as achieved in

Eq. (3.16) and (3.20)

$$\dot{\theta}(\tau) = \omega_1 \left(1 + \frac{R_a}{R_i}\right) \text{ and } \dot{\theta}'(\tau) = \omega_2 \left(1 + \frac{R_a'}{R_i'}\right)$$

Setting Eq. (3.29) equate to zero and compare the same coefficient of internal damping gives the amplitude of the rotor

$$A_1 = \sqrt{\frac{R_c}{R_i \omega_1} \left[\Omega - \omega_1 \left(1 + \frac{R_a}{R_i}\right) \right]} \quad (3.30)$$

and

$$A_2 = \sqrt{\frac{R_c}{R_i' \omega_2} \left[\Omega - \omega_2 \left(1 + \frac{R_a'}{R_i'}\right) \right]} \quad (3.31)$$

where A_1 and A_2 are the amplitude of rotor 1 and rotor 2.

If $R_i = R_i', R_a = R_a'$ and $\omega_1 = \omega_2 = \omega$,

Then, amplitude of the rotor may be achieved as

$$A = \sqrt{\frac{R_c}{2R_i \omega} \left[\Omega - \omega \left(1 + \frac{R_a}{R_i}\right) \right]} \quad (3.32)$$

Further,

$$\lim_{\eta \rightarrow \tau} \left[\frac{dH_i^*}{d\eta} \right] = 0 \quad (3.33)$$

One obtains the following expression

$$\frac{1}{2} \left[\left\{ \frac{\mathbf{p}_{\dot{x}_1}^2(\eta)}{m_1} + \frac{\mathbf{p}_{\dot{y}_1}^2(\eta)}{m_1} \right\} + \{K_1(\eta) - \Delta K(\eta)\} \mathbf{x}_1^2(\eta) + K_1 \mathbf{y}_1^2(\eta) + \left\{ \frac{\mathbf{p}_{\dot{x}_2}^2(\eta)}{m_2} + \frac{\mathbf{p}_{\dot{y}_2}^2(\eta)}{m_2} \right\} + K_2(\eta) \{ \mathbf{x}_2^2(\eta) + \mathbf{y}_2^2(\eta) \} + \frac{1}{J} \mathbf{p}_{\dot{\theta}}^2(\eta) \right] = 0 \quad (3.34)$$

Now $\eta \rightarrow \tau$ and putting $\mathbf{p}_{x_1}(\tau) = \lim_{\eta \rightarrow \tau} \{m_1 \dot{x}_1(\eta)\} = m_1 \dot{x}_1(\tau)$.

Similarly $\mathbf{p}_{y_1}(\tau) = m_1 \dot{y}_1(\tau)$, $\mathbf{p}_{x_2}(\tau) = m_2 \dot{x}_2(\tau)$, $\mathbf{p}_{y_2}(\tau) = m_2 \dot{y}_2(\tau)$ and $\mathbf{p}_{\theta}(\tau) =$

$J\dot{\theta}(\tau)$ in Eq. (3.34), one may obtain the equation as

$$(m_1 \ddot{x}_1 + (K_1 - \Delta K) x_1) \dot{x}_1 + (m_1 \ddot{y}_1 + K_1 y_1) \dot{y}_1 + (m_2 \ddot{x}_2 + K_2 x_2) \dot{x}_2 + (m_2 \ddot{y}_2 + K_2 y_2) \dot{y}_2 = 0 \quad (3.35)$$

The two types of frequencies are available in Eq. (3.35). Applying the method as presented by *Krodkiwski* (2007), In case of first rotor, one may obtain the natural frequency in y-y direction if symmetric part is there, one may have

$$\omega_{y1} = \sqrt{\frac{K_1}{m_1}} \quad (3.36)$$

If unsymmetric part is there, one obtain the natural frequency in x-x direction

$$\omega_{x1} = \sqrt{\frac{K_1 - \Delta K}{m_1}} \quad (3.37)$$

In case of second rotor

$$\omega_{x2} = \sqrt{\frac{K_2}{m_2}}, \quad \omega_{y2} = \sqrt{\frac{K_2}{m_2}} \quad (3.38)$$

The final natural frequency, may be finally represented as

$$\omega^2 = \frac{\omega_{x1}^2 + \omega_{y1}^2}{2}$$

$$\omega_1 = \sqrt{\frac{K_1 - \frac{\Delta K}{2}}{m_1}} \quad (3.39)$$

$$\omega_2 = \sqrt{\frac{K_2}{m_2}} \quad (3.40)$$

The next subsection will present simulation study, which will further validate the analytical model.

3.3.4 Simulation study and validation

The prime objective of this simulation is to achieve an insight dynamics of multi-rotor-system and ascertaining the electromechanical influence of multi-rotor with asymmetries. Moreover, it confirms analytical results. The bondgraph model of multi-rotors with asymmetries with external and internal damping was simulated SYMBOLS-Shakti[®] (*Mukherjee and Samantaray, 2006*) software with parameters presented in Table 3.1. To show the efficiency of the simulation, a series of parametric variation are carried out as the model is significantly sensitive to all such variations in parameters.

The threshold angular speed of instability found to be twice the natural frequency of rotor 1 using the parameters presented in Table 3.1. It is evident from Figure 3.3 that the amplitude of rotor 1 at variable stiffness shows the correctness of an analytical model upto maximum 7 % variation in stiffness. One may find a marginal difference in simulated and analytical value of rotor 1 amplitude beyond 7 % variation

in stiffness. After that the variation is little more due to the parametric sensitivity. The amplitude of the rotor increases with percentage change of stiffness of rotor 1.

Table 3.1: Simulation parameters

	Parameter	Value
Stiffness of the rotor 1 and rotor 2	K_1, K_2	1000 N m ⁻¹
Mass of the rotor 1 and rotor 2	m_1, m_2	10 Kg
Mass Moment of Inertial of rotor	J	1 Kg m ²
Internal damping coefficient of rotor 1 and rotor 2	R_i, R_i'	5 N s m ⁻¹
External damping coefficient of rotor 1 and rotor 2	R_a, R_a'	5 N s m ⁻¹
Damping coefficient of dissipative couplings	R_c	0.2 N s m ⁻¹
Constant excitation frequency	Ω	22 rad s ⁻¹
Range of change in stiffness	ΔK	0-100 N m ⁻¹

Likewise trend is also achieved in Figure 3.4, where analytical frequency nearly matches with the simulated frequency obtained for rotor 1. A general behaviour of reduction in the natural frequencies is noticed at various stiffness variations.

In Figure 3.5, it has been shown that the simulated value of rotor amplitudes at various excitation frequencies with stiffness variation. The amplitude of the rotor increases with increase in stiffness variation. Considerable good agreement between analytical and simulated results has been stated. Here again the parametric variation of asymmetric rotor can be compared reasonably with the numerical simulation. One may easily diagnose any faults in the multi-rotor-system by knowing the amplitude of rotor 1 through Eq. (3.30), which is theoretically obtained through extended Lagrangian methodology.

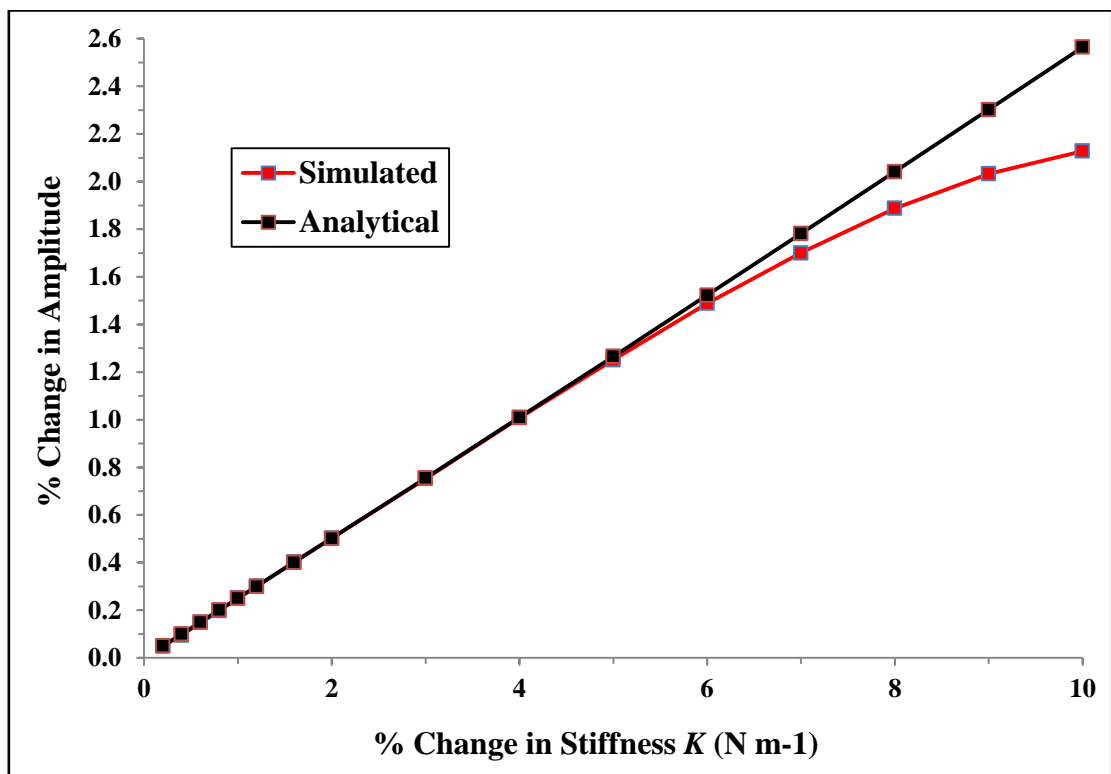


Figure 3.3: % Change in amplitude of rotor 1 Vs % change in stiffness

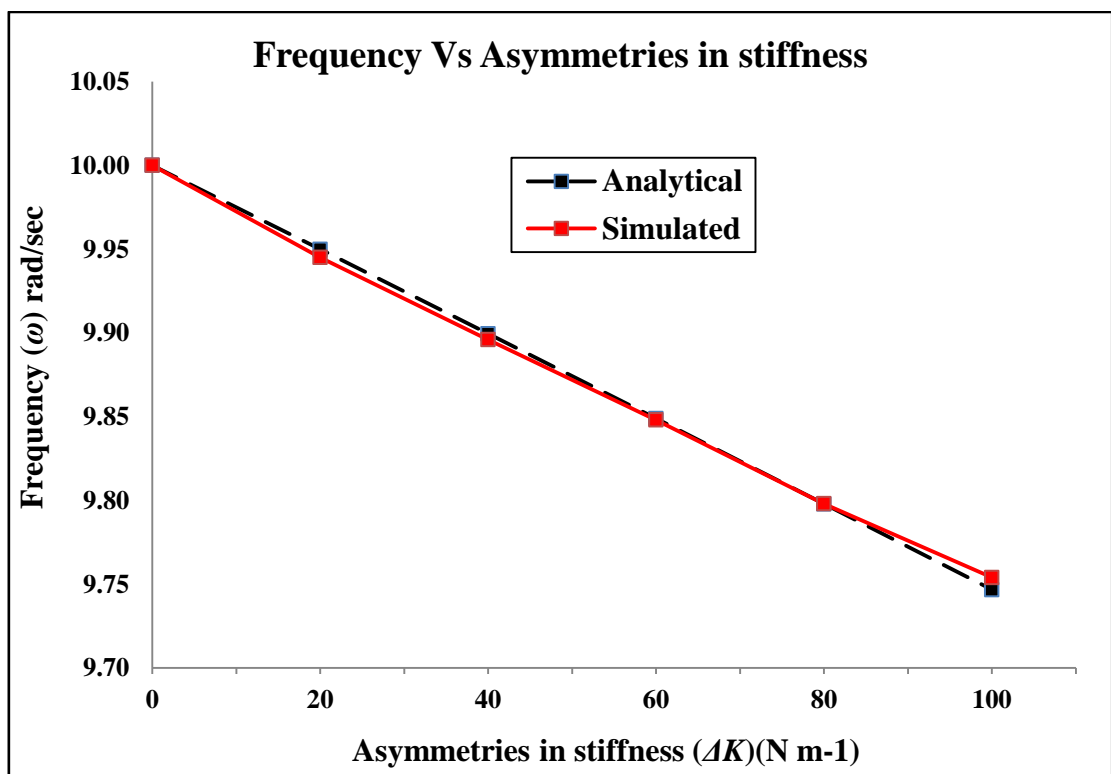


Figure 3.4: Frequency of rotor Vs asymmetries in stiffness

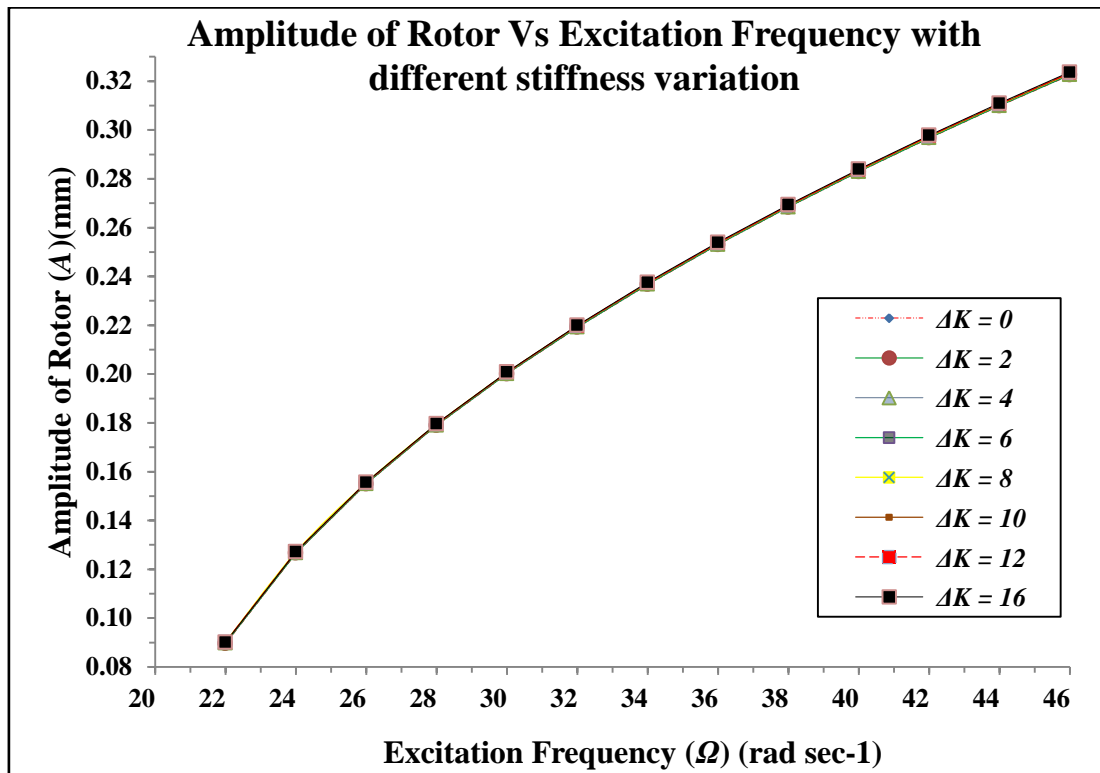


Figure 3.5: Amplitude of the rotor Vs excitation frequency with different stiffness variation

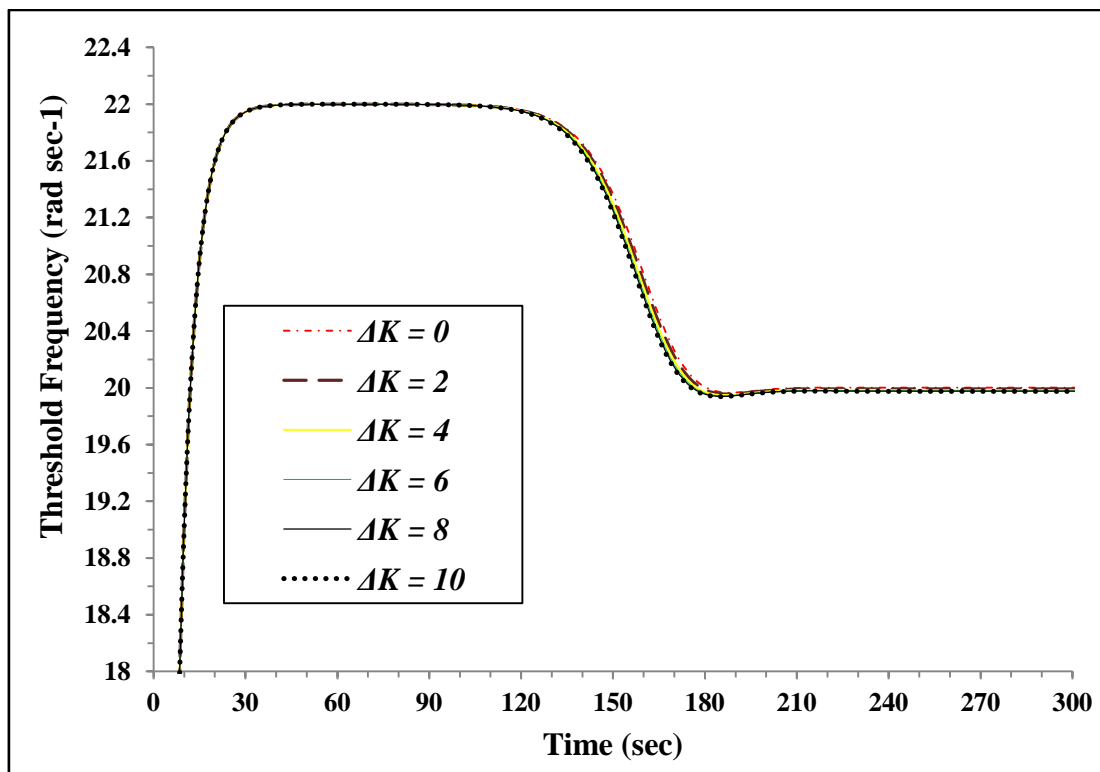


Figure 3.6: Threshold frequency Vs time with different stiffness variation

In Figure 3.6, the simulated value of threshold frequency with stiffness variation is plotted. In this figure, the frequency obtained by simulation results is nearly same as analytical value. It is apparent that the threshold frequency of the rotor 1 decreases with increases in ΔK and conforms to angular speed obtained through extended formalism. This is basically the frequency at which the asymmetric rotor is spinning in actual. This phenomenon has a great application for monitoring and diagnoses the cracks in multi-rotor-system in plants. The next section will highlight another case with asymmetries due to point mass of any rotor in multi-rotor system. The next section will highlight the another case with asymmetries due to point mass of any rotor in multi-rotor system.

3.4 Case study–II: Analysis of finite multi-rotor system with asymmetries due to mass using extended Lagrangian formalism

In recent years, the dynamic behaviour and diagnostic of cracked rotor have been gained momentum. In literature, several studies are available for cracked rotor systems, however very few authors have addressed the issue of asymmetries due to various parameters in multi-cracked rotor system. In order to investigate the dynamical behaviour of the finite rotor system with asymmetries due to mass, extended Lagrangian formulation has been developed in this case study.

In this case, a multi-rotor-system with asymmetries in mass is being analyzed through extended Lagrangian formulation. In this analytical model, a shaft is carrying two rotors, which are mounted on equal distances. The shaft is driven by DC motor as shown in Figure 3.1. In this case, variation of mass is the main cause of asymmetries. Thus, one may evaluate mass and damping properties in two orthogonal directions. In

this evaluation, dampers may incorporate external as well as internal damping. One of the rotors consist small asymmetries due to mass variation of rotor. It is assumed that stiffness is constant in this dynamics.

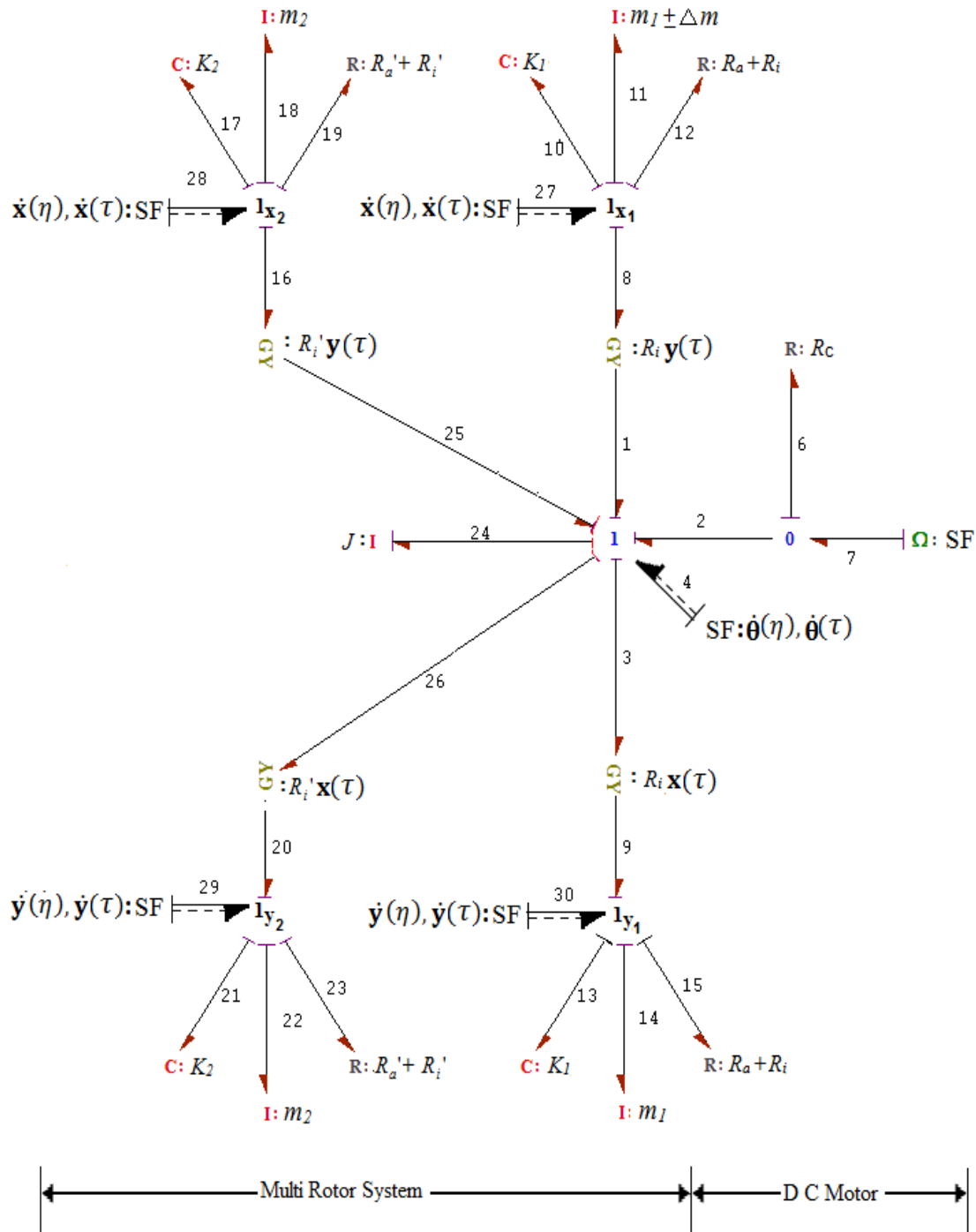


Figure 3.7: Bondgraph model of multi rotors with artificial flow sources to obtain umbra-Lagrangian in mass asymmetries case

The bondgraph model of the physical system is shown in Figure 3.7, which contains causalled bond for generation of system equations and simulation results (Mukherjee *et al.*, 2007). The modulated gyrator element has been used to portray an additional circulatory effects due to internal damping. Bonds 4, 27, 28, 29, 30 represent the artificial flow sources to obtain umbra-Lagrangian of the system. The rate of rotation of shaft has been recorded by flow activated C-bond.

Model represents the interaction of energy in the system. In the pictorial representation, Δm shows the change in mass in X direction in rotor1, which makes the system asymmetric.

3.4.1 Umbra-Lagrangian for multi-rotor system with asymmetric in mass

The umbra-Lagrangian may be formulated following the steps discussed in various published research paper (Jain *et al.*, 2018; Mukherjee, 2001; Rastogi and Kumar, 2009). The umbra-Lagrangian corresponding to the BG model shown in Fig. 3.7 may be expressed as

$$\begin{aligned}
L^* = & \frac{1}{2} [m_1 \{\dot{\mathbf{x}}_1^2(\eta)\} + (m_1 + \Delta m) \{\dot{\mathbf{y}}_1^2(\eta)\} - K_1 \{\mathbf{x}_1^2(\eta) + \mathbf{y}_1^2(\eta)\} + J \dot{\boldsymbol{\theta}}^2(\eta) \\
& + m_2 \{\dot{\mathbf{x}}_2^2(\eta) + \dot{\mathbf{y}}_2^2(\eta)\} - K_2 \{\mathbf{x}_2^2(\eta) + \mathbf{y}_2^2(\eta)\}] \\
& - [\mathbf{x}_1(\eta) \mathbf{y}_1(\eta)] \begin{bmatrix} 0 & R_i \dot{\boldsymbol{\theta}}(\tau) \\ -R_i \dot{\boldsymbol{\theta}}(\tau) & 0 \end{bmatrix} \begin{Bmatrix} \mathbf{x}_1(\tau) \\ \mathbf{y}_1(\tau) \end{Bmatrix} \\
& - [\mathbf{x}_2(\eta) \mathbf{y}_2(\eta)] \begin{bmatrix} 0 & R_i \dot{\boldsymbol{\theta}}(\tau) \\ -R_i \dot{\boldsymbol{\theta}}(\tau) & 0 \end{bmatrix} \begin{Bmatrix} \mathbf{x}_2(\tau) \\ \mathbf{y}_2(\tau) \end{Bmatrix} \\
& - (R_a + R_i) \{\mathbf{x}_1(\eta) \dot{\mathbf{x}}_1(\tau) + \mathbf{y}_1(\eta) \dot{\mathbf{y}}_1(\tau)\} \\
& - (R_a' + R_i') \{\mathbf{x}_2(\eta) \dot{\mathbf{x}}_2(\tau) + \mathbf{y}_2(\eta) \dot{\mathbf{y}}_2(\tau)\} \\
& - [R_i \{\mathbf{x}_1(\tau) \dot{\mathbf{y}}_1(\tau) - \mathbf{y}_1(\tau) \dot{\mathbf{x}}_1(\tau)\} \\
& + R_i' \{\mathbf{x}_2(\tau) \dot{\mathbf{y}}_2(\tau) - \mathbf{y}_2(\tau) \dot{\mathbf{x}}_2(\tau)\} - R_c \{\dot{\boldsymbol{\theta}}(\tau) - \Omega\}] \boldsymbol{\theta}(\eta)
\end{aligned} \tag{3.41}$$

In Eq. (3.41), m_1 and m_2 is the mass of the rotor, K_1 and K_2 is the stiffness of the two span of the shaft, Δm is the change in mass of right span of the shaft. J is the moment of inertia of the rotor mass, R_i and R_a are the internal and external damping of the rotor 1, R_i' and R_a' are the internal and external damping of the rotor 2, $x(\cdot)$ and $y(\cdot)$ are the displacements in real or Umbra time, θ is the angular displacements in η or t times, and R_c is the resistance of dissipative coupling.

3.4.2 Extended Noether's equation for multi-rotor system with asymmetric due to mass variation

From Eq. (3.9), Applying the extended Noether's theorem, one may obtain the Noether's rate equation for rotor 1 as

$$\begin{aligned} \lim_{\eta \rightarrow t} (dL^*(V')) &= \frac{d}{dt} [\{m_1(\dot{\mathbf{x}}_1(\tau)\mathbf{y}_1(\tau) - \dot{\mathbf{y}}_1(\tau)\mathbf{x}_1(\tau)) - \Delta m_1(-\mathbf{y}_1(\tau)\mathbf{x}_1(\tau))\}] \\ &= -\dot{\theta}(\tau)R_i(\mathbf{x}_1^2(\tau) + \mathbf{y}_1^2(\tau)) + (R_a + R_i)(\mathbf{x}_1(\tau)\dot{\mathbf{y}}_1(\tau) \\ &\quad - \dot{\mathbf{x}}_1(\tau)\mathbf{y}_1(\tau)) \end{aligned}$$

or

$$\begin{aligned} \frac{d}{d\tau} [\{m_1(\dot{\mathbf{x}}_1(\tau)\mathbf{y}_1(\tau) - \dot{\mathbf{y}}_1(\tau)\mathbf{x}_1(\tau)) - \Delta m_1(-\mathbf{y}_1(\tau)\mathbf{x}_1(\tau))\}] \\ = -\dot{\theta}(\tau)R_i(\mathbf{x}_1^2(\tau) + \mathbf{y}_1^2(\tau)) + (R_a + R_i)(\mathbf{x}_1(\tau)\dot{\mathbf{y}}_1(\tau) \\ - \dot{\mathbf{x}}_1(\tau)\mathbf{y}_1(\tau)) \end{aligned} \quad (3.42)$$

In Eq. (3.42), the left hand side is the classical Noether's rate equation and this momentum may be equated to by making the modulatory convection term on right side to be zero on some invariant trajectories with following assumptions

$$\mathbf{x}_1(\tau) = A_1 \cos \omega_1 \tau, \quad (3.43)$$

$$\mathbf{y}_1(\tau) = A_1 \sin \omega_1 \tau \quad (3.44)$$

where ω_1 is the natural frequency of limiting orbit of the rotor 1. The modulatory convection term of Eq.(3.42) provides

$$-\dot{\theta}(\tau) R_i A_1^2 = -A_1^2 \omega_1 (R_i + R_a) \quad (3.45)$$

$$\dot{\theta}(\tau) = \frac{\omega_1 (R_a + R_i)}{R_i}$$

$$\dot{\theta}(\tau) = \omega_1 \left(1 + \frac{R_a}{R_i} \right) \quad (3.46)$$

One may achieve Noether's rate equation for the rotor two, which can be expressed as

$$\begin{aligned} \frac{d}{d\tau} [m_2 \{ \dot{\mathbf{x}}_2(\tau) \mathbf{y}_2(\tau) - \dot{\mathbf{y}}_2(\tau) \mathbf{x}_2(\tau) \}] \\ = -\dot{\theta}'(\tau) R_i' \{ \mathbf{x}_2^2(\tau) + \mathbf{y}_2^2(\tau) \} \\ + (R_a' + R_i') \{ \mathbf{x}_2(\tau) \dot{\mathbf{y}}_2(\tau) - \dot{\mathbf{x}}_2(\tau) \mathbf{y}_2(\tau) \} \end{aligned} \quad (3.47)$$

Again, assuming the modulatory convection term of Eq. (3.47) to be zero on some invariant trajectories with following assumptions

$$\mathbf{x}_2(\tau) = A_2 \cos \omega_2 \tau, \quad (3.48)$$

$$\mathbf{y}_2(\tau) = A_2 \sin \omega_2 \tau \quad (3.49)$$

where ω_2 is the natural frequency of limiting orbit of the rotor 2. The modulatory convection term of Eq. (3.47) derives

$$\dot{\theta}'(\tau) = \frac{\omega_2 (R_a' + R_i')}{R_i'}$$

which finally yields

$$\dot{\boldsymbol{\theta}}'(\tau) = \omega_2 \left(1 + \frac{R_a'}{R_i'} \right) \quad (3.50)$$

In Eqs. (3.46) and (3.50), $\dot{\boldsymbol{\theta}}(\tau)$ and $\dot{\boldsymbol{\theta}}'(\tau)$ are the shaft spinning speeds of rotor one and rotor two. The Noether's rate equation of rotor 1 due to asymmetries comes out to be

$$\frac{d}{d\tau} \left[\underbrace{m_1(\dot{\mathbf{x}}_1(\tau)\mathbf{y}_1(\tau) - \dot{\mathbf{y}}_1(\tau)\mathbf{x}_1(\tau))}_{\text{symmetric}} - \underbrace{\Delta m_1(-\mathbf{y}_1(\tau)\mathbf{x}_1(\tau))}_{\text{asymmetric}} \right] = 0 \quad (3.51)$$

The Eq. (3.51) consists two significant terms, if asymmetric term equated to zero, i.e. there is no asymmetry in stiffness, one may obtain invariants of motions as

$$\frac{d}{d\tau} [m_1\{\dot{\mathbf{x}}_1(\tau)\mathbf{y}_1(\tau) - \dot{\mathbf{y}}_1(\tau)\mathbf{x}_1(\tau)\}] = 0 \quad (3.52)$$

3.4.3 Umbra-Hamiltonian for multi rotor system with asymmetric mass

From Eq. (3.23) the umbra-Hamiltonian of the system may be written as

$$H^* = H_i^*\{\mathbf{q}(\eta), \mathbf{p}(\eta)\} + H_e^*\{\mathbf{q}(\eta), \mathbf{p}(\eta), \mathbf{q}(\tau), \dot{\mathbf{q}}(\tau), \tau\}$$

This may be expressed as

$$H^* = H_i^* + H_e^* \quad (3.53)$$

where

$$\begin{aligned} \{H_i^*\} = & \frac{1}{2} \left[\left\{ \frac{\mathbf{p}_{x_1}^2(\eta)}{m_1} + \frac{\mathbf{p}_{y_1}^2(\eta)}{m_1} \right\} + K_1(\eta) \{ \mathbf{x}_1^2(\eta) + \mathbf{y}_1^2(\eta) \} \right. \\ & \left. + \left\{ \frac{\mathbf{p}_{x_2}^2(\eta)}{m_2} + \frac{\mathbf{p}_{y_2}^2(\eta)}{m_2} \right\} + K_2(\eta) \{ \mathbf{x}_2^2(\eta) + \mathbf{y}_2^2(\eta) \} + \frac{1}{J} \mathbf{p}_{\boldsymbol{\theta}}^2(\eta) \right] \end{aligned} \quad (3.54)$$

$$\begin{aligned}
\{H_e^*\} = & [\mathbf{x}_1(\eta)\mathbf{y}_1(\eta)] \begin{bmatrix} 0 & R_i\dot{\boldsymbol{\theta}}_1(\tau) \\ -R_i\dot{\boldsymbol{\theta}}_1(\tau) & 0 \end{bmatrix} \begin{bmatrix} \mathbf{x}_1(\eta) \\ \mathbf{y}_1(\eta) \end{bmatrix} \\
& + [\mathbf{x}_2(\eta)\mathbf{y}_2(\eta)] \begin{bmatrix} 0 & R_i\dot{\boldsymbol{\theta}}_2(\tau) \\ -R_i\dot{\boldsymbol{\theta}}_2(\tau) & 0 \end{bmatrix} \begin{bmatrix} \mathbf{x}_2(\eta) \\ \mathbf{y}_2(\eta) \end{bmatrix} \\
& + (R_a + R_i)\{\dot{\mathbf{x}}_1(\tau)\mathbf{x}_1(\eta) + \dot{\mathbf{y}}_1(\tau)\mathbf{y}_1(\eta)\} \\
& + (R'_a + R'_i)\{\dot{\mathbf{x}}_2(\tau)\mathbf{x}_2(\eta) + \dot{\mathbf{y}}_2(\tau)\mathbf{y}_2(\eta)\} \\
& + [R_i\{\mathbf{x}_1(\tau)\dot{\mathbf{y}}_1(\tau) - \mathbf{y}_1(\tau)\dot{\mathbf{x}}_1(\tau)\} \\
& + R'_i\{\mathbf{x}_2(\tau)\dot{\mathbf{y}}_2(\tau) - \mathbf{y}_2(\tau)\dot{\mathbf{x}}_2(\tau)\} + R_c\{\dot{\boldsymbol{\theta}}(\tau) - \Omega\}]\boldsymbol{\theta}(\eta)
\end{aligned} \tag{3.55}$$

In Eq. (3.53), the interior Hamiltonian H_i^* does not related to any functional of real displacement, real velocities and real time whereas H_e^* depends on rest of umbra-Hamiltonian comprising all real and virtual displacement, velocities and real time.

According to the theorem 2 of Umbra-Hamiltonian:

$$\lim_{\eta \rightarrow \tau} \left[\frac{dH_e^*}{d\eta} \right] = 0 \tag{3.56}$$

Applying the above theorem, one may obtain:

$$\begin{aligned}
\lim_{\eta \rightarrow \tau} \left[\frac{dH_e^*}{d\eta} \right] = & R_i\dot{\boldsymbol{\theta}}_1(\tau)\{\dot{\mathbf{x}}_1(\tau)\mathbf{y}_1(\tau) - \dot{\mathbf{y}}_1(\tau)\mathbf{x}_1(\tau)\} \\
& + (R_a + R_i)\{\dot{\mathbf{x}}_1^2(\tau) + \dot{\mathbf{y}}_1^2(\tau)\} \\
& + R'_i\dot{\boldsymbol{\theta}}_2(\tau)\{\dot{\mathbf{x}}_2(\tau)\mathbf{y}_2(\tau) - \dot{\mathbf{y}}_2(\tau)\mathbf{x}_2(\tau)\} \\
& + (R'_a + R'_i)\{\dot{\mathbf{x}}_2^2(\tau) + \dot{\mathbf{y}}_2^2(\tau)\} \\
& + [R_i\{\mathbf{x}_1(\tau)\dot{\mathbf{y}}_1(\tau) - \mathbf{y}_1(\tau)\dot{\mathbf{x}}_1(\tau)\} \\
& + R'_i\{\mathbf{x}_2(\tau)\dot{\mathbf{y}}_2(\tau) - \mathbf{y}_2(\tau)\dot{\mathbf{x}}_2(\tau)\} + R_c\{\dot{\boldsymbol{\theta}}(\tau) - \Omega\}]\dot{\boldsymbol{\theta}}(\tau)
\end{aligned} \tag{3.57}$$

Assuming once again an orbit

$$\mathbf{x}_1(\tau) = A_1 \cos \omega_1 \tau, \mathbf{y}_1(\tau) = A_1 \sin \omega_1 \tau, \text{ and } \mathbf{x}_2(\tau) = A_2 \cos \omega_2 \tau, \mathbf{y}_2(\tau) = A_2 \sin \omega_2 \tau,$$

one may obtain

$$\begin{aligned} \lim_{\eta \rightarrow \tau} \left[\frac{dH_e^*}{d\eta} \right] = & -R_i \dot{\theta}_1(\tau) A_1^2 \omega_1 + (R_a + R_i) A_1^2 \omega_1^2 - R_i' \dot{\theta}_1(\tau) A_1^2 \omega_2 \\ & + (R_a' + R_i') A_1^2 \omega_2^2 \end{aligned} \quad (3.58)$$

$$\begin{aligned} \lim_{\eta \rightarrow \tau} \left[\frac{dH_e^*}{d\eta} \right] = & + [R_i A_1^2 \omega_1 + R_c \{\dot{\theta}_1(\tau) - \Omega\}] \dot{\theta}_1(\tau) \\ & + [R_i' A_2^2 \omega_2 + R_c' \{\dot{\theta}_2(\tau) - \Omega\}] \dot{\theta}_2(\tau) \end{aligned} \quad (3.59)$$

Setting Eq. (3.58) equal to zero and compare the same coefficient yields as achieved in Eq. (3.46) and (3.50)

$$\dot{\theta}(\tau) = \omega_1 \left(1 + \frac{R_a}{R_i} \right) \text{ and } \dot{\theta}'(\tau) = \omega_2 \left(1 + \frac{R_a'}{R_i'} \right)$$

Setting Eq. (3.59) equal to zero and compare the same coefficient of internal damping gives the amplitude of the rotor

$$A_1 = \sqrt{\frac{R_c}{R_i \omega_1} \left[\Omega - \omega_1 \left(1 + \frac{R_a}{R_i} \right) \right]} \quad (3.60)$$

and

$$A_2 = \sqrt{\frac{R_c}{R_i' \omega_2} \left[\Omega - \omega_2 \left(1 + \frac{R_a'}{R_i'} \right) \right]} \quad (3.61)$$

where A_1 and A_2 are the amplitude of rotor 1 and rotor 2.

If $R_i = R_i', R_a = R_a'$ and $\omega_1 = \omega_2 = \omega$,

Then, amplitude of the rotor may be achieved as

$$A = \sqrt{\frac{R_c}{2R_i\omega} \left[\Omega - \omega \left(1 + \frac{R_a}{R_i} \right) \right]} \quad (3.62)$$

Further,

$$\lim_{\eta \rightarrow \tau} \left[\frac{dH_i^*}{d\eta} \right] = 0 \quad (3.63)$$

One obtains the following expression

$$\begin{aligned} \frac{1}{2} \left[\left\{ \frac{\mathbf{p}_{\dot{x}_1}^2(\eta)}{m_1} + \frac{\mathbf{p}_{\dot{y}_1}^2(\eta)}{(m_1 - \Delta m_1)} \right\} + K_1(\eta) \{ \mathbf{x}_1^2(\eta) + \mathbf{y}_1^2(\eta) \} + \left\{ \frac{\mathbf{p}_{\dot{x}_2}^2(\eta)}{m_2} + \frac{\mathbf{p}_{\dot{y}_2}^2(\eta)}{m_2} \right\} \right. \\ \left. + K_2(\eta) \{ \mathbf{x}_2^2(\eta) + \mathbf{y}_2^2(\eta) \} + \frac{1}{J} \mathbf{p}_{\dot{\theta}}^2(\eta) \right] = 0 \end{aligned} \quad (3.64)$$

Now $\eta \rightarrow \tau$ and putting $\mathbf{p}_{x_1}(\tau) = \lim_{\eta \rightarrow \tau} \{ m_1 \dot{\mathbf{x}}_1(\eta) \} = m_1 \dot{\mathbf{x}}_1(\tau)$.

Similarly $\mathbf{p}_{y_1}(\tau) = m_1 \dot{\mathbf{y}}_1(\tau)$, $\mathbf{p}_{x_2}(\tau) = m_2 \dot{\mathbf{x}}_2(\tau)$, $\mathbf{p}_{y_2}(\tau) = m_2 \dot{\mathbf{y}}_2(\tau)$ and $\mathbf{p}_{\theta}(\tau) = J \dot{\theta}(\tau)$

in Eq. (3.64), one may obtain the equation as

$$\begin{aligned} (m_1 \ddot{\mathbf{x}}_1 + K_1 \mathbf{x}_1) \dot{\mathbf{x}}_1 + (m_1 \ddot{\mathbf{y}}_1 + (m_1 \pm \Delta m_1) \ddot{\mathbf{y}}_1 + K_1 \mathbf{y}_1) \dot{\mathbf{y}}_1 + (m_2 \ddot{\mathbf{x}}_2 + K_2 \mathbf{x}_2) \dot{\mathbf{x}}_2 \\ + (m_2 \ddot{\mathbf{y}}_2 + K_2 \mathbf{y}_2) \dot{\mathbf{y}}_2 = 0 \end{aligned} \quad (3.65)$$

The two types of frequencies are available in Eq. (3.65). Applying the method as presented by *Krodkiwski* (2007), In case of first rotor, one may obtain the natural frequency in y-y direction if symmetric part is there, one may have

$$\omega_{y1} = \sqrt{\frac{K_1}{m_1}} \quad (3.66)$$

If unsymmetric part is there, one may obtain the natural frequency in x - x direction

$$\omega_{x1} = \sqrt{\frac{K_1}{(m_1 \pm \Delta m_1)}} \quad (3.67)$$

In case of second rotor

$$\omega_{x2} = \sqrt{\frac{K_2}{m_2}}, \quad \omega_{y2} = \sqrt{\frac{K_2}{m_2}} \quad (3.68)$$

The final natural frequency, may be finally represented as

$$\omega^2 = \frac{\omega_{x1}^2 + \omega_{y1}^2}{2}$$

$$\omega_1 = \sqrt{\frac{2K_1}{(m_1 \pm \Delta m_1)}} \quad (3.69)$$

and
$$\omega_2 = \sqrt{\frac{K_2}{m_2}} \quad (3.70)$$

The next subsection will present simulation study, which will further consolidate analytical model presented in this section.

3.4.4 Simulations study and validation

The prime objective of this simulation is to validate the mathematical results obtained through the umbra-Lagrangian model of multi-rotor system having mass asymmetry. The bondgraph model of multi-rotors with mass asymmetries in rotor 1 with external and internal damping was simulated on SYMBOLS-Shakti[®] (*Mukherjee and Samantaray, 2006*), a bondgraph simulation software with parameters presented in Table 3.2. In this case, the effects of mass variation are closely linked to the different parameter like

excitation frequency, amplitude, natural frequency, internal and external damping. To show the efficacy of the simulation, a series of parametric variation are carried out. Moreover, it confirms analytical results. However, simulation and mathematical results are provided here to compare the dynamic behavior of mass asymmetric system.

Table 3.2: Simulation parameters

Parameter	Notation	Value
Stiffness of the rotor 1 and rotor 2	K_1, K_2	1000 N m ⁻¹
Mass of the rotor 1 and rotor 2	m_1, m_2	10 Kg
Mass Moment of Inertial of rotor	J	1 Kg m ²
Internal damping coefficient of rotor 1 and rotor 2	R_i, R_i'	5 N s m ⁻¹
External damping coefficient of rotor 1 and rotor 2	R_a, R_a'	5 N s m ⁻¹
Damping coefficient of dissipative couplings	R_c	0.2 N s m ⁻¹
Excitation frequency range	Ω	22 - 46 rad s ⁻¹
Range of change in mass	Δm_1	0 \pm 1 Kg

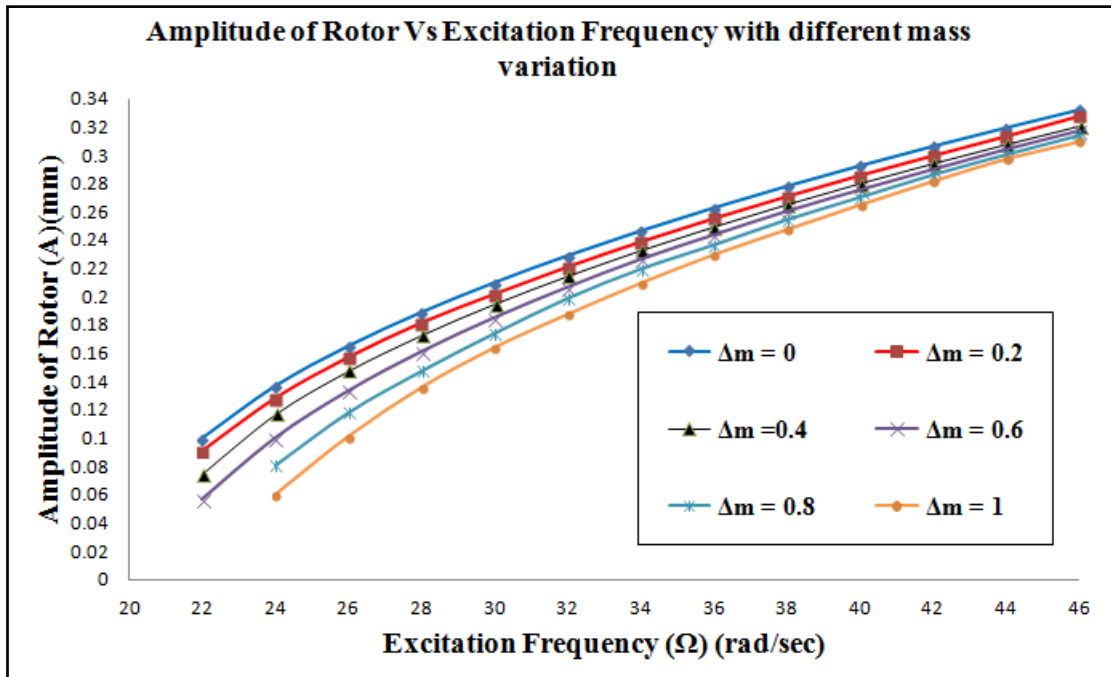


Figure 3.8: Amplitude of the rotor 1 Vs excitation frequency with different mass variation

It has been observed from Figure 3.8 that the simulated value of rotor amplitudes is directly proportional to excitation frequencies. However, the same pattern has been seen for the displacement of the rotor. In addition, when the value of mass asymmetry (Δm) is added in the rotor mass, the value of amplitude is proportionally affected. Amplitude of rotor increases with mass. It is well known concept that the natural frequency of rotor decreases with increase in mass. Moreover, the rotor system is found un-stable at excitation frequency 22 rad/sec, when the value of Δm is 0.8 and 1 kg. Further, the response of rotor system obtained from simulation study has been precisely validated with analytical study. Thus the fault of any multi-rotor system may be diagnosed from the Eq. (3.62), which was theoretically obtained through extended Lagrangian methodology.

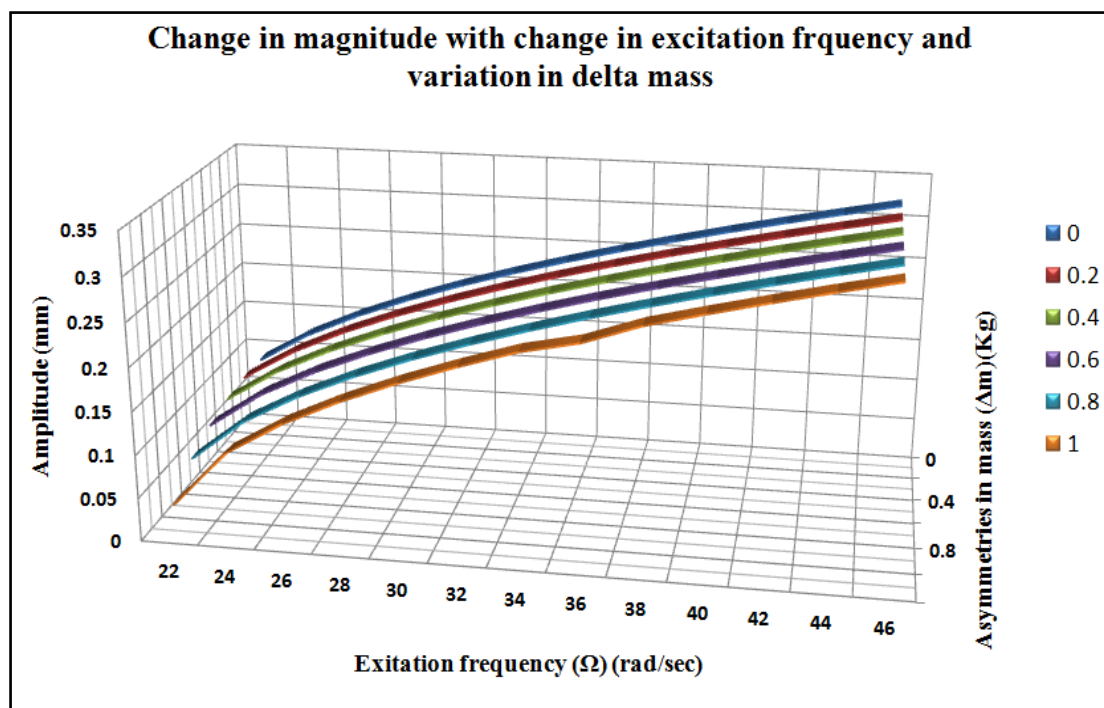


Figure 3.9: 3-Dimensional representation of variation in amplitude of the rotor1, excitation frequency & mass variation

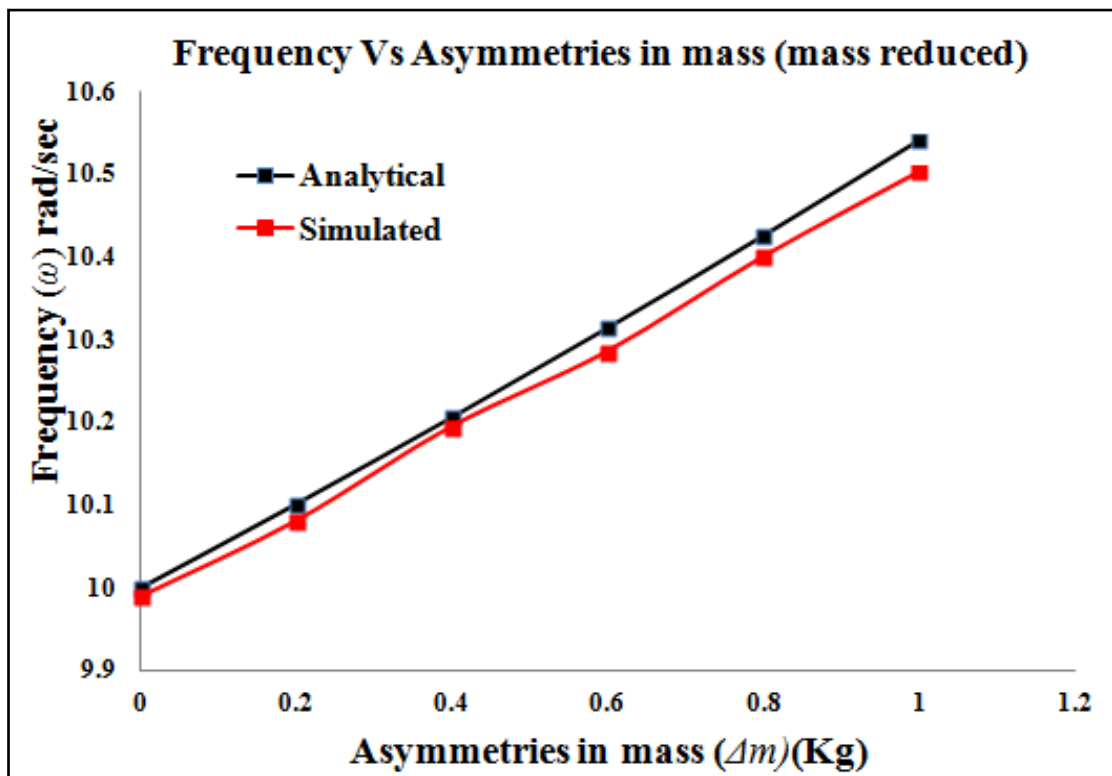


Figure 3.10: Frequency (ω) of rotor 1 Vs mass asymmetries (mass reduced)

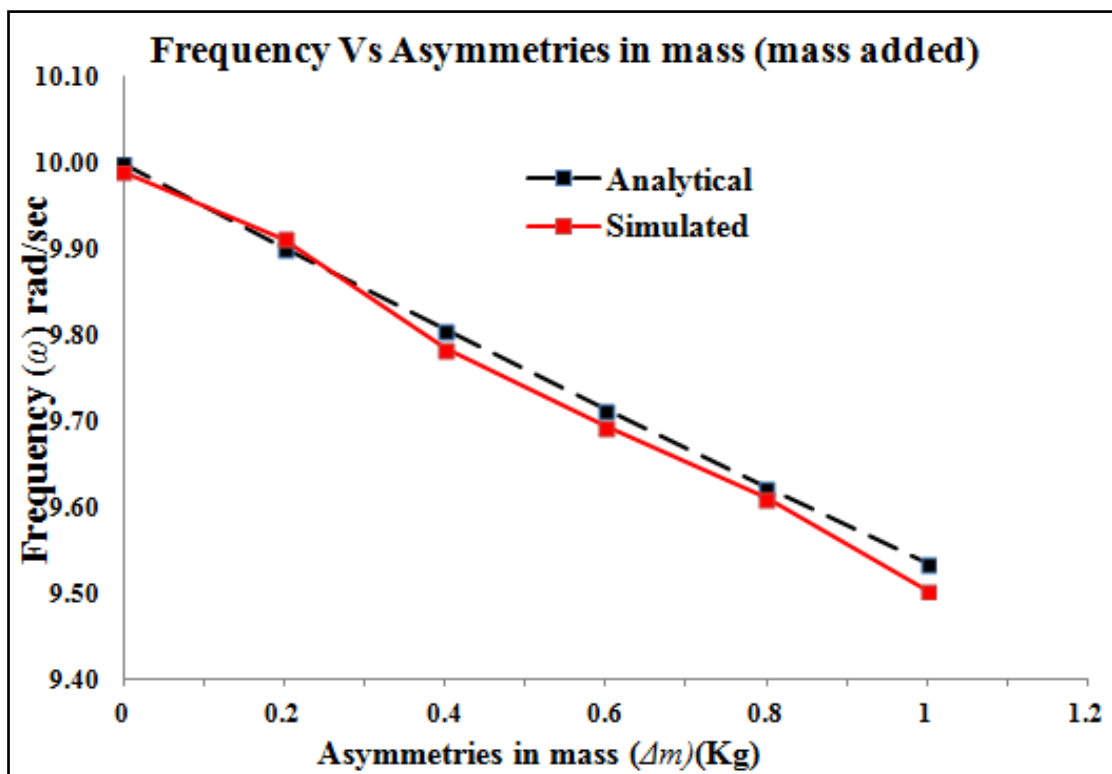


Figure 3.11: Frequency (ω) of rotor 1 Vs mass asymmetries (mass added)

In the Figure 3.9, the amplitude of rotor depends on excitation frequency as well as rotor mass, whereas the same pattern has been followed by all mentioned simulation with variational parameter (excitation frequency and delta mass). It can be seen from the Figure 3.10 & Figure 3.11 that the frequency obtained through simulation at different mass asymmetries almost validated mathematical results obtained in this case study. The simulation results are showing that the analytical result through extended Lagrangian formalism is able to capture the dynamics of asymmetric rotor.

3.5 Summary of the chapter

In this chapter, the work deals with the application of extended Lagrangian-Hamiltonian approach with extended Noether's equation for asymmetric multi rotor system. Analytical framework has been developed to analyze the effect of asymmetries in stiffness and mass. Complete dynamics of variation in asymmetries (due to mass & stiffness) of multi-rotor system is investigated through extended Lagrangian mechanics. Mathematical equations for natural frequency and amplitude have been developed by using umbra concept and Noether's equation.

In both cases, multi-rotor system has been modeled through bondgraph modeling technique. Bondgraph is a unified modeling approach. One can model the rotor motor system in multi energy domain on common platform by using this technique. SYMBOLS-Shakti[®] software has used for the simulation work.

In first case, the amplitude of the rotor increases with percentage change of stiffness of rotor1. Analytical frequency nearly matches with the simulated frequency obtained for rotor 1. A general behaviour of reduction in the natural frequencies is noticed at various stiffness variations. In second case, effects of asymmetries due to

mass have been investigated. All the analytical results have been validated through simulated results. It has been found that there has been a good agreement between analytical and simulated results.

The next chapter will provide an application of extended Lagrangian–Hamiltonian approach. Continuous multi-cracked rotor will be considered for investigation of dynamic behaviour in the next chapter.

Analytical and Computational Framework for Continuous Rotor with Multi-crack

4.1 Introduction

All formulations and theory of umbra-Lagrangian presented in previous chapter are obtained for assuming rotor system as discrete or finite system. However, various systems are there, which consider innumerable DOF (degree of freedom). In this variety of framework, each and every point of the continuous solid particles takes in the oscillations and position coordinates of all points describes complete motion of the system. The main attraction of this chapter is to explore the application of Lagrangian-Hamiltonian mechanics for continuous systems and it also contains with the computational framework for a multi-cracked rotor. A rotor with two transverse cracks on its surface is analyzed and presented in this chapter. Bondgraph modeling technique is used to model this multi-cracked rotor system as it eases the modeling of system from the physical equivalent model. The computation of stiffness matrixes in mathematical form for multi-cracked elements is performed and further validated with analytical results.

4.2 Umbra-field formulation for continuous system through variational approach

4.2.1 Generalized variational approach and umbra-Lagrangian density function

It is a function defined on a stipulated manifold including real time, real and virtual/ umbra velocities and displacements, and up to second order derivatives of pseudo and

real displacement w.r.t. space coordinates x . Lagrangian density function is generally represented as follows

$$\mathcal{L} = f \left(\begin{array}{l} (\tau, x, U(\tau, x, m), V(\tau, x, m), \dot{U}(\tau, x, m), \dot{V}(\tau, x, m), \partial_x U(\tau, x, m), \\ \partial_x V(\tau, x, m), \partial_x \dot{U}(\tau, x, m), \partial_x \dot{V}(\tau, x, m), \partial_{xx} U(\tau, x, m), \\ \partial_{xx} V(\tau, x, m), U(\tau, x, t), V(\tau, x, t), \dot{U}(\tau, x, t), \dot{V}(\tau, x, t), \\ \partial_x U(\tau, x, t), \partial_x V(\tau, x, t), \partial_x \dot{U}(\tau, x, t), \partial_x \dot{V}(\tau, x, t) \\ \partial_{xx} U(\tau, x, t), \partial_{xx} V(\tau, x, t) \end{array} \right) \quad (4.1)$$

From the successive minimization approach of a functional in the umbra-Lagrangian concept, the variables attached by “ m ” and “ t ” arguments would momentarily be termed as *modulatory* and *trajectorial* respectively (Rastogi, 2005). Both these variables are the components of same homotopic family (Munkres, 1994). The Lagrangian density can be presented as components of the same homotopic family, modulatory part ($M(\tau, x, m)$) can be expressed as:

$$\mathbf{M}(\tau, x, m) \approx \left(\begin{array}{l} U(\tau, x, m), V(\tau, x, m), \dot{U}(\tau, x, m), \dot{V}(\tau, x, m), \partial_x U(\tau, x, m), \partial_x V(\tau, x, m), \\ \partial_x \dot{U}(\tau, x, m), \partial_x \dot{V}(\tau, x, m), \partial_{xx} U(\tau, x, m), \partial_{xx} V(\tau, x, m) \end{array} \right)$$

Now the action integral may be represented as

$$I = \int_{\tau_0}^{\tau_1} \int_{x_0}^{x_1} \mathcal{L}(\quad) d\tau dx \quad (4.2)$$

This action integral of the system can be defined using a continuous one-dimensional system and will be related to successive minimization. For a clear understanding, the change in variables may be expressed as follows

$$U^*(\tau, x, t) = U(\tau, x, t) + \varepsilon \hat{U}(\tau, x, t), \partial_x U^*(\tau, x, t) = \partial_x U(\tau, x, t) + \varepsilon \partial_x \hat{U}(\tau, x, t),$$

$$V^*(\tau, x, t) = V(\tau, x, t) + \varepsilon \hat{V}(\tau, x, t), \partial_x V^*(\tau, x, t) = \partial_x V(\tau, x, t) + \varepsilon \partial_x \hat{V}(\tau, x, t),$$

$$\partial_{(\tau,t)} U^*(\tau, x, t) = \partial_{(\tau,t)} U(\tau, x, t) + \varepsilon \partial_{(\tau,t)} \hat{U}(\tau, x, t),$$

$$\partial_{(\tau,t)} V^*(\tau, x, t) = \partial_{(\tau,t)} V(\tau, x, t) + \varepsilon \partial_{(\tau,t)} \hat{V}(\tau, x, t),$$

$$\partial_{xx} U^*(\tau, x, t) = \partial_{xx} U(\tau, x, t) + \varepsilon \partial_{xx} \hat{U}(\tau, x, t),$$

$$\partial_{xx} V^*(\tau, x, t) = \partial_{xx} V(\tau, x, t) + \varepsilon \partial_{xx} \hat{V}(\tau, x, t).$$

A perturbation scheme on fixed end-points is necessarily suggested on the stated trajectorial function $(U(\tau, x, t), \dots)$ associated to the modulatory function $M(\tau, x, m)$ and considering path homotopic loops based at origins as $J: [\tau_1, \tau_2] \times [0,1] \rightarrow Y$ such that $J(\tau_1, \xi) = \theta$ and $J(\tau_2, \xi) = \theta$ where $\xi \in [0,1]$, the action integral with one-dimensional variational problem can be defined as:

$$I(\varepsilon) = \int_{\tau_0}^{\tau_1} \int_{x_0}^{x_1} \mathcal{L}(\tau, x, \mathbf{M}(\tau, x, m), \mathbf{U}^*(\tau, x, t), \mathbf{V}^*(\tau, x, t), \dots) d\tau dx \quad (4.3)$$

The extreme conditions of the action integral signifies $\delta I(\varepsilon)_{\delta=0} = 0$, which finally results in equation $\nabla_{\bar{\varepsilon}} I(\varepsilon)_{\delta=0} = 0$. As a result of extremality condition umbra-Lagrange's field equations are formed along with the boundary conditions at both ends. It is possible to use incisive notation for detailed validation of umbra-Lagrange's field equation, they are provided below

$$U(\tau, x, t) = U_1(\tau, x, t), \quad V(\tau, x, t) = U_2(\tau, x, t),$$

$$\partial_x U_i(\tau, x, t) = U_{ix}(\tau, x, t) \text{ and } \partial_{x^2} U_i(\tau, x, t) = U_{ix^2}(\tau, x, t),$$

where $i=1, 2$.

Although, in the notations stated above, the cognizance of the vector field variance is not considered. Now, τ_1 and τ_2 are considered as the times at which system

configurations are specified and a continuous one-dimensional framework specified over the closed domain $x_0 \leq x \leq x_1$ and δ is the variation. When such notational changes are adopted, variations in the action integral can be presented as

$$\delta I = \varepsilon \int_{\tau_0}^{\tau_1} \int_{x_0}^{x_1} \sum_{i=1}^2 \left[\begin{aligned} & \frac{\partial \mathcal{L}}{\partial U_i(\tau, x, t)} \hat{U}_i(\tau, x, t) + \frac{\partial \mathcal{L}}{\partial \dot{U}_i(\tau, x, t)} \dot{\hat{U}}_i(\tau, x, t) \\ & + \frac{\partial \mathcal{L}}{\partial \dot{U}_{i,x}(\tau, x, t)} \dot{\hat{U}}_{i,x}(\tau, x, t) + \frac{\partial \mathcal{L}}{\partial U_{i,x}(\tau, x, t)} \hat{U}_{i,x}(\tau, x, t) \\ & + \frac{\partial \mathcal{L}}{\partial U_{i,x^2}(\tau, x, t)} \hat{U}_{i,x^2}(\tau, x, t) \end{aligned} \right] \partial \tau \partial x = 0 \quad (4.4)$$

Through integration of Eq. (4.4), one obtains

$$\begin{aligned} \delta I = \varepsilon \int_{\tau_0}^{\tau_1} \int_{x_0}^{x_1} \sum_{i=1}^2 & \left[\left\{ \frac{\partial \mathcal{L}}{\partial U_i(\tau, x, t)} - \frac{\partial}{\partial \tau} \frac{\partial \mathcal{L}}{\partial \dot{U}_i(\tau, x, t)} - \frac{\partial}{\partial x} \left(\frac{\partial \mathcal{L}}{\partial U_{i,x}(\tau, x, t)} \right) \right\} \hat{U}_i(\tau, x, t) + \right. \\ & \left. \frac{\partial}{\partial \tau \partial x} \left(\frac{\partial \mathcal{L}}{\partial \dot{U}_i(\tau, x, t)} \right) \hat{U}_i(\tau, x, t) + \frac{\partial}{\partial x^2} \left(\frac{\partial \mathcal{L}}{\partial U_{i,x^2}(\tau, x, t)} \right) \hat{U}_i(\tau, x, t) \right] \partial \tau \partial x \\ + \int_{\tau_0}^{\tau_1} \sum_{i=1}^2 & \left[\frac{\partial \mathcal{L}}{\partial U_i(\tau, x, t)} \hat{U}_i(\tau, x, t) - \frac{\partial}{\partial \tau} \left(\frac{\partial \mathcal{L}}{\partial \dot{U}_{i,x}(\tau, x, t)} \right) \hat{U}_i(\tau, x, t) \right. \\ & \left. + \frac{\partial \mathcal{L}}{\partial U_{i,x^2}(\tau, x, t)} \hat{U}_i(\tau, x, t) - \frac{\partial}{\partial x} \left(\frac{\partial \mathcal{L}}{\partial U_{i,x^2}(\tau, x, t)} \right) \hat{U}_i(\tau, x, t) \right] d\tau = 0 \quad (4.5) \end{aligned}$$

When equated the first part of the Eq. (4.5) is zero, it gives umbra-Lagrange's field equation for 1-D continuous systems by considering the following notations as $\tau \times m = \tau$, $\tau \times t = \eta$ with $U_i(\tau, x, t) = u_i(\eta, x)$ and $U_i(\tau, x, m) = u_i(\tau, x)$, where $i = 1, 2$. Now, one may rearrange first part in $\eta - \tau$ form, applying the limit $\eta \rightarrow \tau$ umbra field equations can be expressed as

$$\frac{\partial}{\partial \tau} \left\{ \text{Lim}_{\eta \rightarrow \tau} \left(\frac{\partial \mathcal{L}}{\partial u_i(\eta, x)} - \frac{\partial}{\partial x} \left(\frac{\partial \mathcal{L}}{\partial u_{i,x}(\eta, x)} \right) \right) \right\} - \text{Lim}_{\eta \rightarrow \tau} \left(\begin{aligned} & \frac{\partial \mathcal{L}}{\partial \dot{u}_i(\eta, x)} - \frac{\partial}{\partial x} \left(\frac{\partial \mathcal{L}}{\partial \dot{u}_{i,x}(\eta, x)} \right) \\ & + \frac{\partial}{\partial x^2} \left(\frac{\partial \mathcal{L}}{\partial u_{i,x^2}(\eta, x)} \right) \end{aligned} \right) = 0 \quad (4.6)$$

where, $i=1, 2$ and $u_{i,x} = \frac{\partial u_i}{\partial x}$

When the second part of Eq. (4.5) is equated to zero, it provides boundary conditions that depicts the geometric (physical) conditions at the both ends and can be written as

$$\lim_{\eta \rightarrow \tau} \left[\frac{\partial \mathcal{L}}{\partial u_{i,x}(\eta, x)} - \frac{\partial}{\partial x} \left(\frac{\partial \mathcal{L}}{\partial u_{i,x^2}(\eta, x)} \right) - \frac{\partial}{\partial \eta} \left(\frac{\partial \mathcal{L}}{\partial \dot{u}_{i,x}(\eta, x)} \right) \right] \hat{u}_i(\eta, x) = 0 \quad (4.7.a)$$

$$\lim_{\eta \rightarrow \tau} \frac{\partial \mathcal{L}}{\partial u_{i,x^2}(\eta, x)} \hat{u}_{ix}(\eta, x) = 0 \quad (4.7.b)$$

where $i=1,2$

Considering the boundary conditions, one may achieve the following possibilities

Either

$$\lim_{\eta \rightarrow \tau} \left[\frac{\partial \mathcal{L}}{\partial u_{i,x}(\eta, x)} - \frac{\partial}{\partial x} \left(\frac{\partial \mathcal{L}}{\partial u_{i,x^2}(\eta, x)} \right) - \frac{\partial}{\partial \eta} \left(\frac{\partial \mathcal{L}}{\partial \dot{u}_{i,x}(\eta, x)} \right) \right] \lim_{\eta \rightarrow \tau} \hat{u}_i(\eta, x) = 0$$

or $\hat{u}_i(\tau, x) = 0$, and either $\lim_{\eta \rightarrow \tau} \frac{\partial \mathcal{L}}{\partial u_{i,x^2}(\eta, x)} = 0$, $u_{i,x}(\eta, x) = 0$ at one of the ends

$x = x_0$ and $x = x_1$. Equation (4.6) governs the motion of a continuous 1-D system (or field) with generalized co-ordinates. The illustration of this dynamical equation along with the suitable boundary conditions presented by Eqs. (4.7.a–4.7.b) describe the exact motion of this continuous system, the movement that confirms the action integral of Eq. (4.3) to be extremal.

4.2.2 Variational formulation for continuous one-dimensional (1-D) rotor shaft

After formulating the variational theory of umbra-field equation for 1-D continuous system, one may proceed to obtain generalized formulation for a continuous 1-D spinning shaft by defining the system over a closed domain $x_0 \leq x \leq x_1$ as shown in Figure 4.1, where τ_1 and τ_2 are assumed as random times and x is the spatial position of an arbitrary material point of the system. In this generalized formulation, one may assume that the rotor shaft

system is rotated at constant speed without any dissipative coupling. The continuous rotor system includes polar moment of (rotary) inertia, gyroscopic forces, internal and external damping. Umbra-Lagrangian density can be expressed for such system as

$$\mathcal{L} = \left[\sum_{i=1}^2 \left\{ \begin{aligned} & \left(\frac{1}{2} \rho \left(\frac{\partial u_i(\eta, x)}{\partial \eta} \right)^2 - \frac{1}{2} EI \left(\frac{\partial^2 u_i(\eta, x)}{\partial x^2} \right)^2 + \frac{1}{2} I_d \left(\frac{\partial^2 u_i(\eta, x)}{\partial \eta \partial x} \right)^2 \right) \\ & - \mu_a \left(\frac{\partial u_i(\tau, x)}{\partial \tau} u_i(\eta, x) \right) \\ & - \omega I_p \left(\frac{\partial^2 u_1(\tau, x)}{\partial \tau \partial x} \frac{\partial u_2(\eta, x)}{\partial x} - \frac{\partial^2 u_2(\tau, x)}{\partial \tau \partial x} \frac{\partial u_1(\eta, x)}{\partial x} \right) \\ & - \mu_i \left\{ \begin{aligned} & \left(\frac{\partial^3 u_1(\tau, x)}{\partial \tau \partial x^2} + \omega \frac{\partial^2 u_2(\tau, x)}{\partial x^2} \right) \frac{\partial^2 u_1(\eta, x)}{\partial x^2} \\ & + \left(\frac{\partial^3 u_2(\tau, x)}{\partial \tau \partial x^2} - \omega \frac{\partial^2 u_1(\tau, x)}{\partial x^2} \right) \frac{\partial^2 u_2(\eta, x)}{\partial x^2} \end{aligned} \right\} \end{aligned} \right\} \right] \quad (4.8)$$

Where $u_i(\)$ is the displacement coordinate of the rotor system in umbra/virtual-time and real-time, ρ is the density of rotor material, EI is the material rigidity, I_p is the inertia of the rotor through principle axis, I_d the polar moment of (rotary) inertia, ω is the uniform angular velocity, μ_a and μ_i are the external and internal damping of the rotating shaft. Equation (4.8) is formed by two terms of the system, the first and second term is kinetic energy and strain energy for small deflections respectively, where I is the cross-section moment of inertia, and E is the Young's modulus of the shaft material, rotary moments with the angular velocity $\frac{\partial^2 u_i(\eta, x)}{\partial \eta \partial x}$ are the elements of the third term, the fourth term is contributed by umbra-potential because of external damping, the fifth term contains gyroscopic forces with uniform angular velocity ω , and umbra-potential, which is generated by internal damping is the sixth term in the above equation. All these terms are denoted in per unit length. The umbra-Lagrangian density variation has been presented in detailed by *Mukherjee et al. (2009)*. *Rastogi (2016)* has also studied the dynamic behaviour of rotating shaft and effects of discrete

damping on the system. Umbra field equation and boundary conditions at the two ends can be easily obtained by following the steps detailed in the published papers of Mukharjee *et. al* (2009), which is expressed as follow

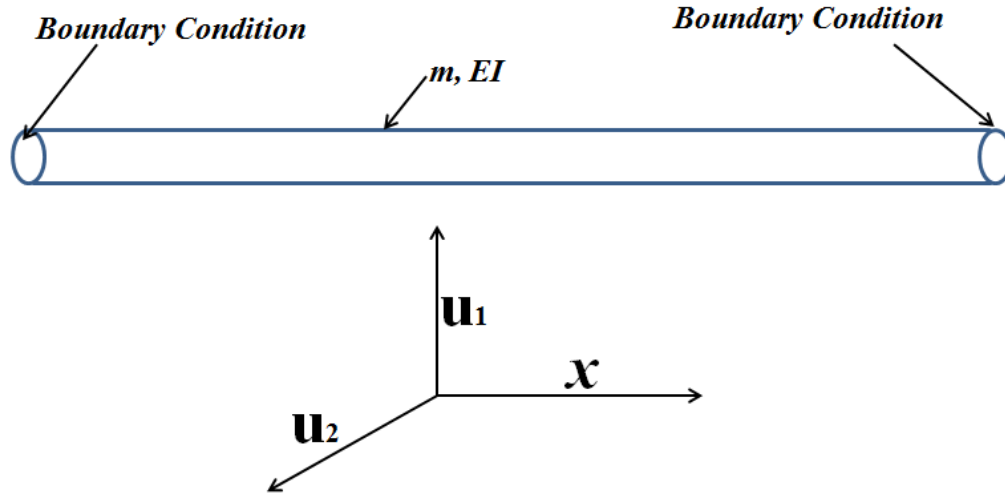


Figure 4.1: Representation of a continuous rotor with homogenous rigidity and mass

$$\left[\begin{array}{l} \left\{ \frac{d}{d\tau} \left(\text{Lim}_{\eta \rightarrow \tau} \rho \dot{u}_1(\eta, x) \right) + \frac{d^2}{dx^2} \left(\text{Lim}_{\eta \rightarrow \tau} EI \frac{\partial^2 u_1(\eta, x)}{\partial x^2} \right) \right\} \\ \left\{ -\frac{d^2}{d\tau dx} \left(\text{Lim}_{\eta \rightarrow \tau} I_d \frac{\partial^2 u_1(\eta, x)}{\partial \eta \partial x} \right) + \mu_a \left(\frac{\partial u_1(\tau, x)}{\partial \tau} \right) \right\} \\ -\omega I_p \left\{ -\frac{d}{dx} \left(\frac{\partial^2 u_2(\tau, x)}{\partial \tau \partial x} \right) \right\} - \mu_i \left\{ \frac{d^2}{dx^2} \left(\frac{\partial^3 u_1(\tau, x)}{\partial \tau \partial x^2} + \omega \frac{\partial^2 u_2(\tau, x)}{\partial x^2} \right) \right\} \end{array} \right] = 0 \quad (4.9.a)$$

and

$$\left[\begin{array}{l} \left\{ \frac{d}{d\tau} \left(\text{Lim}_{\eta \rightarrow \tau} \rho \dot{u}_2(\eta, x) \right) + \frac{d^2}{dx^2} \left(\text{Lim}_{\eta \rightarrow \tau} EI \frac{\partial^2 u_2(\eta, x)}{\partial x^2} \right) \right\} \\ \left\{ -\frac{d^2}{d\tau dx} \left(\text{Lim}_{\eta \rightarrow \tau} I_d \frac{\partial^2 u_2(\eta, x)}{\partial \eta \partial x} \right) + \mu_a \left(\frac{\partial u_2(\tau, x)}{\partial \tau} \right) \right\} \\ -\omega I_p \left\{ \frac{d}{dx} \left(\frac{\partial^2 u_1(\tau, x)}{\partial \tau \partial x} \right) \right\} - \mu_i \left\{ \frac{d^2}{dx^2} \left(\frac{\partial^3 u_2(\tau, x)}{\partial \tau \partial x^2} - \omega \frac{\partial^2 u_1(\tau, x)}{\partial x^2} \right) \right\} \end{array} \right] = 0 \quad (4.9.b)$$

After taking limit $\eta \rightarrow \tau$ and a set of BC (boundary conditions), one may expressed as

$$\left\{ \begin{array}{l} \omega I_p \left(-\frac{\partial^2 u_2(\tau, x)}{\partial \tau \partial x} \right) - \frac{d}{dx} \left(EI \frac{\partial^2 u_1(\eta, x)}{\partial x^2} + \mu_i \left(\frac{\partial^3 u_1(\tau, x)}{\partial \tau \partial x^2} + \omega \frac{\partial^2 u_2(\tau, x)}{\partial x^2} \right) \right) \\ \frac{d}{d\tau} \left(I_d \frac{\partial^2 u_1(\tau, x)}{\partial \tau \partial x} \right) \end{array} \right\} + = 0 \quad (4.10.a)$$

or $u_1(\tau, x)$ at each end.

Likewise, other BC (boundary conditions) can be formulated as either

$$\left\{ \begin{array}{l} \omega I_p \left(\frac{\partial^2 u_1(\tau, x)}{\partial \tau \partial x} \right) - \frac{d}{dx} \left(EI \frac{\partial^2 u_2(\tau, x)}{\partial x^2} + \mu_i \left(\frac{\partial^3 u_2(\tau, x)}{\partial \tau \partial x^2} + \omega \frac{\partial^2 u_1(\tau, x)}{\partial x^2} \right) \right) \\ \frac{d}{d\tau} \left(I_d \frac{\partial^2 u_2(\tau, x)}{\partial \tau \partial x} \right) \end{array} \right\} + = 0 \quad (4.10.b)$$

or, $u_2(\tau, x)$ each end. Either

$$\left\{ EI \frac{\partial^2 u_1(\tau, x)}{\partial x^2} + \mu_i \left(\frac{\partial^3 u_1(\tau, x)}{\partial \tau \partial x^2} + \omega \frac{\partial^2 u_2(\tau, x)}{\partial x^2} \right) \right\} = 0 \quad (4.11.a)$$

or

$$\frac{\partial u_1(\tau, x)}{\partial x} = 0 \quad (4.11.b)$$

and either

$$\left\{ EI \frac{\partial^2 u_2(\tau, x)}{\partial x^2} + \mu_i \left(\frac{\partial^3 u_2(\tau, x)}{\partial \tau \partial x^2} + \omega \frac{\partial^2 u_1(\tau, x)}{\partial x^2} \right) \right\} = 0 \quad (4.12.a)$$

or

$$\frac{\partial u_2(\tau, x)}{\partial x} = 0 \quad (4.12.b)$$

Eqs. (4.9–4.12) reflect various types of physical conditions at both ends. The former Eqs. (4.10.a–4.10.b) express force and moment balance at the end, whereas latter Eqs. (4.11–4.12) reflects geometric constraints at both ends. In above equations, four pairs of BC (boundary conditions) consisting of dynamics and geometry conditions. First part of each equation pair expression having bending moment balance and shear force balance, and shows the dynamic boundary conditions. The second part of each pair depends on slopes or displacement, and is comprised of the geometric or essential BC (boundary conditions). In the next section of this chapter, this umbra-Lagrangian density function will be employed to obtain the extended form of Noether's theorem for 1-D (one dimensional) continuous system.

4.2.3 Extended form of Noether's theorem for continuous system

One of the leading contributions of the Noether's theorem is that constants of motion or conserved quantities for continuous systems can be obtained by employing this theorem. According to the Noether's theorem (*Noether, 1971*) under certain conditions, there exists a set of integrals of motion or dynamical constants that characterize a field or a system of fields. The symmetries stated in the Noether's theorem are analyzed for the umbra-Lagrangian density of the multi-cracked rotor system. The extension of Noether's theorem in umbra-Lagrangian theory can be expressed by using infinitesimal generators of the symmetry groups. Due to this, the umbra-Lagrangian density can be made invariant. This Noether's theorem extension is constrained to amplitude invariance of the rotor only, and therefore not involving the asymmetries with independent variables. Hence, only amplitudes are being transformed. In the present study, one may consider one parameter rotational group

represented by SO (2) group as presented in details in *Appendix C*. The infinitesimal generator of this group over the extended manifold may be expressed as

$$V = -u_2(\tau, x) \frac{\partial}{\partial u_1(\tau, x)} + u_1(\tau, x) \frac{\partial}{\partial u_2(\tau, x)} - u_2(\eta, x) \frac{\partial}{\partial u_1(\eta, x)} + u_1(\eta, x) \frac{\partial}{\partial u_2(\eta, x)} \quad (4.13)$$

This tangent vector is expressed by Eq. (4.13) conserving only the relevant components of a sub-space of the jet space $J^{(3)}$ regulated by the form of umbra-Lagrangian density, which may be presented as

$$p_r^{(3)}V = \sum_{i=1}^2 \left\{ \begin{array}{l} \xi_{u_i(\tau, x)} \frac{\partial}{\partial u_i(\tau, x)} + \xi_{\dot{u}_i(\tau, x)} \frac{\partial}{\partial \dot{u}_i(\tau, x)} + \xi_{u'_i(\tau, x)} \frac{\partial}{\partial u'_i(\tau, x)} \\ + \xi_{\dot{u}'_i(\tau, x)} \frac{\partial}{\partial \dot{u}'_i(\tau, x)} + \xi_{u''_i(\tau, x)} \frac{\partial}{\partial u''_i(\tau, x)} + \xi_{\dot{u}''_i(\tau, x)} \frac{\partial}{\partial \dot{u}''_i(\tau, x)} \\ + \xi_{u_i(\eta, x)} \frac{\partial}{\partial u_i(\eta, x)} + \xi_{\dot{u}_i(\eta, x)} \frac{\partial}{\partial \dot{u}_i(\eta, x)} + \xi_{u'_i(\eta, x)} \frac{\partial}{\partial u'_i(\eta, x)} \\ + \xi_{\dot{u}'_i(\eta, x)} \frac{\partial}{\partial \dot{u}'_i(\eta, x)} + \xi_{u''_i(\eta, x)} \frac{\partial}{\partial u''_i(\eta, x)} + \xi_{\dot{u}''_i(\eta, x)} \frac{\partial}{\partial \dot{u}''_i(\eta, x)} \end{array} \right\} \quad (4.14)$$

In the above equation, derivative with respect to real time or umbra/virtual time are represented by superdot ($\dot{}$) and derivative with respect to space co-ordinate are presented by a superprime ($\acute{}$). Equation (4.14) is a 24-D manifold on which this tangent vector is specified. The relations of ξ 's may be expressed as

$$\xi_{\dot{u}_i(\tau, x)} = \frac{\partial}{\partial \tau} \xi_{u_i(\tau, x)} \Rightarrow \dot{\xi}_{u(\tau, x)}, \xi_{u'_i(\tau, x)} = \acute{\xi}_{u(\tau, x)}, \xi_{\dot{u}'_i(\tau, x)} = \dot{\acute{\xi}}_{u(\tau, x)}, \xi_{u''_i(\tau, x)} = \xi''_{u(\tau, x)},$$

$$\text{and } \xi_{\dot{u}''_i(\tau, x)} = \dot{\xi}''_{u(\tau, x)},$$

and relations for η variable can also be written accordingly. The prolonged infinitesimal generators are formed by two parts as stated below

$$p_r^{(3)}V = p_r^{(3)}V_\eta + p_r^{(3)}V_\tau \quad (4.15)$$

where $p_r^{(3)}V_\tau$ and $p_r^{(3)}V_\eta$ is the prolonged real-time component and prolonged umbra/virtual-time component respectively of the infinitesimal generators $p_r^{(3)}V$. The invariance condition for umbra-Lagrangian density can also be presented as

$$p_r^{(3)}V(\mathcal{L}) = 0 \quad (4.16)$$

Extended Noether's theorem formulation may be obtained by substitution of Eq. (4.15) in above Eq. (4.16) and applying the limit $\eta \rightarrow \tau$, which gives

$$\text{Lim}_{\eta \rightarrow \tau} \{p_r^{(3)}V_\eta(\mathcal{L})\} + \text{Lim}_{\eta \rightarrow \tau} \{p_r^{(3)}V_\tau(\mathcal{L})\} = 0 \quad (4.17)$$

In Eq. (4.17), first term can be written as

$$\lim_{\eta \rightarrow \tau} \{p_r^{(3)}V_\eta(\mathcal{L})\} = \lim_{\eta \rightarrow \tau} \sum_{i=1}^2 \left\{ \begin{array}{l} \xi_{u_i(\eta,x)} \left(\frac{\partial \mathcal{L}}{\partial u_i(\eta,x)} \right) + \dot{\xi}_{u_i(\eta,x)} \left(\frac{\partial \mathcal{L}}{\partial \dot{u}_i(\eta,x)} \right) \\ + \xi'_{u_i(\eta,x)} \left(\frac{\partial \mathcal{L}}{\partial u'_i(\eta,x)} \right) + \dot{\xi}'_{u_i(\eta,x)} \left(\frac{\partial \mathcal{L}}{\partial \dot{u}'_i(\eta,x)} \right) \\ + \xi''_{u_i(\eta,x)} \left(\frac{\partial \mathcal{L}}{\partial u''_i(\eta,x)} \right) + \dot{\xi}''_{u_i(\eta,x)} \left(\frac{\partial \mathcal{L}}{\partial \dot{u}''_i(\eta,x)} \right) \end{array} \right\} \quad (4.18)$$

expanding each term with derivatives of ξ 's in Eq. (4.18) yields after simplification as

$$\lim_{\eta \rightarrow \tau} \{p_r^{(3)}V_\eta(\mathcal{L})\} = \lim_{\eta \rightarrow \tau} \sum_{i=1}^2 \left[\begin{array}{l} D_\tau \left\{ \begin{array}{l} \xi_{u_i(\eta,x)} \left(\frac{\partial \mathcal{L}}{\partial \dot{u}_i(\eta,x)} \right) + \frac{\partial}{\partial x} \left(\xi_{u_i(\eta,x)} \left(\frac{\partial \mathcal{L}}{\partial \dot{u}'_i(\eta,x)} \right) \right) \\ - \xi_{u_i(\eta,x)} \frac{\partial}{\partial x} \left(\frac{\partial \mathcal{L}}{\partial \dot{u}'_i(\eta,x)} \right) \end{array} \right\} \\ + D_x \left\{ \begin{array}{l} \xi_{u_i(\eta,x)} \left(\frac{\partial \mathcal{L}}{\partial u'_i(\eta,x)} \right) - \left(\xi_{u_i(\eta,x)} \frac{\partial}{\partial \tau} \left(\frac{\partial \mathcal{L}}{\partial \dot{u}'_i(\eta,x)} \right) \right) \\ + \xi'_{u_i(\eta,x)} \left(\frac{\partial \mathcal{L}}{\partial u''_i(\eta,x)} \right) - \xi_{u_i(\eta,x)} \frac{\partial}{\partial x} \left(\frac{\partial \mathcal{L}}{\partial u''_i(\eta,x)} \right) \end{array} \right\} \end{array} \right] \quad (4.19)$$

Thus, one may re-write above Equation as

$$\lim_{\eta \rightarrow \tau} p_r^{(3)}V_\eta(\mathcal{L}) = D_\tau Z_1 + D_x Z_2 \quad (4.20)$$

where D_τ is total time derivatives and D_x is the total space derivatives, and may be defined as

$$D_\tau Z_1(\tau, x, u, u_x) = \frac{\partial Z_1}{\partial \tau} + \frac{\partial Z_1}{\partial u} \frac{\partial u}{\partial \tau} + \frac{\partial Z_1}{\partial u_x} \frac{\partial u_x}{\partial \tau},$$

and

$$D_x Z_2(\tau, x, u, u_x, u_{x^2}) = \frac{\partial Z_2}{\partial x} + \frac{\partial Z_2}{\partial u} \frac{\partial u}{\partial x} + \frac{\partial Z_2}{\partial u_x} \frac{\partial u_x}{\partial x} + \frac{\partial Z_2}{\partial u_{x^2}} \frac{\partial u_{x^2}}{\partial x},$$

and function Z_1 and Z_2 may be expressed as

$$Z_1 = \lim_{\eta \rightarrow \tau} \sum_{i=1}^2 \left\{ \xi_{u_i(\eta, x)} \left(\frac{\partial \mathcal{L}}{\partial \dot{u}_i(\eta, x)} \right) + \frac{\partial}{\partial x} \left(\xi_{u_i(\eta, x)} \left(\frac{\partial \mathcal{L}}{\partial \dot{u}'_i(\eta, x)} \right) \right) - \xi_{u_i(\eta, x)} \frac{\partial}{\partial x} \left(\frac{\partial \mathcal{L}}{\partial \dot{u}'_i(\eta, x)} \right) \right\}$$

$$Z_2 = \lim_{\eta \rightarrow \tau} \sum_{i=1}^2 \left\{ \begin{array}{l} \xi_{u_i(\eta, x)} \left(\frac{\partial \mathcal{L}}{\partial u'_i(\eta, x)} \right) + \xi_{u_i(\eta, x)} \frac{\partial}{\partial t} \left(\frac{\partial \mathcal{L}}{\partial \dot{u}'_i(\eta, x)} \right) \\ \xi'_{u_i(\eta, x)} \left(\frac{\partial \mathcal{L}}{\partial u''_i(\eta, x)} \right) + \xi_{u_i(\eta, x)} \frac{\partial}{\partial x} \left(\frac{\partial \mathcal{L}}{\partial u''_i(\eta, x)} \right) \end{array} \right\}$$

Substitution of Eq. (4.20) in Eq. (4.17), finally results in extended Noether's theorem for fields, which may be expressed as

$$D_\tau Z_1 + D_x Z_2 + \lim_{\eta \rightarrow \tau} p_r^{(3)} V_\eta(\mathcal{L}) = 0 \quad (4.21)$$

Equation (4.21) is termed as an extended Noether's field equation for the umbra-Lagrangian. Z_1 and Z_2 may be assumed as local density and current/flux density (often termed as Noether's current density) respectively. The last additional term is the contribution of non-conservative and gyroscopic actions which may be assumed as local rate of production and is termed as the modulatory convection term. The next section will provide an analytical framework for multi-crack rotor system through extended Lagrangian approach.

4.3 Analytical framework for continuous rotor with multi-cracks through extended Lagrangian approach

A multi-crack rotor shaft has been considered to an equivalent of in-span concentrated discrete stiffnesses, which has been shown in Figure 4.2. The rotor shaft material comprises of stiffness and internal damping, whereas shaft is driven by a constant speed DC motor. DC motor is attached with continuous shaft along with dissipative coupling as depicted in Figure 4.2. Change in the flexural behaviour due to the initiation and propagation of the crack in shaft, which ultimately breaks the symmetry of a symmetric rotor. A line diagram of the framework is also shown in Figure 4.3.

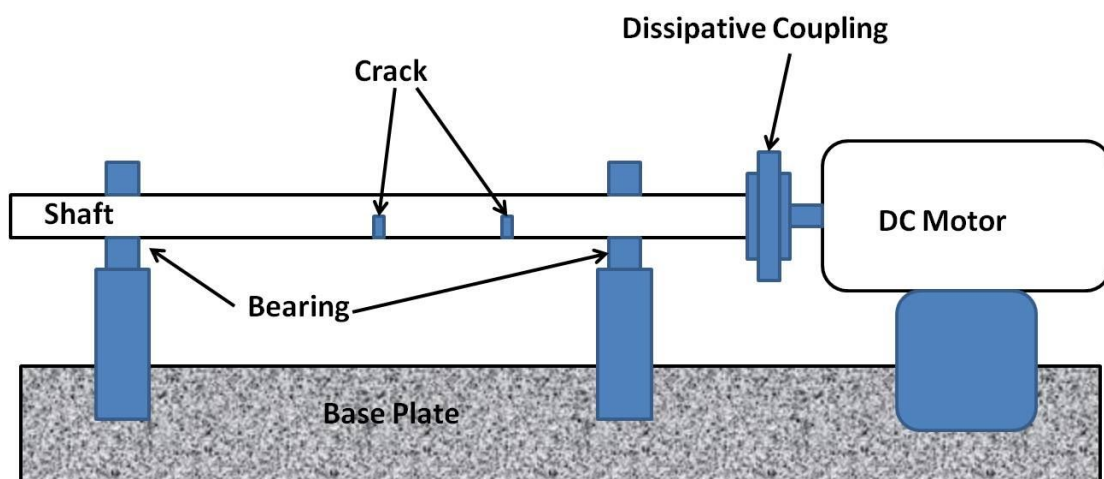


Figure 4.2: Representation of a DC motor driven rotor shaft coupled by a dissipative coupling

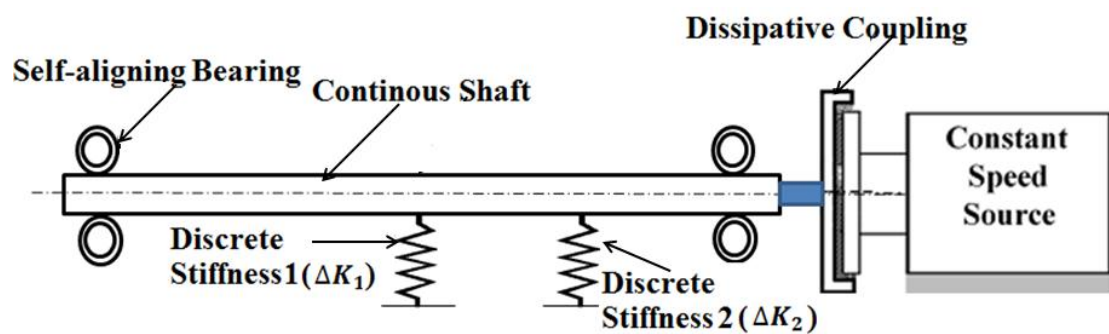


Figure 4.3: Continuous rotor shaft with in-span concentrated discrete stiffness

The umbra-Lagrangian density for 1-D continuous shaft can be expressed taking into account external and internal damping along-with polar moment of (rotary) inertia without assuming gyroscopic coupling as

$$\mathcal{L} = \mathcal{L}_1 + \mathcal{L}_2 \quad (4.22)$$

where

$$\mathcal{L}_1 = \int_{x_0}^{x_l} \left[\sum_{i=1}^2 \left\{ \frac{\rho}{2} \left(\frac{\partial u_i(\eta, x)}{\partial \eta} \right)^2 - \frac{EI}{2} \left(\frac{\partial^2 u_i(\eta, x)}{\partial x^2} \right)^2 + \frac{I_d}{2} \left(\frac{\partial^2 u_i(\eta, x)}{\partial \eta \partial x} \right)^2 \right\} - \mu_a \left(\frac{\partial u_i(\tau, x)}{\partial \tau} u_i(\eta, x) \right) - \mu_i \left\{ \left(\frac{\partial^3 u_1(\tau, x)}{\partial \tau \partial x^2} + \dot{\theta} \frac{\partial^2 u_2(\tau, x)}{\partial x^2} \right) \frac{\partial^2 u_1(\eta, x)}{\partial x^2} \right. \right. \left. \left. \left(\frac{\partial^3 u_2(\tau, x)}{\partial \tau \partial x^2} - \dot{\theta} \frac{\partial^2 u_1(\tau, x)}{\partial x^2} \right) \frac{\partial^2 u_2(\eta, x)}{\partial x^2} \right\} \right] dx \quad (4.23)$$

$$\mathcal{L}_2 = \left[\mu_i \int_{x_0}^{x_1} \left\{ \frac{\partial^2 u_1(\tau, x)}{\partial x^2} \frac{\partial^3 u_2(\tau, x)}{\partial \tau \partial x^2} - \frac{\partial^2 u_2(\tau, x)}{\partial x^2} \frac{\partial^3 u_1(\tau, x)}{\partial \tau \partial x^2} \right\} dx + R_c (\dot{\theta}(\tau) - \Omega) + \int_{x_0}^{x_l} \Delta K_1 \delta(x - \lambda_1) (u_1^2 - u_2^2) dx + \int_{x_0}^{x_l} \Delta K_2 \delta(x - \lambda_2) (u_1^2 - u_2^2) dx \right] \theta(\eta) + \frac{1}{2} J \dot{\theta}^2(\eta) \quad (4.24)$$

where $\lambda_1 \in (0, L)$; $\lambda_2 \in (0, L)$, Ω and R_c is the excitation frequency and the dissipative coupling resistance respectively, ΔK_1 and ΔK_2 is the change in stiffness due to crack at λ_1 and λ_2 position. Transverse fatigue crack at λ_1 and λ_2 position of shaft has been considered as shown in Figure 4.4. In this study, only rotational symmetry is contemplated and infinitesimal generators of the symmetry group and its prolongation are taken from *Mukherjee et al. (2009)*.

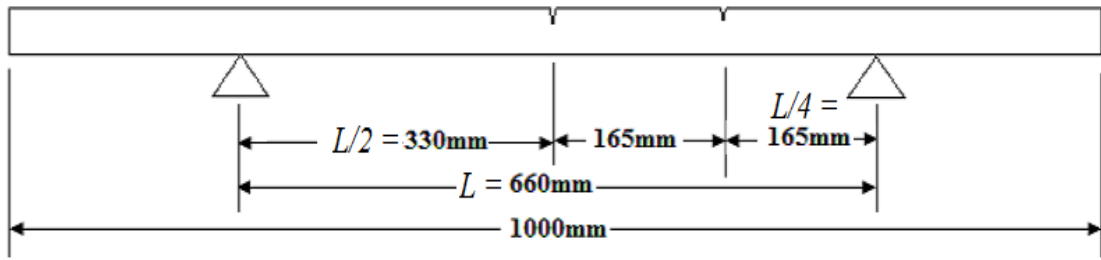


Figure 4.4: Schematic diagram of multi crack test specimen

However, stiffness variation due to the crack may lead to additional term, which may not be taken zero. The symmetries of the system can be achieved if this term is assumed to be zero. So, this factor breaks the symmetry of rotor amplitudes and hence forth, it is quite effective for the dynamic analysis of the multi-cracked rotor.

There are two additional terms in the umbra-Lagrangian density function which are added because of stiffness change accumulated through rotor crack. For this system, the term, which needs special consideration may be written as

$$\int_{x_0}^{x_l} \Delta K_1 \delta(x - \lambda_1) (u_1^2 - u_2^2) dx + \int_{x_0}^{x_l} \Delta K_2 \delta(x - \lambda_2) (u_1^2 - u_2^2) dx = 0 \quad (4.25)$$

where $x_0 = 0$, $x_l = L$ and $\lambda_1 \in (0, L)$; $\lambda_2 \in (0, L)$,

Substitution of the following expression in Eq.(4.25)

$$u_1 = \sum_{n=1}^{\infty} A_n \cos \Omega_n + \sin \frac{n\pi}{L} \cdot x$$

and

$$u_2 = \sum_{n=1}^{\infty} A_n \sin \Omega_n + \sin \frac{n\pi}{L} \cdot x$$

yields

$$\Delta K_1 \left\{ \Omega_n \sum_{n=1}^{\infty} \sum_{m=1}^{\infty} A_n A_m \sin \frac{n\pi}{L} \lambda_1 \sin \frac{m\pi}{L} \lambda_1 \right\} + \Delta K_2 \left\{ \Omega_n \sum_{n=1}^{\infty} \sum_{m=1}^{\infty} A_n A_m \sin \frac{n\pi}{L} \lambda_2 \sin \frac{m\pi}{L} \lambda_2 \right\}$$

where it is considered assumed that $A_n A_m$ varies vary slowly with time.

4.3.1 Extended Noether's theorem for multi-cracked rotating shaft

The modified Noether's rate equation for multi-cracked rotating shaft may be written as

$$\begin{aligned} \sum_{n=1}^{\infty} \frac{L}{2} \Omega_n A_m \left\{ \dot{A}_n + \frac{1}{2\rho} \left(\mu_i \frac{n^4 \pi^4}{L^4} \right) A_n \right\} - \mu_i \frac{n^4 \pi^4}{2\rho L^4} \dot{\theta}(\tau) A_n^2 \\ + \frac{\Omega_n \Delta K_1}{2\rho} \sum_{n=1}^{\infty} \sum_{m=1}^{\infty} A_n A_m \sin \frac{n\pi}{L} \lambda_1 \sin \frac{m\pi}{L} \lambda_1 \\ + \frac{\Omega_n \Delta K_2}{2\rho} \sum_{n=1}^{\infty} \sum_{m=1}^{\infty} A_n A_m \sin \frac{n\pi}{L} \lambda_2 \sin \frac{m\pi}{L} \lambda_2 = 0 \end{aligned} \quad (4.26)$$

$$\begin{aligned} \sum_{n=1}^{\infty} A_n \left[\dot{A}_n + \frac{1}{2\rho} \left(\frac{\mu_i n^4 \pi^4}{L^4} - \frac{\mu_i n^4 \pi^4}{\Omega_n L^4} \dot{\theta}(\tau) \right) A_n \right] \times \frac{L}{2} \\ + \frac{(\Delta K_1 + \Delta K_2)}{2\rho} \sum_{J=1}^{\infty} \sum_{K=1}^{\infty} A_J A_K \sin \frac{J\pi}{L} (\lambda_1 + \lambda_2) \sin \frac{K\pi}{L} (\lambda_1 + \lambda_2) = 0 \end{aligned} \quad (4.27)$$

or one may express as

$$\frac{L}{2} \sum_{n=1}^{\infty} A_n \left[\begin{aligned} & \dot{A}_n + \frac{1}{2\rho} \left(\frac{\mu_i n^4 \pi^4}{L^4} - \frac{\mu_i n^4 \pi^4}{\Omega_n L^4} \dot{\theta}(\tau) \right) A_n + \\ & + \frac{\Delta K_1}{\rho L} \sum_{k=1}^{\infty} A_k \sin \frac{n\pi}{L} \lambda_1 \sin \frac{k\pi}{L} \lambda_1 \\ & + \frac{\Delta K_2}{\rho L} \sum_{k=1}^{\infty} A_k \sin \frac{n\pi}{L} \lambda_2 \sin \frac{k\pi}{L} \lambda_2 \end{aligned} \right] = 0 \quad (4.28)$$

Perturbrbing the independent variable in $A_n + \delta A_n$, the variational equation can be expressed as, (dropping the factor $L/2$)

$$\begin{aligned}
& \sum_{n=1}^{\infty} \delta A_n \left[\begin{aligned} & \dot{A}_n + \frac{1}{2\rho} \left(\frac{\mu_i n^4 \pi^4}{L^4} - \frac{\mu_i n^4 \pi^4}{\Omega_n L^4} \dot{\theta}(\tau) \right) A_n + \\ & + \frac{\Delta K_1}{\rho L} \sum_{k=1}^{\infty} A_k \text{Sin} \frac{n\pi}{L} \lambda_1 \text{Sin} \frac{k\pi}{L} \lambda_1 + \frac{\Delta K_2}{\rho L} \sum_{k=1}^{\infty} A_k \text{Sin} \frac{n\pi}{L} \lambda_2 \text{Sin} \frac{k\pi}{L} \lambda_2 \end{aligned} \right] \\
& + \sum_{n=1}^{\infty} A_n \delta \left[\begin{aligned} & \dot{A}_n + \frac{1}{2\rho} \left(\frac{\mu_i n^4 \pi^4}{L^4} - \frac{\mu_i n^4 \pi^4}{\Omega_n L^4} \dot{\theta}(\tau) \right) A_n + \\ & + \frac{\Delta K_1}{\rho L} \sum_{k=1}^{\infty} A_k \text{Sin} \frac{n\pi}{L} \lambda_1 \text{Sin} \frac{k\pi}{L} \lambda_1 + \frac{\Delta K_2}{\rho L} \sum_{k=1}^{\infty} A_k \text{Sin} \frac{n\pi}{L} \lambda_2 \text{Sin} \frac{k\pi}{L} \lambda_2 \end{aligned} \right] = 0
\end{aligned} \tag{4.29}$$

This is for the symmetries being valid for neighboring paths, which needs the following conditions to be satisfied.

$$\begin{aligned}
& \dot{A}_n + \frac{1}{2\rho} \left\{ \frac{\mu_i n^4 \pi^4}{L^4} - \frac{\mu_i n^4 \pi^4}{\Omega_n L^4} \dot{\theta}(\tau) \right\} A_n + \frac{\Delta K_1}{\rho L} \sum_{k=1}^{\infty} A_k \text{Sin} \frac{n\pi}{L} \lambda_1 \text{Sin} \frac{k\pi}{L} \lambda_1 \\
& + \frac{\Delta K_2}{\rho L} \sum_{k=1}^{\infty} A_k \text{Sin} \frac{n\pi}{L} \lambda_2 \text{Sin} \frac{k\pi}{L} \lambda_2 = 0
\end{aligned} \tag{4.30}$$

The condition for entraining the n^{th} mode is $A_n \rightarrow$ finite limit and $A_k \rightarrow 0$, if $k \neq n$ for $\tau \rightarrow \infty$, obtained as

$$\frac{1}{2\rho} \left\{ \frac{\mu_i n^4 \pi^4}{L^4} - \frac{\mu_i n^4 \pi^4}{\Omega_n L^4} \dot{\theta}(\tau) \right\} + \frac{\Delta K_1}{\rho L} \text{Sin}^2 \frac{n\pi}{L} \lambda_1 + \frac{\Delta K_2}{\rho L} \text{Sin}^2 \frac{n\pi}{L} \lambda_2 = 0 \tag{4.31}$$

The value of $\dot{\theta}(\tau)$ will be obtained from Eq.(4.31) and written as

$$\frac{1}{2\rho} \frac{\mu_i n^4 \pi^4}{\Omega_n L^4} \dot{\theta}(\tau) = \frac{1}{2\rho} \frac{\mu_i n^4 \pi^4}{L^4} + \frac{\Delta K_1}{\rho L} \text{Sin}^2 \frac{n\pi}{L} \lambda_1 + \frac{\Delta K_2}{\rho L} \text{Sin}^2 \frac{n\pi}{L} \lambda_2 = 0 \tag{4.32}$$

$$\dot{\theta}(\tau) = \Omega_n \left[1 + \frac{2L^3}{\mu_i n^4 \pi^4} \left\{ \Delta K_1 \text{Sin}^2 \frac{n\pi}{L} \lambda_1 + \Delta K_2 \text{Sin}^2 \frac{n\pi}{L} \lambda_2 \right\} \right] \tag{4.33}$$

Amplitude may be expressed as

$$A_n = \sqrt{\frac{2R_c \left[\Omega - \min_{n \in I} \Omega_n \left\{ 1 + \frac{2L^3}{\mu_i n^4 \pi^4} \left(\Delta K_1 \sin^2 \frac{n\pi}{L} \lambda_1 + \Delta K_2 \sin^2 \frac{n\pi}{L} \lambda_2 \right) \right\} \right]}{\xi_n \Omega_n}} \quad (4.34)$$

where

$$\xi_n = \frac{\mu_i n^4 \pi^4}{L^4}$$

The next section will present the computational framework for multi-crack rotor system to ascertain the dynamic behaviour numerically.

4.4 Development of computational framework and analysis of multi-cracked rotor system

Computational analysis provides valuable information relating to dynamics of multi-crack rotor. It involves the study of the dynamic characteristics and effects of crack on the shaft and its various components or regions. It provides a great deal of information of various contact forces and various asymmetries developed during the working cycle. It also provides online response (changes of its dynamics behaviour), which are responsible for catastrophic failure. This section describes the modeling of multi-cracked flexible rotor possessing internal and external damping and driven by a flexible and dissipative coupling as shown in Figure 4.2. The coupling in the framework is extremely flexible in lateral direction and also in bending but it is torsionally rigid. In modeling, it is assumed that the effects of torsional vibration are negligible, henceforth not considered in this modeling.

Bondgraph (BG) is a novel modeling technique which amalgamates several energy domains. In addition to that a complex system can also be modeled in commutable form by forming sub- system models and combining them, in order to

develop an integrated system model. Bondgraphs are pictorial representations of the physical system, where we represent the energy transformation and flow among the components of a dynamic system in a graphical form and formulating the system equations as provided details in *Appendix 1*. Models of cracked element, uncracked element and power source element generated through bondgraph have been further simulated with the help of fourth order Runge-Kutta method on software SYMBOLS-Shakti[®] (*Mukherjee and Samantaray, 2006*) to evaluate some interesting phenomena due to various asymmetries in multi-cracked rotor. Simulated results were further validated through experimental results. The next subsection will focus on the generation of motion equation for the cracked rotating shaft.

4.4.1 Generation of motion equation

Dynamic response of a cracked rotor shaft with time is being shown, which is derived by the theory presented by *Shekhar and Prabhu (1994)*. *Gasch (1983)* has presented an inclusive survey of the dynamic stability of a cracked shaft, and evaluation of the vibrational force due to imbalance and due to crack. The static sink of the rotor is usually comparatively large, for example in case of turbo-generators it is generally more than 1mm. According to *Gasch (1983)*, a simple hinged model can also be used for small cracks in such rotors. When the vibration remains small, the equation of nonlinear motion may be converted to linear, periodically time-variant equations. Some potential for detection of cracks at the early stage are reported by *Keiner and Gadala (2002)*. Figure 4.5 represents a simple cracked rotor system with inertial co-ordinates X_f - Y_f and also with rotating co-ordinates X_r - Y_r . The motion equation of cracked rotor system may be expressed in the form,

$$\mathbf{M}\ddot{\mathbf{X}} + \mathbf{D}\dot{\mathbf{X}} + \mathbf{K}(X, \tau)\mathbf{X} = \mathbf{P}_0 + \mathbf{P}_u \quad (4.35)$$

where,

$$\mathbf{M} = \begin{bmatrix} m & 0 \\ 0 & m \end{bmatrix}, \quad \mathbf{D} = \begin{bmatrix} d & 0 \\ 0 & d \end{bmatrix}, \quad \mathbf{K}(X, \tau) = \begin{bmatrix} K_{11} & K_{12} \\ K_{21} & K_{22} \end{bmatrix}, \quad \mathbf{X} = \begin{Bmatrix} X_f \\ Y_f \end{Bmatrix},$$

$$\mathbf{P}_0 = \begin{Bmatrix} mg \\ 0 \end{Bmatrix}, \quad \mathbf{P}_u = \varepsilon m \Omega^2 \begin{Bmatrix} \cos \alpha \\ \sin \alpha \end{Bmatrix}$$

and in the above notation, Ω is constant angular velocity and $\alpha = \Omega\tau + \psi$.

where X_f and Y_f are the displacement at mid-span in the plane of m mass disc, K is stiffness, d is damping. P_0 is gravitational force. ε is the unbalance eccentricity of the disc, and ψ is the angle between centre of crack and eccentricity.

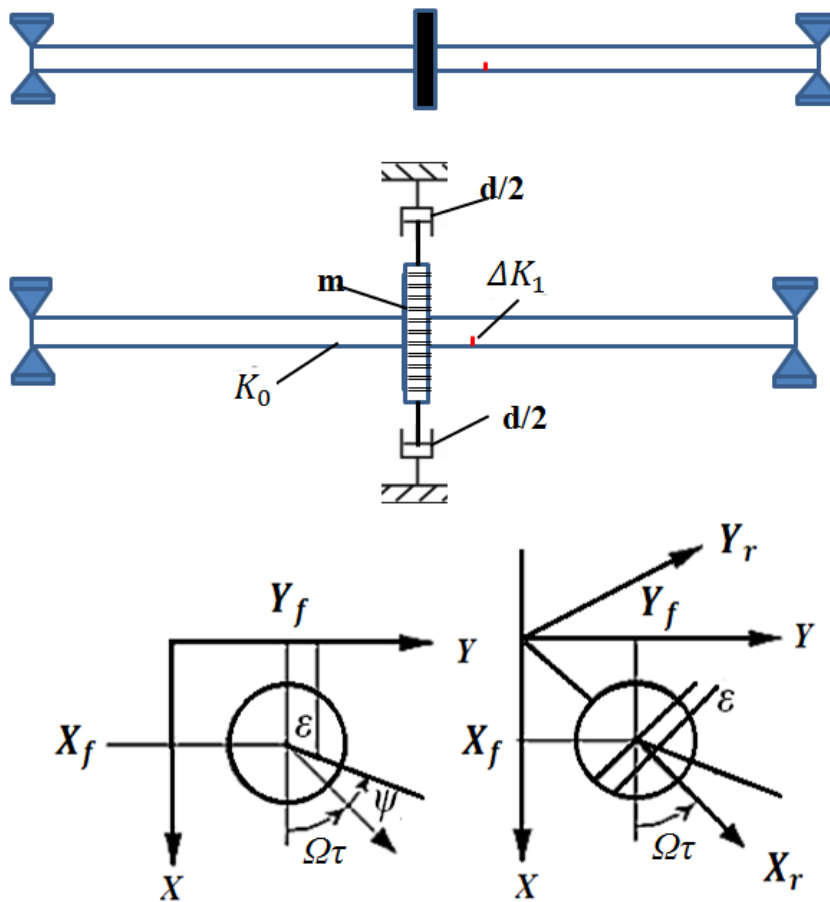


Figure 4.5: Co-ordinate system representation of a cracked rotor

According to *Gasch* (1983), by assuming weight dominance ($\Delta U(\tau) \ll U_o$), it is required to simplify the equations with the time-variant and non-linear stiffness matrix into equations with linear and periodical time-variant stiffness terms for the elastic deflection, which results into the following equation, where $\Delta K(\tau)\Delta U$ can be neglected if stability is ensured.

$$M\Delta\ddot{U} + D\Delta\dot{U} + [K_o + \Delta K(\tau)]\Delta U = -\Delta K(\tau)U_o + P_u \quad (4.36)$$

where $\Delta U(\tau)$ vector describes the vibration behavior, U_o denotes the static deflection of un-cracked shaft and ε is the unbalance eccentricity, which generates force denoted by P_u . Since $\Delta K(\tau)$ denotes change in stiffness, generated due to cracking, Eq. (4.36) is significant. For uncracked shaft the whole equation converts back to Eq. (4.35).

4.4.2 Cracked model

In similarity to the notches, there are cracks that always remain open. These cracks are generally known as gaping cracks. If crack size is small and shaft rotating speed is also slow, then the crack breathing phenomenon occurs regularly per revolution due to its own weight. The equation of the flexibility matrix of a crack-shaft with hinge model in rotational co-ordinates can be obtained as

$$\begin{Bmatrix} X_{x_r} \\ Y_{y_r} \end{Bmatrix} = \left(\begin{bmatrix} K_o & 0 \\ 0 & K_o \end{bmatrix} + \frac{1}{F(\tau)} \begin{bmatrix} \Delta K_{x_r, max} & 0 \\ 0 & 0 \end{bmatrix} \right) \begin{Bmatrix} F_{x_r} \\ F_{y_r} \end{Bmatrix} \quad (4.37)$$

In Eq. (4.37), first matrix represents the flexibility of the uncracked shaft (K_o), the additional flexibility is $\Delta K_{x_r, max}$ when crack is fully open in addition to flexibility K_o of un-cracked shaft. K_{x_r} denotes the main flexibility with F_{x_r}, F_{y_r} loadings, since the effect of cross-flexibility K_{y_r} can be neglected for small cracks. K_{x_r}/K_o is the

stiffness parameter, which describes the influence of the crack. *Papadopoulos and Dimarogonas* (1987) generated a 6x6 flexible matrix for cracked section, which may be utilized for the determination of variation in stiffness due to change in crack depth.

The steering function $F(\tau)$ switches between 1 (open) to 0 (closed). Generally, this function depend on the position X_{x_r} . The rectangular function of the hinge model as presented in Figure 4.6 provides a better illustration of breathing for small cracks. Some angular position of the crack is also depicted in Figure 4.7 during one revolution.

$$F(\tau) = \begin{cases} 0 & \text{for } X_{x_r} \leq 0 \\ 1 & \text{for } X_{x_r} > 0 \end{cases} \quad (4.38)$$

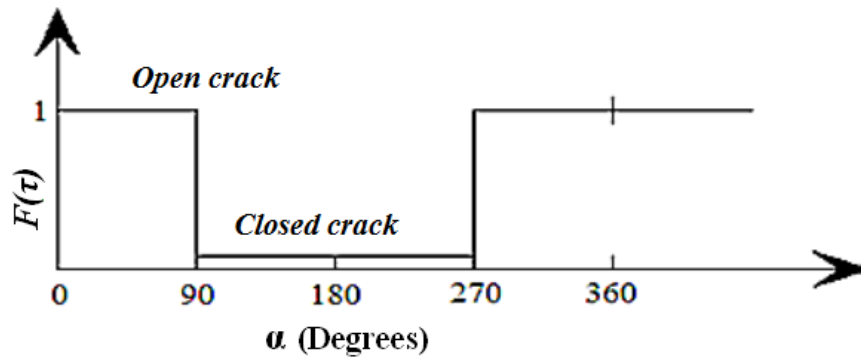


Figure 4.6: The closing-opening behavior of a hinge model for small cracks

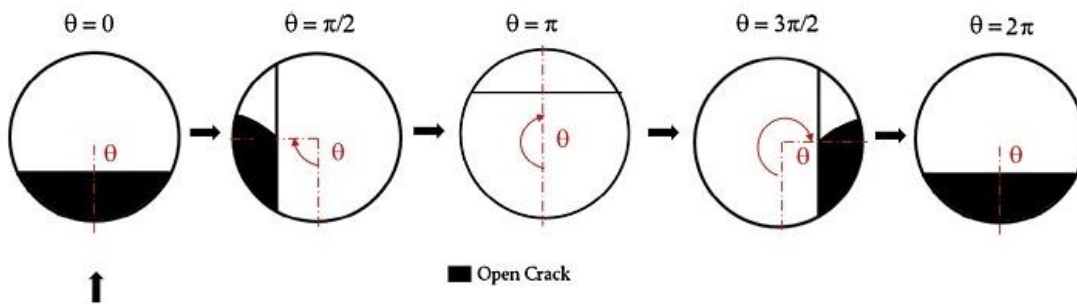


Figure 4.7: Different angular positions of the crack during single rotation of the cracked shaft

Figure 4.8 is self explanatory that the change in rotational angle (at $\theta = 90^\circ$ and $\theta = 270^\circ$) is change the sign of X_{x_r} . By presuming the weight dominance, change of sign in X_{x_r} can be obtained by $X_{x_r,stat}$. The transformation matrix relating the two co-coordinate (rotational and inertial) systems can be written as

$$\begin{Bmatrix} X_r \\ Y_r \end{Bmatrix} = \begin{bmatrix} \cos\alpha & \sin\alpha \\ -\sin\alpha & \cos\alpha \end{bmatrix} \begin{Bmatrix} X_f \\ Y_f \end{Bmatrix} \quad (4.39)$$

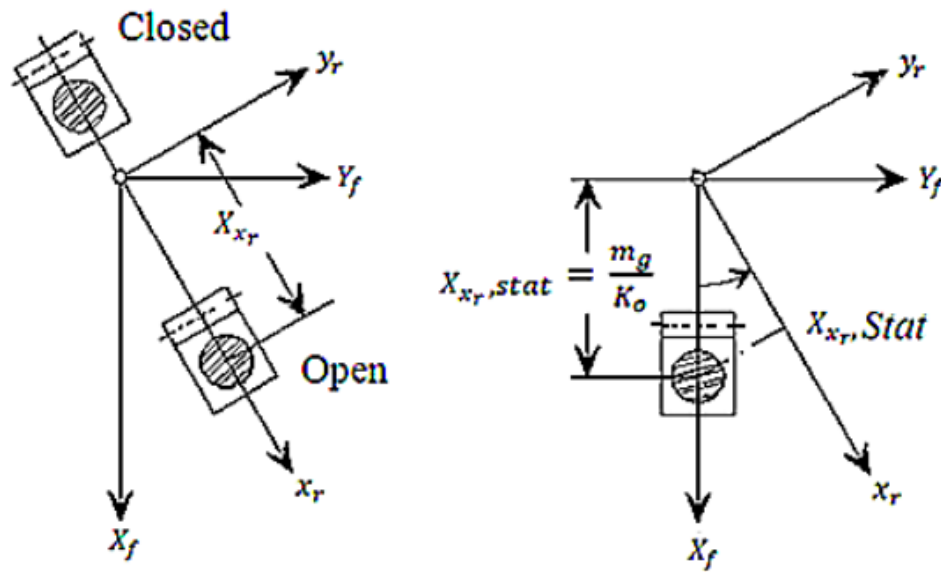


Figure 4.8: Closing-opening hinge crack model and static displacement in rotational co-ordinate

Stiffness matrix required can be obtained by inverting the flexibilities in Eq. (4.39) and using these values in Eq. (4.37). This can be shown as

$$K_o + \Delta K(\tau) = \begin{bmatrix} K_o & 0 \\ 0 & K_o \end{bmatrix} - \frac{1}{2} F(\tau) \Delta K_{x_r} \begin{bmatrix} 1 + \cos 2\alpha & \sin 2\alpha \\ \sin 2\alpha & 1 - \cos 2\alpha \end{bmatrix} \quad (4.40)$$

By introducing the unbalance forces including the angular acceleration terms and by substituting the stiffness matrix from the Eq. (4.39) into Eq. (4.36), the equation may be expressed as

$$\begin{aligned}
\begin{bmatrix} m & 0 \\ 0 & m \end{bmatrix} \begin{Bmatrix} \Delta \ddot{X}_f \\ \Delta \ddot{Y}_f \end{Bmatrix} + \begin{bmatrix} d & 0 \\ 0 & d \end{bmatrix} \begin{Bmatrix} \Delta \dot{X}_f \\ \Delta \dot{Y}_f \end{Bmatrix} + \begin{bmatrix} K_0 & 0 \\ 0 & K_0 \end{bmatrix} \begin{Bmatrix} \Delta X_f \\ \Delta Y_f \end{Bmatrix} \\
= \frac{1}{2} F(\tau) \Delta K_{x_r} \begin{bmatrix} 1 + \cos 2\alpha & \sin 2\alpha \\ \sin 2\alpha & 1 - \cos 2\alpha \end{bmatrix} \begin{Bmatrix} X_{x_r, stat} \\ 0 \end{Bmatrix} + \begin{Bmatrix} F_y \\ F_x \end{Bmatrix}
\end{aligned} \tag{4.41}$$

The excitation forces F_y and F_x may be presented as

$$F_y = m\varepsilon\{\ddot{\alpha} \sin\alpha + \dot{\alpha}^2 \cos\alpha\} \tag{4.42}$$

$$F_x = m\varepsilon\{\ddot{\alpha} \cos\alpha + \dot{\alpha}^2 \sin\alpha\} \tag{4.43}$$

where rotation angle $\alpha = \beta + \Omega\tau$.

Due to breathing phenomenon, change in stiffness is a time dependent function in crack shaft rotation. Generally, the system response is generated in steady-state amplitude data form at various operational speeds, for rotor dynamic analysis. In Eq. (4.38), the term ΔK_{x_r} is important as it is derived in terms of flexibility matrix by the principle of strain energy as provided in the next section.

A substantial local flexibility is introduced by a crack on a beam element because of strain energy concentration in the nearby zone at the tip of the crack subjected under load. In accordance of the Saint-Venant principle, the stress field is changed only in the vicinity of the crack. Under element size constraints, the element stiffness matrix can be considered as unchanged except for the region of cracked element. Determination of appropriate shape function in order to express the kinetic energy and elastic potential energy approximately is quite cumbersome because of the discontinuity of deformation in the cracked element. However, it is easily possible to derive the additional stress energy of the crack and the flexibility coefficient expressed by a stress intensity factor by means of Castigliano's theorem in the linear-

elastics range and it has been explored in fracture mechanics. After dividing the shaft in two elements, crack can be assumed to be in the center of the right hand side elements and left hand side elements. The behaviour of the former can be regarded as external forces applied to the cracked element, whereas the behaviour of latter may be considered as constraints. Thereafter the flexibility matrix of a cracked element with constraints may be evaluated. Local flexibility matrix are generated due to the additional strain energy formed because of the crack.

The flexibility matrix of a cracked section given by *Papadopoulos and Dimarogonas* (1987) and utilized in the FEM analysis of *Sekhar and Prabhu* (1994) has been presented in this section. The additional displacement in i -direction due to a crack of depth α is given as

$$U_i = \frac{\partial}{\partial P_i} \int_0^a J(\alpha) d\alpha \quad (4.44)$$

where $J(a)$ is the strain energy release rate and P_i corresponding load. $J(a)$ for general loading of the cracked section is

$$J(a) = \left[\left(\sum_{i=1}^6 \bar{K}'_{II} \right)^2 + \left(\sum_{i=1}^6 \bar{K}'_{III} \right)^2 + \left(\sum_{i=1}^6 \bar{K}'_{III} \right)^2 \right] / E^I \quad (4.45)$$

where $E^I = E/(1 - \nu^2)$ for plane strain and \bar{K}' are the stress intensity factors for modes of fracture I , II , and III . The local flexibility due to the crack is given by,

$$c_{ij} = \frac{\partial^2}{\partial P_j \partial P_i} \int_0^a J(\alpha) d\alpha \quad (4.46)$$

The strain energy release rate J_α for a local crack depth α has to be integrated along the crack length b to yield,

$$c_{ij} = \frac{\partial^2}{\partial P_j \partial P_i} \int_0^a \int_{-b}^b J(\alpha) d\alpha dz \quad (4.47)$$

On substituting the stress intensity factors given by *Papadopoulos and Dimarogonas* (1987), the local flexibilities can be obtained. If only bending terms are considered here, then the flexibility matrix for the cracked section may given as

$$C_c = \frac{1}{F_0} \begin{bmatrix} \bar{c}_{11}/R & 0 & 0 & 0 \\ 0 & \bar{c}_{22}/R & 0 & 0 \\ 0 & 0 & \bar{c}_{33}/R & \bar{c}_{34}/R \\ 0 & 0 & \bar{c}_{43}/R & \bar{c}_{44}/R \end{bmatrix} \quad (4.48)$$

where $F_0 = ER^2 / (1-\nu^2)$; R =radius of shaft; $\nu=0.3$

The dimensionless compliance coefficients, \bar{c}_{ij} of C_c are computed from the derivations discussed in *Papadopoulos and Dimarogonas* (1987). The off diagonal terms of the flexibility matrix indicate vibration coupling.

$$C_0 = \frac{1}{F_0} \begin{bmatrix} \frac{l^2}{3EI} & 0 & 0 & \frac{l^2}{2EI} \\ 0 & \frac{l^3}{3EI} & -\frac{l^2}{2EI} & 0 \\ 0 & \frac{l^2}{2EI} & \frac{l}{EI} & 0 \\ \frac{l^2}{2EI} & 0 & 0 & \frac{l}{EI} \end{bmatrix} \quad (4.49)$$

By neglecting the shearing action and by using the strain energy, the flexibility coefficient for a section of rotor without a crack can be obtained in the form expressed by Eq. (4.49). The next section will present the bondgraph modeling of multi-crack shaft.

4.4.3 Bondgraph modeling of multi-crack rotating shaft

Bondgraph modeling technique is a unique modeling technique, when one can model several energy domains at one platform. It is also convenient to model a complex system through this modeling technique. This can be done by forming subsystem model and consolidating them to generate an integrated system model. Bondgraphs represents the physical systems in pictorial form, where the energy exchange between the components of a dynamic system are reproduced graphically and formulating the system equations. The bondgraph technique is a useful tool for modeling and the model of the system is generated using object-oriented reusable subsystem (capsules) as the model can be extended to incorporate any change at the later stage. The bondgraph model is also helpful in studying the effect of various parameters like stiffness, damping and rotor mass on the dynamical behaviour of the shaft. Following subsections will present the modeling of a cracked rotor system.

4.4.3.1 Bondgraph modeling of velocity transformation

The coordinate transformation from fixed to rotating frame may be expressed as

$$\begin{bmatrix} X_r \\ Y_r \end{bmatrix} = \begin{bmatrix} \cos\alpha & \sin\alpha \\ -\sin\alpha & \cos\alpha \end{bmatrix} \begin{Bmatrix} X_f \\ Y_f \end{Bmatrix} \quad (4.50)$$

where α is the angular rotation of the shaft. Differentiating above Equation with respect to time, one obtains

$$\begin{bmatrix} \dot{X}_r \\ \dot{Y}_r \end{bmatrix} = \begin{bmatrix} \cos\alpha & \sin\alpha \\ -\sin\alpha & \cos\alpha \end{bmatrix} \begin{Bmatrix} \dot{X}_f \\ \dot{Y}_f \end{Bmatrix} - \omega \begin{bmatrix} \sin\alpha & -\cos\alpha \\ \cos\alpha & \sin\alpha \end{bmatrix} \begin{Bmatrix} X_f \\ Y_f \end{Bmatrix} \quad (4.51)$$

In above equation $\omega = \dot{\alpha}$

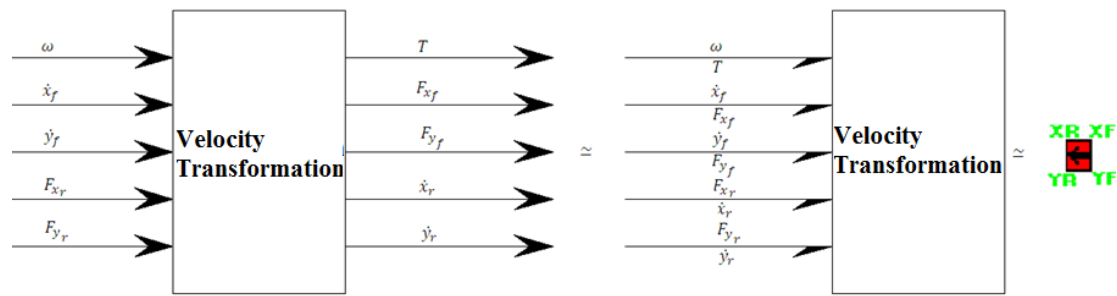


Figure 4.9: Word bondgraph and capsule representation of fixed-rotating frame velocity transformation in block diagram

In Figure 4.9, it is shown that fixed coordinate frame is converting into rotating coordinate. The shaft is rotating at a constant angular speed ω . The word bondgraph depicts the power and flow variable on either side. The unique aspect of this sub model is that it has separate angular speed port to model the spinning speed of the rotor shaft.

4.4.3.2 Bondgraph modeling of uncracked rotating shaft

The spinning shaft model (capsule) is based on Rayleigh beam model, where the effect of polar moment of (rotary) inertia as also considered as well as those of the linear inertia (m , mass per unit length). The deformations related with transverse shear are not included as well.

The stiffness of the rigid beam elements relates the generalized Newtonian forces to the generalized displacements at the ends of the element as given by the following equations in X-Z plane and Y-Z plane direction as

$$\begin{Bmatrix} V_{xL} \\ M_{xL} \\ V_{xR} \\ M_{xR} \end{Bmatrix} = [K] \begin{Bmatrix} X_L \\ \Psi_L \\ X_R \\ \Psi_R \end{Bmatrix} \tag{4.52}$$

$$\begin{Bmatrix} V_{yL} \\ M_{yL} \\ V_{yR} \\ M_{yR} \end{Bmatrix} = [K] \begin{Bmatrix} Y_L \\ \theta_L \\ Y_R \\ \theta_R \end{Bmatrix} \quad (4.53)$$

In Eq. (4.52-4.53), V_{xL} and V_{xR} are the generalized forces, bending moments are denoted by M_{xL} and M_{xR} , whereas generalized displacements notations are X_L , X_R , Ψ_L and Ψ_R . Subscript “R” and “L” represents the right and left side of the model in X-Z plane direction. V_{yL} and V_{yR} are the generalized forces, M_{yL} and M_{yR} are the bending moments whereas X_L , X_R , θ_L and θ_R are the generalized displacements. Subscript “L” and “R” represents the left and right side of the model in Y-Z plane direction. In terms of flexural rigidity “ EI ” and element length “ l ”, the stiffness matrix can be modeled as a 4-port C-field storing energy due to the four generalized displacements as shown in Figure 4.11 and 4.12. Finally compliance field in X-Z direction may be expressed as

$$\begin{Bmatrix} V_{xL} \\ M_{xL} \\ V_{xR} \\ M_{xR} \end{Bmatrix} = \frac{EI}{l^3} \begin{bmatrix} 12 & 6l' & -12 & 6l' \\ 6l' & 4l'^2 & -6l' & 2l'^2 \\ -12 & -6l' & 12 & -6l' \\ 6l' & 2l'^2 & -6l' & 4l'^2 \end{bmatrix} \begin{Bmatrix} X_L \\ \Psi_L \\ X_R \\ \Psi_R \end{Bmatrix} \quad (4.54)$$

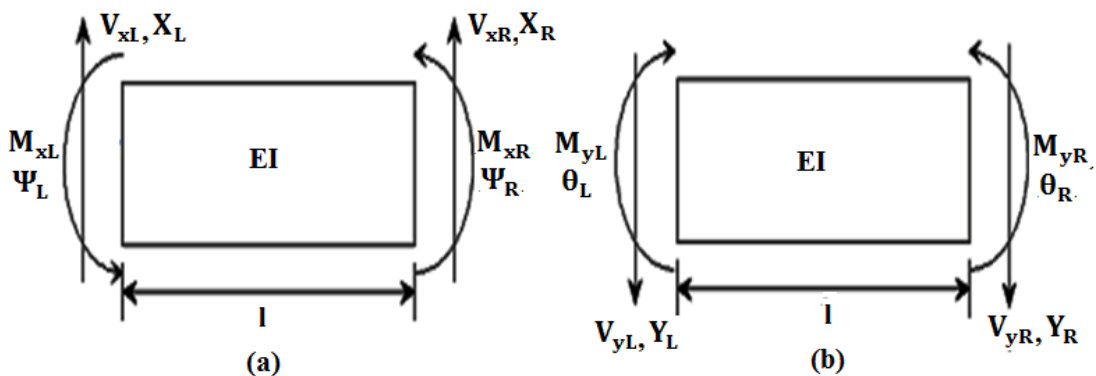


Figure 4.10: Generalized forces, displacements and moments of a Rayleigh beam in (a) X-Z plane direction and (b) Y-Z plane direction

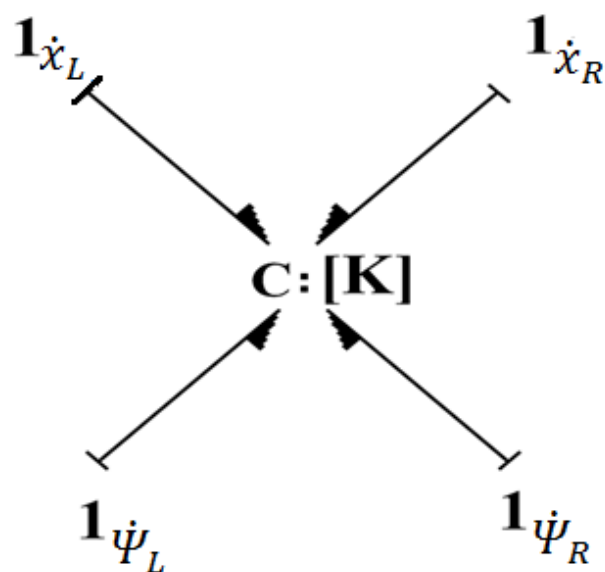


Figure 4.11: C- field representing the beam element stiffness matrix in X-Z direction

Compliance field in X-Z direction may be expressed as

$$\begin{Bmatrix} V_{yL} \\ M_{yL} \\ V_{yR} \\ M_{yR} \end{Bmatrix} = \frac{EI}{l^3} \begin{bmatrix} 12 & 6l' & -12 & 6l' \\ 6l' & 4l'^2 & -6l' & 2l'^2 \\ -12 & -6l' & 12 & -6l' \\ 6l' & 2l'^2 & -6l' & 4l'^2 \end{bmatrix} \begin{Bmatrix} Y_L \\ \theta_L \\ Y_R \\ \theta_R \end{Bmatrix} \quad (4.55)$$

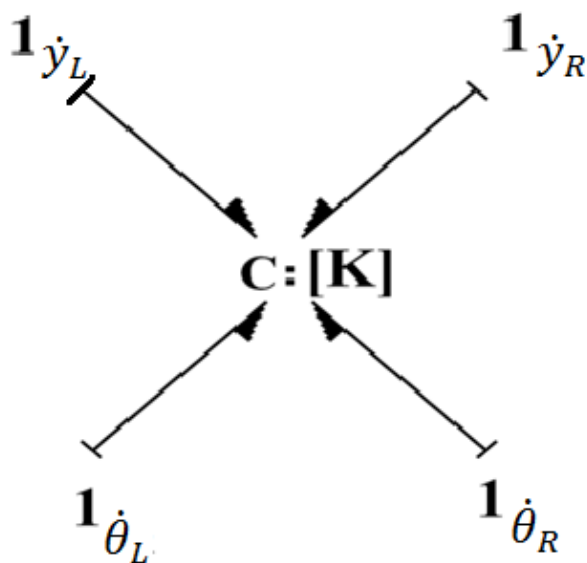


Figure 4.12: C- field representing the beam element stiffness matrix in Y-Z direction

In bondgraph formulation, the potential energy storage is represented as a four port C-field. The i^{th} beam element is influenced by displacements x_i and x_{i+1} and rotations ψ_i and ψ_{i+1} in x - directions and similarly in y -directions are computed. The flow variables in four ports of C-fields are the corresponding linear and rotational velocities. The effort variables are shear forces and bending moments. They are related with the following expressions:

$$\begin{Bmatrix} V_i \\ M_i \\ V_{i+1} \\ M_{i+1} \end{Bmatrix} = [K]_{4 \times 4} \begin{Bmatrix} X_i \\ \Psi_i \\ X_{i+1} \\ \Psi_{i+1} \end{Bmatrix} \quad (4.56)$$

or $e = [K]_{4 \times 4} f$, where $e = [V_i \quad M_i \quad V_{i+1} \quad M_{i+1}]^T$ and $f = [X_i \quad \Psi_i \quad X_{i+1} \quad \Psi_{i+1}]^T$ are the vectors of efforts and flow variables respectively. The elements of stiffness matrix $[K]_{4 \times 4}$ are already given in previous expressions of Eqs. (4.54-4.55). By lumping the element inertias and attaching them to 1- junction that represents displacement and rotation at the ends of the elements, bondgraph model of the beam element can be created. The stiffness of the rotor shaft can be modeled as four-port compliance fields storing energy due to the four generalized displacement are integrated in a model of beam element as shown in Figure 4.11 and 4.12. The compliance field models the bending of the shaft in any direction (either X-Z or Y-Z planes) as shown in Figure 4.13 and 4.14.

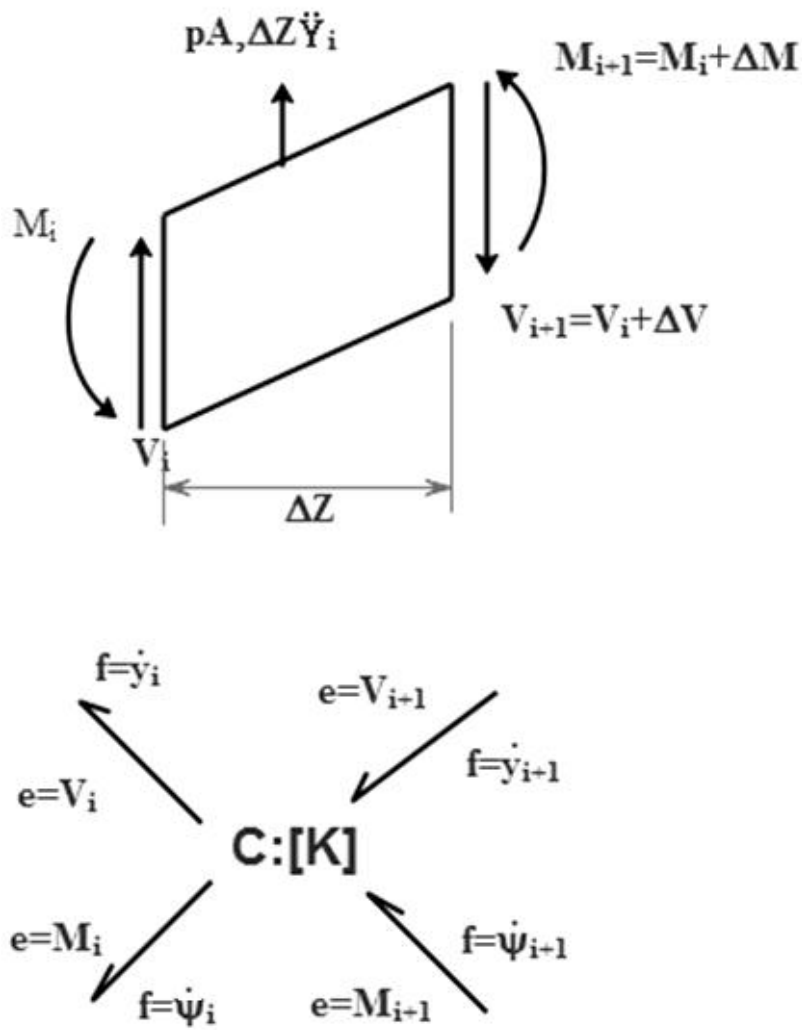


Figure 4.13: C- field representing the beam element modeling for the stiffness of the shaft in any direction

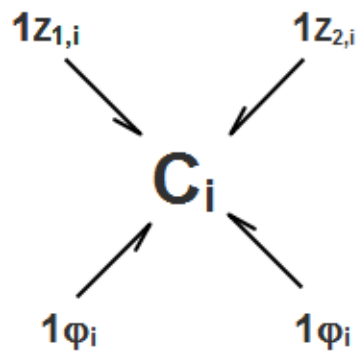


Figure 4.14: Generalized C- field representing the beam element modeling for stiffness of the shaft

Internal damping of shaft is also considered as the damping accounts for the restoring force proportional to the strain rate. Thus, internal damping of the shaft (R_i) is also modeled in the transformed X and Y frame in the model. Masses and rotary inertia have been lumped as its left and right ends. Thus, total shear force and bending moment due to flexural condition may be expressed as

$$\begin{Bmatrix} V_i \\ M_i \\ V_{i+1} \\ M_{i+1} \end{Bmatrix} = [K]_{4 \times 4} \begin{Bmatrix} \int \dot{X}_i d\tau \\ \int \dot{\Psi}_i d\tau \\ \int \dot{X}_{i+1} d\tau \\ \int \dot{\Psi}_{i+1} d\tau \end{Bmatrix} + [R_i]_{4 \times 4} \begin{Bmatrix} \dot{X}_i \\ \dot{\Psi}_i \\ \dot{X}_{i+1} \\ \dot{\Psi}_{i+1} \end{Bmatrix} \quad (4.57)$$

where $[R_i]_{4 \times 4}$ represents the internal damping matrix offered by lumber bones. The damping matrix $[R_i]_{4 \times 4}$ may be expressed as presented as

$$[R_i]_{4 \times 4} = \frac{\mu_i l}{l^3} \begin{bmatrix} 12 & 6l' & -12 & 6l' \\ 6l' & 4l'^2 & -6l' & 2l'^2 \\ -12 & -6l' & 12 & -6l' \\ 6l' & 2l'^2 & -6l' & 4l'^2 \end{bmatrix} \quad (4.58)$$

where μ_i represents the internal damping of shaft. The bondgraph representation of the combined stiffness and damping of the beam element is shown in Figure 4.15.

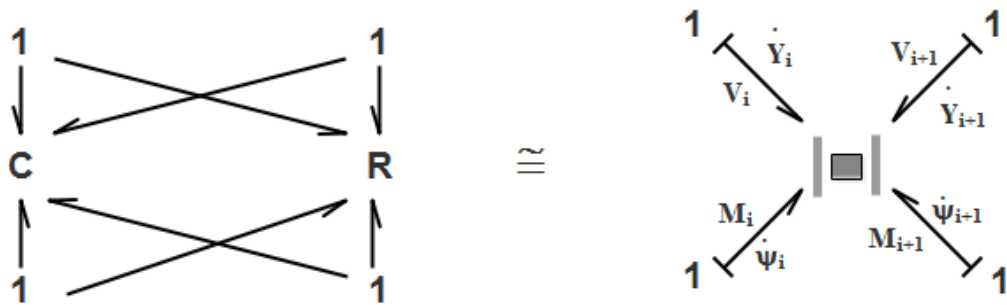


Figure 4.15: Bondgraph model of single rigid element of shaft

In a fixed X and Y frame, external damping (R_{ex}) has been modeled. By using two GY elements in the model, gyroscopic coupling has also been integrated between two rotations in the fixed frame. Lumping of mass and polar moment of (rotary) inertia can be taken on the left and right end of the shaft element in the plane, for shaft bending in any one transverse plane.

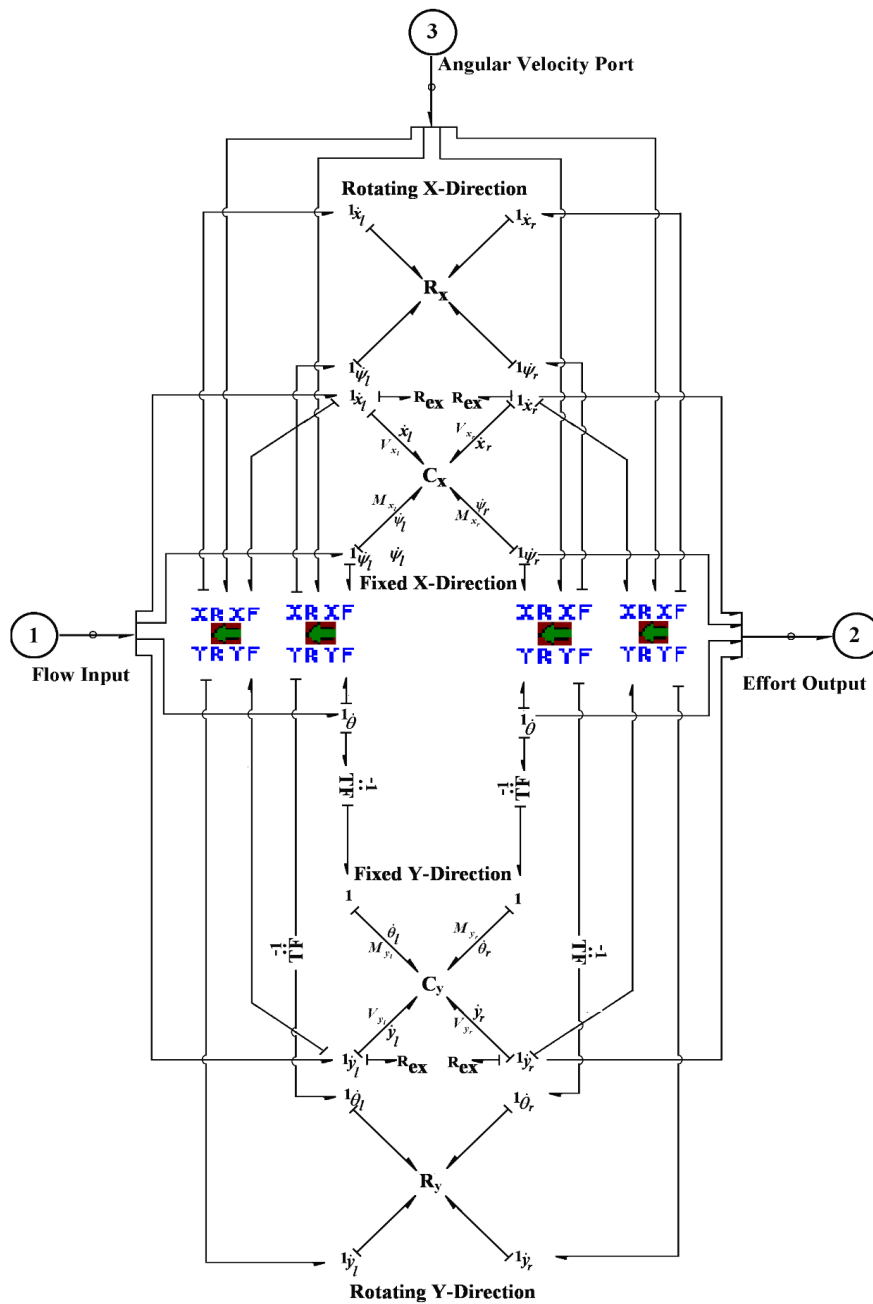


Figure 4.16: Bondgraph model of un-cracked rotating shaft

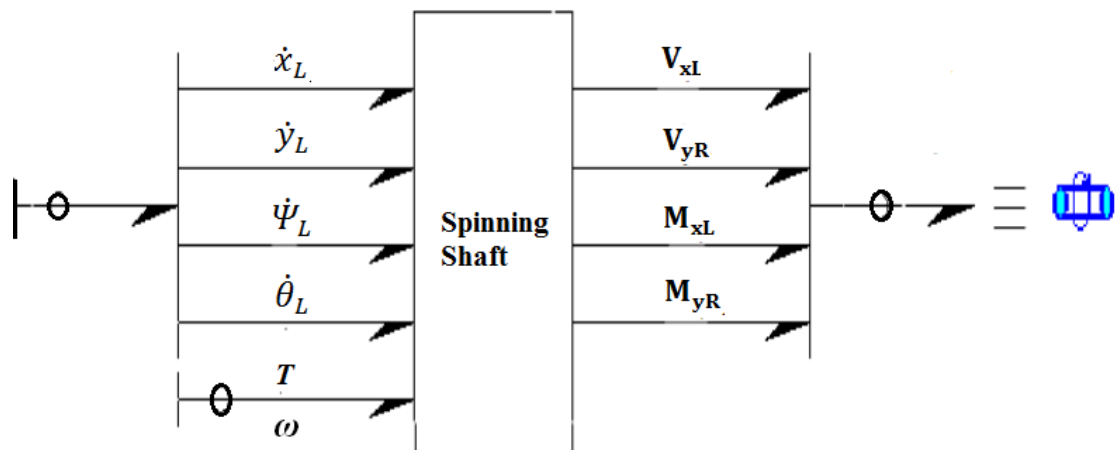


Figure 4.17: Word bondgraph capsule representation of a rotating shaft

In addition to that, one angular speed or spinning port is attached in fixed to rotating frame velocity transform sub-model (all four capsule) in order to model the spinning speed of the rotating shaft. Rotations θ about X-axis and the rotation of the ends of the shaft because of bending in Y-Z planes as used in deriving C-field matrix are different. Consequently, two-transformer elements (TF) have been used in the model as presented in Figure 4.16 with negative unitary modulus. The right interface vector glue port (flow input) has four scalar components namely the two translational and two rotational velocities in the fixed frame. The left interface vector glue port (flow output) has also the same attributes. The top interface glue port (angular velocity port) has spinning speed port. The capsule representation may also be given through word-bondgraphs as shown in Figure 4.17.

4.4.3.3 Bondgraph modeling of cracked rotating shaft

The beam element with a transverse crack and its sub model representation is shown in Figures 4.14 and 4.15. The flexibility matrix of cracked rotor may be given as

$$[K]^e = \begin{bmatrix} \bar{C}_{22} & 0 & 0 & 0 \\ 0 & \bar{C}_{33} & 0 & 0 \\ 0 & 0 & \bar{C}_{44} & \bar{C}_{45} \\ 0 & 0 & \bar{C}_{54} & \bar{C}_{55} \end{bmatrix} \quad (4.59)$$

where \bar{C}_{22} , \bar{C}_{33} , \bar{C}_{44} , \bar{C}_{45} , \bar{C}_{54} and \bar{C}_{55} are the six nonzero dimensionless terms of flexibility and given by Dirr et al. [9]. As the flexibility matrix is symmetric, off diagonal flexibility may be denoted as

$$\bar{C}_{54} = \bar{C}_{45} \quad (4.60)$$

Total five independent flexibility co-efficients define the crack model for the transverse loading, in which four (\bar{C}_{22} , \bar{C}_{33} , \bar{C}_{44} , \bar{C}_{55}) are direct co-efficients and one (\bar{C}_{54} or \bar{C}_{45}) is the cross coupled co-efficient.

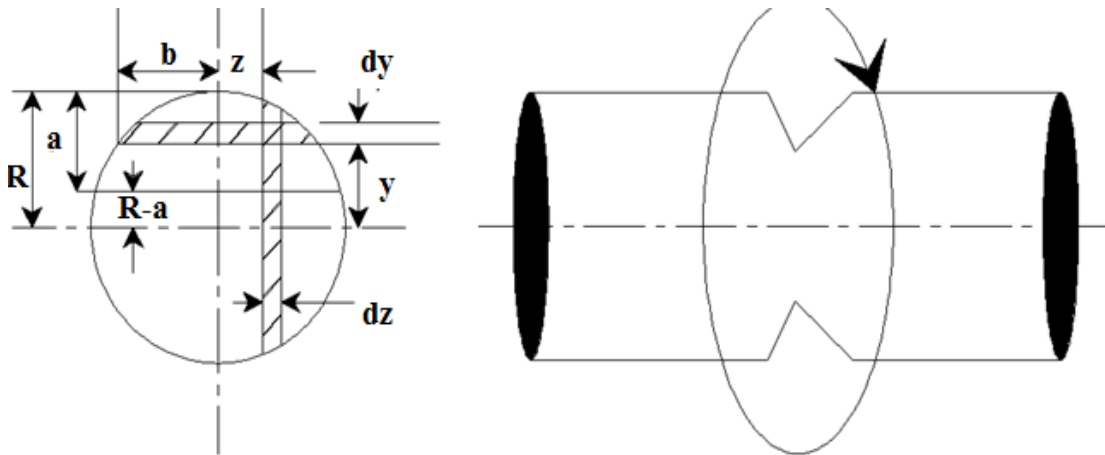


Figure 4.18: Beam element model

Figure 4.19: Representation of cracked rotor element

In Figure 4.18, radius of the spinning shaft is “R”, “a” is the crack depth and “2b” is width of the elemental strip. “ α ” is local crack depth that is varying along with the cross section. Now total flexibility matrix of the cracked beam element is obtained as

$$[K_o]^e = \begin{bmatrix} \frac{l'^3}{3EI} & 0 & 0 & \frac{l'^2}{2EI} \\ 0 & \frac{l'^3}{3EI} & \frac{l'^2}{2EI} & 0 \\ 0 & \frac{l'^2}{2EI} & \frac{l'}{EI} & 0 \\ \frac{l'^2}{2EI} & 0 & 0 & \frac{l'}{EI} \end{bmatrix} \quad (4.61)$$

$$[K_c]^e = \begin{bmatrix} \bar{C}_{22} & 0 & 0 & 0 \\ 0 & \bar{C}_{33} & 0 & 0 \\ 0 & 0 & \bar{C}_{44} & \bar{C}_{45} \\ 0 & 0 & \bar{C}_{54} & \bar{C}_{55} \end{bmatrix} \quad (4.62)$$

$$[K]^e = \begin{bmatrix} \frac{l'^3}{3EI} + \bar{C}_{22} & 0 & 0 & \frac{l'^2}{2EI} \\ 0 & \frac{l'^3}{3EI} + \bar{C}_{33} & \frac{l'^2}{2EI} & 0 \\ 0 & \frac{l'^2}{2EI} & \bar{C}_{44} + \frac{l'}{EI} & \bar{C}_{45} \\ \frac{l'^2}{2EI} & 0 & \bar{C}_{54} & \frac{l'}{EI} + \bar{C}_{55} \end{bmatrix} \quad (4.63)$$

The bondgraph model of cracked beam element is similar to previous uncracked beam model of Figure 4.16 except the flexibility matrix is changed in the C-field and may be shown in Figure 4.20.

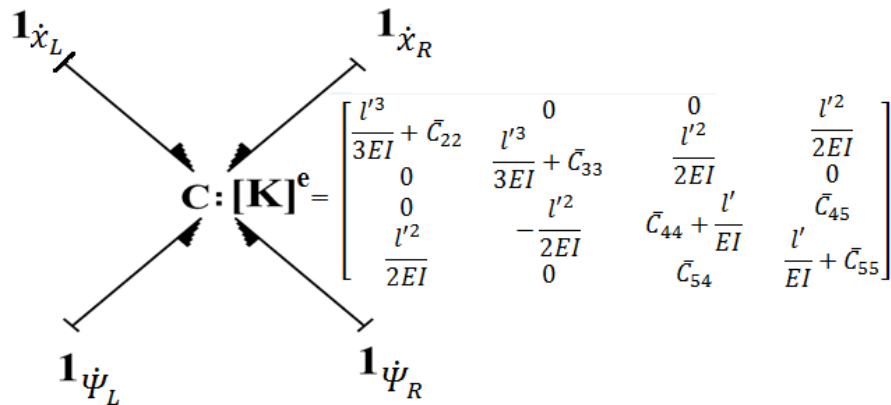


Figure 4.20: C- field representing the stiffness matrix for cracked beam element

4.4.3.4 Lumping of mass and polar moment of (rotary) inertia

Lumping is an approximation method, in which a simplified system model is obtained through the real system. In this modeling of the rotating shaft, the rotary inertia and

mass may be lumped at both ends of shaft element by taking the contribution from adjacent right and left shaft elements, if required.

(a) Lumping of mass

The masses lumped at the left and right end of the shaft elements are M_L and M_R respectively as shown in Figure 4.21.

$$M_L = \frac{\rho\pi}{2} (R^2) l'_{prev} \quad (4.64)$$

$$M_R = \frac{\rho\pi}{2} (R^2) l'_{next} \quad (4.65)$$

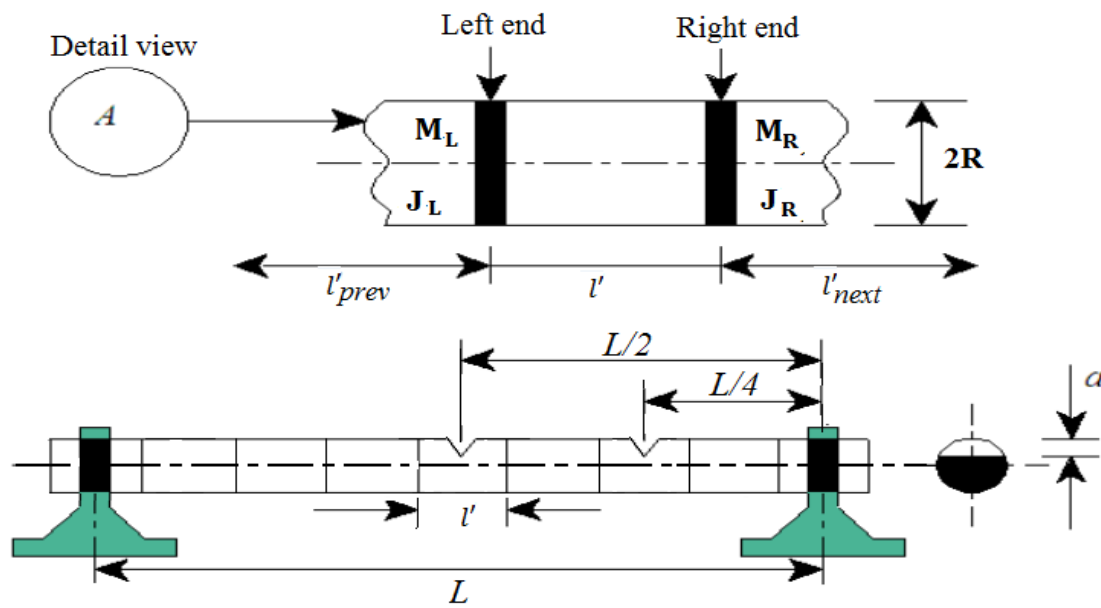


Figure 4.21: Lumping of three consecutive shaft elements (capsules) showing mass and rotary inertia on the middle element

where ρ is density of rotor material, l'_{prev} is the previous shaft element length, l'_{next} is the length of next shaft element and R is external radius of rotor shaft. In this model,

l'_{prev} and l'_{next} are taken as l'_{elem} ,

where $l'_{elem} = \frac{\text{Length of the shaft}}{\text{No. of elements}}$

(b) Lumping of rotary inertia

The procedure of lumping of rotary inertia of shaft element is similar as that for mass lumping by taking the contribution from the adjacent left and the right shaft elements. The mass moment of inertia of a solid circular shaft of length Δh along the perpendicular direction to the axis may be given as

$$\Delta I = \frac{\Delta M}{2} \left(\frac{R^2}{2} - \frac{\Delta h^2}{2} \right) \quad (4.66)$$

and rotary inertia density is defined by

$$\lim_{\Delta h \rightarrow 0} \frac{\Delta I}{\Delta h} = \rho_i = \frac{\rho \pi R^2}{4} \quad (4.67)$$

where ρ_i is rotary inertia density.

For solid shaft

$$\rho_i = \frac{\rho \pi}{4} \quad (4.68)$$

The expressions for J_L and J_R are as follows:

$$J_L = \frac{\rho \pi}{8} (R^4) l'_{prev} \quad (4.69)$$

$$J_R = \frac{\rho \pi}{8} (R^4) l'_{next} \quad (4.70)$$

where J_L and J_R are the rotary inertia at the left and right end of the shaft.

4.4.3.5 Integrated model of a multi-cracked rotor shaft

It is a vectorized bondgraph model, which interfaces various sub-models (capsules) respectively by their respective icons as shown in Figure 4.22. The shaft is modeled

with seven reticules (shaft elements). By analyzing through the second left and the fourth capsule in this model which are showing the cracked shaft, and more significant as compared to others. This is because of the fact that these portray the real power and dynamics of the multi-cracked shaft. Rest of the capsules (1st, 3rd and 5th-7th) are depicting only the spinning uncracked shaft element. These capsules are unfavorable from the dynamics point of view; although, the use of such capsules is necessary for improving the accuracy of the modeling, predominantly in the higher modes. The dissipative coupling is modeled by the resistive element (R_c) and shaft is rotated by a constant speed (Ω), as shown in Figure 4.22

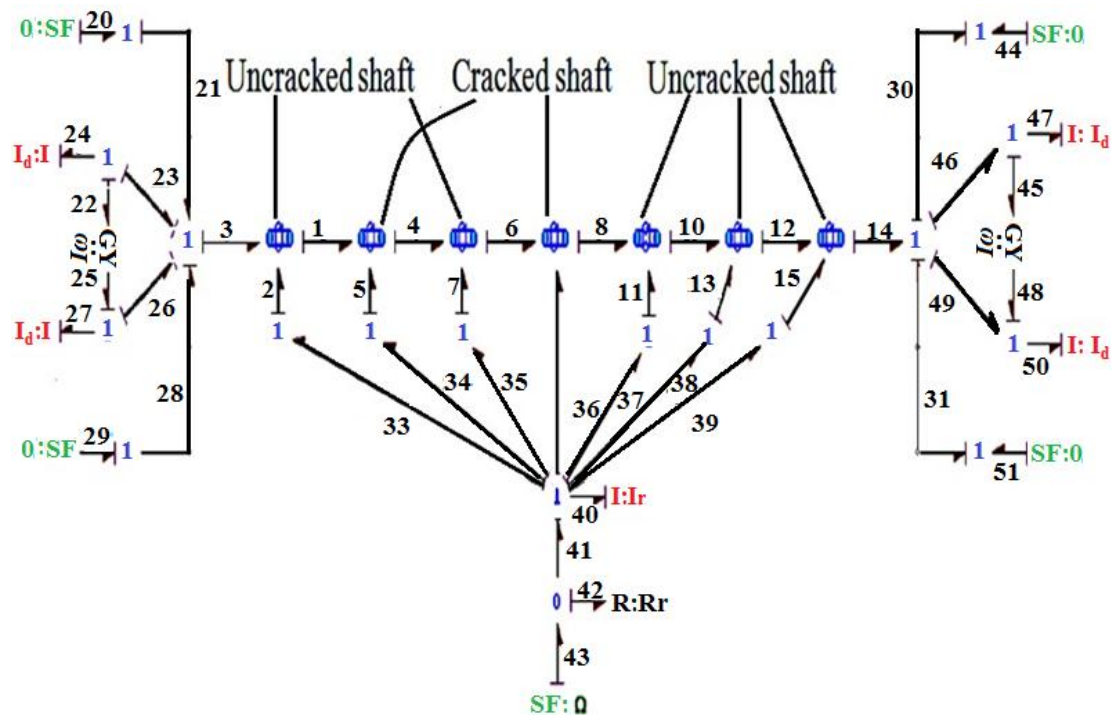


Figure 4.22: Integrated system of multi-crack rotor shaft connected by dissipative coupling using capsules represented through bondgraph

4.4.4 Simulation study of multi-cracked rotor system

As shown in Figure 4.22, pin-pin end conditions have been selected for simulation of bondgraph model of the multi-cracked rotor shaft. Simulation work has been

completed on the software SYMBOLS Shakti[®] (Mukherjee and Samantaray, 2006). Shaft is rotated at Ω excitation frequency by a uniform speed source. Simulation test rig is discretized into seven reticules (capsules). The ends of the Rotor are well supported on a self-aligning double groove ball bearing.

Table 4.1: Simulation parameters

	Parameter	Value
Shaft length	L	0.65 m
Number of elements	N	7
Young's Modulus of elasticity for steel (Rotor shaft material)	E	210 GPa
Density of steel (rotor shaft material)	P	7850 Kg /m ³
Shaft Diameter	D	0.022 m
Dissipative coupling co-efficient	R_c	2×10^{-3} N m s
Excitation frequency	Ω	22 rad s ⁻¹
Internal damping co-efficient of the rotor shaft	μ_i	0.0002 N s m ⁻¹
External damping co-efficient of the rotor shaft	μ_{ex}	0.00003 N s m ⁻¹ , 0.0006 N s m ⁻¹

4.4.4.1 Simulation results for un-cracked rotor

Simulation is carried out for parameters given in Table 4.1 with various combinations of external damping (μ_{ex}) and excitation frequency (Ω). An initial momentum of 0.0001 Kg-m² was given to 7th reticules of the shaft so that the simulation may be started. Initial momentum is used to accelerate the simulation and reducing the simulation time. Figures 4.23 – 4.24 show that the trajectories of the rotating un-crack shaft and 1 mm single crack shaft reaching the limiting orbit. This is due to loading of the motor of the electromechanical system.

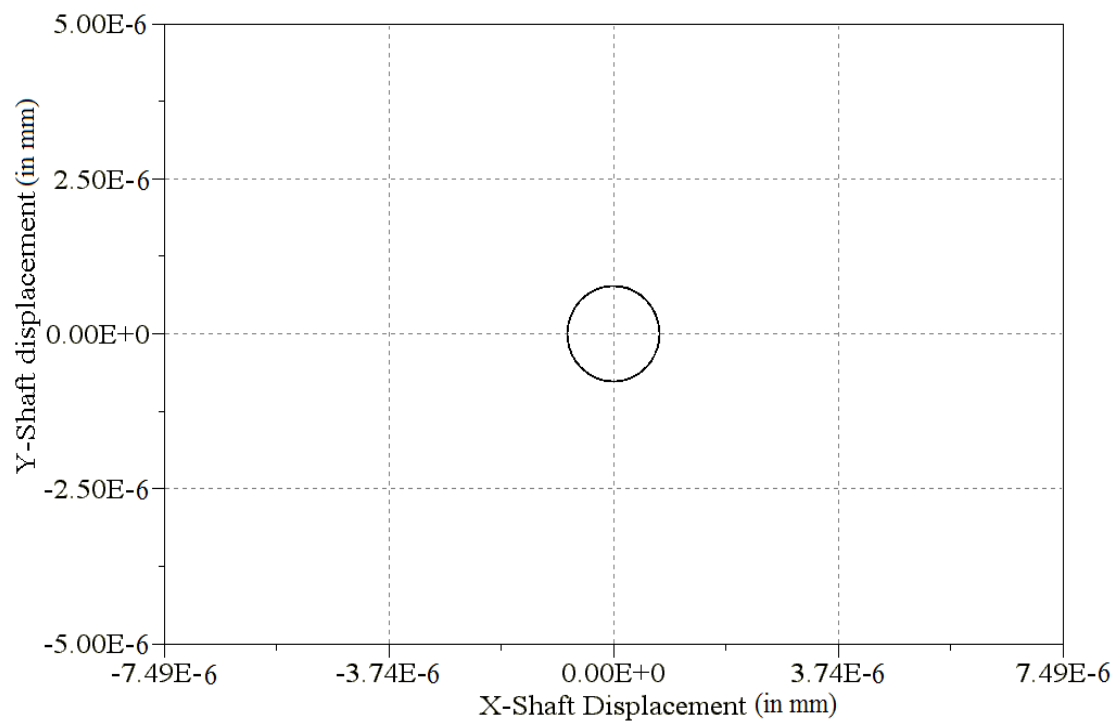


Figure 4.23: Limit orbits of rotor shaft for uncracked shaft

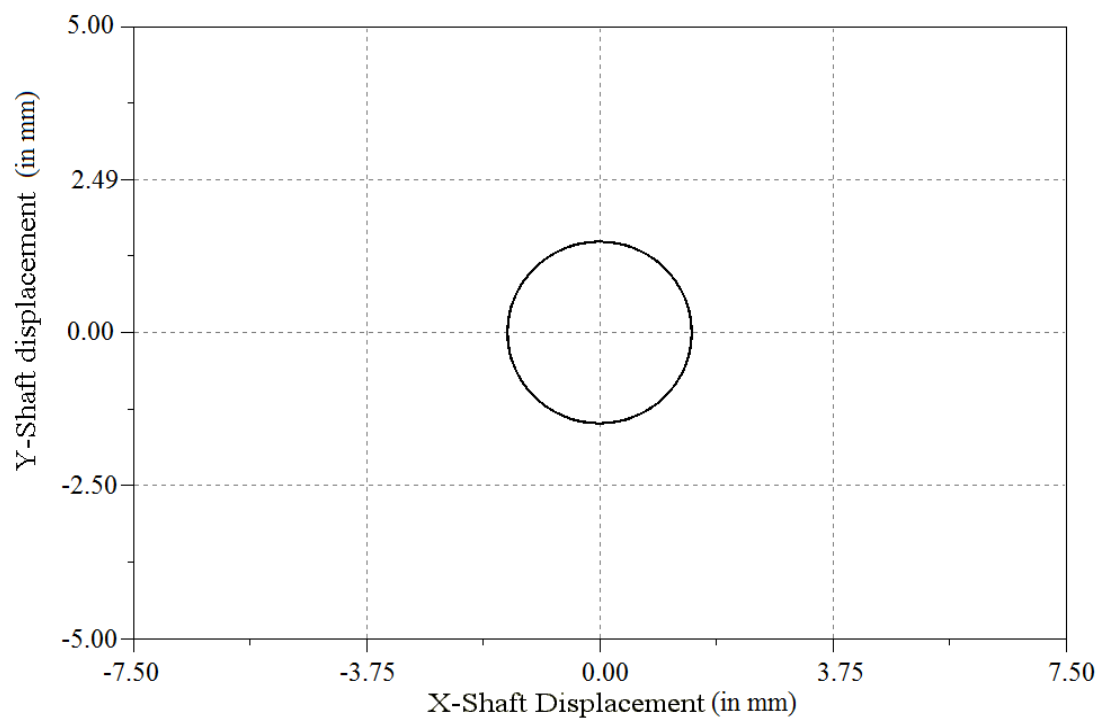


Figure 4.24: Limit orbits of rotor shaft for 1 mm cracked shaft

When the value of excitation frequency is changed from 1000 rpm to 5000 rpm, one obtains increased amplitudes of the rotor shaft. The limiting orbits of the rotating shaft may be obtained through simulation at different value of excitation frequency.

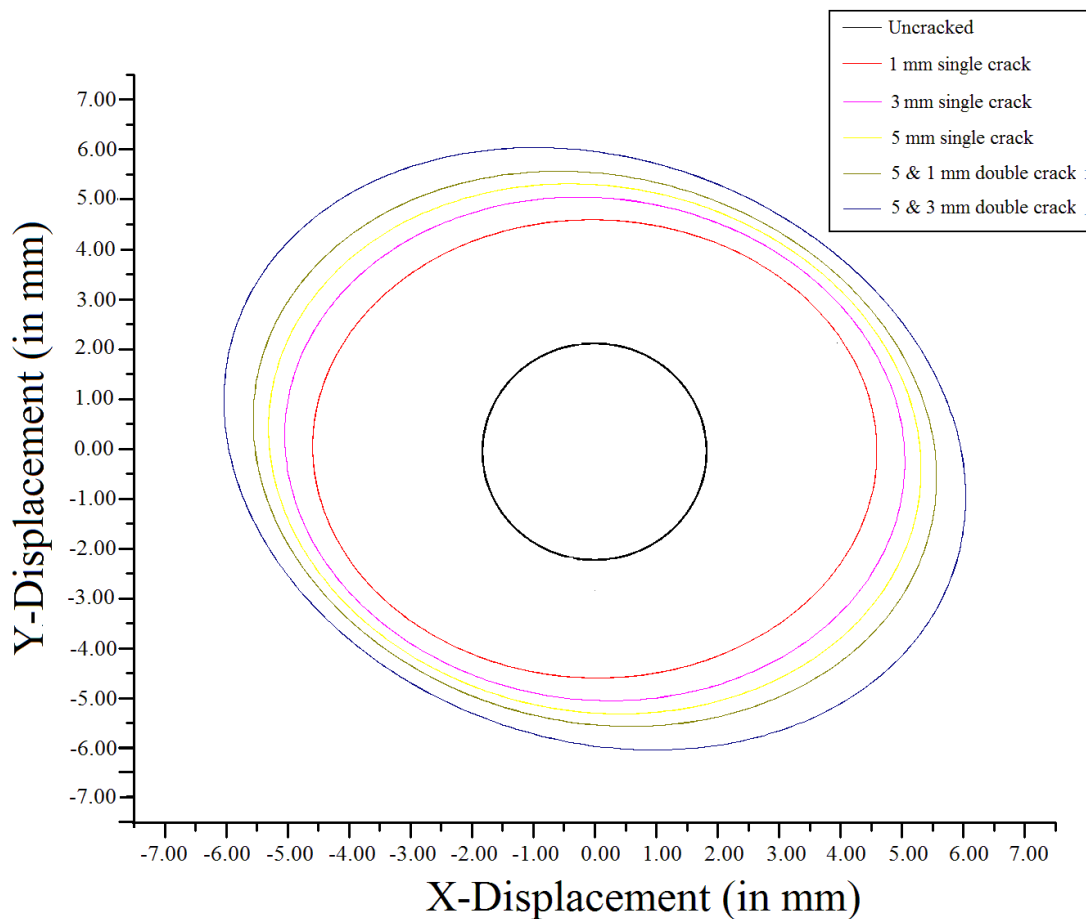


Figure 4.25: Limiting orbits of the trajectories of the different test specimen (Intact, single and double crack shaft) at different crack depth

As shown in Figure 4.25, the limiting orbits of rotating shaft with different conditions have been obtained through simulation at different crack depth. In this case, each section of the shaft is moving in a circular trajectory with common angular velocity. On such limit orbits, the regenerative work due to internal damping and the net dissipative work balance each other (*Mukherjee et al., 2009*). Limiting dynamics is

resulted when the power imported by internal damping from shaft spin is balanced by dissipation of power by external damping, dissipation in coupling and a part of action of internal damping, which acts like an external damping. When such balance takes place, the shaft behaves as if it was under damped and sustains transverse motion. However, the above said balance take place for one of the modes of the shaft showing limiting dynamics (or so called limit cycle or instability) depending upon the relative value of various parameters. Displacement of the cracked rotor shaft in X and Y direction increases with the crack depth and number of cracks. It means that instability of high speed rotating shaft increases with the crack depth and number of cracks in a rotor shaft.

4.5 Summary of the chapter

An extended form of Lagrangian-Hamiltonian mechanics for double crack continuous systems has been presented through an addition of umbra (virtual) time. The variational formulation for a 1-D continuous shaft has been achieved, which provides the boundary conditions and the motion governing equations. The amplitude asymmetry of umbra-Lagrangian density of 1-D continuous rotor shaft has been obtained by extending form of Noether's theorem, in which polar moment of (rotary) inertia, gyroscopic forces; external and internal damping terms have been incorporated. The interesting case of a cracked rotating shaft with external and internal damping driven through a dissipative coupling has been examined. The dynamical behaviour analysis has been carried out through an extended form of Noether's theorem and umbra-Hamiltonian theoretically as well as analytically. Finite stiffness has been assumed for the crack in the study.

The dynamic framework for double-cracked rotor system has been presented using the bondgraph technique that has shown the object-oriented reusable capsules, used to model the system. Bondgraph modeling of this system has effectively incorporated the internal damping in the model. It has provided an added features in studying turbo machinery (like turbine, generator etc.) stability. The flexibility matrix of the cracked rotor shaft has been obtained and modeled as a *C*-field element. Model presented in this chapter only consider transverse dynamics. Torsional dynamics has not been considered. The effect of multi-cracks on the rotor shaft has been investigated. The vibration characteristics of the rotor shaft have been observed through simulation of computational model. The effects of crack depth on system response have clearly seen through simulation. It is further shown that amplitude of the rotor has increased inversely with the stiffness of the rotor. Results obtained through simulation for uncracked and cracked rotor shaft have clearly shown the effect of crack on the amplitude of vibration. For small crack depth, there is very small disturbance in the system response. However the response can be clearly noticed, as well as observed when the crack depth was more. Due to the presence of crack, the amplitude of the rotor increases. Moreover, the propagation of cracks will further make these amplitudes too high so that catastrophic failure may occur.

The next chapter will present the development of an experimental framework for analysis of multi-cracked rotor and validation of analytical and computational results.

Development of Experimental Framework and Validation for Multi-crack Rotor

5.1 Introduction

Development of a test rig is an essential part of any research work. It is again, very important to validate the simulation and analytical results with experimental results. Many researchers (*Darpe et al., 2003; Ishida and Inoue, 2006*) have been developed test rig for validation of simulation and analytical results. So one may use the method with live / online industrial application. In this way, our society may be benefited directly in terms of time or money. In the previous *Chapter 3* and *Chapter 4*, analytical model of multi-cracked rotor has been developed through the extended Lagrangian–Hamiltonian formalism. Computational model has been also created on Symbol Shakti[®] software by using the bondgraph concept. The main focus of these experiments was directed towards to evaluate an amplitude of vibration of a single and multi cracked shaft with different crack depth at various excitation frequencies. Another objective is also to find out the variation of stiffness, natural frequency in single and multi cracked shaft. Silent features of the test rig developed include variation in cross section, length, material of the shaft. The source of excitation is provided through variable speed DC motor, which produces sinusoidal forces. Data acquisition system with display system is integrated with this test rig. The test rig developed enable to execute a wide range of experiments with minimum assembly time and maximum adaptability. The next section will explain the various details of components of the experimental test rigs.

5.2 Experimental test rig

Experimental test rig used for dynamic analysis of multi-cracked rotor system is shown in Figure 5.1. Various major components like analyzer, signal display device, speed control device, techo sensor (tachometer), accelerometer, DC motor and flexible coupling are shown in this Figure 5.1, which presents an actual picture of the test rig.

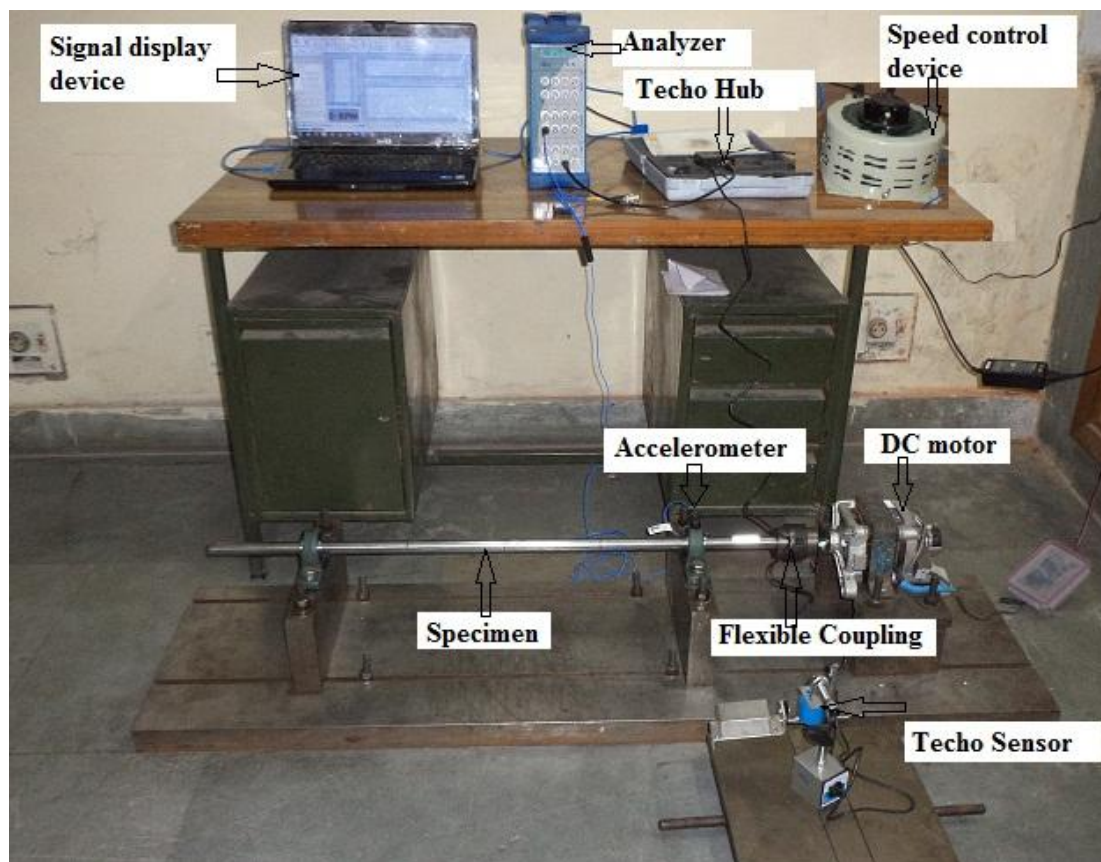


Figure 5.1: Experimental test rig for dynamic analysis

The brief details of various components are presented in next subsection.

5.2.1 Rotor system and its metallic structure

Base platform is an essential part of any rotor system. Since rotor shaft is rotating at very high speed (6000 rpm), so it is very necessary to use heavy base plate as a platform, on which all parts are mounted. Base plate is made of mild steel. Rotor system

consists of a DC motor, bearings, coupling and fasteners. All parts are assembled mounted on this robust mechanical frame together as presented in Figure 5.2. The structure is designed in such a way that it assures enough rigidity and sufficient strength. Top view and front view of rotor system are also shown in Figure 5.3.



Figure 5.2: Actual rotor system for dynamic analysis

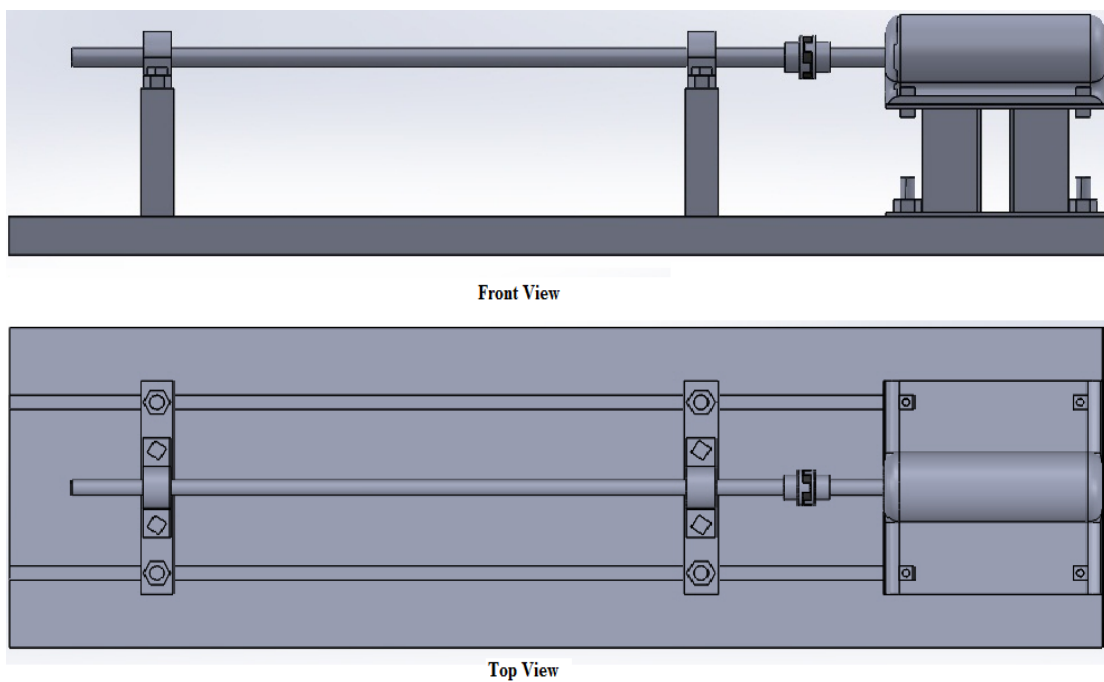


Figure 5.3: Front view and top view of rotor system

Test specimen was similar as referred by American Society for Testing Material Engineering (ASTM) as standard for the shaft material (0.3% – 0.6%). It was made from steel with 0.3% carbon. This specimen is also used by the various researchers in its experimental analysis as reported in research paper. Details of test specimen are presented in Table 5.1 and schematic diagram of test specimens are shown in Figure 5.4.

Table 5.1: Detail of test specimen

Shaft (Specimen) Material	Mild steel
Effective Length (Bearing to bearing)	660 mm
Overhang (each side)	170 mm
Diameter of the shaft	22 mm
Weight of the shaft	1.83 kg
Density	7850 kg/m ³
I_{xx} and I_{yy}	11503 mm ⁴
Stiffness	285 N/mm

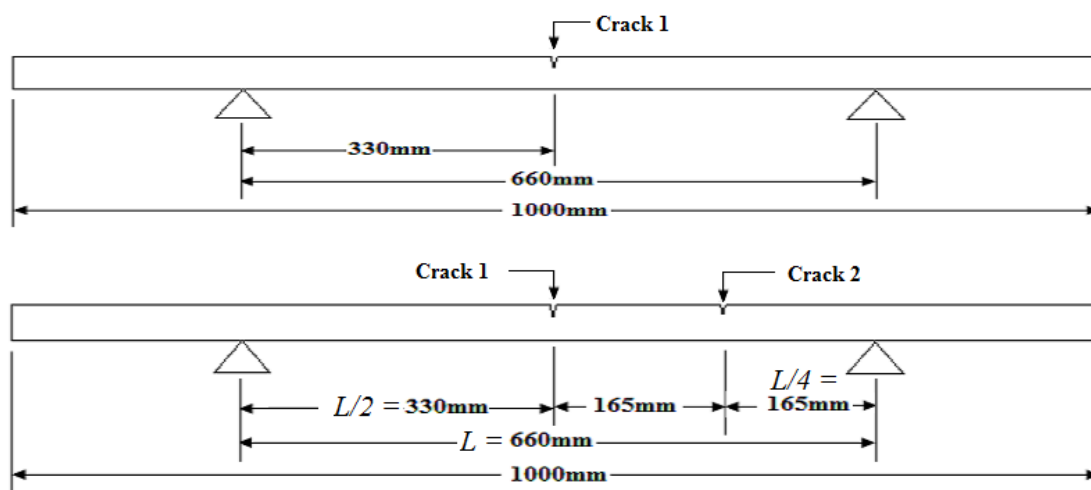


Figure 5.4: Schematic diagram of test specimens

5.2.2 DC motor and speed controller

In dynamic analysis of a rotating shaft, a variable speed DC motor is used to rotate the shaft specimen at various speeds. This motor is connected to the rotor on extreme right of

the frame with the help of fasteners and washers. The specification of DC motor is shown in Table 5.2. Figure 5.5(a) is showing a DC motor, which are used in experimental test rig. Speed controller is used to control the speed of the rotor shown in Figure 5.5(b).

Table 5.2: Specification of DC motor

Phase	Single
RPM	1440 rpm to 7000 rpm
Power	1 KW
Pole	4 pole (electromagnetic)
Current, voltage	5 Amp, 240 volts

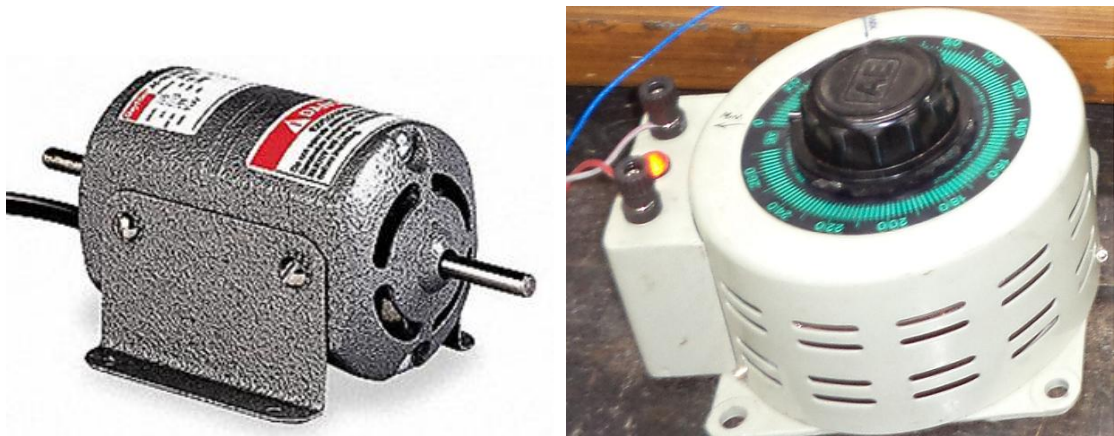


Figure 5.5: (a) DC Motor (b) Speed controller

5.2.3 Flexible coupling

A flexible coupling is also used to connect a DC motor shaft to the specimen rotor shaft. There is a lateral and angular misalignment between the specimen shaft and motor shaft in dynamic condition. These coupling reduce the effect of misalignment. These are also called dissipative coupling. Neoprene rubber is compressed and press fitted between the two flanges, so this coupling become highly flexible and durable. Figure 5.6 shows the flexible coupling, which are used in experimental test rig.

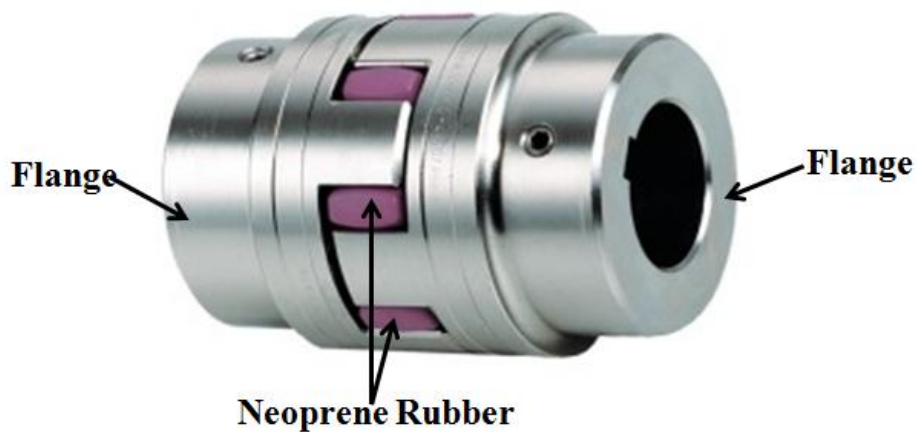


Figure 5.6: Flexible coupling

5.2.4 Self aligned bearing

In the development of an experimental test rig, the bearing selection is also very important part. Moreover, due to lateral displacement of the shaft, alignment of shaft and high variational speed is a measure issue. In order to balance misalignment, self aligning ball bearings are selected as shown in Figure 5.7. The standard specification of bearings is 1204 K C3 NTN. Bearings are fixed on the frame at respective block with proper nut-bolt and washer. Main functions of bearings are to provide a relative motion to the specimen shaft with respect to the frame and to take care of misalignment introduced if any, due to the lateral deflection of the shaft. Moreover, it provides a good running condition without increasing the temperature at high speeds.



Figure 5.7: Self aligned bearing

5.2.5 Acceleration sensor & tachometer

In this experimental test rig, an acceleration sensor (accelerometer) has been used to capture the signal. Sensor was fixed at bearing housing in dynamic analysis and at different position of the test specimen in static analysis. Figure 5.8 is showing acceleration sensor, which is used in experimental test rig. The specifications of accelerometer are also presented in Table 5.3.



Figure 5.8: Acceleration sensor

Table 5.3: Accelerometer specification

Transducer Type	Acceleration Sensor
Unit/ Magnitude	Acceleration (m/s^2)
Identifier	PCB-78534
Model	356A16
Coupling	ICP
Sensitivity	1×10^{-2} V/g or $\text{V}/(\text{m/s}^2)$

The analysis of an instantaneous angular speed inside each shaft rotation provides essential information. The common way to measure such instantaneous velocity is to install a black and white stripe or disk on the shaft as well as an accurate tachometer. The TAC-O02, an interference-free and non-contact high speed optical fiber sensor providing

up to 50000 rpm/sec from an optical fiber probe is the perfect tool for such measurement. Figure 5.9 is showing an tachometer sensor, which are used in dynamic experimental analysis. The specification of tachometer is shown in Table 5.4.



Figure 5.9: Tachometer sensor

Table 5.4: Tachometer specification

Operating distance	61 cm and 45° offset from target
Speed range	1 – 50,000 RPM
Operating temperature	-13° to 257° F (-25° to 125° C)
Power input	6 – 24 Vdc, 40 mA
Output Signal	TTL same as source
Standard Cable	7.6 m
Dimensions	73 X 16 mm

5.3 Signal acquisition and display system

A perfect measurement and proper conditioning of signal data are essential to execute the experiment successfully. OR36/OR38 is designed for high channel count capacity without comprising the analyzer geographies. All channels are handled in real-time whatever the analysis mode: FFT, 1/3rd Octave, CPB or synchronous order analysis. OR36 and OR38 keep these real-time capabilities up to 20 kHz. There are blue LCD screen controls on the OR36 and OR38 hardware that allow you to run, stop the analyzer and change the fan speed etc.

The type of use of universal inputs is selectable by NVGate® software during the analyzer operations. NVGate® software provides a comprehensive set of tools for noise and vibration acquisition, recording and analysis. The universal inputs gather dynamic as well as parametric input in the same connector. For each input connector, a green LED indicates that the input is active and a red LED indicates that the input is overloaded. Front panel of OR36 is shown in Figure 5.10.

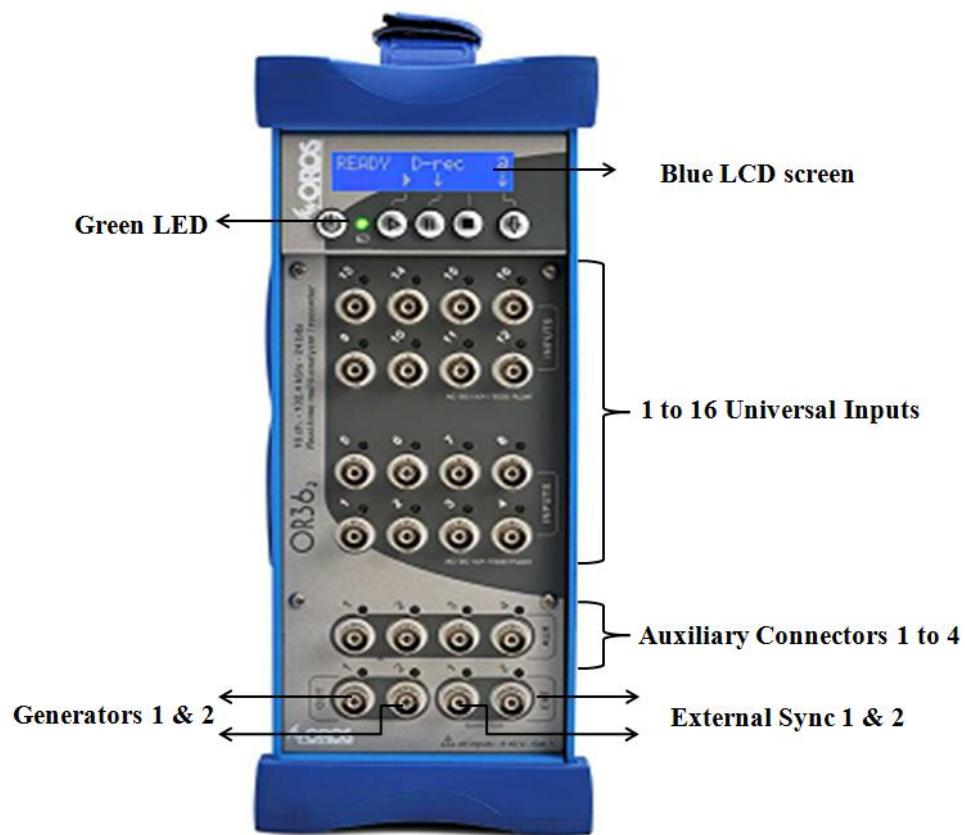


Figure 5.10: Front panel of OR36

With the universal input and the connection kit, OR36 can receive signal conditioning modulus called XPod. The XPod is a device that can be fixed on OR36 side, which is associated to a block of 8 inputs. The XPod line starts with a bridge signal conditioning for strain gauges, dynamic force, and pressure and acceleration measurements. Back

panel of OR36 is shown in Figure 5.11. Back panel consists the various components like ethernet connector, data emission / reception LED, connection PC/OR36, auxiliary DB9 connector, interface connector and DC power connector.

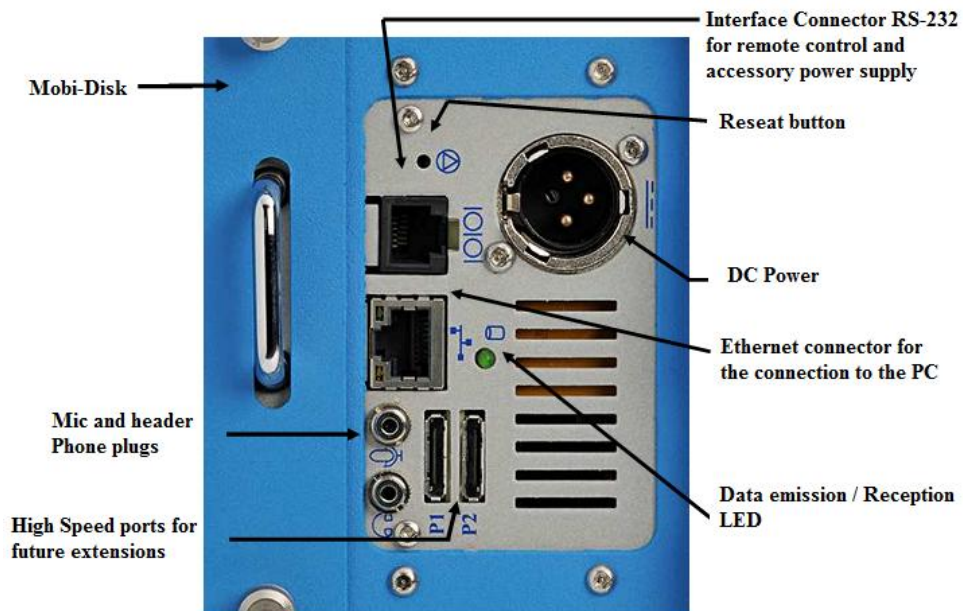


Figure 5.11: Back panel of OR36

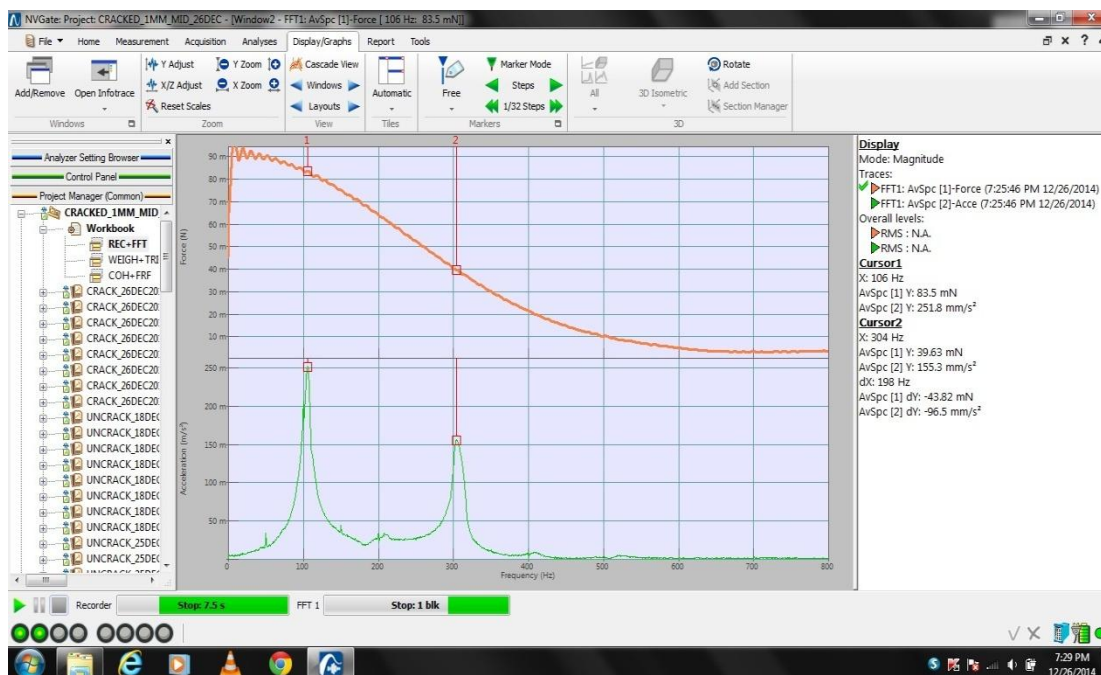


Figure 5.12: Display of signal

Personal computer/laptop may be easily used for online display and store the experimental data for post analysis. In Figure 5.12, laptop screen shows the display during the signal receiving with the help of NVGate® software and OR36. The next section will present details of experimental set-up for stiffness measurement.

5.4 Experimental setup for stiffness measurement

Stiffness plays a vital role in any structure's dynamic behaviour. Dynamic behaviour of any rotating shaft regularly changes with the stiffness variation. When any small defects or cracks initiate and propagate in rotating shaft due to breathing phenomenon, stiffness of the shaft varies with time in every revolution. It is necessary to determine the stiffness at different crack depths for experimental analysis of a cracked rotor.

Figure 5.13 is showing a block diagram of an experimental setup, which was build up to measure the static deflection under gradually applied known load. By using of following mathematical relationship between deflection and known load, one may easily determine the stiffness of the specimen with different cracks at different position.

$$k = P / x \quad (5.1)$$

where k is stiffness in N/mm, P is applied load in N , and x is deflection of shaft at the mid span in mm.

In this simple test rig, major components are vertical column with semi circular ring, base plate, dial gauge stand with magnetic base, dial gauge, load holding device and various load. Vertical columns are made of a cast iron. Height of columns is kept 800 mm and the cross section of the column is 50 mm X 50 mm. Rings are welded on the top of the column to hold the specimen. In the bottom of columns, a base plate was

welded having the cross section 100 mm X 100 mm and thickness 10 mm. This plate provided the vertical stability to the column. An arrangement has been made to carry the weights (N), which are applied on the shaft. A weight holding device is also formed from a rod of diameter 10 mm and length 250 mm, which was used in this experiment. One end of holding device was given round shape so that it can be hanged on test specimen. Another end of this rod was welded with a 2 mm thick circular plate on which different weights can be placed.

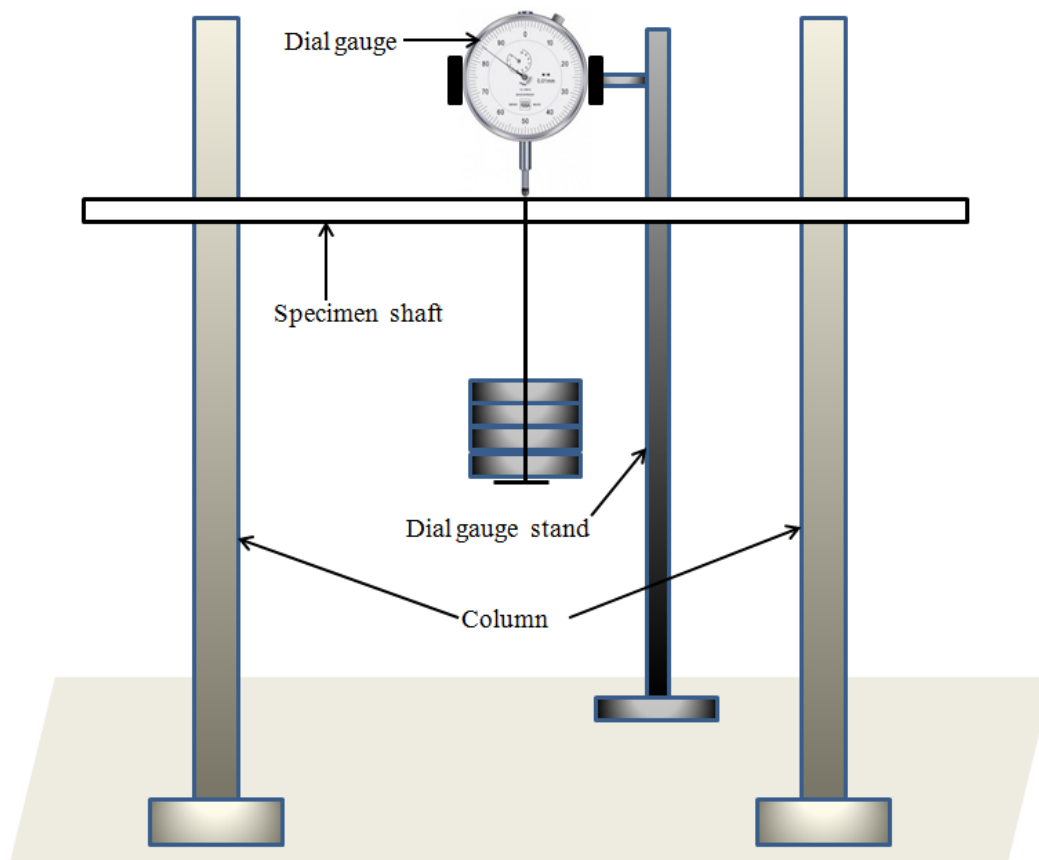


Figure 5.13: Schematic diagram of experimental set-up of stiffness measurement

Digital dial gauge is used to measure the deflection (x) of specimen under the applied load. This dial gauge can measure the deflection from 0.01mm to 13.5mm. The known weights are used to apply the force on the shaft.

5.5 Experimental methodology

5.5.1 Formation of crack in the test specimen

Creating an artificial transverse crack is one of the most challenging tasks in this present study. It is a well-known fact that fatigue cracks could be initiated at the point, which has minimum local strength and maximum local stress. As reported in the research literature, transverse crack (*Adeswusi and Bedoor, 2001; Sawicki et al., 2009*) was created artificially in the workshop. Cracks were created in shaft by using a very fine jewel saw. Initially the dimension of crack was considered 1mm depth and width 0.2mm. Therefore, a single crack has a range of depth between 0 to 23% (5mm) of the diameter. Moreover, the following crack depths were considered for analysis: 4.54% (1mm), 9.09% (2mm), 13.64% (3mm), 18.18% (4mm) and 22.73% (5mm). First crack was formed at the centre of the two bearing support. The second crack was created between the first crack and the right bearing support. Crack location of first and second crack from the right bearing support is 330 mm and 165 mm respectively. Schematic diagram of a single cracked and multi cracked test specimen is shown in Figure 5.4.

5.5.2 Stiffness evaluation

Stiffness of the intact shaft and single cracked shaft has been determined on experimental set up as shown in Figure 5.13. The specimen was positioned in circular ring fitted at top of the both column. The dial gauge and load holding device was also fitted as per schematic diagram as shown in Figure 5.13. Initially, the dial gauge indicator was showing zero, which depicts that there was no deflection in the test specimen. Subsequently, loads are gradually placed on holding device and the deflection of the shaft was recorded by a digital dial gauge. By using the Eq. (5.1),

stiffness may be effectively calculated. Similarly, at different crack depth of a single and multi crack, the stiffness measured and change in stiffness were evaluated. Variation of stiffness with respect to crack depth is shown in Table 5.5.

In this studies and in archival literature also, it is point out that no significant change observe in stiffness, when shafts having a very small cracks. In second part of this experiment, stiffness of shaft was measured at different angular position of transverse crack with respect to initial position. In this experiment, the circumference of the shaft has been divided into 12 sections, each making 30° angle at the center of the shaft cross section. One may got thirteen values for one crack depth at different rotation angle, which are shown in Figure 5.18. Figure 5.14 is showing the cross sectional view of rotating angle between crack and the loading axis.

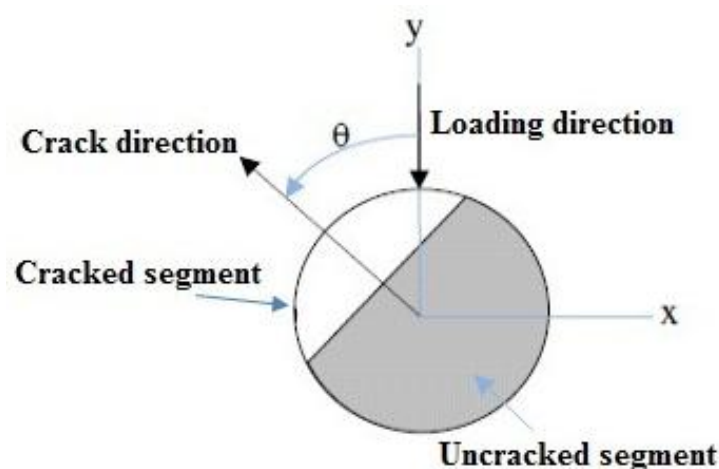


Figure 5.14: Cross sectional view of rotating angle between crack and loading direction

5.5.3 Dynamic analysis of multi-cracked rotor

The amplitude of rotational shaft at various rotational speeds/excitation frequencies and at various single/multi crack depth were determined experimentally. Figure 5.1 shows the actual picture of the experimental test rig. For cooling the DC motor and bearings

lubrication is incorporated before the start the experiment. The shaft is being rotated at various speeds in the range 1200-5500 rpm, which is used for dynamic investigation. The signal is transformed through signal analyzer, which is further analyzed through NVGate® software. It has been found from literature that probes are generally placed near the bearing or over the bearing for analysing shaft behaviour (*Zhou et al., 2005*). The accelerometer is attached on the top of bearing for capturing a signal, which is further transmitted to display monitor. The amplitudes of the vibration of intact and crack shaft at various excitation frequencies have been recorded in the range of 1000 – 5500 rpm with the interval of 100 rpm.

Further, an impact hammer test has also been conducted to find out the static natural frequencies. This test was performed through equipment OR36 (maximum range 20 KHz) integrated with compact real time multi-analyzer. A single accelerometer is used, which was mounted at the mid of the shaft. Experiments have been conducted on the un-cracked, single-cracked and multi-cracked shafts. Each specimen is hit by the hammer (with ICP coupling) at the centre of the shaft to create a force and vibration, which is further captured by OROS hammer and accelerometer respectively. For each shaft the input force, trigger levels and the accelerometer response had to be calibrated in the NVGate ® analyzer project for measurement and analysis.

Initially, the crack depth at which the amplitude of vibration was considered has a range of depths between 0 to 23% (5mm) of diameter and width 0.2mm. Moreover, the following crack depths were considered for analysis: 4.54% (1mm), 9.09% (2mm), 13.64% (3mm), 18.18% (4mm) and 22.73% (5mm). First crack was formed at the centre of the two bearing support. The arrangement of second transverse crack is shown

in Figure 5.4. In this case, depth varies in the range 0 to 13.64% (3mm) of diameter. Further, the following crack depths were considered for analysis: 4.54% (1mm), 9.09% (2mm), and 13.64% (3mm). This crack is generated at a distance of 165 mm from the middle crack. Stiffness of the double cracked shaft has been evaluated through experiments and further used in analytical formulation of amplitude equation.

5.6 Results and discussions

Dynamic and static analysis was performed successfully on both the experimental test rig shown in Figure 5.1 and 5.13. The effect of crack initiation and propagation has been examined taken into account various input parameters like stiffness, amplitude, natural frequency etc. The next subsection will present variation in stiffness due to crack initiation and propagation.

5.6.1 Variation in shaft stiffness

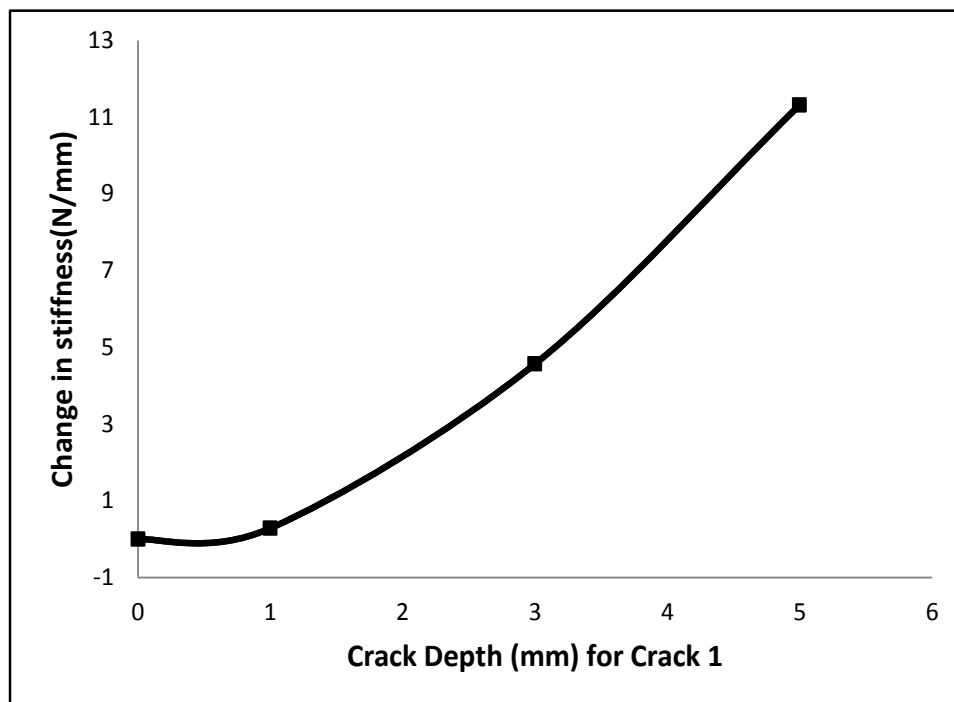


Figure 5.15: Variation in stiffness with the single crack depth

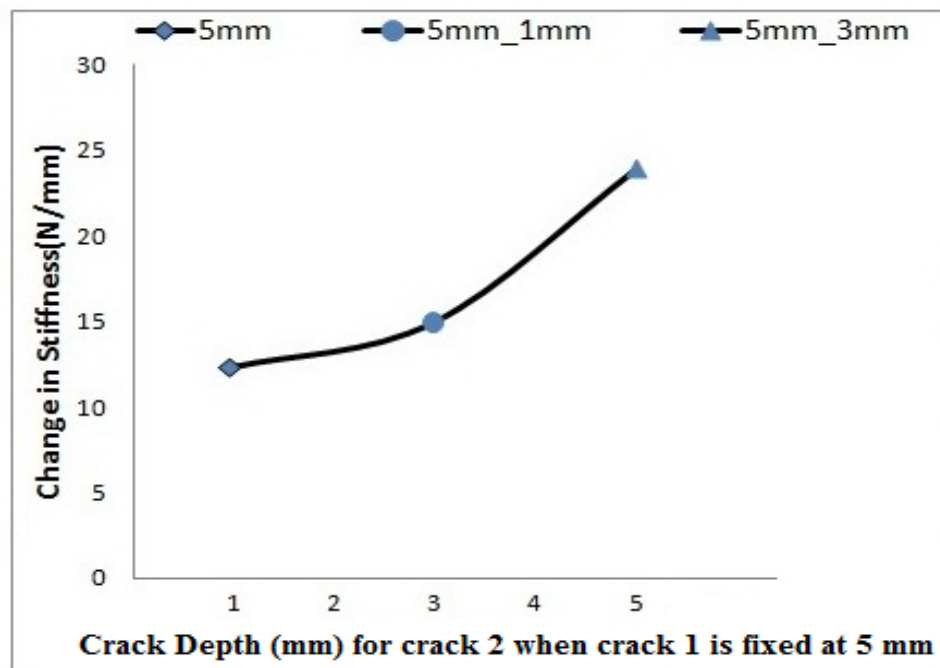


Figure 5.16: Variation in stiffness with the multi crack depth (when crack 1 depth is fixed at 5 mm)

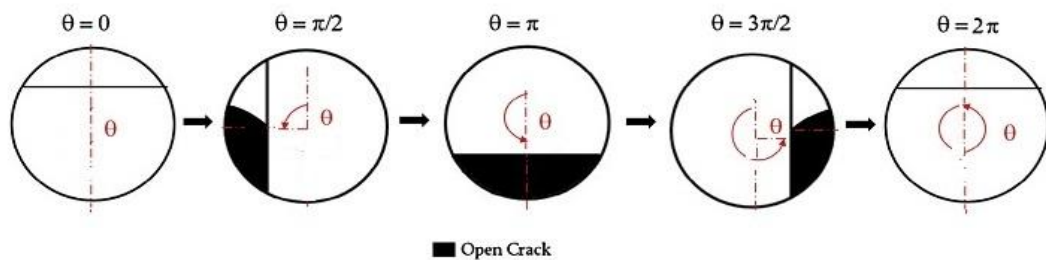


Figure 5.17: Some of the angular positions of the crack during one rotation of the shaft

In the static experimental analysis on stiffness test rig, the change in stiffness of specimen is determined at various crack depth, which is tabulated in Table 5.5. Figure 5.15 shows the variation in stiffness with a single crack depth variation. It shows that the stiffness variation increases with increase in crack depth. Figure 5.16 shows the variation in stiffness due to second crack.

In case of multi crack shaft, slope of the stiffness curve decreases due to second crack as compare to single crack shaft. Thus, increase in the stress concentration is marginal near the first (middle) crack as compare to the middle crack depth.

Table 5.5: Change in stiffness in various crack depth

Crack Depth (mm)		Change in stiffness (N/mm)
Crack 1 (at mid of specimen)	Crack 2 (Between crack1 and Right hand side bearing)	
0	0	0
1	0	0.28432
3	0	4.566739
5	0	11.31678
5	1	15.5739
5	3	25.97405

In other experiment, stiffness of four different circular shafts was measured as a function of rotation of the shafts and presented in Table 5.6. Different positions of rotating cracked shaft are shown in Figure 5.17. For various crack depths, the slope of the curve decreased as the shaft rotated from fully closed (0° and 360°) to partially closed (90° and 270°) to fully open (180°), which is termed as breathing phenomenon.

Table 5.6: Stiffness of shaft as a function of rotation angle

Angle (Degree)	Intact shaft stiffness (N/mm)	5 mm single cracked shaft stiffness (N/mm)	5 mm & 1 mm multi -cracked shaft stiffness (N/mm)	5 mm & 3 mm multi-cracked shaft stiffness (N/mm)
0	288.74	280.61	276.06	269.64
30	287.85	279.70	274.48	268.04
60	287.61	278.86	273.49	266.53
90	287.56	278.28	272.10	265.03
120	287.34	277.18	272.10	264.03
150	285.86	275.84	270.82	263.07
180	285.03	273.91	269.47	259.06
210	285.86	275.84	270.82	263.07
240	287.34	277.19	272.10	264.03
270	287.56	278.28	272.10	265.03
300	287.61	278.86	273.49	266.53
330	287.85	279.70	274.48	268.03
360	288.75	280.61	276.03	269.64

It is observed from Table 5.6 and Figure 5.18 that for any un-cracked shaft, the stiffness remain unchanged. There is no effect of angular orientation on stiffness. Slight fluctuation observed due to experimental and random errors. Whenever, crack depths increases, stiffness decreases. Slope of the curve decreased as the crack rotated gradually from fully closed, partially open to the fully open position. After creating the second crack, stiffness further reduces but the effect of second crack on the stiffness is found marginal. Stress concentration for the shaft is marginally affected at the middle of the crack. It has been observed that larger crack depth has more dominant effect on the shaft. Crack at the mid of the rotor shaft has optimum effect on the stiffness as compared to the second crack, created at any other position of the shaft. Position of crack plays a significant parameter in multi-crack rotor detection. These values of variation in stiffness obtained experimentally are further used in amplitude equation, which has been obtained analytically through extended Lagrangian–Hamiltonian formalism discussed in previous chapter.

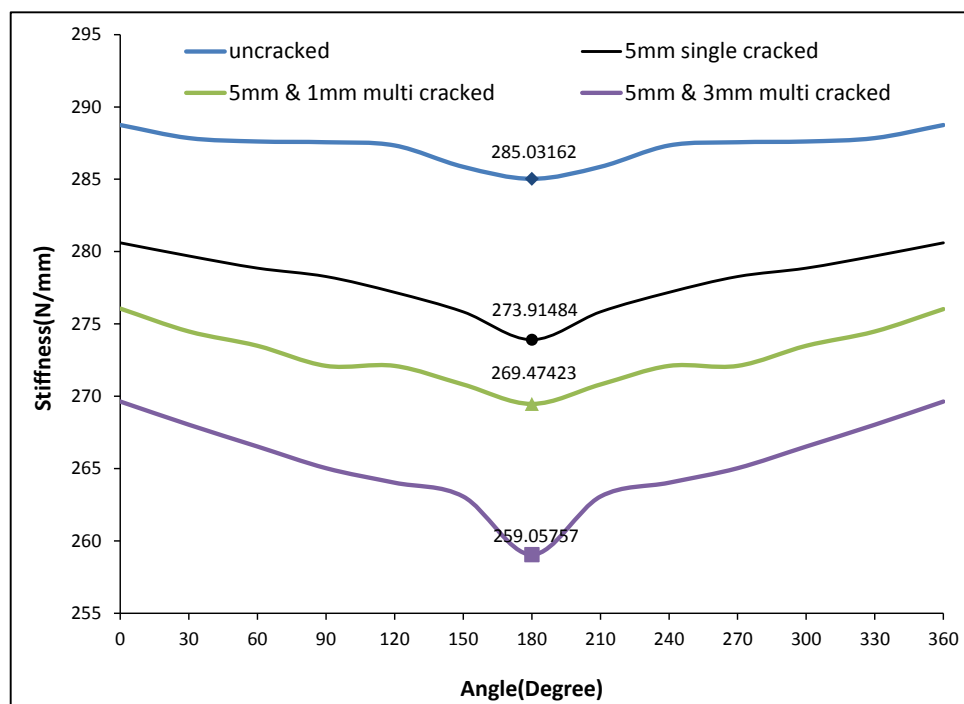


Figure 5.18: Stiffness of cracked rotor at different angular orientation

The natural frequencies at various crack depth have also been presented in Figure 5.19 – 5.21. For a single crack, natural frequency of the shaft decreases rapidly, which is clearly observed in Figure 5.19.

In case of multi-crack, the changes in natural frequency are marginally noticed in Figure 5.20. First natural frequency obtains to be 114.5 Hz for intact shaft and 96.5 Hz for 1mm cracked shaft, 86.5 Hz for 3 mm cracked shaft, 85Hz for 5 mm cracked shaft. In Figure 5.20, natural frequency obtains comes out to be 84.5Hz for a multi-cracked shaft (5 mm and 1 mm crack) and 83.5 Hz for second case of a multi-cracked shaft (5 mm and 3 mm crack). The next sub section will present the comparison between analytical and experimental amplitude.

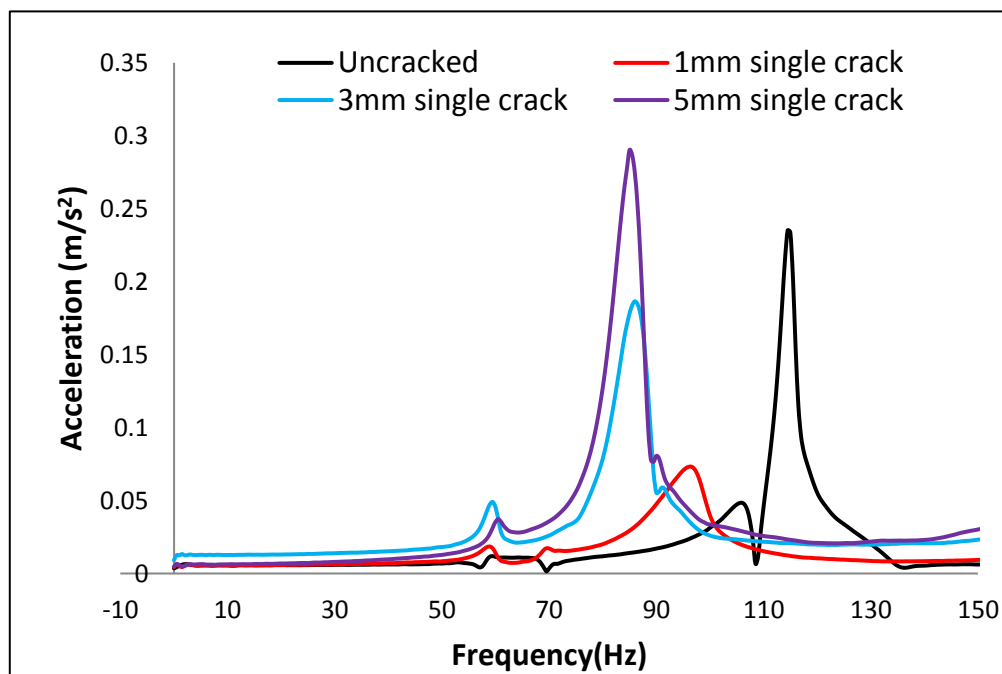


Figure 5.19: Frequency Vs acceleration for un-cracked shaft and single cracked shaft

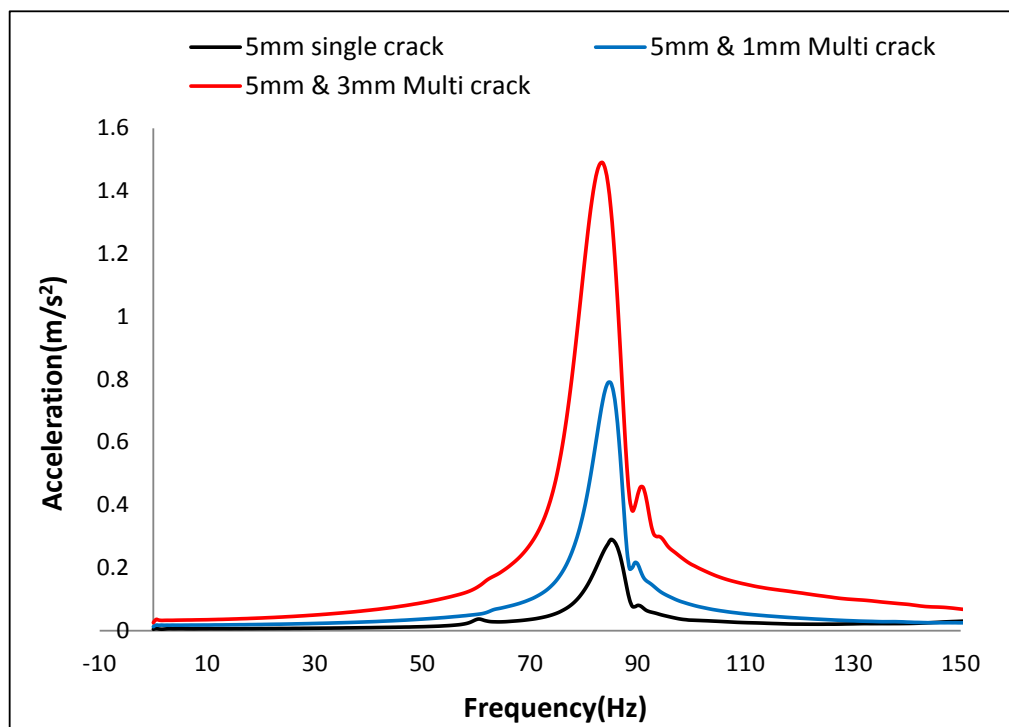


Figure 5.20: Frequency Vs acceleration for multi-cracked shaft.

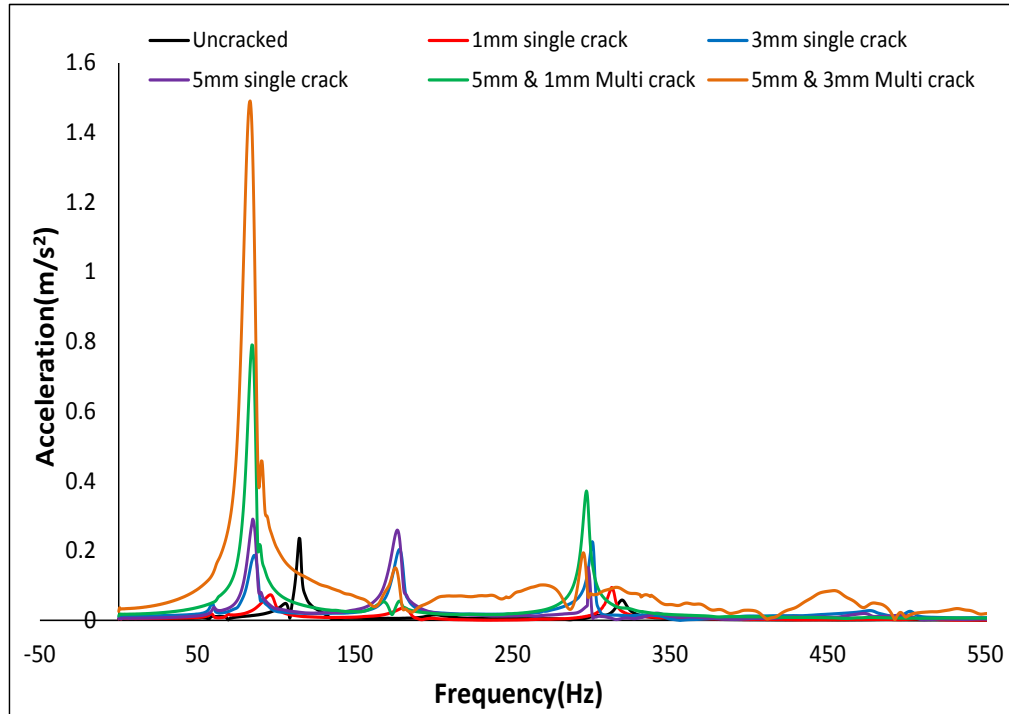


Figure 5.21: Frequency Vs acceleration for intact shaft, single cracked shaft & multi-cracked shaft various mode.

5.6.2 Comparison between analytical and experimental amplitude

Amplitudes of vibration of different cracked shaft specimen are presented in Figure 5.22. The amplitude of vibration in cracked rotor increases with increase in crack depth. In this way increase in amplitude can be quick and reliable indicator of crack propagation. Resonance condition may also become a cause of catastrophic failure due to this crack propagation. Considerable good agreement between analytical and experimental results has been stated. Complete dynamic analysis is carried out through extended Lagrangian methodology for a continuous system. It has also been focused on the effect of stress concentration factor. Amplitude further decreases when second crack is appeared, which is basically due to stress concentration. It is further shown that amplitude of the rotor increases inversely with the stiffness of the rotor.

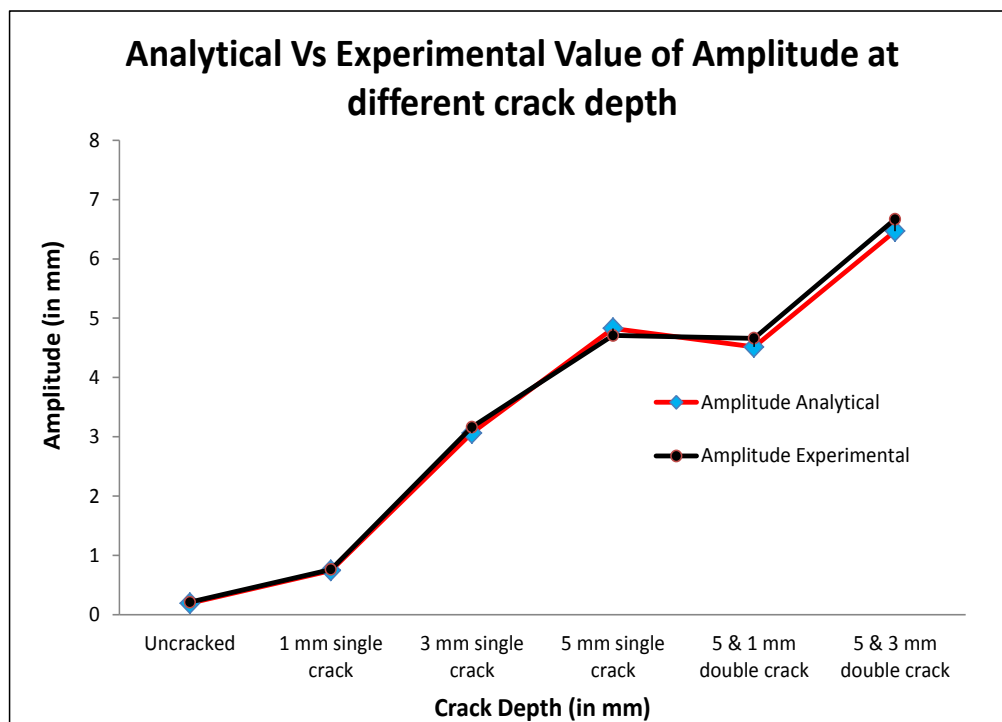


Figure 5.22: Analytical Vs experimental value of amplitude at different crack depth

Experimental test rig presented in this chapter is capable to analyze the dynamic behaviour of a cracked rotor to validate the theoretical and computational result to a large range. However, there are some deviations in analytical and experimental results because of some limitations and random error. In specimen, presented crack is not a fatigue crack. Transverse crack is created manually. A separate system is required to create fatigue crack. There may be some error in signal adopting process as accelerometer has been placed at bearing housing. Some environmental noise also affects the results up to a certain limit. DC motor also shows jumping phenomenon so one may have to leave some signal data. The next subsection will present the impact hammer test which is used for validation of natural frequency of static condition,

5.6.3 Validation of natural frequency through impact hammer test

The natural frequency of a system is dependent only on the stiffness of the structure and the mass, which participates with the structure (including self-weight). When structure temporarily excited by an external load, it will vibrate at natural frequency. When external excitation applied to the structure at the same frequency as the structure's natural frequency, it will result in resonance. Resonance can be dangerous for the structure. So, the natural frequency of a structure / machinery may be determined by measuring frequency response signal. A moving hammer impact test using a single static motion transducer is a mutual example of single reference testing. An impact hammer with a load cell attached to its head to measure the input force. An accelerometer to measure the response acceleration at a fixed point and direction. Here, one may determined the natural frequency for a simply supported beam to make sure that the results, one find through computational analysis are correct or not, also to check variation from analytical results. Different observations have been taken at different

frequency band, using different tip of hammer by hitting at different location on the component. This experimental analysis is carried out for frequency of 800 Hz, 16 KHz, 32 KHz with different tips of hammer like rubber tip, plastic tip and metallic tip. An accelerometer is mounted on the shaft at different location. In Figure 5.23, accelerometer is mounted in mid span of the shaft. Experimental setup of impact hammer test is shown in Figure 5.23. Accelerometer and vibration analyzer are used to measure the response signal created by external source impact hammer.

The natural frequency response for intact shaft with 5 mm single crack and multi crack with 5 mm and 3 mm crack shaft 1 received by NVGate® software as shown in Figures 5.24 – 5.29. The value of natural frequency obtained is 114.5 Hz for intact shaft as shown in Figure 5.24. In another experiment, the value of natural frequency is obtained at 85 Hz for a single cracked shaft with 5 mm crack as shown in Figure 5.26.

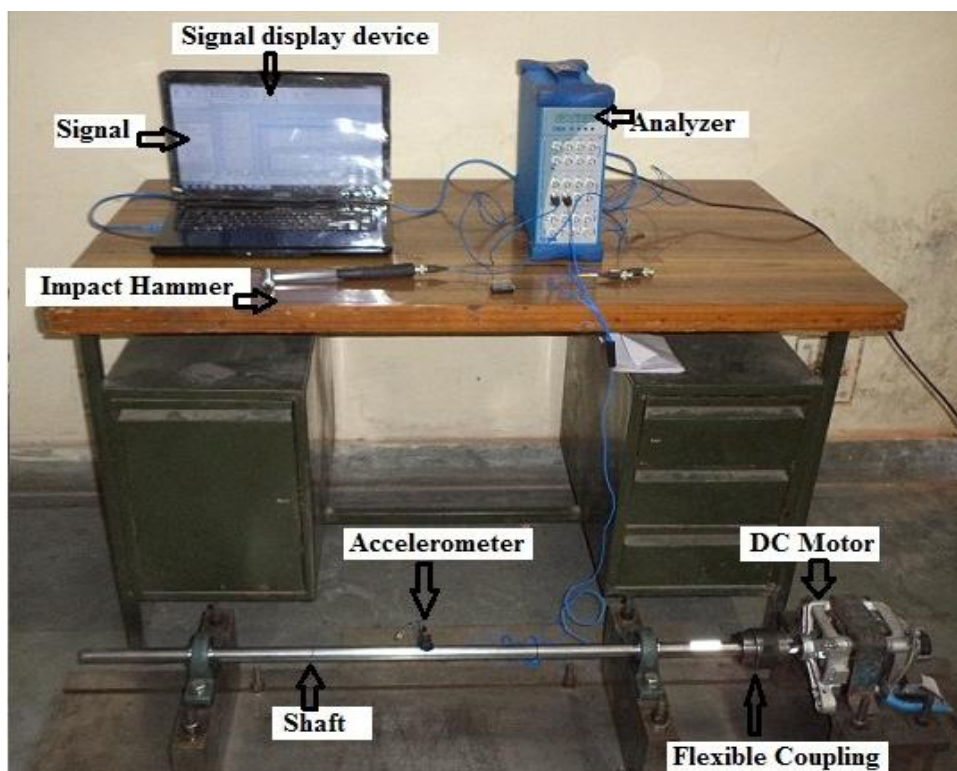


Figure 5.23: Experimental set-up for impact hammer test

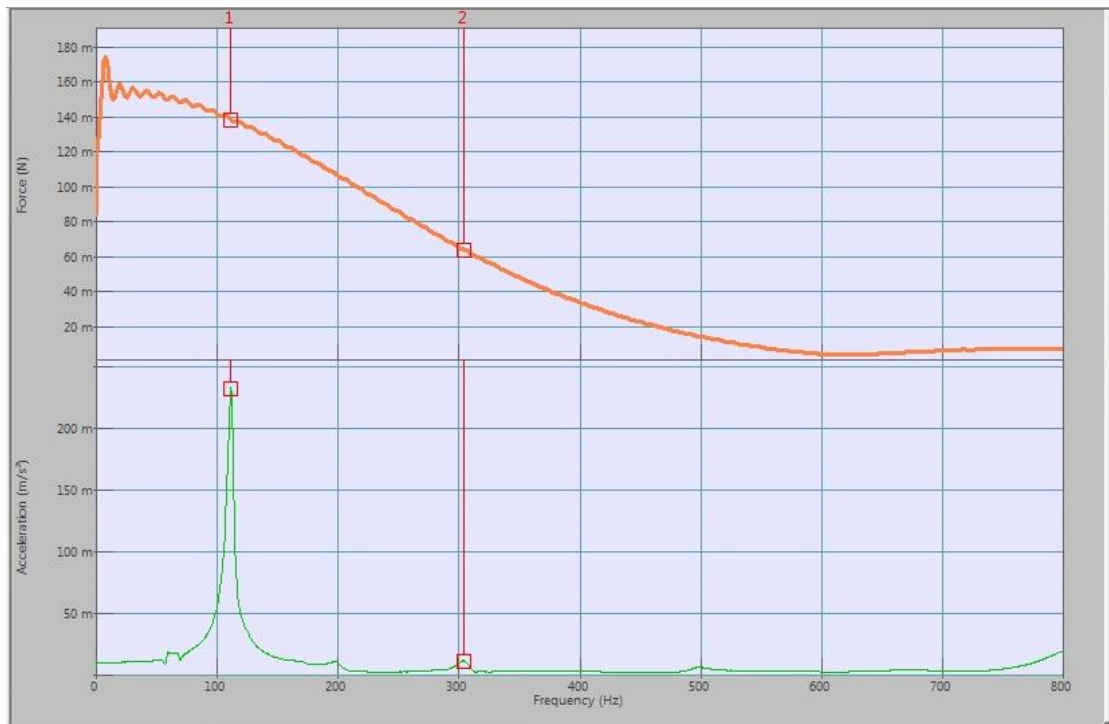


Figure 5.24: Frequency Vs acceleration and frequency Vs forces for intact shaft (FFT analysis)

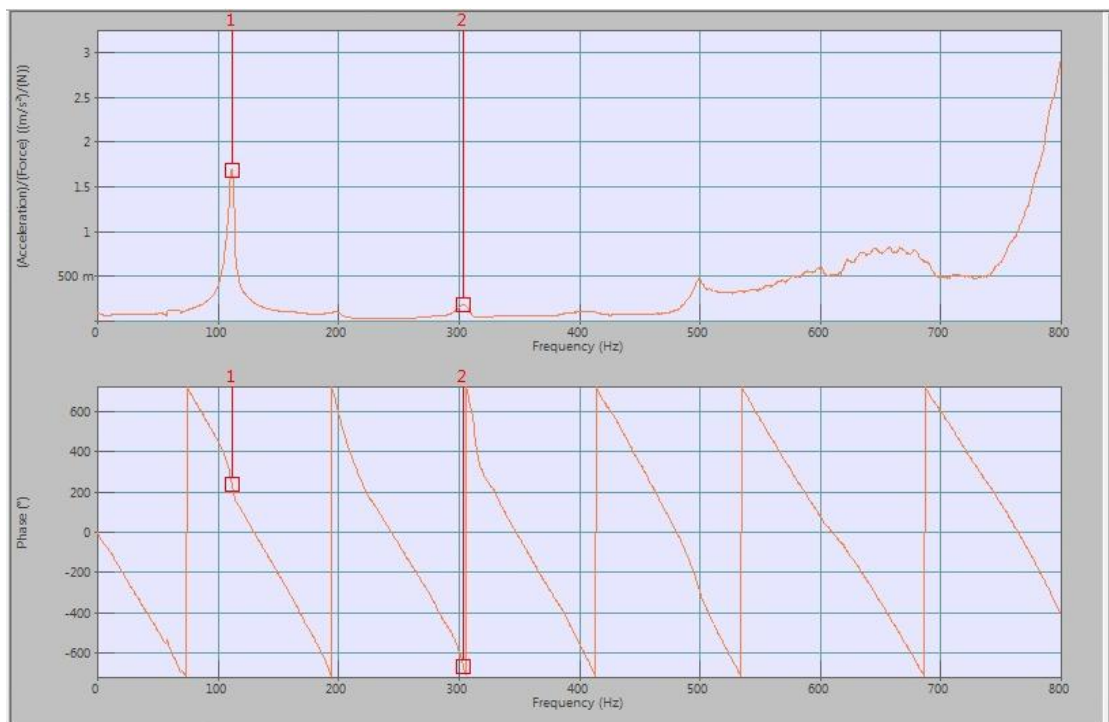


Figure 5.25: Frequency Vs phase change and frequency Vs (acceleration/force) for intact shaft

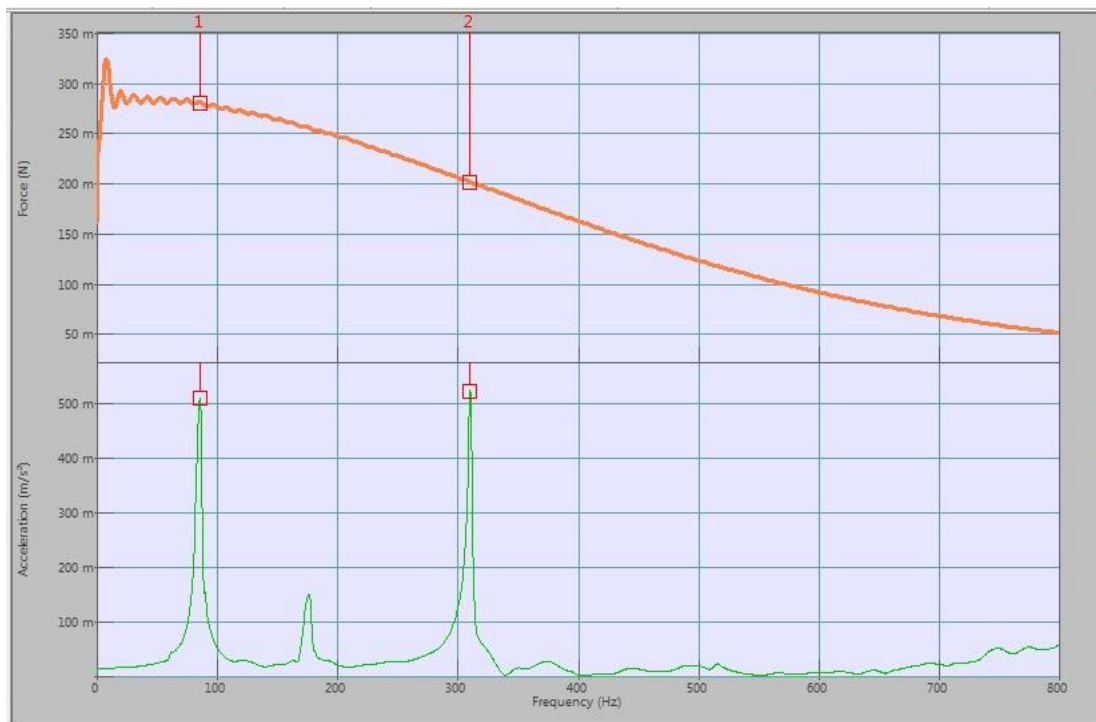


Figure 5.26: Frequency Vs acceleration and frequency Vs forces for 5 mm single crack shaft (FFT analysis)

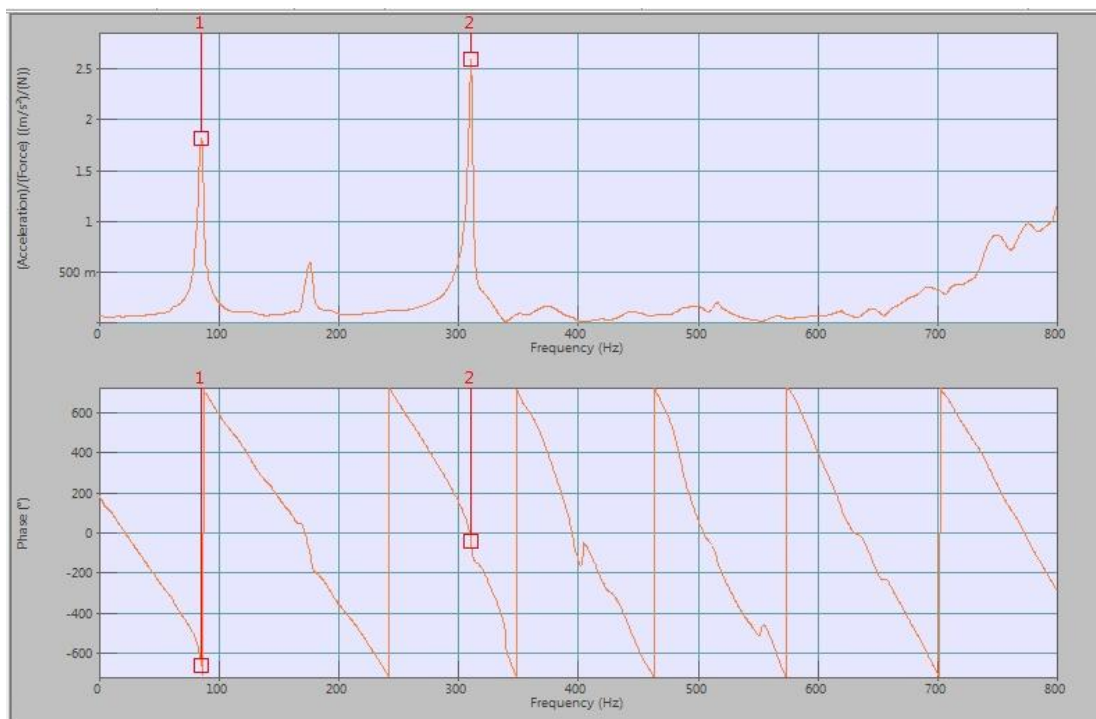


Figure 5.27: Frequency Vs phase change and frequency Vs (acceleration/force) for 5 mm single crack shaft

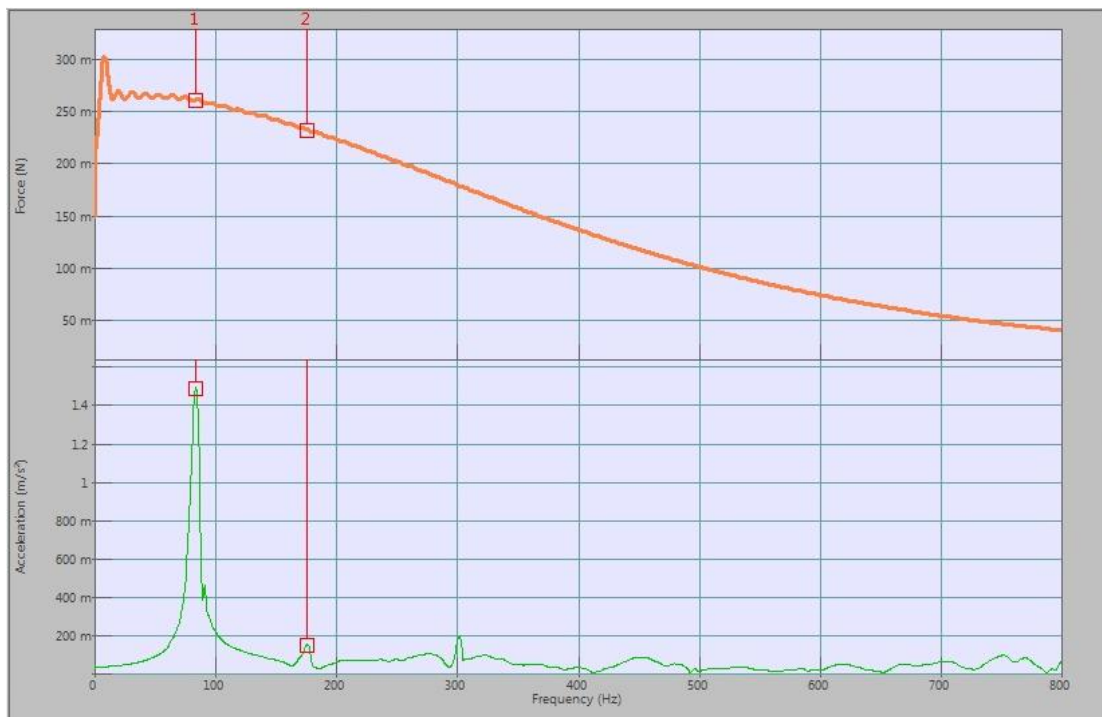


Figure 5.28: Frequency Vs acceleration and frequency Vs forces for a multi-crack shaft of 5 mm and 3 mm crack (FFT analysis)

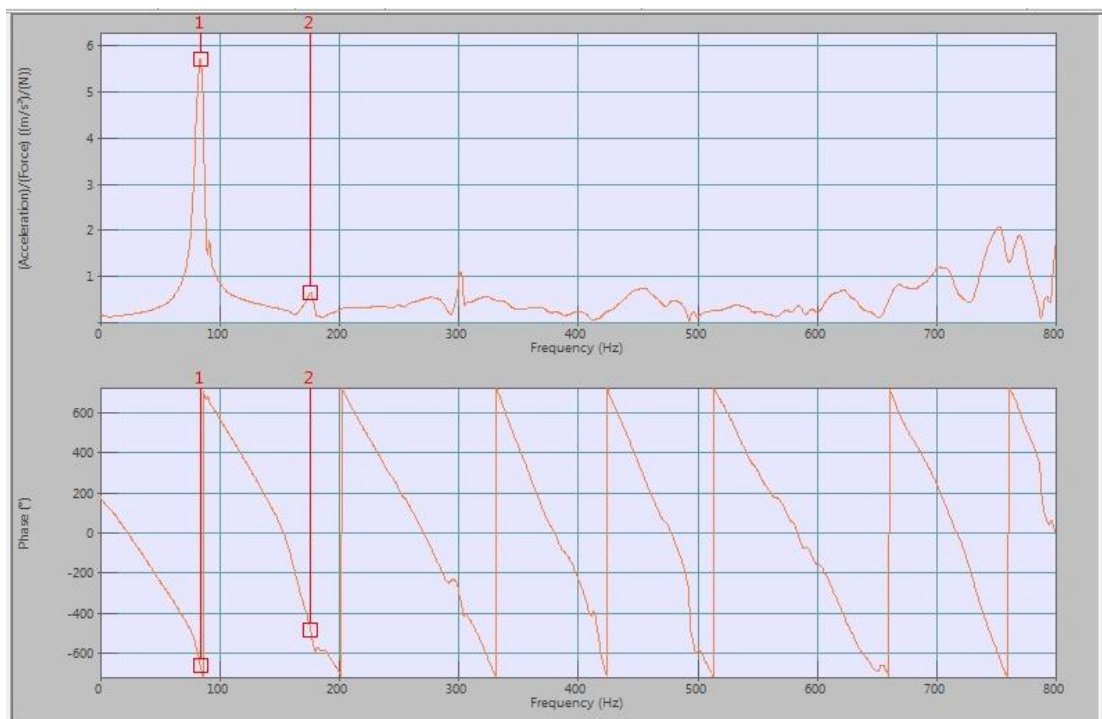


Figure 5.29: Frequency Vs phase change and frequency Vs (acceleration/force) for a multi-crack shaft of 5 mm and 3 mm crack

Table 5.7: Comparison of natural frequencies

Test specimen	Natural frequency (Hz) (Through analytical analysis)	Natural frequency (Hz) (Through impact hammer test)
Intact Shaft	119.36	114.50
Single-cracked shaft with 5 mm single crack	89.43	85
Multi-cracked shaft with 5 mm and 3 mm single crack	86.58	83.50

The value of natural frequency was 83.5 Hz for multi cracked shaft with 5 & 3 mm crack as shown in Figure 5.28. Natural frequency of analytical and impact hammer test were compared and the results are presented in Table 5.7. It may be shown that there is a marginal gap in natural frequency values between both cases. The possible reasons may be transients presents and the parametric value of various components of the system. However it is under 4% variation, which is a good agreement between the experimental and analytical studies carried out in this work. In Figures 5.24 – 5.29 various modes of natural frequencies are clearly depicted. Natural frequencies are also varying with the change in crack depth and types of test specimen like intact, single-crack and multi-crack shaft.

5.7 Summary of the chapter

The major focus of this chapter is to design and development of an experimental test rig for the dynamic analysis of a multi cracked rotor. In experimental static analysis, stiffness and its variation has been determined for various test specimen like single and multi cracked rotor shaft. The effect of crack depth variations have been analyzed on various parameters like natural frequency, stiffness and amplitude of the vibration.

Breathing phenomenon has also been validated experimentally. The stiffness has changed due to the rotation of the shaft. Stiffness is varying between two values regularly due to the breathing of a crack in the rotation process. It is also experimentally validated that the stiffness is also a function of an angular rotation. Besides this, the amplitude of vibration of rotor at different crack depth has also been determined. The experimental analysis has been employed for the validation of theoretical results of rotor system presented in the previous chapter.

It has been seen through the results that the experimental frame work developed in this chapter has capability to analyze the dynamic behaviour of a multi-cracked rotor accurately, efficiently and effectively. This experimental test rig model may further be applied as on line monitoring system. The experimental test rig model may be effectively used for the fault diagnosis of a rotor dynamic system in the various industries like power plant, aircraft and heavy rotating machinery.

Conclusions and Future Directions

6.1 Conclusions

This research work has a crucial impact on the sustainability of rotating machinery. The approaches that have been presented in this study is an application of the extended form of the Lagrangian mechanism. The main objective and motivation for this work was to develop an extended form of the Lagrangian-Hamiltonian formalism and the Noether's theorem. Further, these extended formulations were applied to multi-cracked, discrete and continuous rotor system. This work had augmented the scope of umbra-Lagrangian in the field of rotor dynamic research. Effective outcomes were obtained from the umbra-Lagrangian theory, while studying invariants of motion for non-conservative mechanical and thermo-mechanical systems, which have time fluctuating parameters, gyroscopic forces and non-holonomic constraints. The dynamic response signal of asymmetric rotor has been received and captured by NVGate® software.

Further, these outcomes have been investigated through umbra-Lagrangian-Hamiltonian equations. The main causes of these asymmetries are initiation and propagation of cracks and variation in rotor mass. In the analysis of asymmetries concept of cyclic symmetries has been efficiently used to uncover the dynamics of multi-cracked rotor. This may be used to diagnose the defects online in various industrial applications. Further, extended form of Noether's theorem has been used to obtain constants of motion of dynamical system. An experimental test rig is also developed for the experimental validation of obtained simulation and analytical results. Based on research work, some conclusions have been made.

- A novel approach of umbra-Lagrangian and umbra-Hamiltonian has been applied to analyze the dynamic behaviour of multi-cracked rotor.
- Umbra-Hamiltonian has been used with the extended form of Noether's theorem to provide the complete insight of dynamics of the system with asymmetries due to crack depth and rotor mass variation.
- Expression of amplitude of vibration and natural frequencies were derived through the novel concept of umbra-Lagrangian mechanism.
- Bondgraph software has been used for modeling. Umbra-Lagrangian of the multi-crack system and multi-rotor system were developed through this bondgraph technique.

Analytical and computational framework for discrete rotor with asymmetries has been presented through extended form of Lagrangian-Hamiltonian formulation. Multi-crack rotor has been driven by DC motor. Following points have been concluded through this work:

- Mathematical equations for natural frequency and amplitude of vibrations have been developed by using umbra concept and Noether's equation for both cases such as asymmetries in stiffness as well as in mass.
- In both cases, multi-rotor system has been modeled through bondgraph modeling technique. SYMBOLS-Shakti[®] software has used for the simulation work. These models provide insight of the dynamics of the rotor system. Analytical results are also compared with computational results.
- In first case, the amplitude of the rotor increases with percentage change of stiffness of rotor 1. Analytical frequency nearly matches with the simulated

frequency obtained for rotor 1. A general behaviour of reduction in the natural frequencies is noticed at various stiffness variations.

- In second case, effects of asymmetries due to mass have been investigated. All the analytical results have been validated through simulated results. It has been found that there was a good agreement between analytical and simulated results.

Further, extended form of Lagrangian-Hamiltonian mechanism has been presented for analytical and computational framework for continuous rotor with two cracks. Following points have been concluded through this work:

- Analytical frame work for a multi-crack rotor has been developed to determine the amplitude as well as natural frequency. Double-crack rotor system has been effectively analyzed through extended form of Lagrangian formalism and Noether's theorem concept.
- Computational framework through bondgraph modeling has been presented. The effects of crack depth on system response are clearly seen through simulation. It is further shown that amplitude of the rotor increases inversely the stiffness of the rotor.
- Results obtained through simulation for uncracked and cracked rotor shaft clearly show the effect of crack on the amplitude of vibration. For small crack depth, there is very small disturbance in system response. However, the response can be clearly noticed, as well as observed when crack depth is more.
- After creating the second crack, stiffness also reduces but the effect of second crack on the stiffness is found marginal. Stress concentration for the shaft is marginally affected at the middle crack. It has been observed that larger crack depth has the more significant effect on the shaft.

- Finally, a crack initiation and propagation has affected the dynamical characteristics of any rotating parts of machinery. So, it is necessary to replace components. Because, it may become a major cause of catastrophic failure due to resonance. In resonance conditions, amplitude has high magnitude value.

6.2 Directions for future research

Extended form of Lagrangian-Hamiltonian mechanism has been applied for the analysis of dynamics of discrete and continuous multi-cracked rotor system. Umbra time concept has been used to develop the various equations of amplitude and natural frequencies. In this thesis, analysis of double-cracked rotor system has been presented.

The methodology of current research can be extended further to meet diverse applications of rotating shaft. Therefore, following suggestions can be focused for future developments:

- Analysis of discrete rotor may be analysed considering torsional rigidity through extended form of Lagrangian formulation. Measurement of torsional rigidity along with bending stiffness of cracked rotor can be done experimentally.
- Rotor with more than two transverse cracks may also be considered for analysis.
- Continuous rotor system with different types cracks like slant, longitudinal and elliptical crack etc. can be further analyzed through the extended Lagrangian formalism and bondgraph modelling.
- This work is further extended for real time project work related to rotordynamics industries like aerospace, power producing plant etc. So one may stop the catastrophic failure and reduce the economical loss and production.
- In future, one may develop high quality test-rig for dynamic analysis of various type of rotor used in different industries and research organization. One may also used tri-axial transducer for capturing the signal in three directions.

Appendix A

Bondgraph Elements

A.1 Introduction

The best way to study the dynamics of a system residing in multi-energy domain is to start with a schematic diagram, which includes its important components and portrays how they are connected together. Then one can show details of each component and specify the constitutive laws governing the components and subsystems they are in. Each energy domain has its own concepts, symbolic notations and equation. However, a basic similarity exists in the common underlying energy structure.

Bond graph is an explicit graphical tool for capturing the common energy structure of systems. It increases one's insight into systems behavior. In the vector form, they give concise description of complex systems. Moreover, the notation of causality provides a tool not only for formulation of system equations, but also for qualitative analysis of system behavior, viz. controllability, observability, fault diagnosis, etc.

In 1960, Paynter (*Paynter, 1961*) gave the revolutionary idea of portraying systems in terms of power bonds, connecting the elements of the physical system to the so called junction structures which were manifestations of the constraints. This power exchange portrait of a system is called **Bond Graph** (some prefer to write as **Bondgraph**), which can be both power and information oriented. Later on, Bondgraph theory has been developed further by many researchers like *Karnopp et al. (1990)*, *Thoma (1990)*, *Brown (1981, 2006)*, *Cellier (1991)*, *Breedveld and Dauphin-Tanguy*

(1992), *Gawthrop and Smith* (1996), *Mukherjee and Karmakar* (2000), etc. who have worked on extending this modeling technique to power hydraulics, mechatronics, general thermodynamic systems and recently to electronics and non-energetic systems like economics and queuing theory.

Through Bondgraph approach, a physical system can be represented by symbols and lines, identifying the power flow paths. The lumped parameter elements of resistance, capacitance and inertance are interconnected in an energy conserving way by bonds and junctions resulting in a network structure. From the pictorial representation of the bondgraph, the derivation of system equations is so systematic that it can be algorithmized. The whole procedure of modeling and simulation of the system may be performed by some of the existing software e.g., **ENPORT**, **Camp-G**, **SYMBOLS**, **20Sim**, **Dymola** etc.

The language of bondgraphs aspires to express general class of physical systems through power interactions. The factors of power, i.e., Effort and Flow, have different interpretations in different physical domains. Yet, power can always be used as a generalized co-ordinate to model coupled systems residing in several energy domains. In bondgraphs, one needs to recognize only four groups of basic symbols, i.e., three basic one port passive elements inertance (I), capacitance (C), and resistance (R); two basic active elements source of effort (SE), and source of flow (SF); two basic two port elements gyrator (GY), and transformer (TF); and two basic junctions i.e., constant effort junction (0), and constant flow junction (1). The basic variables are effort (e), flow (f), time integral of effort (P) and the time integral of flow (Q).

Table A.1: Definition of Bond graph Elements with integral causality







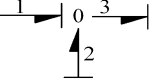
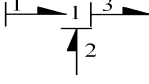
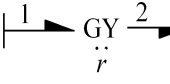
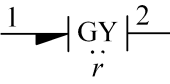
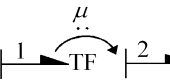
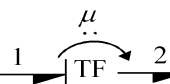



Type	Name	Symbol	Definition	
			Linear	Nonlinear
Storages	Inertance	 I	$e = \frac{dp}{dt}, f = (1/I)P$	$e = \frac{dp}{dt}, f = \phi_F(P)$
	Capacitance	 C	$e = (1/C)Q$ $f = \frac{dQ}{dt}$	$e = \phi_K(Q)$ $f = \frac{dQ}{dt}$
Dissipation	Resistance	 R	$f = e/R$	$f = e/\phi_R$
	Resistance	 R	$e = R * f$	$e = \phi_R * f$
Sources	Effort	 SE	$e = e(t)$	
	Flow	 SF	$f = f(t)$	
Junctions	Zero (0)		$e_1 = e_2 = e_3, f_1 + f_2 = f_3$	
	One (1)		$f_1 = f_2 = f_3, e_1 + e_2 = e_3$	
Transducers (ideal)	Gyrator I		$e_2 = r f_1, e_1 = r f_2$	$e_2 = r(x) f_1$ $e_1 = r(x) f_2$
	Gyrator II		$f_2 = (1/r)e_1$ $f_1 = (1/r)e_2$	$f_2 = [1/r(x)]e_1$ $f_1 = [1/r(x)]e_2$
	Transformer I		$f_2 = \mu f_1, e_1 = \mu e_2$	$f_2 = \mu(x) f_1$ $e_1 = \mu(x) e_2$
	Transformer II		$e_2 = (1/\mu)e_1$ $f_1 = (1/\mu)f_2$	$e_2 = [1/\mu(x)]e_1$ $f_1 = [1/\mu(x)]f_2$
Activated Bond	Effort		$f = 0$	
	Flow		$e = 0$	
Detector	Effort, flow		e_1, f_1	

Table A.1 gives definition of Bondgraph elements with integral causality. In a bondgraph, the assignment of power directions may be as arbitrary as fixing co-ordinate systems in classical analysis. The assignment of bond number also fixes the name of the elements or junctions. This is the best bookkeeping technique adopted by most of the existing software products.

A.2 Causality

Causality establishes the cause and effect relationships between the factors of power. In bondgraphs, the inputs and the outputs are characterized by the causal stroke. The causal stroke indicates the direction in which the effort signal is directed. The end of the bond that does not have a causal stroke is the end towards which the flow signal is directed. The proper causality for a storage element (I or C) is called *Integral Causality*, where the cause is integrated to generate the effect. Sometimes the causal strokes will have to be inverted, which means the constitutive relationship for the corresponding element is written as a differential equation. Genuine differential causality is not commonly encountered during system modeling except in certain cases of modeling mechanisms, robotics, etc., where link flexibilities or other aspects are neglected in the model. The occurrence of *differential causalities* in a system may indicate serious violations of principles of conservation of energy. At a 1 junction, only one bond should bring the information of flow. This uniquely causalled bond at a junction is termed as the *Strong bond*. Similarly at a 0 junction, only one bond can be stroked at the junction side. This strong bond determines the effort at the junction. The *weak bonds* are the bonds other than the strong bond.

A.3 Activation

Some bonds in a bondgraph may be only information carriers. These bonds are not power bonds. Such bonds, where one of the factors of the power is masked are called Activated bonds. For example in a bond representing the velocity pick-up, the information of force must be masked and on the bond representing the exciter the information of the flow must be masked. A full arrow somewhere on the bonds shows that some information is allowed to pass and some information is masked. The information which is allowed to pass may be written near that full arrow. The concept of activation is very significant to depict feedback control systems.

The term activation initially seems a misnomer. However, Paynter's idea was based on the fact that though the information of a factor of power is masked on one end, an activated bond on the other end can impart infinite power which is derived from a tank circuit used for both the measurement or actuation device (for instance, the pick-up, the amplifier and the exciter, all have external power sources).

A.4 Observers

Additional states can be added for measurement of any factor of power on a bondgraph model using the observer storage elements. A flow activated C-element would observe the time integral of flow (and consequently flow), whereas an effort activated I-element would observe the generalized momentum (and consequently effort). Activated elements are perceived as conceptual instrumentation on a model. They do not interfere in the dynamics of the system.

A.5 Multi and vector bondgraphs

When similarities in various sub-system components in the model morphology can be established, they can be represented in form of a concise notation called vector or multi-bondgraphs. Multi bonds are drawn as two parallel lines augmented with power directions. The dimension of the multi-bond (number of scalar bonds, it is composed of) is indicated between these parallel lines. Thus multi-bondgraphs are compact representation of large systems with identical subsystems. Since a multi-bond can accept only one power direction and causal orientation, all the subsystems represented by that multi-bond must have same power and causal structure

Flexibility Co-efficient of an Open Crack

B.1 Flexibility co-efficient

The general flexibility co-efficient of an open crack is presented in this *Appendix*. Initiation and propagation of crack in any element reduces the stiffness of the element. Reduction in stiffness indicates that there is variation in total flexibility in the element. Moreover, when a shaft rotates, its flexibility changes due to breathing phenomena of crack. One can approximate breathing of crack either by sinusoidal stiffness variation or by assuming stepwise stiffness fluctuation. A truly breathing behaviour can be represented by considering gradual opening and closing of the crack using the sign of stress intensity factor.

Dimensionless terms of flexibility matrix $[K_c]$ are given by *Papadopoulos and Dimarogonas* (1987)

$$C_{22} = \frac{C_{22}F_0}{R} = 4 \int_0^{\bar{a}} \int_0^{\bar{b}} \bar{y} F_{III}^2(\bar{h}) d\bar{z} d\bar{y} \quad (\text{B.1})$$

$$C_{33} = \frac{C_{33}F_0}{R} = 4 \int_0^{\bar{a}} \int_0^{\bar{b}} \bar{y} F_{II}^2(\bar{h}) d\bar{z} d\bar{y} \quad (\text{B.2})$$

$$C_{44} = C_{44}F_0R = 32 \int_0^{\bar{a}} \int_0^a z^2 \bar{y} F_I^2(\bar{h}) d\bar{z} d\bar{y} \quad (\text{B.3})$$

$$C_{55} = C_{55}F_0R = 64 \int_0^{\bar{a}} \int_0^a \bar{y} (1 - \bar{z}^2) F_2^2(\bar{h}) d\bar{z} d\bar{y} \quad (\text{B.4})$$

$$C_{45} = \bar{C}_{54} = C_{45} F_0 R = 64 \int_0^{\bar{a}} \int_0^a \bar{z}\bar{y} (1 - \bar{z}^2) F_I^2(\bar{h}) d\bar{z} d\bar{y} \quad (\text{B.5})$$

where $F_0 = \frac{\pi ER^2}{1-\nu^2}$, $\bar{z} = \frac{z}{R}$, $\bar{a} = \frac{a}{R}$, $\bar{y} = \frac{y}{R}$, $\bar{b} = \frac{b}{R}$, $\bar{h} = h/R$ and

$$F_I = \frac{\alpha}{h} = \sqrt{\frac{\tan\lambda}{\lambda}} \left[0.752 + 2.02 \left(\frac{\alpha}{h}\right) + 0.37(1 - \sin\lambda)^4 \right] / \cos\lambda$$

$$F_2 = \frac{\alpha}{h} = \sqrt{\frac{\tan\lambda}{\lambda}} [0.923 + 0.199(1 - \sin\lambda)^4] / \cos\lambda$$

$$F_{II} = \frac{\alpha}{h} = \sqrt{\frac{\tan\lambda}{\lambda}} \left[1.122 - 0.561 \left(\frac{\alpha}{h}\right) + 0.085 \left(\frac{\alpha}{h}\right)^2 + 0.18 \left(\frac{\alpha}{h}\right)^3 \right] / \sqrt{1 - \frac{a}{h}}$$

$$F_{III} \left(\frac{\alpha}{h}\right) = \sqrt{\frac{\tan\lambda}{\lambda}}$$

where $\lambda = \frac{\pi a}{2h}$

In the above Eqs. (B.1-B.5), R is the radius of beam, h is the height of assumed elemental strip, a is the crack depth, $2b$ is the elemental strip and α is the local crack depth, which varies along the cross section.

Terminology of Manifolds and Vector Fields

C.1 Introduction

The extended Lagrangian-Hamiltonian mechanics is proposed over vector fields throughout this study. Some of the important terms of manifolds and vector fields (*Hassani, 1999; Pennacchi, 2006*) are presented here.

C.2 Differentiable manifolds and differential operator

The **differentiable manifolds** or simply ‘manifolds’ are abstract surfaces that locally look like linear spaces. So, it can be defined as, “A differentiable manifold is a collection of all objects called points that are connected to each other in a smooth fashion such that the neighbourhood of each point looks like the neighbourhood of an n -dimensional space, n is called the dimension of manifold.” A **differential operator** is a mapping that transforms a function into another function by means of partial derivative and multiplication by other function. It is an operator, which operates on tangent vector in tangent space and converts it into scalar.

C.3 Tangent space, tangent bundle, cotangent bundle and vector fields

A tangent vector v to a manifold M , at point $m \rightarrow M$ is an equivalence class of curves at m . it is a theorem that the set of all tangent vector to M at m forms a vector space, called as **tangent space**. It is denoted by $T_m M$. The union of all tangent space at different points of a manifold M at the points $m \rightarrow M$ is called the **tangent bundle** of M and denoted by TM . That is given by $TM = \bigcup_{m \in M} T_m M$.

The **cotangent bundle** of a manifold M is similar to the tangent bundle, except that it is set of (x, f) where $x \rightarrow M$ and f is a dual vector in the tangent space to $x \rightarrow M$. The cotangent bundle is denoted by T^*M .

A **vector field** X on a subset U of a manifold M is a mapping $X: U \rightarrow TM$ such that $X(P) \equiv X|_P \equiv X_P \in \mathfrak{T}_P(M)$.

C.4 Infinitesimal generators

The change of an arbitrary function $f(x)$ due to an infinitesimal transformation is given by

$$\begin{aligned} df &= \frac{\partial f}{\partial x_i} dx_i = \frac{\partial f}{\partial x_i} u_{ik}(x) da_k && \text{(using Einstein convention)} \\ &= d a_k \left(u_{ik}(x) \frac{\partial}{\partial x_i} \right) f. \end{aligned}$$

The term $X_K = \sum_{i=1}^n u_{ik}(x) \frac{\partial}{\partial x_i}$ is the infinitesimal generator

The two-dimensional rotation group $SO(2)$ is defined by

$$\begin{bmatrix} x' \\ y' \end{bmatrix} = \begin{bmatrix} \cos \theta & -\sin \theta \\ \sin \theta & \cos \theta \end{bmatrix} \begin{bmatrix} x \\ y \end{bmatrix}$$

The infinitesimal generator of the group can be given as

$$\Delta f(x, y) = \frac{\partial f}{\partial x} \cdot \frac{\partial x}{\partial \theta} \Big|_{\theta=0} \Delta \theta + \frac{\partial f}{\partial y} \cdot \frac{\partial y}{\partial \theta} \Big|_{\theta=0} \Delta \theta$$

Finding infinitesimal transformation of the group due to parameter θ

$$\begin{bmatrix} \Delta x \\ \Delta y \end{bmatrix} = \begin{bmatrix} 0 & -1 \\ 1 & 0 \end{bmatrix} \begin{bmatrix} x \\ y \end{bmatrix} \Delta \theta$$

$$\text{or } \begin{bmatrix} \frac{\Delta x}{\Delta \theta} \\ \frac{\Delta y}{\Delta \theta} \end{bmatrix} = \begin{bmatrix} -y \\ x \end{bmatrix}$$

Now, the infinitesimal generator of the group will be

$$\begin{aligned} \frac{\Delta f(x, y)}{\Delta \theta} &= \left(-y \frac{\partial f}{\partial x} + x \frac{\partial f}{\partial y} \right) \\ &= \left(-y \frac{\partial}{\partial x} + x \frac{\partial}{\partial y} \right) f \end{aligned}$$

C.4.1 Derivation of infinitesimal generators of the rotational SO (2) Group

As the umbra-Lagrangian admits rotational transformation parameterized by an angle variable 's', the first infinitesimal generator \mathbf{V} for this group may be obtained over extended single manifold consist of umbra and real displacements and velocities, and real time. The variation of a sufficiently smooth function f with s at $s=0$ may be obtained as the generator \mathbf{V} operating on f ,

$$\begin{aligned} \Delta f(x(\eta), y(\eta), x(\tau), y(\tau), \dot{x}(\eta), \dot{y}(\eta), \dot{x}(\tau), \dot{y}(\tau)) &= \left[\frac{\partial f}{\partial x(\eta)} \cdot \frac{\partial x(\eta)}{\partial s} \Big|_{s=0} + \frac{\partial f}{\partial y(\eta)} \cdot \frac{\partial y(\eta)}{\partial s} \Big|_{s=0} \right. \\ &+ \frac{\partial f}{\partial x(\tau)} \cdot \frac{\partial x(\tau)}{\partial s} \Big|_{s=0} + \frac{\partial f}{\partial y(\tau)} \cdot \frac{\partial y(\tau)}{\partial s} \Big|_{s=0} + \frac{\partial f}{\partial \dot{x}(\eta)} \cdot \frac{\partial \dot{x}(\eta)}{\partial s} \Big|_{s=0} + \frac{\partial f}{\partial \dot{y}(\eta)} \cdot \frac{\partial \dot{y}(\eta)}{\partial s} \Big|_{s=0} \\ &\left. + \frac{\partial f}{\partial \dot{x}(\tau)} \cdot \frac{\partial \dot{x}(\tau)}{\partial s} \Big|_{s=0} + \frac{\partial f}{\partial \dot{y}(\tau)} \cdot \frac{\partial \dot{y}(\tau)}{\partial s} \Big|_{s=0} \right] \Delta s = \mathbf{V}(f) \Delta s. \end{aligned} \tag{C.1}$$

The generator \mathbf{V} may however, be obtained from the action of this group as follows

$$\Delta \mathbf{Z} = \frac{d}{ds} [R(s)] \otimes [I] \mathbf{Z} \Delta s, \tag{C.2}$$

$$\text{with } \mathbf{Z} = \mathbf{Z}_\eta \oplus \dot{\mathbf{Z}}_\eta \oplus \mathbf{Z}_t \oplus \dot{\mathbf{Z}}_t, \quad \mathbf{Z}_\eta = \begin{Bmatrix} x(\eta) \\ y(\eta) \end{Bmatrix} \text{ and } \mathbf{Z}_t = \begin{Bmatrix} x(\tau) \\ y(\tau) \end{Bmatrix},$$

where \oplus is direct sum of vectors and \otimes is Kronecker or tensor product of matrices. $[I]$

being a 4×4 identity matrix and $[R(s)]$ is 2-dimensional orthogonal matrix given as

$$[R(s)] = \begin{bmatrix} \cos s & \sin s \\ -\sin s & \cos s \end{bmatrix}$$

Equation (C.2) now yields

$$\frac{\Delta Z}{\Delta s} = \begin{bmatrix} 0 & 1 \\ -1 & 0 \end{bmatrix} \otimes [I] \mathbf{Z}. \quad (\text{C.3})$$

The infinitesimal generator of the group may be written through Eq. (C.1) as

$$\begin{aligned} \mathbf{V} = & y(\eta) \frac{\partial}{\partial x(\eta)} - x(\eta) \frac{\partial}{\partial y(\eta)} + y(\tau) \frac{\partial}{\partial x(\tau)} - x(\tau) \frac{\partial}{\partial y(\tau)} + \dot{y}(\eta) \frac{\partial}{\partial \dot{x}(\eta)} - \dot{x}(\eta) \frac{\partial}{\partial \dot{y}(\eta)} \\ & + \dot{y}(\tau) \frac{\partial}{\partial \dot{x}(\tau)} - \dot{x}(\tau) \frac{\partial}{\partial \dot{y}(\tau)}. \end{aligned}$$

C.4.2 Derivation of Infinitesimal generators of translational group

As the gauge variant umbra-Lagrangian admits translational transformation parameterized by a linear shift 's', the infinitesimal generator \mathbf{V} for this group may be obtained as

$$x' = x + s$$

The variation of a sufficiently smooth function f with s at $s=0$ may be obtained as the generator \mathbf{V} operating on f ,

$$\Delta x' = \Delta s$$

$$\text{or } \frac{\Delta x'}{\Delta s} = 1,$$

in other words, the infinitesimal generator may be written as

$$\mathbf{V} = \frac{\partial}{\partial x(\eta)} + \frac{\partial}{\partial x(\tau)} \quad (\text{C.4})$$

C.5 Prolongation of a function

The prolongation is a vector function from the space of the independent variables to the space U^n , whose entries represents the values of f and all its derivatives up to order n . In this way, some nebulous notions of a system of differential equations need to be replaced by a concrete geometric object that is characterized by the vanishing of certain functions. The aforementioned space $X \times U$ needs to be extended or prolonged, to include not only the variables under consideration, but also the other partial derivatives that exit in the system. Let U_k represent the Euclidean space of all different k^{th} order derivatives of the function and let $U^{(n)} = U_1 \times U_2 \times \dots \times U_n$ be the Cartesian product space of all the different derivatives of the function from order 0 to n .

Given a smooth function $u = f(x)$, so $f: X \rightarrow U$, there is an induced function $u^{(n)} = pr^{(n)}f(x)$, called the n^{th} prolongation of f , which is defined by the equations

$$u_j^\alpha = \partial_j f^\alpha(x) \quad (\text{C.5})$$

Thus $pr^{(n)}f$ is a function from X to the space $U^{(n)}$, and for each x in X , $pr^{(n)}f(x)$ is a vector whose $q.p^{(n)}$ entries represent the value of f and all its derivatives up to order

n at the point x . The total space $X \times U^{(n)}$, whose coordinates represent the independent variables, the dependent variables and the derivatives of the dependent variables up to order n is called n^{th} order *jet space* of the underlying space $X \times U$.

Classical Lagrange's Equation

D.1 Classical Lagrange's equation

Lagrange (1788) had given a general treatment of dynamical systems formulated from scalar quantities of kinetic energy, potential energy and work expressed in terms of generalized coordinates. The difference between the kinetic and potential energy is termed as Lagrangian, which is expressed as

$$L = T - V \quad (\text{D.1})$$

where L is the Lagrangian, T is the total kinetic energy and V is the total potential energy. Since V does not depend on the velocities, Lagrange's equations of motion for n generalized co-ordinates may be represented as

$$\frac{d}{d\tau} \left(\frac{\partial L}{\partial \dot{q}_i} \right) - \frac{\partial L}{\partial q_i} = 0, \text{ for } i = 1 \dots n \quad (\text{D.2})$$

Lagrange developed these equations of motion from the principle of virtual work. Lagrange's equations are applicable when the system is closed, constraints are integrable and there is no gyroscopic coupling. The relationship of Lagrange's equations of motion and the variational principle is discussed in following subsection.

D.2 Relationship between classical Lagrange's equation and variational principle

It is significant that Lagrange's equations resemble the equations, one obtains from a variational principle. Variational problems are classified in mathematics, and numerous

variational problems arise more often in physics and engineering. Variational principle defines that a dynamical systems moves in such a way to minimize or maximize something. One may generalize it by showing that the dynamical systems moves in such a way to minimize the action (*Calkin, 2000; Goldstein, 1980*) expressed as

$$S = \int L(q, \dot{q}, \tau) d\tau \quad (\text{D.3})$$

The equation (D.3) may be explained more accurately, if it is supposed that an initial time τ_0 , a final time τ_1 , and a dynamical path $q(\tau)$ are given. Then the action associated with them can be represented as

$$S(q; \tau_0, \tau_1) = \int_{\tau_0}^{\tau_1} L(q, \dot{q}, \tau) d\tau \quad (\text{D.4})$$

When the given $q(\tau)$ is inserted into the expression for $L(q, \dot{q}, \tau)$, the integrand becomes a function of t alone, so it can be integrand with respect to τ . It is clear that the value of S depends on the trajectory $q(\tau)$, for it depends not only one value of τ , but one function q and all of τ in the interval $\tau_0 \leq \tau \leq \tau_1$. In this way, one may deal only with the trajectories that start and end at the same two points in configuration space M as shown in Figure D.1 and these trajectories are given by functions $q(\tau; m)$ and $q(\tau; t)$.

To explain the variational concept, one may assume two continuous functions $q(\tau_0)$ and $q(\tau_1)$ which map the real line R to a n dimensional configuration space M on the real field. It is assumed that $q(\tau_0)$ is homotopic to $q(\tau_1)$, i.e., there exists a continuous map $F: R \times I \rightarrow M$ such that $q(\tau_0; m) = q(\tau_0; t) \equiv q(\tau_0)$ and $q(\tau_1; m) = q(\tau_1; t) \equiv q(\tau_1)$, where I is the closed interval $[m, t]$. If $q(\tau; m) \neq q(\tau; t)$, the

corresponding actions will not be equal and there are many possible trajectories with the same end points and each one yields a characteristic value of S , and physical problem is to choose among all these possibilities, to find particular $q(\tau)$ that the dynamical system takes in making the trip from $q(\tau_0)$ to $q(\tau_1)$.

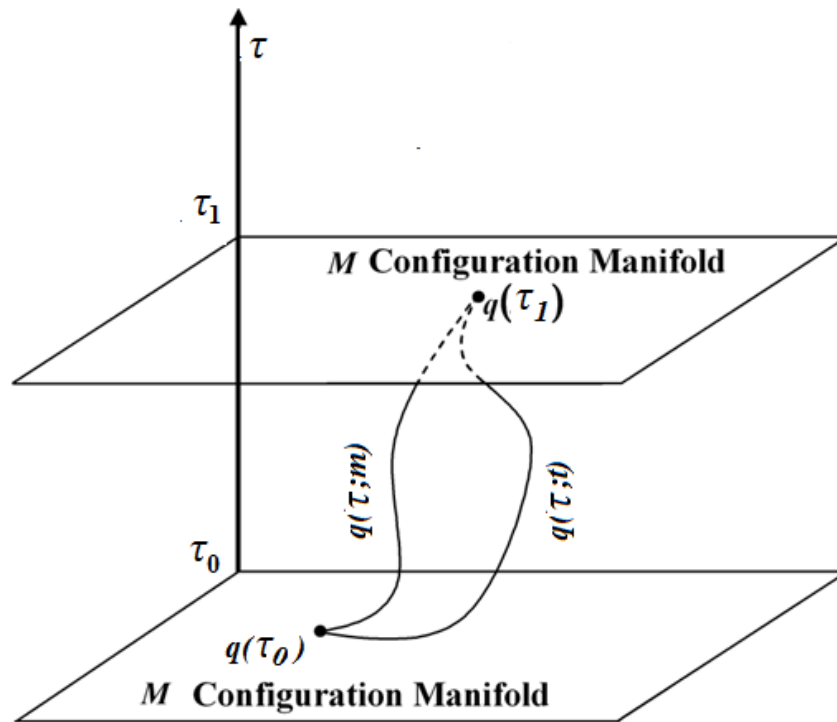


Figure D.1: Two possible trajectories $q(\tau; m)$ and $q(\tau; t)$ from $q(\tau_0)$ to $q(\tau_1)$ in configuration space M at two times

It may be further shown that the physical trajectory is one that yields the minimum value of S and minimizing S leads to Lagrange's equations. If a family of many trajectories are considered as $q(\tau; \varepsilon)$ with all starting and ending at $q(\tau_0)$ and $q(\tau_1)$, where ε is an index labeling each particular trajectory of the family. As $q(\tau; m)$ and $q(\tau; t)$ leads to different actions, each $q(\tau; \varepsilon)$ leads to its corresponding action $S(\varepsilon)$. In this way variational principle states that the physical trajectory is the one for which the action is

minimum and independent of the way in which the ε family of trajectories is chosen, provided it contains the physical one. This principle is Hamilton's variational principle.

The Lagrange's equations provide one of the most convenient ways of writing down the equations of motion for a wide range of mechanical systems. The foremost advantage of Lagrange's equations is that it is easier to apply to dynamical systems. Beside this it brings out the close connection between conservation laws and symmetry properties of dynamical systems.

Another advantage about Lagrange's equations is that it can be derived from a variational principle, a method that turns out to be quite general and applicable in many branches of physics. However, it suffers a lot due to its inherent limitations in presence of time fluctuating parameters, general dissipation and gyroscopic coupling. That is why the classical Lagrange's equation cannot analyze the dynamics of systems under such situations as such Lagrangian cannot be work out in the reverse depending on the nature of nonconservative forces involved in the system, which leads to a loss of generality. At this stage, some additional information of system interior and exterior is needed in generating extended Lagrange's equation, which may be applicable to a broader class of systems.

D.3 Mathematical interpretation of classical Noether's theorem

The presence of constant of motion or even their absence reveals much valuable information regarding the dynamical behaviour of the system. The classical Noether's theorem as presented by *Arnold* (1974) employs the following definition of *symmetries*: "If the Lagrangian for a system admits some transformation of the phase variables, then these transformations are called symmetries of the system." The term *admits* means that the Lagrangian remains unchanged under these transformations. Thus, Noether's

theorem states that with every (infinitesimal) symmetry there exists a conserved quantity or a first integral (invariants of motion).

Mathematically, the aforementioned theorem states that if the Lagrangian system (M, L) admits a one parameter group of diffeomorphisms $h^s : M \rightarrow M, s \in R$, then the Lagrangian system of equations corresponding to L has a first integral $I : TM \rightarrow R$, where M is a manifold and TM is a tangent bundle of the manifold, and R is the set of all real numbers.

In local co-ordinates q on M , the integral I may be written in the form

$$I(q, \dot{q}) = \left. \frac{\partial L}{\partial \dot{q}} \frac{dh^s}{ds} \right|_{s=0} \tag{D.5}$$

and $\frac{dI}{d\tau} = 0$ (D.6)

The Noether's theorem may be compactly written by using infinitesimal generators or vector fields (*Hassani, 1999; Olver, 1986*) of the symmetry groups. The condition that the given Lagrangian is invariant under the j^{th} transformation may then be expressed as

$$\mathbf{V}^j(L) = 0 \tag{D.7}$$

where \mathbf{V}^j is the j^{th} infinitesimal generators of a symmetry group and L is Lagrangian of the system. In the context of extended Lagrangian formulation, umbra-Lagrangian being invariant under the j^{th} transformation may be expressed as

$$\mathbf{V}^j(L^*) = 0 \tag{D.8}$$

where L^* is umbra-Lagrangian of the system.

Umbra-Hamiltonian Theorem

E.1 Concept of umbra-Hamiltonian

Mathematically, the umbra-Hamiltonian (*Mukherjee*, 1994, 2001) may be represented as

$$H^*[\mathbf{q}(\eta), \mathbf{p}(\eta), \mathbf{q}(\tau), \dot{\mathbf{q}}(\tau), \tau] = \dot{\mathbf{q}}(\eta)\mathbf{p}(\eta) - L^*[\mathbf{q}(\eta), \dot{\mathbf{q}}(\eta), \mathbf{q}(\tau), \dot{\mathbf{q}}(\tau), \tau] \quad (\text{E.1})$$

where the umbra-momentum is

$$\mathbf{p}(\eta) = \frac{\partial L^*}{\partial \dot{\mathbf{q}}(\eta)}$$

The real momentum may be obtained as

$$\mathbf{p}(\tau) = \lim_{\eta \rightarrow \tau} \frac{\partial L^*}{\partial \dot{\mathbf{q}}(\eta)}$$

Taking total differential of Eq. (E.1), one obtains

$$\begin{aligned} dH^* &= \frac{\partial H^*}{\partial \mathbf{p}(\eta)} d\mathbf{p}(\eta) + \frac{\partial H^*}{\partial \mathbf{q}(\eta)} d\mathbf{q}(\eta) + \frac{\partial H^*}{\partial \mathbf{q}(\tau)} d\mathbf{q}(\tau) + \frac{\partial H^*}{\partial \dot{\mathbf{q}}(\tau)} d\dot{\mathbf{q}}(\tau) + \frac{\partial H^*}{\partial \tau} d\tau \\ &= \dot{\mathbf{q}}(\eta) d\mathbf{p}(\eta) - \frac{\partial L^*}{\partial \mathbf{q}(\eta)} d\mathbf{q}(\eta) - \frac{\partial L^*}{\partial \mathbf{q}(\tau)} d\mathbf{q}(\tau) - \frac{\partial L^*}{\partial \dot{\mathbf{q}}(\tau)} d\dot{\mathbf{q}}(\tau) \\ &\quad - \frac{\partial L^*}{\partial \tau} d\tau + \left(\mathbf{p}(\eta) - \frac{\partial L^*}{\partial \dot{\mathbf{q}}(\eta)} \right) d\dot{\mathbf{q}}(\eta) \end{aligned}$$

The relations which may be derived, are

$$\dot{\mathbf{q}}(\eta) = \frac{\partial H^*}{\partial \mathbf{p}(\eta)} \quad (\text{E.2})$$

$$\frac{\partial H^*}{\partial \mathbf{q}(\eta)} = -\frac{\partial L^*}{\partial \mathbf{q}(\eta)} \Rightarrow \lim_{\eta \rightarrow \tau} \frac{\partial H^*}{\partial \mathbf{q}(\eta)} = -\dot{\mathbf{p}}(\tau) \quad (\text{E.3})$$

and the other relations acquired are

$$\frac{\partial H^*}{\partial \mathbf{q}(\tau)} = -\frac{\partial L^*}{\partial \mathbf{q}(\tau)}$$

$$\frac{\partial H^*}{\partial \tau} = -\frac{\partial L^*}{\partial \tau}$$

The umbra-Hamiltonian H^* is comprised of two components as H_i^* and H_e^* . H_i^* is the interior form of Hamiltonian, which is independent of any function of real time, real velocity and real displacement, and H_e^* is the rest of the umbra-Hamiltonian, termed as the exterior Hamiltonian. Thus, one may write

$$H^* = H_i^*\{\mathbf{q}(\eta), \mathbf{p}(\eta)\} + H_e^*\{\mathbf{q}(\eta), \mathbf{p}(\eta), \mathbf{q}(\tau), \dot{\mathbf{q}}(\tau), \tau\} \quad (\text{E.4})$$

The theorems of the umbra-Hamiltonian (Mukherjee, 1994, 2001) are now presented:

Theorem 1

$$\lim_{\eta \rightarrow \tau} \left[\frac{\partial H^*}{\partial \eta} \right] = 0$$

Proof

$$\frac{dH^*}{d\eta} = \frac{\partial H^*}{\partial \mathbf{p}(\eta)} \dot{\mathbf{p}}(\eta) + \frac{\partial H^*}{\partial \mathbf{q}(\eta)} d\dot{\mathbf{q}}(\eta) = \dot{\mathbf{q}}(\eta) \dot{\mathbf{p}}(\eta) + \frac{\partial H^*}{\partial \mathbf{q}(\eta)} \dot{\mathbf{q}}(\eta)$$

Now taking the limit $\eta \rightarrow \tau$, one obtains

$$\lim_{\eta \rightarrow \tau} \left[\frac{\partial H^*}{\partial \eta} \right] = \lim_{\eta \rightarrow \tau} (\dot{\mathbf{q}}(\eta) \dot{\mathbf{p}}(\eta)) + \lim_{\eta \rightarrow \tau} \left(\frac{\partial H^*}{\partial \mathbf{q}(\eta)} \dot{\mathbf{q}}(\eta) \right) = \dot{\mathbf{q}}(\tau) \dot{\mathbf{p}}(\tau) + \left(\lim_{\eta \rightarrow \tau} \frac{\partial H^*}{\partial \mathbf{q}(\eta)} \right) \lim_{\eta \rightarrow \tau} \dot{\mathbf{q}}(\eta)$$

Substitution of Eq. (E.3) gives

$$\text{Lim}_{\eta \rightarrow \tau} \left[\frac{\partial H^*}{\partial \eta} \right] = \dot{\mathbf{q}}(\tau) \dot{\mathbf{p}}(\tau) - \dot{\mathbf{p}}(\tau) \dot{\mathbf{q}}(\tau) = \mathbf{0}$$

Theorem 2

$$\frac{\partial H_i^*}{\partial \tau} = - \text{Lim}_{\eta \rightarrow \tau} \left[\frac{\partial H_e^*}{\partial \eta} \right]$$

Proof: From theorem 1 and Eq. (E.4), one may write

$$\text{Lim}_{\eta \rightarrow \tau} \frac{dH_i^*(\mathbf{q}(\eta) \mathbf{p}(\eta))}{d\eta} = - \text{Lim}_{\eta \rightarrow \tau} \left[\frac{dH_e^*}{d\eta} \right]$$

or

$$\text{Lim}_{\eta \rightarrow \tau} \frac{dH_i^*(\mathbf{q}(\tau) \mathbf{p}(\tau))}{d\tau} = - \text{Lim}_{\eta \rightarrow \tau} \left[\frac{dH_e^*}{d\eta} \right]$$

Corollary

If, for a system

$$\text{Lim}_{\eta \rightarrow \tau} \left[\frac{dH_e^*}{d\eta} \right] = 0$$

Then $H_i^*(\mathbf{q}(\tau) \mathbf{p}(\tau))$ is a constant of motion.

Proof: It follows directly from theorem 2 that

$$\frac{dH_i^*(\mathbf{q}(\tau) \mathbf{p}(\tau))}{d\tau} = 0$$

Hence, $H_i^*(\mathbf{q}(\tau) \mathbf{p}(\tau))$ is a constant of motion.

Karnopp's Algorithm

F.1 Karnopp's Algorithm

Karnopp (1977) proposed an algorithm to arrive at Lagrange's equations for complex systems through its bondgraph model. The steps of Karnopp's algorithm may be briefed as

- Apply the required causality at all effort and flow sources and use the junction structure elements (only) to extend the causality as far as possible within the bondgraph. If causal conflicts arise at this stage, there is a fundamental contradiction within the model and it must be reformulated.
- Choose a '1' junction for which the flow is not yet causally determined or insert a '1' junction into any causally undetermined bond and attach an artificial flow source to '1' junction.
- Apply the required causality to the artificial source and extend the causality as far as possible into the bondgraph using junction structure element.
- Return to step (2) and continue until all bonds have been causally oriented.

F.2 Extension of Karnopp's Algorithm for Generation of Umbra-Lagrangian

An extension of Karnopp's algorithm (*Karnopp*, 1977) is presented with a detailed procedure and may appear more elaborate for generation of umbra-Lagrangian of the system. The models may be classified as follows:

- (a) System with no modulated two-port transformers. Such bondgraph models may be called as holonomic.
- (b) System with modulated two-port transformers. Such bondgraph may be called as nonholonomic.

To explain the procedure, one may take an example as shown in Figure F.1 (a) with its bondgraph model. Now, the additional steps for generation of umbra-Lagrangian may be given as

- (i) Create two copies of the part of the junction by excluding two-port elements, side by side associate one with η -variable (the umbra-time) and other with τ -variable (the real time). The space between these two may be designated as trans-temporal space.
- (ii) Insert the artificial sources to their corresponding junctions. Those inserted in the η -component should be designated as function of η and their copies inserted in the τ -component would be designated as function of τ .
- (iii) Insert the original flow sources at their respective junctions on the η and τ component designating them as function of τ ; the effort sources in η component.
- (iv) Insert all I -and C -elements and fields at their respective junctions on η -component.
- (v) R -elements and fields (including gyrators) observe the motion in real time τ and activations as shown in Figure F.1 (b). Such bondgraph may be termed as umbra-Lagrangian generator bondgraphs.

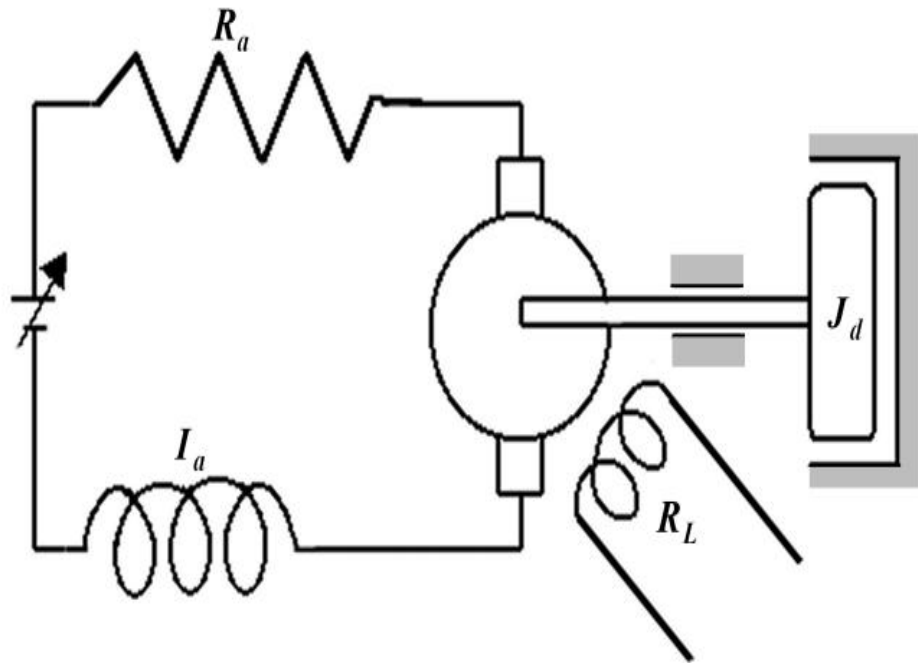


Figure F.1 (a): Schematic diagram of a system with a DC motor and a rotating disk in viscous medium

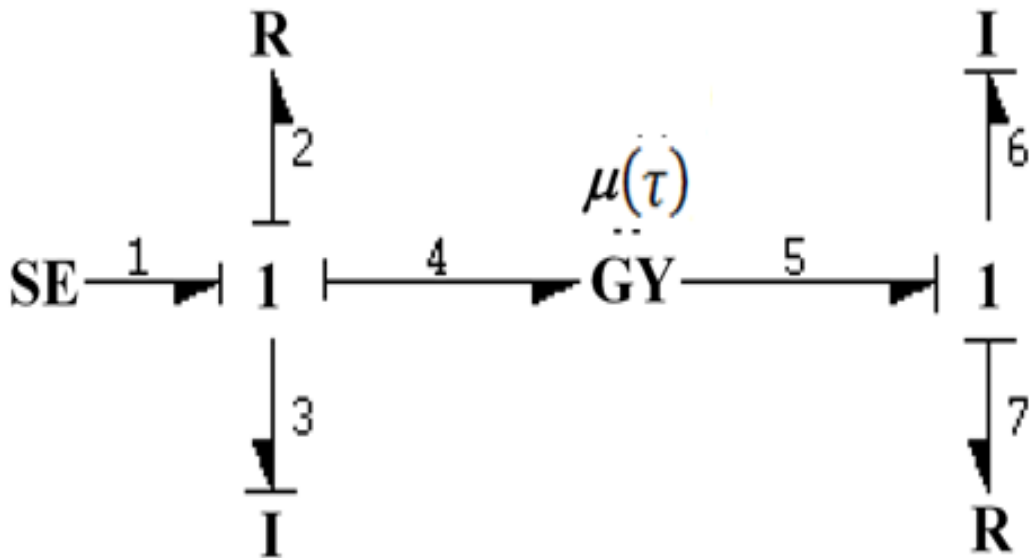


Figure F.1 (b): Bondgraph model of system represented by Figure F.1 (a)

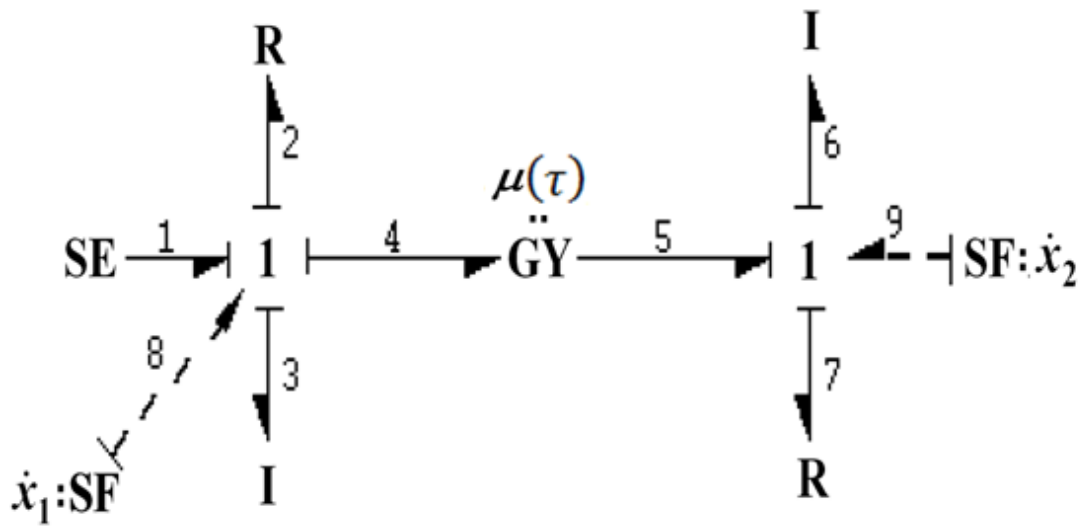


Figure F.2 (a): Causalled bondgraph model of system represented by Figure F.1 (a) with artificial flow sources

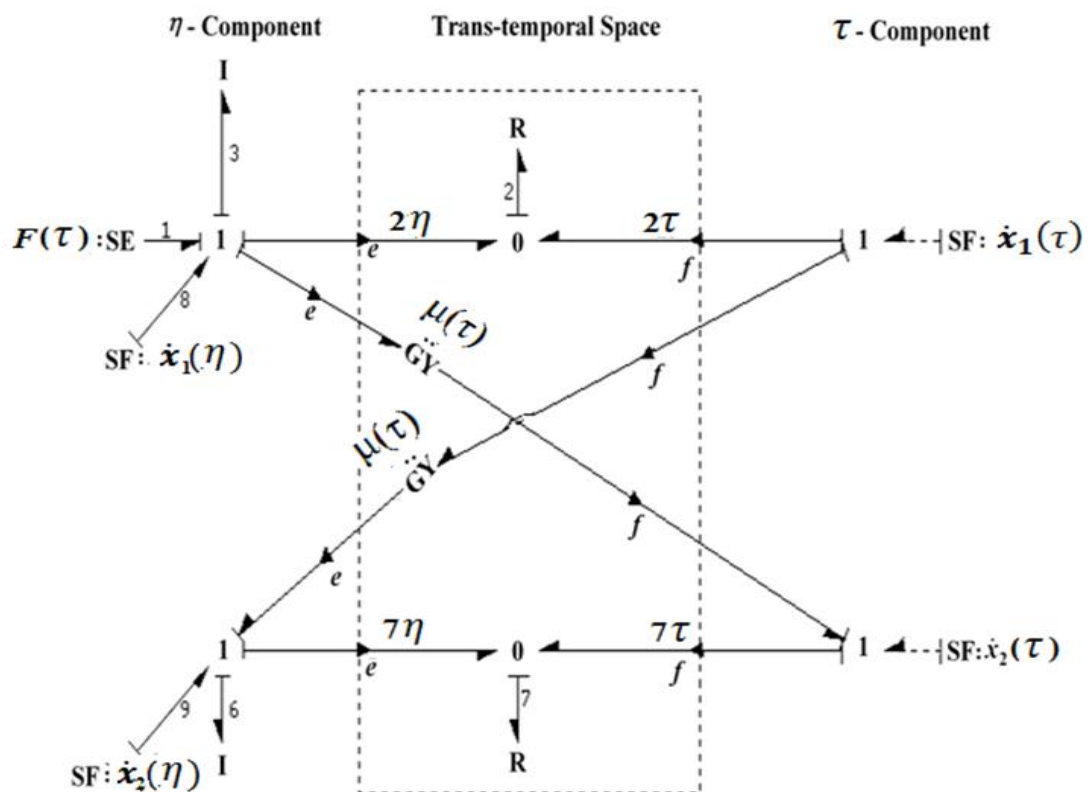


Figure F.2 (b): Umbra-Lagrangian generator bondgraph of system represented by Figure F.1 (a)

The umbra-Lagrangian for Figure F.2 (b) may be expressed as

$$L^* = \frac{1}{2} m_3 \dot{x}_1^2(\eta) + \frac{1}{2} m_6 \dot{x}_2^2(\eta) - R_2 \dot{x}_1(\tau) x_1(\eta) - R_7 x_2(\tau) x_2(\eta) - \mu(\tau) \{ \dot{x}_2(\tau) x_1(\eta) - x_1(\tau) x_2(\eta) \}. \quad (\text{F.1})$$

Now, it is easy to verify that umbra-Lagrangian of Eq. (F.1) renders the right equation of motion through Eq. (2.12) for this system.

Nonholonomic situations may also be handled through this method.

- (i) If after the completion of steps (i-iv), an I-element (or field) receives flow through modulated transformer, then that I-element (or field) should be brought to the trans-temporal space. It should receive flow from τ -component through effort activated copy of the modulated transformer and return force to η -component, which then produces umbra-potential through the work done for the corresponding umbra-displacements.
- (ii) If after steps (i-iv), any C-element (or field) receives its flow through modulated transformer, then that C-element (or field) should be transformed into an I-element (or field) by incorporation of a (or set of) unit gyrator (s) and 1-junctions. This 1-junction (s) should be now appended with the additional artificial flow sources and then the entire graph may be reduced by combining the original transformer and unit gyrator to render a modulated gyrator.
- (iii) For any element connected to 0-junction (other than junctions and artificial flow source in the model) returns flow information to the junction structure after incorporation of artificial flow source as per steps (i-vii), then the bond connecting this element and 0-junction must be broken in two bonds by incorporating a 1-junction. On this newly 1-junction, one may incorporate

additional artificial flow sources associated with a new variable. This should be followed for all such elements in the model.

One may consider the following example as shown in Figure F.3 (a). The umbra-Lagrangian generator bondgraph model of the system is represented in Figure F.3 (b), after adding 1-junction in between 0-junction and R-element, to change its causality, and additional artificial sources associated with a new variable are appended to this 1-junction.

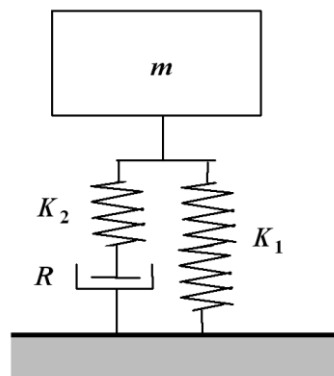


Figure F.3 (a): Schematic diagram of a mass-spring-damper system

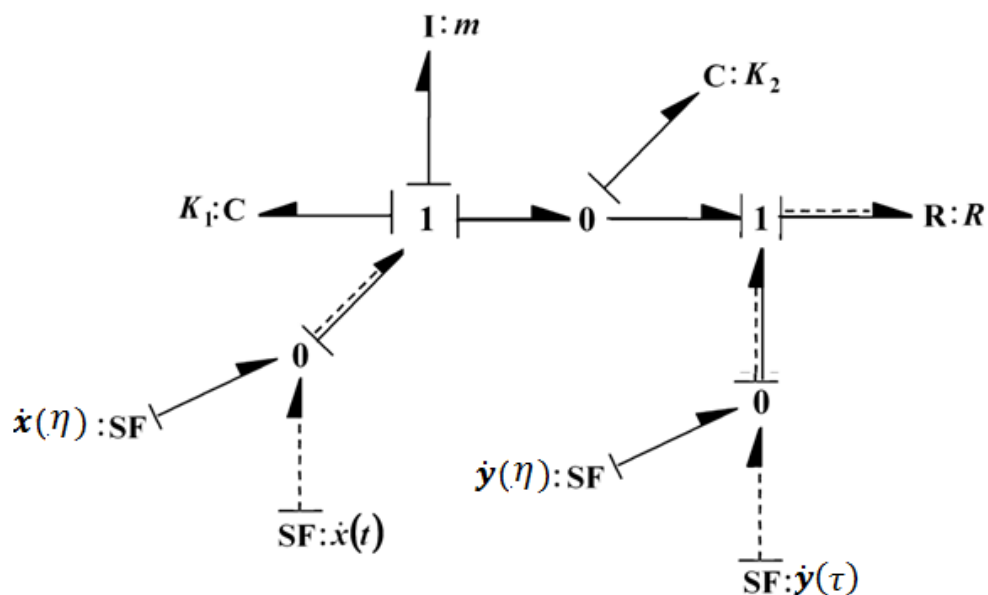


Figure F.3 (b): Umbra-Lagrangian generator bondgraphs of system as shown in Figure F.3 (a)

The umbra-Lagrangian of the system may be obtained as

$$L^* = \frac{1}{2} m \dot{x}^2(\eta) - \frac{1}{2} K_1 x^2(\eta) - \frac{1}{2} K_2 (x(\eta) - y(\eta))^2 - R y(\tau) y(\eta) \quad (\text{F.2})$$

The above Lagrangian yields following equations of motion through Eq. (2.12)

$$\frac{d}{dt} (m \dot{x}(\tau)) + K_1 x(\tau) + K_2 (x(\tau) - y(\tau)) = 0 \quad (\text{F.3.a})$$

$$- K_2 (x(\tau) - y(\tau)) + R \dot{y}(\tau) = 0 \quad (\text{F.3.b})$$

In another example, when C-element is in differential causality, one may consider the same step as mentioned above and yields the exact equation of motion after obtaining umbra-Lagrangian of the system. The system bondgraph model after insertion of artificial flow sources may be shown as Figure F.4, where artificial flow sources are shown by a double arrow with dotted and solid lines.

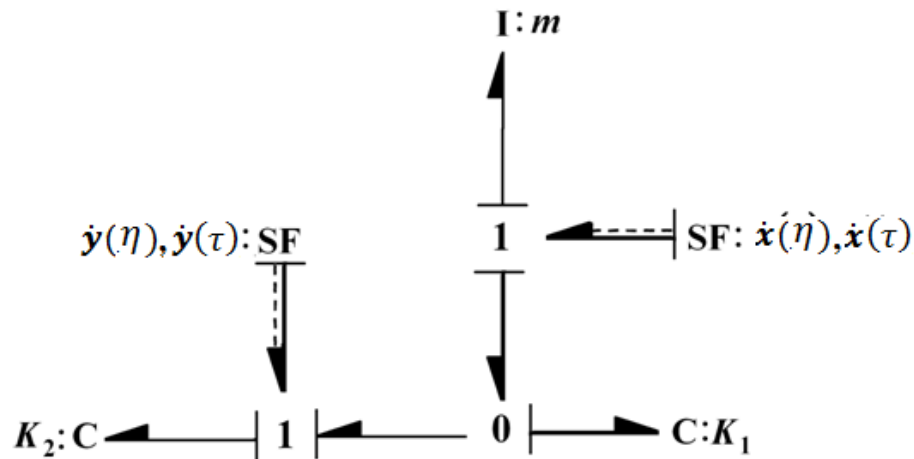


Figure F.4: Umbra-Lagrangian generator bondgraphs with compacted artificial flow sources

The umbra-Lagrangian of the system may be written as

$$L^* = \frac{1}{2} m \dot{x}^2(\eta) - \frac{1}{2} K_1 (x(\eta) - y(\eta))^2 - \frac{1}{2} K_2 y(\eta)^2 \quad (\text{F.4})$$

The equation of motion may be obtained through Eq. (2.12) as

$$m\ddot{x}(\tau) + K_1(x(\tau) - y(\tau)) = 0 \quad (\text{F.5.a})$$

$$\text{and condition } K_1(y(\tau) - x(\tau)) + K_2y(\tau) = 0. \quad (\text{F.5.b})$$

The condition of Eq. (F.5.a) is substituted in Eq. (F.5.b) and the equation of motion may be finally expressed as

$$m\ddot{x}(\tau) + \frac{K_1K_2}{K_1 + K_2}x(\tau) = 0 \quad (\text{F.6})$$

In Figure F.4, the real-time and umbra-time artificial flow sources are represented by a dotted and solid line as it is not always possible to make umbra-Lagrangian generator bondgraphs by elaborating η and τ -component and trans-temporal portion as shown in Figure F.2 (b). So, some compaction is needed to show these umbra-Lagrangian generator bondgraphs by a single bondgraph model. In present work, the convention of compacted bondgraph models is used, to obtain umbra-Lagrangian of the system as represented by Figure F.4.

Another additional feature of bondgraph modeling is that one may easily recognize Hamiltonian and non-Hamiltonian component through umbra-Lagrangian generator bondgraphs as represented in the Figure F.5, where R-elements and anti-symmetric C-fields are shown by a superscript (*). The solid line shows the umbra-time flows and dotted line shows the real-time flows. Purely Hamiltonian components are only components of umbra-time flows as shown by I and C-elements. In this way, bondgraphs provide a facility to distinguish Hamiltonian and non-Hamiltonian components, and to obtain umbra-Lagrangian. One may keep these two points in his

mind, while drawing umbra-Lagrangian generator bondgraphs. In present research work, only artificial flow sources are shown by a dotted and solid line, whereas other elements are shown by a single solid line and this convention is used throughout the work.

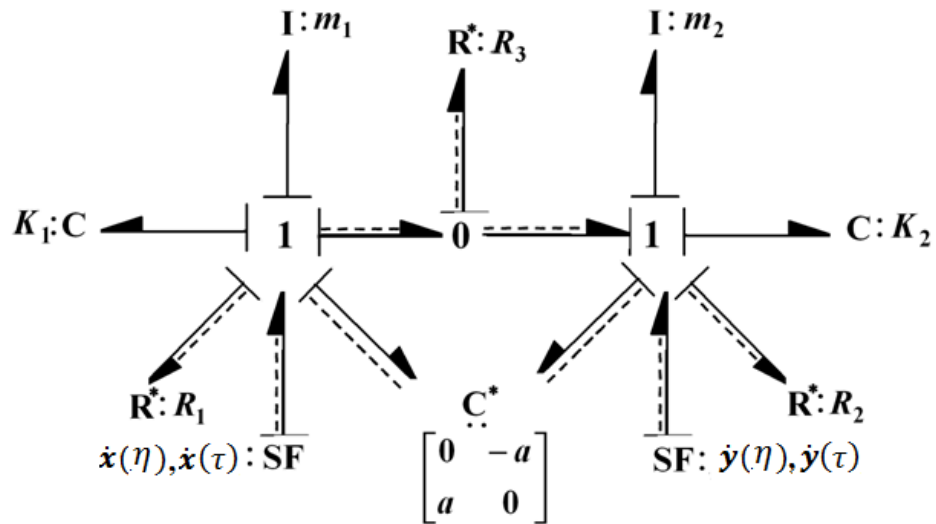


Figure F.5: Umbra-Lagrangian generator bondgraphs showing non-Hamiltonian components

Appendix G

General Condition for Symmetry

The most general description of the action functional with integrand as a function of time, multiple space variables and homotopic family of amplitudes and their derivative as follows

$$I = \int_{\tau_0}^{\tau_1} \int_{\Omega_0} \mathcal{L} \left(\tau, x_1, \dots, x_p, \mathbf{M} \left(\tau, \mathbf{x}, u_m^{(n)} \right), u_{1t}^{(n)}(\tau, \mathbf{x}) \dots u_{mt}^{(n)}(\tau, \mathbf{x}) \right) \quad (\text{G.1})$$

where $u^{(n)}$ stands for the function and all derivative up to order n . However, it will be more convenient to write the modulatory and the trajectorial member using $\eta \rightarrow \tau$ notations. Now, let us proceed to write the generalized condition for admissibility (or invariance) of $\mathcal{L}(\cdot)$ under a single parameter group, which transforms η, τ, \mathbf{x} and amplitudes $u_i(\tau, \mathbf{x})$ and $u_i(\eta, \mathbf{x})$, for $i = 1, \dots, \alpha$. Let us denote $y_i = x_i$ for $i = 1, \dots, p$, $y_{p+1} = \eta$ and $y_{p+2} = \tau$. Then, a generalized infinitesimal generator may be written as

$$\mathbf{V} = \sum_{i=1}^{p+2} \xi^i \frac{\partial}{\partial y_i} + \sum_{i=1}^{\alpha} \eta \phi_i(y_{p+1}, \mathbf{x}) \frac{\partial}{\partial u_i(y_{p+1}, \mathbf{x})} + \sum_{i=1}^{\alpha} \tau \phi_i(y_{p+2}, \mathbf{x}) \frac{\partial}{\partial u_i(y_{p+2}, \mathbf{x})} \quad (\text{G.2})$$

In principle, ξ^i could be function of all y 's and u 's. However as in umbra-dynamics, we do not assume coupling between η and τ as ξ^{p+1} will not be function of y_{p+2} and ξ^{p+2} will not be function of y_{p+1} . We are now concerned about n^{th} prolongation of the generator vector field of Eq. (G.2) and it may be written as

$$p_r^{(n)}(\mathbf{V}) = \mathbf{V} + \sum_{i=1}^{\alpha} \sum_{\#J_{\eta}=1}^{\#J_{\eta}=n} \eta \phi_i^{(J_{\eta})} \frac{\partial}{\partial u_{iJ_{\eta}}(y_{p+1}, \mathbf{x})} + \sum_{i=1}^{\alpha} \sum_{\#J_{\tau}=1}^{\#J_{\tau}=n} \tau \phi_i^{(J_{\tau})} \frac{\partial}{\partial u_{iJ_{\tau}}(y_{p+2}, \mathbf{x})} \quad (\text{G.3})$$

where # denotes the order and J_η as subscript stands for all partial derivatives up to order n barring those which involve partial derivative with respect to y_{p+2} , (that is with respect to τ), likewise J_τ as subscript stands for all partial derivatives up to order n barring those which involve partial derivative with respect to y_{p+1} , (that is with respect to η), and

$$\begin{aligned} {}_\eta \phi_k^{(J_n)} &= D_{J_\eta} \left({}_\eta \phi_k(y_{p+1}, \mathbf{x}) - \sum_{i=1}^{\alpha} \xi^i u_{k,j,i}^{(y_{p+1}, \mathbf{x})} \right) + \sum_{i=1}^{\alpha} \xi^i u_{k,j,i}^{(y_{p+1}, \mathbf{x})} \\ {}_\tau \phi_k^{(J_t)} &= D_{J_t} \left({}_\tau \phi_k(y_{p+2}, \mathbf{x}) - \sum_{i=1}^{\alpha} \xi^i u_{k,j,i}^{(y_{p+2}, \mathbf{x})} \right) + \sum_{i=1}^{\alpha} \xi^i u_{k,j,i}^{(y_{p+2}, \mathbf{x})} \end{aligned}$$

Now the admissibility of L under this group of one parameter transformation will be given as

$$p_r^{(n)} \mathbf{V}(\mathcal{L}) + \mathcal{L} \nabla \bullet \xi = 0 \quad (\text{G.4})$$

The simplified situations addressed so far in present study are those, in which the independent variables, i.e., τ , η and x are not transformed. Only the amplitudes are transformed by one parameter group of transformations. The infinitesimal generator vector field and their prolongations may be written as

$$\mathbf{V} = \sum_{i=1}^{\alpha} {}_\eta \phi_i(y_{p+1}, \mathbf{x}) \frac{\partial}{\partial u_i(y_{p+1}, \mathbf{x})} + \sum_{i=1}^{\alpha} {}_\tau \phi_i(y_{p+2}, \mathbf{x}) \frac{\partial}{\partial u_i(y_{p+2}, \mathbf{x})} \quad (\text{G.5})$$

$$p_r^n \mathbf{V} = \mathbf{V} + \sum_{i=1}^{\alpha} \sum_{\#j_\eta=1}^{\#J_\eta=n} D_{J_\eta} ({}_\eta \phi_i(y_{p+1}, \mathbf{x})) \frac{\partial}{\partial u_{j_\eta}(\eta)} + \sum_{i=1}^{\alpha} \sum_{\#j_\tau=1}^{\#J_\tau=n} D_{J_\tau} ({}_\tau \phi_i(y_{p+2}, \mathbf{x})) \frac{\partial}{\partial u_{j_\tau}(\tau)} \quad (\text{G.6})$$

Equation (G.6) may be written in $\eta - \tau$ form as

$$p_r^n \mathbf{V} = \sum_{i=1}^{\alpha} \sum_{\#j_\eta=0}^{\#J_\eta=n} D_{J_\eta} ({}_\eta \phi_i(\eta, \mathbf{x})) \frac{\partial}{\partial u_{J_\eta}(\eta)} + \sum_{i=1}^{\alpha} \sum_{\#j_\tau=0}^{\#J_\tau=n} D_{J_\tau} ({}_\tau \phi_i(\tau, \mathbf{x})) \frac{\partial}{\partial u_{J_\tau}(\tau)} \quad (\text{G.7})$$

In this situation $\xi^i = 0$, for $i = 1, p + 2, \dots$, the admissibility of Lagrangian density reduce to

$$p_r^n \mathbf{V}(\mathcal{L}) = 0 \quad (\text{G.8})$$

Even from these limited forms of symmetries, many interesting results are obtained for symmetric rotors with internal and external dissipation, gyroscopic couplings and drives. More generalized symmetries involving independent and dependent variables can also be proposed for symmetrizing rotors with special classes of asymmetries.

References

- Adeswusi, S.A., and Al-Bedoor, B. O. (2001). Wavelet analysis of vibration signals of an overhung rotor with a propagating transverse crack. *Journal of Sound and vibration*, 246(5), 777-793.
- Akira, S. (2009). Non linear vibration analysis of cracked structure- Application to turbo machinery rotors with crack blades. *Ph.d Thesis, University of Michigan*.
- Al-Shudeifat, M. A., and Butcher, E. A., and Stern, C. R. (2010). General harmonic balance solution of a cracked rotor-bearing-disk system for harmonic and sub-harmonic analysis: Analytical and experimental approach. *International Journal of Engineering Science*, 48(10), 921-935.
- Al-Shudeifat, M. A., and Butcher, E. A. (2011). New breathing functions for the transverse breathing crack of the cracked rotor system: Approach for critical and subcritical harmonic analysis. *Journal of Sound and Vibration*, 330(3), 526–544.
- Al-Shudeifat, M. A. (2013). On the finite element modeling of the asymmetric cracked rotor. *Journal of Sound and Vibration*, 332(11), 2795–2807.
- Arnold, V. I. (1974). *Mathematical methods of classical mechanics*, Springer-Verlag, New York –Heidelberg-Berlin, pp. 88-89.
- Bachschnid, N., Tanzi, E., and Audebert, S. (2008). The effect of helicoidal cracks on the behaviour of rotating shafts. *Engineering Fracture Mechanics*, 75(3-4), 475–488.
- Babu, T. R., and Sekhar, A. S. (2008). Detection of two cracks in a rotor-bearing system using amplitude deviation curve. *Journal of Sound and Vibration*, 314(3-5), 457–464.
- Babu, T. R., Srikanth, S. and Sekhar, A. S. (2008). Hilbert-Huang transform for detection and monitoring of crack in a transient rotor. *Mechanical Systems and Signal Processing*, 22(4), 905–914.
- Baliño, J. L. (2009). Galerkin finite element method for incompressible thermofluid flows framed within the bond graph theory. *Simulation Modelling Practice and Theory*, 17(1), 35-49.

- Banarjee, N., and Karmakar, R. (2007). Bond graph modeling of rail wheelset on curved track. *Simulation, Transaction of Society of Modeling and Simulation International*, 83(10), 695-706.
- Banarjee, N., and Karmakar, R. (2007). Modelling of a free rail wheelset using non-linear creep force, *International Journal of Heavy Vehicle Systems*, 21(4), 310-327.
- Banarjee, N., Saha, A. K, Karmakar, R., and Bhattacharyya, R. (2009). Bond graph modelling of a railway track on curved track. *In proceeding of Simulation Modeling practice and theory*, 22-34.
- Bera, T. K., Bhattacharya, K., and Samantaray, A. K. (2011). Evaluation of antilock braking system with an integrated model of full vehicle system dynamics. *Simulation Modelling Practice and Theory*, 19, 2131-2150.
- Bovsunovsky, A. (2012). Energy dissipation in the non-propagating surface cracks in steel round bar at torsional vibration. *Engineering Fracture Mechanics*, 92, 32–39.
- Borutzky, W. (2015). Bond graph model-based fault diagnosis of hybrid systems. *Springer International Publishing*, ISBN - 978-3-319-11859-8, 277.
- Breedveld, P. C., and Dauphin-Tanguy, G. (1992). Bond graphs for engineers. *North-Holland*, Amsterdam.
- Breedveld, P. C., and Hogan, N. (1994). Multibond graph representation of Lagrangian mechanics: The elimination of euler junction structure. *Proc. Math. Mod'94, International Association for Mathematics and Computers in Simulation (IMACS) Symposium on Mathematical Modelling*, Vienna, Austria, 24-28.
- Brown, F.T. (1981). Energy- based modeling and quasi-coordinates. *Journal of the Dynamic Systems, Measurement, and Control, ASME Trans.*, 103(1), 5-13.
- Brown, F. T. (2006). Engineering system dynamics. *Marcel Dekker, Inc*, New York.
- Calkin, M. G. (2000). Lagrangian and Hamiltonian Mechanics, *Allied Publisher Limited, First Indian Reprint*, New Delhi, 2000.
- Cellier, F. E. (1991) Continuous System Modeling, *Springer-Verlag*, New York.

- Chasalevris, A.C. and Papadopoulos, C.A. (2008). Coupled horizontal and vertical bending vibrations of a stationary shaft with two cracks. *Journal of Sound and Vibration*, 309(3-5), 507–528.
- Chasalevris, A.C. and Papadopoulos, C.A. (2009). A continuous model approach for cross-coupled bending vibrations of a rotor-bearing system with a transverse breathing crack. *Mechanism and Machine Theory*, 44(6), 1176–1191.
- Cheng, L., Li, N., Chen, X.-F., and He, Z.-J. (2011). The influence of crack breathing and imbalance orientation angle on the characteristics of the critical speed of a cracked rotor. *Journal of Sound and Vibration*, 330(9), 2031–2048.
- Cho, W. (1998). A bond graph approach to the modeling of general multi body dynamic systems. *Journal of Mechanical Science and Technology*, 12(5), 888-898.
- Darpe A. K. (2007). A novel way to detect transverse surface crack in rotating shaft. *Journal of Sound and Vibration*, 305(1-2), 151-171.
- Darpe, A.K. (2007). Coupled vibrations of a rotor with slant crack. *Journal of Sound and Vibration*, 305(1-2), 172-193.
- Darpe, A.K., Gupta, K., and Chawla, A. (2003). Experimental investigations of the response of a Cracked rotor to periodic axial excitation. *Journal of Sound and Vibration*, 260(2), 265-286.
- Darpe, A. K., Gupta, K., and Chawla, A. (2004). Coupled bending longitudinal and torsional vibrations of a cracked rotor. *Journal of Sound and Vibration*, 269 (1-2), 33-60.
- Darpe, A.K., Gupta, K., and Chawla, A. (2006). Dynamics of bowed rotor with a transverse surface crack. *Journal of Sound and Vibration*, 296(4-5), 888-907.
- Dasgupta, K., and Murrenhoff, H. (2011). Modelling and dynamics of a servo-valve controlled hydraulic motor by bondgraph. *Mechanism and Machine Theory*, 46(7), 1016-1035.
- Deng, X., and Wang, Q. (1998). Crack detection using spatial measurements and wavelets analysis. *International Journal of Fracture*, 91(2), 23–28.
- Dijk, J. V. (1994). On the role of bond graph causality in modelling mechatronic systems. *Ph.d thesis, University of Twente, Enschede, Netherlands*.

- Dimarogonas, A. D. (1996). Vibration of cracked structures: A state of the art review. *Engineering Fracture Mechanics*, 55(5), 831-857.
- Dimarogonas, A. D., and Papadopoulos, C.A. (1983). Vibration of cracked shaft in bending. *Journal of Sound and Vibration*, 91(4), 583-593.
- Dimarogonas, A. D. and Papadopoulos, C. A. (1987). Coupling of bending and torsional vibration of a cracked Timoshenko shaft" *Ingenieur Archiv, springer*, 57(4), 257-266.
- Djukic, D.S. (1973). A procedure for finding first integrals of mechanical systems with gauge-variant Lagrangians. *International Journal of Nonlinear Mechanics*, 8(5), 479-488.
- Djukic, D.S., and Vujanovic, B. (1975). Noether's theory in classical nonconservative mechanics. *Acta Mechanica*, 23(1-2), 17-27.
- Dong, H.B., Chen, X.F., Li, B., Qi, K.Y. and He, Z.J. (2009). Rotor crack detection based on high-precision modal parameter identification method and wavelet finite element model. *Mechanical Systems and Signal Processing*, 23(3), 869-883.
- Durali, M. and Borhan, H. (2003). Discrete dynamic modeling of shafts with transverse cracks using bond graph. *Proceedings of DETC.03, ASME 2003 International Design Engineering Technical Conferences and Computers and Information in Engineering Conference, Chicago, Sharif University of Technology, Illinois, USA, 1579-1584.*
- Fakri, A., and Vilakazi, J.P. (2014). Wheelchair and electric drive add-on a whole bond graph modelling. *Proceedings of the 11th International Conference on Bond Graph Modeling and Simulation (ICBGM'14).*
- Gasch, R. (1993). A survey of the dynamic behavior of a simple rotating shaft with a transverse crack. *Journal of Sound and Vibration*, 160(2), 313-332.
- Gasch, R. (2008). Dynamic behaviour of the Laval rotor with a transverse crack. *Mechanical Systems and Signal Processing*, 22(4), 790-804.
- Gawthrop, P., and Smith, L. (1996). Meta modeling: Bond graphs and dynamic Systems. *Prentice-Hall, NJ, USA.*
- Georgantzinou, S.K., and Anifantis, N.K. (2008). An insight into the breathing mechanism of a crack in a rotating shaft," *Journal of Sound and Vibration*, 318(1-2), 279-295.

- Goldstein, H. (1980). *Classical Mechanics*, Addison-Wesley, MA.
- Gosiewski, Z. (2009). Control oriented approach to the rotor dynamics. *IUTAM Symposium on Emerging Trend in Rotor Dynamics*, Springer, 63-70.
- Granda, J. J. (1985). Computer generation of physical system differential equations using bond graphs. *Journal of the Franklin Institute*, 319(1-2), 243-255.
- Guo, C., Al-Shudeifat, M. A., Yan, J., Bergman, L. A., McFarland, D. M., and Butcher, E. A. (2013). Stability analysis for transverse breathing cracks in rotor systems. *European Journal of Mechanics A/Solids*, 42, 27-34.
- Guo, C., Yan, J., and Yang, W. (2017). Crack detection for a Jeffcott rotor with a transverse crack: An experimental investigation. *Mechanical Systems and Signal Processing*, 83, 260-271.
- Guo, D., and Peng, Z. K. (2007). Vibration analysis of a cracked rotor using Hilbert-Hung transform. *Mechanical System and Signal Processing*, 21(8), 3030-3041.
- Han, Q., and Chu, F. (2011). Local flexibility of an elliptical cracked shaft under bending and tension. *Mechanical Systems and Signal Processing*, 25(8), 3198-3203.
- Han, Q., Zhao, J., and Chu, F. (2012). Dynamic analysis of a geared rotor system considering a slant crack on the shaft. *Journal of Sound and Vibration*, 331(26), 5803-5823.
- Hassani, S. (2013). *Mathematical physics: A modern introduction to its foundations*. Springer international.
- Hou, J. F. (2006). Cracking induced mistuning in bladed disk. *AIAA Journal*, 44(11), 2542-2546.
- Ichimonji, M., and Watanabe, S. (1988). The dynamics of a rotor system with a shaft having a slant crack: A qualitative analysis using a simple rotor model. *JSME International Journal Ser. 3, Vibration, Control Engineering, Engineering for Industry*, 31(4), 712-718.
- Ishida, Y. and Inoue, T. (2006). Detection of a rotor crack using a harmonic excitation and nonlinear vibration analysis. *Journal of Vibration and Acoustics*, 128(6), 741-749.

- Jain, A. K., Rastogi, V., and Agrawal, A. K. (2018). A novel approach to study effects of asymmetric stiffness on parametric instabilities of multi-rotor-system. *Journal of Sound and Vibration*, 413, 159–172.
- Jain, J. R., and Kundra, T. K. (2004). Model based online diagnosis of unbalance and transverse fatigue crack in rotor systems. *Mechanics Research Communications*, 31(5), 557-568.
- Jun, O. S., and Gadala, M. S. (2008). Dynamic behavior analysis of cracked rotor. *Journal of Sound and Vibration*, 309(1-2), 210–245.
- Jun, O. S., Eun, H. J., Earmme, Y. Y., and Lee, C. W. (1992). Modelling and vibration analysis of a simple rotor with breathing crack. *Journal of Sound and Vibration*, 155(2), 273-290.
- Karnopp, D. C. (1977). Lagrange's equations for complex bond graph systems. *Journal of Dynamic Systems, Measurement, and Control*, 99(4), 300–306.
- Karnopp, D. C. (1983). Alternative bond graph causal patterns and equation formulations for dynamic systems. *Journal of the Dynamic Systems, Measurement, and Control, ASME Trans.*, 105(1), 58-63.
- Karnopp, D. C., Margolis, D. L., and Roasenberg, R. C. (1990). System dynamics: A unified Approach. *John-Wiley and Sons Inc. publications, USA*.
- Karthikeyan, M., Tiwari, R., and Talukdar, S. (2007). Crack localization and sizing in a beam based on the free and forced response measurements. *Mechanical Systems and Signal Processing*, 21(3), 1362-1385.
- Khurshid, A., and Malik, M. A. (2007). Bond graph modeling and simulation of impact dynamics of a car crash. *Paper presented in International Bhurban Conference on Applied Science & technology*.
- Krodkiewski, J. M. (2007). Dynamics of Rotors. *The University of Melbourne, Australia*.
- Kumar, C. (2013). Investigation of dynamics of cracked rotor through extended Lagrangian Mechanics, *Ph. D. thesis, SLIET, Longowal*.
- Kumar, C. and Rastogi, V. (2009). A brief review on dynamics of cracked rotor. *International Journal of Rotating machinery*, doi:10.1155/2009/758108, 1-6.

- Kumar, C., and Rastogi, V. (2012). Vibration analysis of multi-rotor system through extended Lagrangian formalism. *World Journal of Modelling and Simulation*, 8(2), 103 – 110.
- Lagrange, J. L. (1788). *Mechanique analytique*, Paris
- Lee, S.-Y., and Cheng, Y.-C. (2005). Hunting stability analysis of high-speed railway vehicle trucks on tangent tracks. *Journal of Sound and Vibration*, 282 (3-5), 881-898.
- Li, B., Zhang, C., and He, Z. (2012). HHT-based crack identification method for start-up rotor. *Frontiers of Mechanical Engineering, Springer*, 7(3), 300–304.
- Li, Y., Fantuzzi, N., and Tornabene, F. (2013). On mixed mode crack initiation and direction in shafts: Strain energy density factor and maximum tangential stress criteria. *Engineering Fracture Mechanics*, 109, 273–289.
- Lin, Y., and Chu, F. (2009). Numerical and experimental investigations of flexural vibrations of a rotor system with transverse or slant crack. *Journal of Sound and Vibration*, 324(1), 107–125.
- Lin, L., and Chu, F. (2012). HHT-based AE characteristics of natural fatigue cracks in rotating shafts. *Mechanical Systems and Signal Processing*, 26, 181–189.
- Liong, R. T., and Proppe, C. (2013). Application of the cohesive zone model for the evaluation of stiffness losses in a rotor with a transverse breathing crack. *Journal of Sound and Vibration*, 332(8), 2098–2110.
- Lozano, J., Félez, J., Mera, J. M. and de Dios Sanz, J. (2010). Using bond-graph technique for modelling and simulating railway drive systems. *Paper presented at the 2010 12th International Conference on Computer Modelling and Simulation (UKSim)*.
- Margolis, D., and Shim, T. (2001). Bond graph model incorporating sensors, actuators, and vehicle dynamics for developing controllers for vehicle safety. *Journal of the Franklin Institute*, 338(1), 21-34.
- Mayes, I. W. and Davis, W. G. R. (1984). Analysis of the response of a multi-rotor-bearing system containing a transverse crack in a rotor” *ASME Journal of Vibration, Acoustics, Stress, and Reliability in Design*, 1106(1), 139-145.

- Mukherjee, A. (1994). Junction structures of bondgraph theory from analytical mechanics viewpoint. *Proc. of CISS-1st Conference of International Simulation Societies*. Zurich, Switzerland, 661-666.
- Mukherjee, A. (2001). The issue of invariants of motion for general class of symmetric systems through bond graph and umbra-Lagrangian. *Proc. of Int. Conf. of Bond Graph Modelling and Simulation ICBGM'01*, Phoenix, Arizona, USA, 295.
- Mukherjee, A., and Karmakar, R. (2000). Modelling and simulation of engineering system through bond graph. *Narosa publishing House*, New Delhi, reprinted by CRC press for North America and by Alpha Science for Europe.
- Mukherjee, A., and Samantaray, A. K. (1997). Umbra-Lagrange's equations through bond graphs. *Proceedings of International Conference on Bond Graph Modeling and Simulation (ICBGM)*, Phoenix, Arizona, USA, 168-174.
- Mukherjee, A., and Samantaray, A. K. (2006). SYMBOLS- Shakti User's Manual. *High tech consultants, STEP*, Indian Institute of technology, Kharagpur, India.
- Mukherjee, A., Rastogi, V., and Dasgupta, A. (2006). A methodology for finding invariants of motion for asymmetric systems with Gauge-transformed umbra Lagrangian generated by bond graphs. *Simulation*, 82(4), 207-226.
- Mukherjee, A., Rastogi, V., and Dasgupta, A. (2007). A study of a bi-symmetric electro-mechanical system through umbra Lagrangian generated by bondgraphs, and Noether's theorem. *Simulation*, 83(9), 611-630.
- Mukherjee, A., Rastogi, V., and Dasgupta, A. (2009). Extension of Lagrangian-Hamiltonian mechanics for continuous systems: Investigation of dynamics of a one-dimensional internally damped rotor driven through a dissipative coupling. *Non-linear Dynamics, Springer*, 58 (1-2), 107-127.
- Mukherjee, A., Rastogi, V., and Dasgupta, A. (2011) "Revisiting umbra Lagrangian Hamiltonian mechanics: Its variational foundation and extension of Noether's theorem and Poincare-cartan integral" *International Journal of Non linear mechanics*, 46(5), 745-757.
- Munkres, J. R. (1994). *Topology: A First Course*. *Prentice Hall of India Private Limited*, New Delhi, India.

- Nacusse, M., and Junco, S., J. (2015). Generalized controlled switched bond graph junctions. *Proceedings of the Institution of Mechanical Engineers, Part I: Journal of Systems and Control Engineering*, 229(9), 851-866, doi.org/10.1177/0959651815583593.
- Nandi, A. (2004). Reduction of finite element equation for a rotor model on non-isotropic spring support in a rotating frame. *Finite Elements in Analysis and Design*, 40(9-10), 935-952.
- Noether, E. (1918). Invariant Variations problem. *Ges. Wiss. Gottington*, 2, 235.
- Noether, E. (1971). Invariant variation problems, *Transport Theory and Statistical Physics*, 1(3), 186–207.
- Olver, P. J., (1993)“Applications of Lie Groups to Differential Equations” Springer-Verlag New York.
- Pacejka, H. B. (1987). Bond graph in vehicle dynamics. *Vehicle System Dynamics, International Journal of Vehicle Mechanics and Mobility*, 16(sup1), 263-287.
- Papadopoulos, C.A. (2008). The strain energy release approach for modeling cracks in rotors: a state of the art review. *Mechanical Systems and Signal Processing*. 22, 763–789.
- Papadopoulos, C. A., and Dimarogonas, A. D. (1987). Coupled longitudinal and bending vibrations of a cracked shaft. *Journal of Vibration, Acoustics, Stress and Reliability in Design*, 117, 81-93.
- Patel, T. H. and Darpe, A. K. (2008). Influence of crack breathing model on nonlinear dynamics of a cracked rotor, *Journal of Sound and Vibration*, 311 (3-5), 953-972.
- Patel, T. H. and Darpe, A. K. (2009). Coupled bending-torsional vibration analysis of rotor with rub and crack,” *Journal of Sound and Vibration*, 326(3-5), 740–752.
- Pathak, P. M., Mukherjee, A., and Dasgupta, A. (2009). Interaction torque control by impedance control of space robots. *Simulation*, 85(7), 451-459.
- Paynter, H. M. (1961). Analysis and design of engineering systems. *M. I. T. Press*, Cambridge.
- Pennacchi, P., Bachschmid, N., Vania, A., Zanetta, G. A., and Gregori, L. (2006). Use of modal representation for the supporting structure in model-based fault identification of large rotating machinery: part1-theoretical remarks. *Mechanical Systems and Signal Processing*, 20(3), 662-681.

- Prabhakar, S., Sekhar, A. S., and Mohanty, A. R. (2001). Detection and monitoring of cracks in a rotor-bearing system using wavelet transforms. *Journal of the Mechanical Systems and Signal Processing*, 15(2), 447–450.
- Prigogine, I. (1967). Structure dissipation and life, theoretical physics and biology. *Versailles*.
- Rastogi, V. (2005). Extension of Lagrangian-Hamiltonian mechanics, study of symmetries and invariants, *Ph. D. thesis., Indian Institute of Technology, Kharagpur*.
- Rastogi, V. (2016). Effects of discrete damping on the dynamic behaviour of rotating shaft through extended Lagrangian formulation. *Journal of Theoretical and Applied Mechanics*, 46(3), 35-64.
- Rastogi, V., and Kumar, C. (2009). Investigation of dynamics of asymmetric rotor through Lagrangian formalism. *Proc. of the IUTAM Symposium on Emerging Trends in Rotor Dynamics (IURATOR '09)*, IIT Delhi, Delhi, India.
- Rastogi, V., and Mukherjee, A. (2011). Conservation laws for Gauge-variant umbra-Lagrangian in classical mechanics using bond graphs. *Simulation*, 87(4), 301–312.
- Ricci, R., and Pennacchi, P. (2012). Discussion of the dynamic stability of a multi-degree-of-freedom rotor system affected by a transverse crack. *Mechanism and Machine Theory*, 58, 82–100.
- Rubio, L., Munoz-Abella, B., and Loaiza, G. (2011). Static behaviour of a shaft with an elliptical crack. *Mechanical Systems and Signal Processing*, 25(5), 1674–1686.
- Sabnavis, G., Kirk, R. G., Kasarda M., and Quinn, D. D. (2004). Cracked shaft detection and diagnostics: A literature review. *The Shock and Vibration Digest*, 36(4), 287-296.
- Saha, A. K., Karmakar, R., and Bhattacharyya R. (2008). Lateral dynamics of a railway truck on flexible tangent track. *Vibration Problems ICOVP-2007*, 339-345: Springer.
- Saridakis, K.M., Chasalevris, A.C., Papadopoulos, C.A. and Dentsoras, A.J. (2008). Applying neural networks, genetic algorithms and fuzzy logic for the identification of cracks in shafts by using coupled response measurements. *Computers and Structures*, 86(11-12), 1318–1338.

- Sawicki, J. T., Sen, A.K. and Litak, G. (2009). Multi resolution wavelet analysis of the dynamics of a cracked rotor. *International Journal of Rotating Machinery, Hindawi publication ,USA, Article ID 265198, 8.*
- Sekhar, A. S. (1999). Vibration characteristics of a cracked rotor with two open cracks. *Journal of Sound and Vibration, 223(4), 497-512.*
- Sekhar, A. S. (2003). Crack detection through wavelet transform for a run-up rotor.” *Journal of Sound and Vibration. 259(2), 461–472.*
- Sekhar, A. S. (2003). Identification of crack in a rotor system using a model-based wavelet approach. *International Journal of Structural Health Monitoring, 2(4), 293–308.*
- Sekhar, A. S. (2011). Some recent studies on cracked rotors. *IUTAM Symposium on Emerging Trends in Rotor Dynamics, IUTAM Conference Proceeding, 491-503.*
- Sekhar, A.S., and Dey, J. K., (2000). Effects of cracks on rotor system instability,” *Mechanism and Machine Theory, 35(12), 1657–1674.*
- Sekhar, A. S., and Prabhu, B. S. (1994). Vibration and stress fluctuation in cracked shafts. *Journal of Sound and Vibration, 169(15), 655-667.*
- Sekhar, A. S., and Prasad, B. P. (1999). Dynamic analysis of a rotor system considering a slant crack in the shaft. *Journal of Sound and Vibration, 223(4), 497-512.*
- Silani, M., Ziaei-Rad., S., and Talebi, H. (2013). Vibration analysis of rotating systems with open and breathing cracks. *Applied Mathematical Modelling, 37(24), 9907-9921.*
- Singh, S., and Tiwari, R. (2018). Model based identification of crack and bearing dynamic parameters in flexible rotor systems supported with an auxiliary active magnetic bearing”, *Mechanism and Machine Theory, 122, 292-307.*
- Singh, S. K., and Tiwari, R. (2010). Identification of a multi-crack in a shaft system using transverse frequency response functions. *Mechanism and Machine Theory, 45(12), 1813–1827.*
- Sinou, J-J. (2008). Detection of cracks in rotor based on the 2X and 3X super-harmonic frequency components and the crack–unbalance interactions. *Communications in Nonlinear Science and Numerical Simulation, 13, 2024–2040.*

- Stoisser, C.M., and Audebert, S. (2008). A comprehensive theoretical, numerical and experimental approach for crack detection in power plant rotating machinery. *Mechanical Systems and Signal Processing*, 22(4), 818–844.
- Szolc, T., Tazowski, P., Stocki, R., and Knabel, J. (2009). Damage identification in vibrating rotor-shaft systems by efficient sampling approach. *Mechanical Systems and Signal Processing*, 23(5), 1615–1633.
- Thoma, J. U. (1990). Simulation by bond graphs: Introduction to a graphical method. *Springer Verlag*, Berlin, New York.
- Tsai, T. C., and Wang, Y. Z. (1997). The vibration of a multi-crack rotor. *International Journal of Mechanical Sciences*, 39(9), 1037–1053.
- Vaz, A., Kansal, H., and Singla, A. (2003). Some aspects in the bond graph modelling of robotic manipulators: angular velocities from symbolic manipulation of rotation matrices. *Proceedings of the Institution of Mechanical Engineers, Part F: Journal of Rail and rapid Transit*, 208(1), 1-13.
- Vujanovic, B., and Jones, S. E. (1989). *Variational Methods in Non conservative Phenomena*, Academic press, Boston.
- Vujanovic, B. (1978). Conservation laws of dynamical systems via d'Alembert's principle. *International Journal of Nonlinear Mechanics*, 13, 185-197.
- Wauer, J. (1990). On the dynamics of cracked rotors, A literature survey. *Applied Mechanics Reviews, Transactions of the ASME*, 43(1), 13-17.
- Weyl, H. (1992). *Symmetry*. Princeton University press, New jersey, USA.
- Xiang, J., Zhong, Y., Chen, X., and He, Z. (2008). Crack detection in a shaft by combination of wavelet-based elements and genetic algorithm. *International Journal of Solids and Structures*, 45(17), 4782–4795.
- Xiang, J. W., Chen, X. F., Li, B., He, Y. M. and He, Z. J. (2006). Identification of crack in a beam based on the finite element method of a B-spline wavelet on the interval. *Journal of Sound and Vibration*, 296(4-5), 1046-1052.
- Zhou, T., Sun, Z., Xu, Z and Han, W. (2004). Experimental analysis of cracked rotor, *Journal of Dynamic Systems, Measurement and Control*, 127(3), 313-320.

Publication from the Present Work

International Journals

1. Anuj Kumar Jain, Vikas Rastogi, Atul Kumar Agrawal, 2018 “A novel approach to study effects of asymmetric stiffness on parametric instabilities of multi-rotor-system”, Journal of Sound and Vibration, Volume 413, pp 159-172 (Thomson Reuter “Web of Science”, Impact factor: 2.593, Pub: Elsevier).
2. Anuj Kumar Jain, Vikas Rastogi, Atul Kumar Agrawal, 2016, “Experimental investigation of vibration analysis of multi-crack rotor shaft”, Procedia Engineering, Volume 144, 1451 – 1458, (SCImago Journal Rank (SJR): 0.282, Pub: Elsevier).
3. Anuj Kumar Jain, Vikas Rastogi, Atul Kumar Agrawal, 2016, “Investigation of dynamics of multi crack rotating shaft through extended Lagrangian-Hamiltonian formulism”, Nonlinear Dynamics (Communicated).